

Advanced characterization methods for self-assembled organization on nanoparticles

THÈSE N° 8181 (2018)

PRÉSENTÉE LE 16 MARS 2018

À LA FACULTÉ DES SCIENCES ET TECHNIQUES DE L'INGÉNIEUR
LABORATOIRE DES NANOMATÉRIAUX SUPRAMOLÉCULAIRES ET INTERFACES - CHAIRE CONSTELLUM
PROGRAMME DOCTORAL EN SCIENCE ET GÉNIE DES MATÉRIAUX

ÉCOLE POLYTECHNIQUE FÉDÉRALE DE LAUSANNE

POUR L'OBTENTION DU GRADE DE DOCTEUR ÈS SCIENCES

PAR

Zhi LUO

acceptée sur proposition du jury:

Prof. D. Grondler, président du jury
Prof. F. Stellacci, directeur de thèse
Prof. X. Zhang, rapporteur
Prof. X. Liu, rapporteur
Prof. R. Mezzenga, rapporteur



ÉCOLE POLYTECHNIQUE
FÉDÉRALE DE LAUSANNE

Suisse
2018

Acknowledgements

Time flies so fast. I still remember the first day when I came to Lausanne four years ago. The campus, the lake, the city and the country are the reason why I decided to start my PhD here. But it is all my friends, colleagues and families who have supported and accompanied me through this wonderful journey. I would like to thank everyone in my life during the past four years, especially...

My supervisor, Professor Francesco Stellacci. Throughout the four years, I have always felt being trusted, supported and motivated. Without the guidance and the great opportunities he provided, none of the works could have been possible. For me, he is not only a mentor in science, his passion and optimistic attitude are the valuable sources in my life.

All the collaborators that I have worked with. I feel extremely fortunate to be supported by so many people around world during my PhD. Prof. Paola Posocco and Domenico Marson at Trieste are the most efficient, kind and supportive collaborators I ever have. Dr. Dmitri Svergun and his group in Hamburg are the ones from whom I learned most of the things in small angle scattering. Prof. Sylvie Roke and her group at EPFL are the people that I sincerely admire. Their lab is the place that I spent the most of the time except SUNMIL at EPFL. The help from Dr. Tamim Darwish and his group in Sydney on deuterated molecules is absolutely indispensable for my PhD research. The beamline scientists, Dr. Aurel Radulescu at MLZ and Dr. Joachim Kohlbrecher at PSI, helped me with all the scattering experiments. I truly appreciate their supports and discussions. Dr. David Wilkins and Prof. Michele Ceriotti have the most amazing expertise and could not be replaced in my work. There are many more collaborators, for example, Dr. Laure Menin and Dr. Daniel Ortiz at the mass spectrometry facilities, Dr. Florence Pojer and Aline Reynaud at the crystallization facilities, Dr. Sandor Balog at Fribourg, Prof. Raffaella Buonsanti and Dr. Anna Loiudice at Sion, Prof. Rongchao Jin and his group at CMU, Dr. Lionel Porcar at ILL and a lot of others. I am always proud to have worked with them.

All the members of SUNMIL group. I have received incredible amount of assistances from Benjamin, Paulo and Kellen to start my PhD on the correct track; incredible amount of guidance and support from Quy to accomplish many projects; incredible amount of help and discussions with Anna to deal with all the difficult tasks. I feel happy to have spent four years with this wonderful group of people: Evi, Sergio, Marie, Nikos, Ozgun, Ahmet, Elif, Ula,

Pelin, Marta, Simone, Matteo, Lina, Huayan, Suiyang, Xiaowang, Pratap, Badra, Stefan, Maria, Sam, Rosie, Matej, Iuliia, Marta, Shun, Mauro, Javier, Kislun, Yun and also Chiara.

All my Chinese friends. I've had so much happy and special times with Jing and Ye. Huayan, Xiaotong, Suiyang and Xiaowang are like my sisters and brothers. Xiaoyu, Jian, Shun, Huachuan, Hongzhe, Xi, Xiaokang, Jun, Xiao, Yanfei, Yue, Hao and many others have made up the beautiful memories of mine in Switzerland.

Last, my beloved family. I am deeply grateful to my parents for their unconditional love, sacrifice and support for any single decision I made. And I am especially thankful for my lovely wife. We cross half the globe together and will continue the journey forever.

Abstract

The complex organizations of amino acid residues on protein surfaces give rise to a wide space of functions for proteins. Great efforts are devoted in biology to understand such structure-property relationships. Many advanced characterization techniques have been developed for this purpose. Nanomaterials are regarded as a close resemblance to proteins, as they share similar sizes and, when coated with different types of ligand molecules, can present patchy surfaces (e.g. stripe-like, patchy, or Janus) that bear some similarities to the surfaces of proteins. So far, most characterization methods developed for nanoparticles come from classic material sciences and consequently deliver a precise description of the inorganic and well defined core of the nanoparticles. Yet big challenges remain to accurately describe the morphologies of the ligand shell of nanoparticles that is closer to a biological entity rather than small sized materials.

This thesis establishes two new techniques for the characterization of the morphology of the ligand shell of nanoparticles. The first stems directly from structural biology, i.e. small angle neutron scattering combined with *ab initio* reconstructions. 3D models could be obtained by fitting the scattering data, allowing for the quantitative determination of different morphologies. The second one is based on the statistical analysis of the MALDI-TOF MS spectra. Adopting Monte Carlo calculations, the structures of mixed ligands could be visualized by fitting the fragmentation patterns that represents a sampling of the nanoparticle surfaces.

Thanks to the advancement in characterization provided by these newly development methods, two phenomena are studied in this thesis. First, the evolution of the ligand shell morphology during a ligand replacement reaction called place-exchange is uncovered for the first time. Also the evolution of the ligand shell morphology upon gentle heating is uncovered. These results provide a new way to control the morphology of the nanoparticle ligand shells.

Second, an in-depth study of the water structure around patchy surfaces is presented. Two nanoparticles with the same core size and composition but varying in the ligand shell structures are synthesized. The morphologies of the heterogeneous nanoparticle surfaces on top of chemical nature are thus directly correlated to the structure of interfacial water. This work offers molecular explanation on the structural factor in the interfacial energy of multiple component systems, which has not been discussed in physical chemistry textbooks before.

This latter work offers new insights on how patchy nanoparticles could be used as model systems to understand the interfacial properties of proteins, which are often very difficult to be studied directly due to the complex and dynamic structures of the proteins.

Keywords: Mixed self-assembled monolayer; Small angle neutron scattering; Mass spectrometry; Monte Carlo calculations; Ligand exchange reaction; Ligand organization control; Interfacial water structure.

Abstrait

Les organisations complexes des résidus d'acides aminés sur les surfaces protéiques donnent lieu à un large espace de fonctions pour les protéines. De grands efforts sont consacrés en biologie pour comprendre ces relations structure-propriété. De nombreuses techniques de caractérisation avancées ont été développées à cette fin. Les nanomatériaux sont considérés comme une ressemblance étroite avec les protéines, car ils partagent des tailles similaires et, lorsqu'ils sont revêtus de différents types de molécules de ligand, peuvent présenter des surfaces inégales (par exemple des bandes, des taches ou des Janus) qui ressemblent aux surfaces des protéines. Jusqu'à présent, la plupart des méthodes de caractérisation développées pour les nanoparticules proviennent des sciences classiques des matériaux et fournissent par conséquent une description précise du noyau inorganique et bien défini des nanoparticules. Cependant, de grands défis demeurent pour décrire avec précision les morphologies de la couche de ligand des nanoparticules qui sont plus proches d'une entité biologique que de matériaux de petite taille.

Cette thèse établit deux nouvelles techniques pour la caractérisation de la morphologie de la coquille de ligand des nanoparticules. Le premier provient directement de la biologie structurale, c'est-à-dire de la diffusion des neutrons aux petits angles combinée à des reconstructions *ab initio*. Des modèles 3D pourraient être obtenus en ajustant les données de diffusion, permettant la détermination quantitative de différentes morphologies. Le second est basé sur l'analyse statistique des spectres SM MALDI-TOF. En adoptant des calculs de Monte Carlo, les structures des ligands mixtes ont pu être visualisées en ajustant les modèles de fragmentation qui représentent un échantillonnage des surfaces des nanoparticules.

Grâce à l'avancement de la caractérisation fournie par ces nouvelles méthodes de développement, deux phénomènes sont étudiés dans cette thèse. Tout d'abord, l'évolution de la morphologie de la coquille de ligand au cours d'une réaction de remplacement de ligand appelée place-échange est découvert pour la première fois. De même, l'évolution de la morphologie de l'enveloppe du ligand lors d'un chauffage doux est découverte. Ces résultats fournissent une nouvelle façon de contrôler la morphologie des enveloppes de ligands de nanoparticules.

Deuxièmement, une étude approfondie de la structure de l'eau autour des surfaces inégales est présentée. Deux nanoparticules ayant la même taille de noyau et la même composition mais

variant dans les structures de l'enveloppe du ligand sont synthétisées. Les morphologies des surfaces de nanoparticules hétérogènes en plus de la nature chimique sont donc directement corrélées à la structure de l'eau interfaciale. Ce travail offre une explication moléculaire sur le facteur structurel dans l'énergie interfaciale des systèmes à composants multiples, qui n'a pas été discutée dans les manuels de chimie physique avant.

Ce dernier travail offre de nouvelles perspectives sur la façon dont les nanoparticules peuvent être utilisées comme systèmes modèles pour comprendre les propriétés interfaciales des protéines, qui sont souvent très difficiles à étudier directement en raison des structures complexes et dynamiques des protéines.

Mots-clés: monocouche mélangé auto-assemblé; Diffusion de neutrons aux petits angles; Spectrométrie de masse; Calculs de Monte Carlo; Réaction d'échange de ligands; Contrôle de l'organisation du ligand; Structure de l'eau interfaciale.

Table of Contents

Acknowledgements	iv
Abstract.....	vi
Abstrait	viii
Chapter 1 Self-assembled monolayers on nanoparticles and their characterization	1
1.1 Self-assembled monolayers on nanoparticles	3
1.2 Thermodynamic considerations on the organization of mixed ligands.....	4
1.3 Unique structure-property relationship of mixed ligand nanoparticles.....	6
1.4 Synthesis of mixed ligand nanoparticles	11
1.5 Characterization techniques for mixed ligand nanoparticles	13
1.5.1 Microscopy	13
1.5.2 Spectroscopic characterization of mixed ligand nanoparticles.....	19
Chapter 2 Analogy in proteins and nanoparticles: insights from structural biology.....	27
2.1 Protein as a patchy nanoparticle.....	28
2.2 Solution X-ray and neutron scattering of biomacromolecules.....	33
2.2.1 Experimental setup for small angle scattering.....	34
2.2.2 Basic concepts and overall parameters	35
2.2.3 <i>Ab initio</i> and other advanced data analysis methods	40
2.2.4 Recent advances in the application of SAS	43
2.3 Mass spectrometry study of the structure and dynamics of proteins	44
2.3.1 Chemical cross linking	45
2.3.2 Hydrogen exchange and chemical labelling mass spectrometry	46
2.4 Scope of this thesis.....	48
Chapter 3 Quantitative 3D analysis of the morphology of mixed ligand nanoparticles by small angle scattering	51
3.1 Introduction	52
3.2 Test of the SANS/MONSA method	54
3.3 Robustness of the method	57
3.4 Random morphology.....	59
3.5 Janus morphology	59
3.6 Stripe-like morphology	61
3.7 Bandage-like morphology	65

3.8 Ternary self-assembled monolayer	67
3.9 Analysis of SANS data and MONSA modelling	68
3.10 Interpretation of SANS data	69
3.11 Polydispersity and ensemble based analysis	69
3.12 Limitations and scope of the technique	74
3.13 Conclusion on SANS study of mixed ligand nanoparticles	75
3.14 Materials and Methods	76
Chapter 4 Solution structures and molecular weight determination of atomically precise nanoclusters determined by small angle neutron scattering.....	85
4.1 Introduction	86
4.2 SANS analysis of silver nanoclusters with known crystal structures	87
4.3 SANS analysis on the solution structure of gold nanoclusters.....	90
4.4 Power-law relationship for the molecular weight of nanoclusters.....	91
4.5 Materials and Methods	92
Chapter 5 Reverse Monte Carlo analysis of MALDI-TOF spectra	95
5.1 Reverse Monte Carlo and description of the algorithm	97
5.2 Validity and efficiency of the algorithm	99
5.3 Analysis of experimental MALDI data for silver nanoparticles	103
5.4 Comparison with SANS results	106
5.5 Materials and methods	108
5.5.1 Synthesis of mixed-ligand silver nanoparticles (Ag NPs).....	108
5.5.2 Preparation of samples for MALDI-MS analysis.....	109
Chapter 6 Control the morphology of mixed ligand nanoparticles	111
6.1 Evolution of the ligand shell morphology during ligand exchange reactions.....	113
6.1.1 Ligand exchange reaction on nanoparticles.....	113
6.1.2 Monitoring the morphologies	115
6.2 Effect of thermal annealing on the ligand shell morphologies.....	121
6.2.1 Synthesis and annealing of the nanoparticles	122
6.2.2 Morphology evolution during heating and annealing.....	124
6.2.3 Thermal treatment of other ligand pair protected nanoparticles.....	127
6.3 Materials and Methods	129
Chapter 7 Structure of interfacial water at nanoscale heterogeneous surfaces.....	137
7.1 Introduction to the non-additivity of interfacial energy	138
7.2 Model patchy nanoparticles	139

7.3 Structure of interfacial water surrounding the patchy surfaces.....	142
7.4 Molecular interpretation of the non-additivity	144
7.5 Materials and Methods	145
Chapter 8 Conclusions and perspectives	151
8.1 Summary on the current status of mixed ligand nanoparticle characterization	151
8.2 Advanced data analysis methods.....	153
8.3 Integrative characterization	154
8.4 In situ characterization	156
8.5 Enriching the library of mixed self-assembled monolayer morphologies	157
8.6 Translating back to proteins and other systems	158
Bibliography	161
Curriculum Vitae	175

Chapter 1 Self-assembled monolayers on nanoparticles and their characterization

This chapter gives an overall introduction to the self-assembled monolayer protected nanoparticles. Special focuses are on the unique structure-property relationships of patchy nanoparticles as well as current characterization techniques.

***Disclosure:** This chapter is partly a stand-alone original description, and partly (from Section 1.5 onward) a lightly rewritten version of the article, "Characterization of Ligand Shell for Mixed-Ligand Coated Gold Nanoparticles." Ong Quy*, Zhi Luo*, and Francesco Stellacci. *Accounts of chemical research* 50, no. 8 (2017): 1911-1919.*

Much of the interests on nanoparticles arise from their distinct surface properties¹⁻³. Comparing to macroscopic materials, the surface to volume ratio of the nanoparticle is much higher^{2,4}. For example, the percentage of surface atoms constitute around 50% of the core for a gold nanoparticle with 3 nm diameter. Therefore, both the physical properties of nanoparticle itself and the its interaction with other objects are dominated by the its surface structures⁵⁻⁷.

The surfaces/interfaces could also be regarded as a boundary between two bulk materials, i.e. the core of the nanoparticles and the surrounding medium. The chemical potentials at the interfaces would naturally build up a sharp transition and the surface free energy of nanoparticles is usually very high. As a result, bare nanoparticles are very unstable. They tend to aggregate with each other or get corroded quickly. Many methods are thus developed in order to stabilize the nanoparticles, for example, by dispersing the nanoparticles within a matrix or by forming a protecting shell around the nanoparticles^{5,8,9}. Self-assembled monolayer (SAM) is one of the most common way to coat the nanoparticles¹⁰.

Besides the ability to stabilize the nanoparticles, SAM has been found to play important roles on a number of properties of the nanoparticles^{6,11–14}. The versatility of SAM has become one of the most widely studied platform for the structure-property relationships at nanoscale since the chemical properties and composition of SAM could be tuned almost at will. While the SAM are evolving towards more and more complicated structures for various applications, its characterization has also become a challenge^{15–17}. In this chapter, an overview on the structures and unique properties of SAM is given with a particular focus on the multi-component SAM, i.e. mixed ligand shell on nanoparticles. A review on the existing characterization techniques for SAM is presented¹⁷.

1.1 Self-assembled monolayers on nanoparticles

When organic molecules or polymers are adsorbed on the nanoparticles, they spontaneously form ordered structures. Nanoparticles with different sizes, shapes and core compositions could all be protected by a variety of different SAMs⁵. Although SAM is only a thin layer of molecules, e.g. the thickness of a typical organic molecule SAM is within a few nanometers, it determines surprisingly a large fraction of the nanoparticles' properties^{1,18–24}, as presented in Figure 1.1. Meanwhile, the small dimensions and complex chemical nature pose great challenges both theoretically and experimentally to understand its structure and property relationships.

Self assembled monolayer on nanoparticles

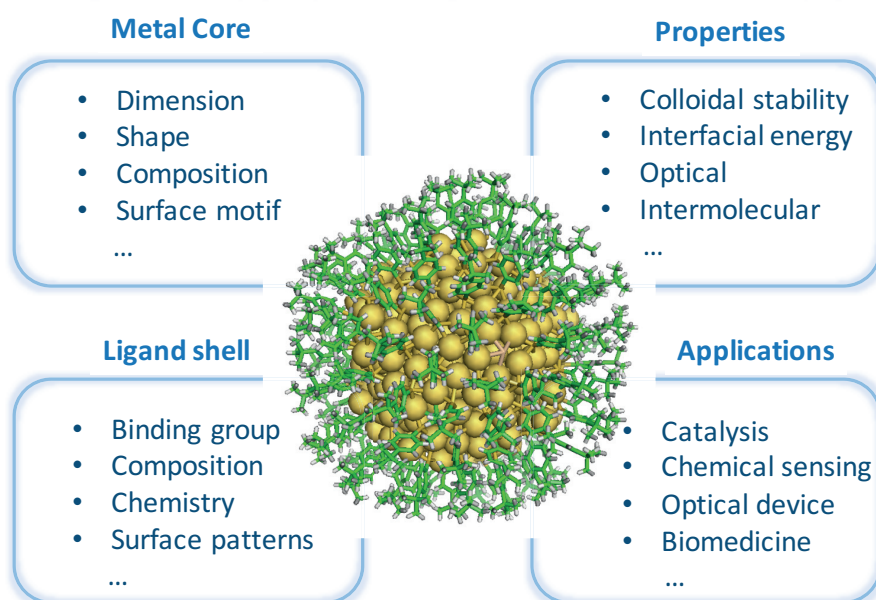


Figure 1.1 A typical but not exhaustive summary for the structures and properties of self-assembled monolayers on nanoparticles. The nanoparticle model is drawn based on the reference²⁵.

The integration of SAM with nanoparticles have many advantages. On top of the increase in stability, the nanoparticles could gain also chemical functionality. For example, by changing the head-groups of the protecting molecules, one can tune the wettability of the nanoparticles in different solvents^{26–29}, which is the first step for the application of nanoparticles in biology and other solution processing. SAM could also be used to tune the interaction between the nanoparticles and other objects such as proteins^{30–32}, cell membranes^{1,33–35}, small organic molecules^{3,36,37} and other types of nanoparticles. In this way, nanoparticles could become

good chemical sensors, building blocks for hierarchical structures^{38–40} and drug carriers^{41–43} for biomedical uses. The properties of nanoparticles' metal cores could also be altered by introducing the SAM. For example, due to the large differences in the refractive indexes of organic ligands as well as charge transport from the ligand to the metal cores, the optical properties and conductivity of nanoparticles could be tuned^{44,45}. The catalytic ability of the core is also influenced in the presence of the ligand shell both by changing the chemical reactivity of the metals and through steric or geometrical contributions⁴⁶.

Therefore, the diversity of the choice of SAMs is one of the keys to the success of nanoparticle researches. Besides tuning the type of ligands, the library of functional nanoparticles could be further enriched when a mixture of multiple components is used in SAM³¹. The most straight forward benefit of the mixed SAM is that nanoparticles with multiple functions could be synthesized^{47,48}. In drug delivery, mixed SAM is important to maintain good solubility of the nanocarriers while presenting recognition molecules for target delivery^{42,49}. For chemical sensing or catalysis, using multiple component ligand shells could help with the sensitivity, selectivity and/or catalytic efficiency of the nanoparticles⁵⁰. Furthermore, the organization or morphology of the mixed SAM, such as random, patchy, stripe-like and Janus, add another degree of complexity in the SAM structures and functions⁵¹.

1.2 Thermodynamic considerations on the organization of mixed ligands

Promising as mixed SAMs are, their structures on nanoparticles and corresponding properties are not simple and straightforward. The Au-S bond is covalent with the binding energy being around 45 kcal/mol. But the bond has certain mobility, although slow at room temperature. Such mobility could be enhanced at higher temperature or in the presence of other thiol molecules. The behaviour and structure of mixed SAM on various flat surfaces has long been explored⁵². Early works of Whitesides and co-workers reported that the final surface composition of ligands is different as the feed ratio in solution^{5,53,54}. This process has been found to be affected by many factors such as the solubility differences and the inter-molecular interactions on the surfaces. Using scanning tunneling microscopy (STM), Weiss and coworkers have found phase separated nanodomains on various different combinations of binary SAM⁵⁵. The size of the domains depends on the similarities, such as chain length, chemical functionalities of the two ligands. However, whether the phase separation morphologies are at the thermodynamic equilibrium or not remains under explored.

It has been discovered in 2004 by Stellacci and coworkers that when a mixture of two different types of thiols self-assembles on nanoparticle surfaces, stripe-like phase separation domains are formed³¹. Various types of different organizations such as random, Janus and patchy have then been identified^{56,57}. To understand such phenomena, great efforts on both experimental studies as well as theoretical considerations have been devoted from many groups. Glotzer group has addressed with coarse-grained simulations the problem of the equilibrium structure for such mixed SAMs^{51,58}. The central argument is that if separation were to be driven solely by enthalpy, macroscopic phases should form. Instead it is found that in these mixed SAMs, there is a significant component of interfacial entropy, typically due to the conformational entropy that longer ligands gain sitting at the interface with shorter ones, as shown in Figure 1.2⁶. The balance between the separation enthalpy and the interfacial entropy leads to the formation of stripe-like domains at composition close to the 1:1 and of small quasi-ordered domains at composition away from it. Meanwhile, as NPs become smaller or the chain length mismatch increases, the interfacial entropy contribution becomes less and less relevant, since the increase in the cone angle that delimits the ligands yields an overall increase in conformational entropy for the entire chain. Under this condition, the final morphology is primarily determined by the enthalpy of phase-separation, hence larger phase separation like Janus morphology would dominate^{57,59,60}. Similar thermodynamic considerations also apply for binary assembly of molecules on flat surfaces. Compared to the case on nanoparticle surfaces, phase separation domains with larger sizes (in the order of 10 nm) are often reported in literature. However, it is also likely that that such domains are in kinetically trapped states as the diffusion of thiol molecules on gold flat surfaces are slow at room temperature to allow the system reaching thermodynamic equilibrium.

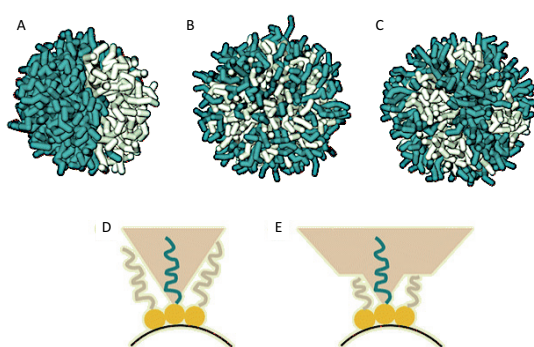


Figure 1.2 Thermodynamic equilibrium organization of two different ligands on nanoparticles. Three typical configurations are (A) Janus (B) Random and (C) Stripe-like. Entropic contribution of the long ligand chains when surrounded by another ligand with (D) same or (E) different length. Image adopted from reference⁶.

Many more realistic MD simulations for different ligand pairs were reported since then and the existence of different degree of phase separation was confirmed^{61–65}. Notable, MD simulations with explicit solvents starting at three configurations (random, striped, and Janus) were performed leading to different final morphologies, suggesting the presence of kinetically trapped states⁶⁵.

1.3 Unique structure-property relationship of mixed ligand nanoparticles

As a consequence of these complex morphologies, many unique interfacial properties have been discovered^{21,26,27,66}. In most of the properties and the corresponding applications are associated with the mixed ligand nanoparticles, both the composition and the organization/morphology of the ligands play an important role. Here, I attempt to summarize several main structural uniqueness of such nanoparticles and correlate such features with the unconventional properties and applications.

- Non-additive structural features

The types of morphologies of the mixed SAM have been found to vary with the SAM composition⁶⁷. Thermodynamically, since the formation of the stripe-like domains are largely driven by entropy, certain compositions are more favoured for such geometry. When the ratio of the two ligands is low, stripe-like domains would allow a lower fraction of molecules at the interfaces and thus micelle-like domains are more favoured. The characteristic dimensions of the nanodomains is thus a non-linear function with composition. Furthermore, recently, I have also found that the depending on the synthetic procedures, equilibrium morphologies are not always obtained⁶⁸. The search-space of ligand organizations are so large that transient kinetically trapped morphologies are possible. Therefore, due to both thermodynamic and kinetic reasons, the structure of the mixed ligand shell is non-additive and could not be simply predicted by its composition. One of the comprehensive overviews is shown in Figure 1.3, in which morphology evolution of ternary ligand shell protected nanoparticles are predicted by computer simulations⁶⁹.

As a result, many of the interfacial properties are found to be non-additive. For example, it has been found that the solubility of 1-octanethiol (OT) and 3-mercaptopropionic acid (MPA) protected nanoparticles shows a non-linear trend against the composition of the nanoparticles²⁶. Such result goes against the classical notion of ‘like-dissolves-like’, as one

might predict that for polar solvents, the solubility of the nanoparticle will increase as the fraction of MPA increases. Understanding of such solvation phenomena could lead to many interesting applications such as selective separation of solvent mixtures.

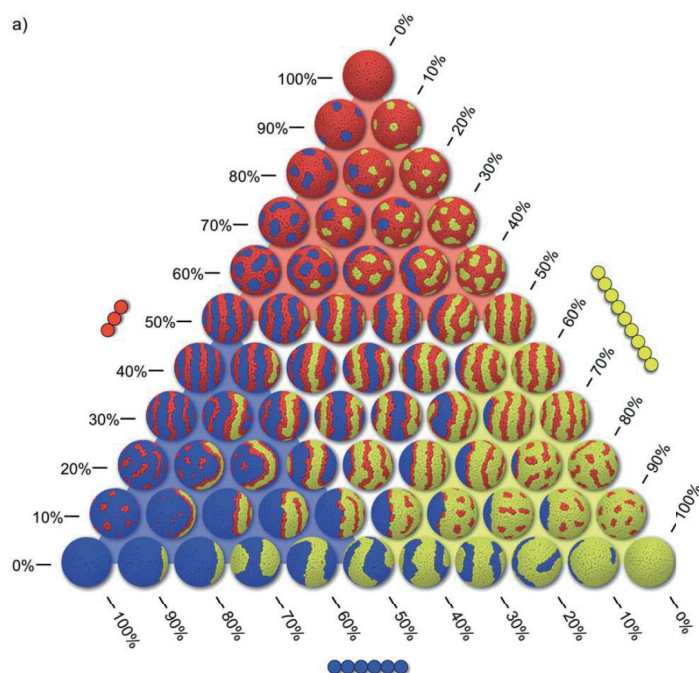


Figure 1.3 Structure of ternary ligand organization on nanoparticles as predicted by computer simulations. Non-additivity of the morphology with regard to composition is presented. Image reproduced from reference⁶⁹.

Another related interesting effect has been reported as the interfacial energy between the nanoparticles and water is non-monotonic with the ratio of hydrophobic and hydrophilic components^{21,70,71}. Conventional physical chemistry would define interfacial energy as a function of composition and hence it should be additive. However, as the phase separation domains vary in size, the cavitation and confinement of water molecules would both vary, which in return makes the wetting behaviour of such patchy surfaces very complex.

There could be many potential applications of such structural non-additivity. For example, by forming certain ‘pockets’ of binary ligands, the nanoparticles have been proven to be very efficient sensors with high selectivity⁵⁰, while the targeting molecules could be tuned through varying composition⁷². The same goes for catalysis, it has been found that catalytic ability of molecules on nanoparticles depends also on the mixed ligand morphology⁴⁶.

- Length-scale of the patchy domains

Comparing to other phase separated structures such as block copolymers and lipid vesicles, the dimensions of the ligand domains are smaller in the range of sub-2nm, due to the fact that the core diameter of the nanoparticles are usually around 5 nm. Such length-scale is comparable to the size of solvent molecules, thus many theories for micrometer-sized colloids do not apply⁷. Assumptions such as charges on the nanoparticles are regarded point-like in order to derive electrostatic interactions from Poisson-Boltzmann theory do not hold. The solvation of the nanoparticles must take into account the complex and sometimes collective interplay between the ligand and solvent molecules⁷³. Furthermore, proteins and other biomacromolecules also show surface heterogeneities at this scale, which often leads to unexpected interactions between nanoparticles⁷⁴.

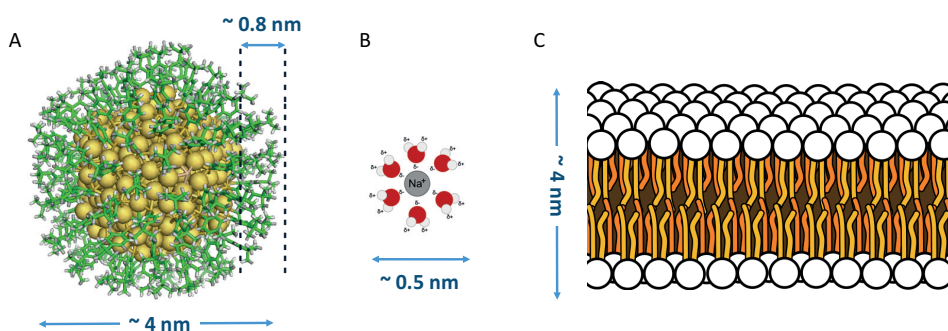


Figure 1.4 Comparison between the length scale of self-assembled monolayer protected nanoparticles (A) with that of hydrated ion (B) and lipid bilayer (C). Classical assumptions in colloidal science may not hold at such length scale and explicit interactions between molecules should always be considered. Image of the nanoparticle is adopted from reference²⁵; Image of lipid bilayers is adopted from Wikipeda (https://en.Wikipedia.org/wiki/Lipid_bilayer).

The non-monotonic trend of the nanoparticles' interfacial energy is one of the best demonstrations of the effect of nanodomain sizes²¹. On flat surfaces, where the phase separation of mixed ligand leads to larger domains, i.e. in the order of 10 nm, the interfacial energy and surface composition follows nicely the linear relationship. The significant effects of both the cavitation and confinement on water appear when the surface features have commensurate size to the scale of the hydrogen bonding network of water. Water is not only the small molecules that have complicated interaction with patchy nanoparticles. Other solvents as well as liquid crystals all show interesting wetting behaviour with the nanoparticles⁷⁵⁻⁷⁷. The solubility as well as the effect on the long rang order of liquid crystals are the macroscopic properties that reflect the nanoscale heterogeneity at the interfaces.

Besides small molecules, the interaction of mixed ligand protected nanoparticles also show remarkable dependence on its ligand shell morphologies^{31,74,78–80}. While the overall size of a protein is in the same range of core-shell nanoparticles, so do the surface patches of hydrophobic and hydrophilic residues on proteins compared to the ligand domains on nanoparticles. Through molecular simulations and experimental studies, it has been shown that the binding affinity of a protein, cytochrome C, to the mixed ligand nanoparticles surprisingly increases as the content of hydrophilic molecules increases⁷⁴. The amphiphilic nature of protein surface determines the interaction with both hydrophobic and hydrophilic domains on nanoparticles.

- Unification of the ligands with different/opposite properties

One prized advantage of SAM on nanoparticles is that the functional head groups of ligands could be tuned all most at will, which allows the incorporation of two ligands with even very large differences in chemical properties. For example, a very hydrophilic ligand such as charged molecules could be combined with very hydrophobic ones such as alkanethiols or even fluorinated molecules⁸¹. The reward is that the nanoparticles become amphiphilic at the surfaces and their interactions with surrounding media could be fine-tuned.

In the pioneering work of exploring how the surface structures regulate the interaction of nanoparticles with cell membranes, Stellacci and coworkers have shown that a mixture of 11-mercapto-1-undecanesulfonate (MUS) and OT protected gold nanoparticles could enter into cells in an energy independent manner⁶⁶. Such phenomena resemble natural cell penetrating peptides on which the surfaces also present both large amount of charge and hydrophobic contents. Detailed theoretical studies have illustrated that it is the amphiphilic surface and the hydrophobic interior of the ligand shell that facilitate the self-assembly of the nanoparticles with lipid bilayers^{79,82}.

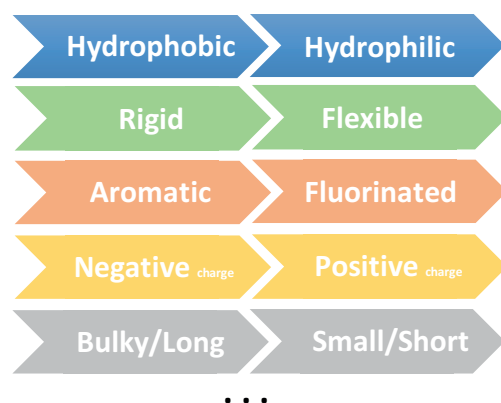


Figure 1.5 A list of combinations of two ligands with distinct differences on nanoparticles.

Similar effect on the ion-capturing ability of nanoparticles protected by ethylene glycol derivatives together with hydrophobic molecules have also been demonstrated⁵⁰. The ligands containing ethylene glycol segments endorse the hydrophilicity of nanoparticles and act as the chelating moiety of ions, while the effects of hydrophobic ligand could not be neglected. It helped the formation of binding pockets to ions and also decreases entropy penalty when the conformation of ethylene glycol ligands is restricted after ion binding.

Other examples include the combination of oppositely charged ligands on the nanoparticles^{24,83,84}. Unlike other types of nanoparticles that are not very stable in high salt concentrations due to the decrease of the thickness of electric double layer, the zwitterionic type nanoparticle is colloidal stable even in nearly saturated salt solution.

- Anisotropy at nanoscale

One last but very important feature is the anisotropy resulted from the patchy morphology of the nanoparticles. The distribution of patchy domains breaks the spherical symmetry of the nanoparticles, which exerts great influence on the intermolecular interactions of nanoparticles.

The topological defects of stripe-like nanoparticles has been characterized and utilized to generate pole-functionalized nanoparticles, i.e. divalent nanoparticle³⁹. Unlike other unguided self-assembly of most of the nanoparticles, the divalent nanoparticles could form chains. The anisotropy thus makes the nanoparticles behave as an artificial atom, which is the dream building block of nanoparticle chemists for the hierarchical structures that mimics Nature.

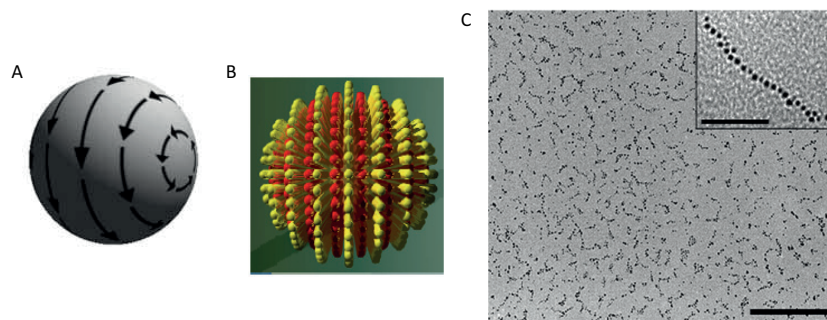


Figure 1.6 An example of anisotropic morphology guided self-assembly of nanoparticles. (A) Hairy ball theorem and the corresponding stripe-like morphology of mixed ligand nanoparticles (B). (C) TEM image showing the self-assembly of the nanoparticles into chain-like structures. Images reproduced from reference³⁹.

The self-assembly of mixed ligand nanoparticle in solution is also very interesting. Patchy nanoparticles have been predicted to assemble into a variety of different supramolecular structures. For example, chain-like structures were found by cryoTEM for nanoparticles coated by a mixture of charged and hydrophobic ligands⁸⁵. When the ligand shell morphology becomes Janus-like, i.e. the largest deviation from spherical symmetry, the nanoparticles have been found to be able to form micelle-like structures⁸⁶, which will have great potential for applications such as drug delivery. With the anticipation of more defined and complex morphologies to be developed, the space for the fabrication of controllable supra-structures of nanoparticle self-assembly would be greatly increased.

1.4 Synthesis of mixed ligand nanoparticles

Although the synthesis of ligand shell protected nanoparticles is a well-explored topic, especially for gold nanoparticles, the synthesis of mixed ligand protected nanoparticle is still state-of-art. Currently there are mainly two pathways for the synthesis of mixed ligand nanoparticles, i.e. direct synthesis³¹ and ligand exchange reaction^{68,86}. The mechanisms of both still remain under explored.

For the direct synthesis, it is often very hard to control the core size and the final ligand ratio of the nanoparticles. There are many degrees of complexity in this chemical process. While generally the solution synthesis of nanoparticles follows the mechanism of nucleation and growth, it has been found that the ligand plays an important role during both stages. Take

thiolated ligands, which are the most commonly used protecting ligands for gold and silver nanoparticles, for example. The head groups of thiol molecules, e.g. alkane-chain, aromatic and fluorinated affect the pKa, as well as the binding affinity of thiol to metals⁸⁷. It has been reported that different ligands would lead to different core sizes or even different crystallinity of the core⁸⁸. The effects of mixed ligands on the nucleation process could then be non-additive as the ligands not only affect the size/radius of nucleates but also its reactivity. The growth of nanoparticles also is accompanied by the evolution of mixed monolayer morphologies both in terms of composition as well as the organization of the two ligands. Moreover, especially for the cases where two ligands have significant differences in solubility, the interplay between solvents and nanoparticles is further complicated. Therefore, the mechanism of the mixed ligand nanoparticle synthesis remains largely unknown.

The ligand exchange reaction is also an important tool to generate mixed SAM protected nanoparticles. The advantage of ligand exchange is that it can be applied to nanoparticles of all kinds of sizes, shapes and original protecting molecules^{89–92}. For example, it is possible to transfer hydrophobic gold nanoparticles into aqueous solutions using a variety of polar ligands while keeping metal cores unaffected⁹³. The mechanism of how ligand shell evolves during ligand exchange process still lacks a clear picture. The reason lies in both the complicated nature of the reaction mechanism as well as lacking suitable characterization tools. Previous studies have utilized several techniques such as nuclear magnetic resonance spectroscopy (NMR)⁹⁴, Fourier transform infrared spectroscopy (FTIR)^{95,96}, gas chromatography (GC)⁹⁷ and electron paramagnetic resonance (EPR)⁹⁸ to investigate the kinetics and the chemical mechanisms of the ligand exchange reaction. Most of these studies only provide information on the exchange kinetics, i.e. molecule identities and compositions in the ligand shell as a function of reaction time. It has been found that ligand exchange reaction is a first order reaction via associative (SN2) mechanism with thiols⁴⁸, while it follows a dissociative (SN1) mechanism with disulfide⁹⁹. The addition of incoming ligand molecules starts mainly from the defect sites of metal core surfaces and ligand monolayers. Two possible pathways for the secondary ligand addition were identified, i.e. exchange and backfilling⁹⁴. Moreover, thiol molecules were also found to diffuse and reorganize on the nanoparticle surfaces. While all these kinetic factors complicate the mechanisms, the thermodynamic equilibrium morphology of binary ligands shells are further influenced by many parameters such as ligand chain length mismatch, bulkiness and various intermolecular interactions. Governed by both kinetics and thermodynamics, the reaction very often leads to batch to batch differences for the mixed ligand nanoparticle synthesis.

There are also other ways to synthesize and control the morphology of mixed SAM such as post functionalization of nanoparticles¹⁰⁰, interfacial ligand exchange reactions¹⁰¹ and molecular imprinting techniques¹⁰². Although they all have certain problems such as the yield of one batch of synthesis and the reproducibility, these novel techniques hold great promises considering the importance of synthesis on the application of mixed ligand nanoparticles.

1.5 Characterization techniques for mixed ligand nanoparticles

While the development in the mixed ligand nanoparticles hold great promises for many fields, the need to understand "property-structure" relationship of such material is continuously driving the characterization techniques for nanoparticles towards higher resolutions and versatility. When it comes to experiments, it is truly challenging to obtain morphological details of the ligand shell, due to the complexity of the distribution of ligands, conformation, and structure of phase separation domains. Currently, the available toolset of techniques for probing precise location of each type of ligand on the surface of nanoparticles is still lacking. Below a detailed review of existing techniques (both microscopic and spectroscopic methods) for the characterization of mixed ligand nanoparticles together with their limitations is presented. An urge for novel types of characterization technique is shown, which is the main motivation of my thesis work.

1.5.1 Microscopy

Due to the size of the gold cores and the small dimensions of ligand shell domains, not many microscopic tools are available for direct visualization of ligand structures. So far, scanning probe techniques such as scanning tunneling microscopy (STM) and atomic force microscopy (AFM) have been the main suitable microscopy techniques. STM uses as a feedback the tunneling current between a sharp metallic tip and a substrate. Imaging gold NPs greatly benefits from the resolution this technique can provide. Once the particles are clean from free ligands and are attached firmly to a conductive flat surface such as Au (111) or HOPG, the ligand shell morphology can be resolved based on the conductivity and height difference of the molecular component of the ligand shell. Here, we emphasize that any attempt to image gold NPs by STM has to consider three important issues. The first is the cleanliness of gold NPs. The particles must be as free from organic residues (such as the unattached ligands) as possible. This requirement is crucial because the unattached ligands can easily contaminate

the scanning tip, quickly degrading its ability to produce good images. In our experience, a necessary condition for particles to be image-able is that their ^1H NMR spectrum is free from sharp peaks. The second issue is that gold NPs must be anchored firmly onto the surface. The anchoring is needed to avoid the particle movement and/or vibrations when the tip traverses across the surface. Even a small movement of the NPs will compromise the resolution of the image. The latter condition can be circumvented when imaging in vacuum at low temperature, or in the rare cases when a particle adheres to a crevice in the surface. In order to routinely achieve substrates that meet ideal imaging conditions, typically we prepare a thiolated self-assembled monolayer (SAM) on Au(111) on a mica substrate. The SAM is composed of a short ‘filler’ molecule (butanethiol) and an anchoring dithiol molecule considerably longer (e.g. 1,16-hexadecane dithiol). On such a substrate we deposit a monolayer of NPs by either the Langmuir-Schaeffer approach or by drop-casting a dilute dispersion of NPs. The third issue is to achieve a single NP layer as imaging through thick NP films is challenging. We have managed to image bilayers and occasionally thicker layers but all our best images are from single layers, Figure 1.7.

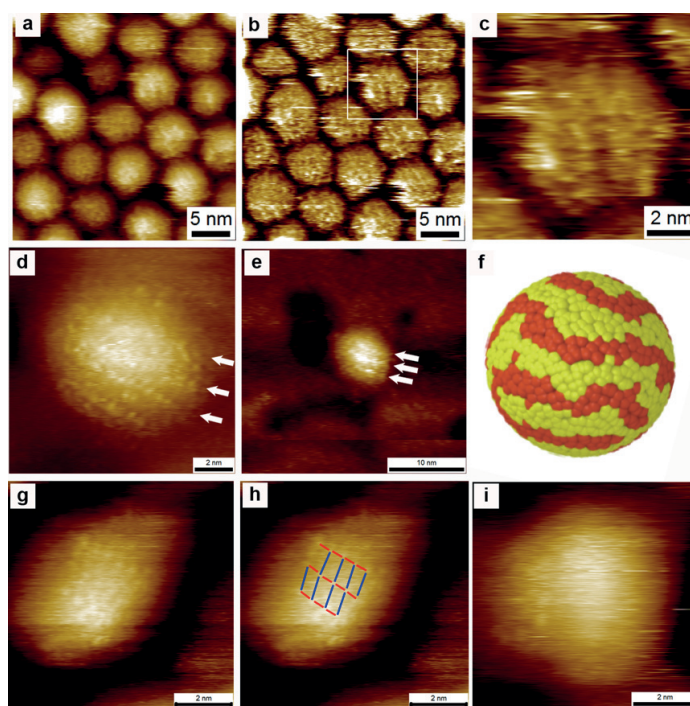


Figure 1.7 STM images of mixed ligand coated NPs showing stripe-like features of the ligand shell. a) STM topography image of gold NPs coated with dodecanethiol and hexanethiol; the image was recorded in phenyloctane. b) STM topography of the image a after the low frequency contribution is removed to show the crispness of the domains. c) an enlargement of one particle in image b. d) molecular resolution STM topography image of a gold NP coated

with mercaptopropionic acid and octanethiol. e) a low resolution image of this particle showing that the stripes are smooth and appear uniform. f) A coarse grain simulation model of a nanoparticle showing stripe-like domains. Red and yellow beads represent two dislike molecules; for example, short and long molecules respectively. g) a high resolution STM image of a gold NP coated with 11-mercapto-1-undecanol (C11OL) and 4-mercapto-1-butanol (C4OL). h) the same image presented in g with blue dashes having a dimension of 1 nm, and red dashes of 0.5 nm to guide visualization of stripes. i) An STM image of a gold NP coated with C11OL and C4OL showing the Janus structure. Image reproduced from reference¹⁷.

Taking advantage of high topographical resolution achievable by STM, in 2004 our group showed the existence of nano-domains that resembled ripples, or stripe-like domains on gold NP coated with a binary mixture of ligands³¹. For instance, STM images of gold NPs coated with octanethiol and mercaptopropionic acid OT: MPA (2: 1) present stripe-like domains with ~ 1 nm in thickness. Caution has to be exercised when acquiring and interpreting images of striped NPs as these STM images bear similarities to feedback loop artefacts if the imaging gains are not set properly.¹⁰³ Visually, the latter appear as parallel or wavy lines. It was shown that to differentiate the features due to true tip-sample interactions from feedback loop artifacts one needs to produce various images at different tip velocities and show that the features are invariant^{16,104–106}. It was demonstrated that in plots of the average spacing of the features as a function of tip velocity, feedback loop artifacts are characterized by a linear trend that passes through the origin; while the plots of stripe-like domains are characterized by lines that are close to being horizontal^{106–108}. For imaging NPs, scanning the same area at different angles can provide an additional verification of real stripe-like features against the feedback loop artifacts¹⁰⁸. This latter control can be challenging as stripe-like domains reveal complexity (e.g. variation in thickness and local defects) that renders the interpretation of the images at different angles complex.

Due to such high complexity, quantitative measurements can be tedious and the quantification of stripe dimension can be subject to operator's bias. Biscarini et al. developed a fast and powerful technique based on power spectral density (PSD) to extract correlation lengths from STM images of NPs¹⁰⁶. PSD of an STM image is its norm squared fast Fourier transform (FFT), and it represents the contribution, i.e. power, of different length scales displayed in the frequency domain of the image. A PSD curve of a representative STM image of NP can be usually decomposed to three segments as shown in Figure 1.8A. As illustrated in the figure,

characteristic features of the curve depend on the particle size and on the distribution (in size and orientation) of the stripe-like domains. Due to its quantitative nature, this PSD-based method can also be conveniently used to judge differences between samples in a straightforward manner. For example, if the shoulder is located at a higher spatial frequency, the average size of the features on gold NP is smaller. A whole PSD curve could also be fit with a phenomenological functional from which quantitative measurements of particle size, and domain features can be extracted. Biscarini et al. showed that by using this PSD technique, STM images from different laboratories, different scales, or different scanning conditions can be analyzed efficiently, and reported that striped features with a correlation length of ~ 1 nm could be cross-checked and indeed confirmed¹⁰⁶. The correlation length of ~ 0.5 nm on the other hand is measured in homoligand coated gold NPs. PSD estimation can be easily computerized and enables analysis of a large amount of images in short period of time. Lately, Ong et al. imaged stripe-like domains both in air and in solvent to attempt to evaluate the consistency of the imaging¹⁰⁵. Indeed, large datasets were acquired and PSD analysis helped to show that equivalent spatial frequency is present in both cases, as shown in Figure 1.8B.

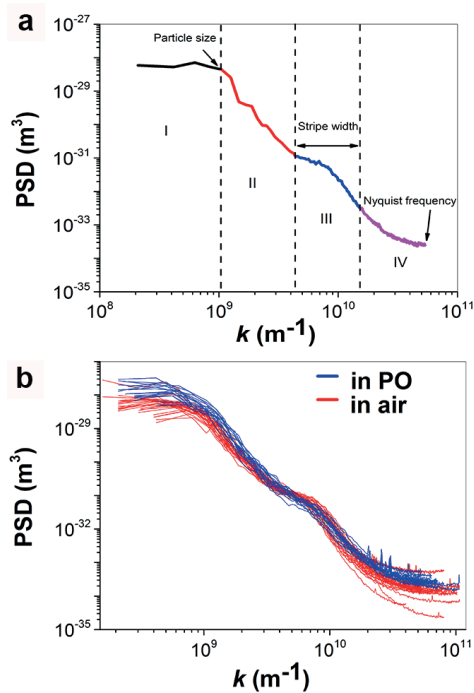


Figure 1.8 A) A representative PSD curve of an STM image containing striped NPs. The curve has been split into regions that have been colored differently in order to facilitate the explanation of its meaning. The PSD curve is the norm squared fast Fourier transform (FFT) averaged for horizontal direction, representing the contribution, i.e. power, of different length scales displayed in the frequency domain of the image. A PSD curve of an STM image of gold NP is usually examined at four segments: (I) plateau at low frequency (black segment)

that stop at the frequency from which the particle size can be estimated, (II) a decay that is related to the particle curvature and the characteristic $1/f$ noise of the microscope (red segment), (III) a broad shoulder or peak at high frequency that contains the length scale of the features on the surface of gold NP (blue segment), (IV) a flat part that ends at the Nyquist frequency which indicates length scales that lack content in the image (violet segment). B) Comparative study of STM images recorded from gold NP coated with 1-nonanethiol (NT) and 4-methylbenzenethiol (MBT). The imaging was performed in air (blue) or with the particle substrate and STM tip submerged in phenyloctane (red). The overlap of the curves demonstrates a consistency in the correlation of length of the stripe-like domains. Image reproduced from reference¹⁷.

Stripe domains have also been imaged on the surface of binary-coated gold NPs (hexanethiol-dodecanethiol) when they were completely submerged in a high-boiling point solvent such as phenyloctane. Such clear images of the stripe-like domains have been acquired due to the fact that the phenyloctane maintains a clean environment during image recording, and partially solvates the hydrophobic ligand molecules¹⁰⁸.

High-resolution images of the ligand shell of gold NPs coated with a binary mixture, in which positions of individual thiols are molecularly resolved, have been acquired only recently, Figure 1.7G and D. Figure 1G shows an STM image of a single nanoparticle coated with 11-hydroxyl-undecanethiol and 4-hydroxyl-butanethiol C11OL:C4OL (1:1). Single C11OL molecules are imaged on the nanoparticle and appear as dots. The dots align in two stripes with a spacing of ~ 0.5 nm along and ~ 1 nm across the stripes.

AFM has also shown a capacity to resolve the structure of the ligand shell when operating in liquid, in small-amplitude mode. Molecular resolution images, equivalent to STM images, of stripe-like domains on gold NP covered with 1-octanethiol and 6-mercaptohexan-1-ol (MHol), could be obtained using this technique²¹.

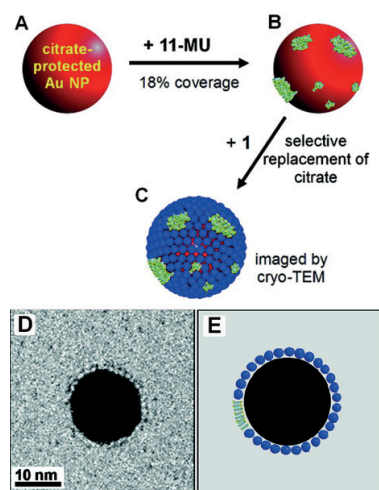


Figure 1.9 Presence of molecular patchy domains on a gold nanoparticle revealed by the use of α -AIW11O399 and cryo-TEM. The mixed ligand shell in nanoparticle B is made by partial replacement of citrate on nanoparticle A with mercapto-undecacarboxylate (11-MU) followed by substituting the leftover citrate on B with the cluster to form C for imaging. D) Cryo-TEM image of the nanoparticle C. E) The illustration of the 2D projection of the particle C. Image reproduced from reference¹⁷.

Scanning/Transmission electron microscopy (S/TEM) is a versatile physical characterization tool for NPs. It is mostly used for obtaining shape and size distribution and elemental composition of NP cores. The organic ligand shell is often invisible under the electron beam. The use of monolayer graphene as a supporting film and low acceleration voltage (80KV) in an aberration-corrected TEM has allowed direct visualization of the ligand shell of the citrate-coated gold NPs as demonstrated in a seminal work by Lee et al¹⁰⁹. Discerning different ligand molecules and ligand shell morphology remains an open challenge for this technique.

Yang et al. used osmium tetroxide as a staining agent to help image the ligand shell of gold NPs (tens of nm in size) functionalized with mixed lipid layers that form patchy domains by molecular phase separation¹¹⁰. Some ligands (e.g. metal oxide cluster -AIW11O399-) that have strong contrast for cryo-TEM can be used for direct imaging, Figure 1.9. This and other approaches are useful but limited to large particles¹¹¹.

1.5.2 Spectroscopic characterization of mixed ligand nanoparticles

1.5.2.1 NMR

Nuclear magnetic resonance (NMR) is a versatile and well established technique that has been widely used in various field, from structure determination of chemicals, drug discovery to in situ monitoring of chemical reactions. In particular, along with the advancement of instrumentation and methodology in the past decades, great achievements have been made in structural biology such as solving sophisticated protein structures and dynamics^{112,113}. Core-shell nanoparticles share a great deal of similarities with protein systems such as overall size range, surface properties and functions. Mixed ligand protected nanoparticles show more complex surface structures than homo-ligand shell protected nanoparticles and to a first approximation sharing similar features of proteins. Therefore, in principle many biological NMR techniques can also be adopted to study complex nanoparticles morphologies. Indeed, there are a growing number of studies demonstrating the powerfulness and broad utility of NMR in nanoparticle research. The reader is referred to a recent excellent review by Millstone et. al. for other topics such as the nanoparticle formation mechanism, metal core structures, dynamics of ligand shells and physical properties¹¹⁴.

Core shell nanoparticles synthesized from chemical approaches normally need lengthy purification steps in order to remove the residue salts, reducing agents and free ligands. NMR is then a straightforward technique to check the purity of the nanoparticles and helps to determine the structure of molecular species on the nanoparticle surfaces. These applications become more useful for mixed ligand nanoparticles. Besides the identity of ligands, it is also of great importance to determine the final ligand ratio on the nanoparticle surfaces, which very often is not simply equal to the feed ratio in the synthesis due to different binding affinities of ligands¹¹⁵. It has been shown in a large number cases that the ligand ratio of mixed SAM affects greatly the property of nanoparticles, such as interfacial energy, solubility, cell permeability, catalysis efficiency and ion-binding affinity. Therefore, knowing the composition of mixed ligand shell is the first step of the characterization.

To accurately determine the final ligand identity and ratio on nanoparticles, first one need to make sure that the nanoparticles solution is free from unbounded ligands. Different from NMR of free small molecules in solution, once the ligands are attached onto the nanoparticle surfaces, the line broadening of resonance peaks is normally observed, together with the

changes of chemical shifts¹¹⁴. These effects could be due to multiple factors such as restricted motion of ligands, dipole-dipole coupling and isotropic chemical environments due to the polydispersity and shape anisotropy of the metal cores (e.g. facets and curvatures). The absence of peaks from nuclei that are close to the core is an indication that the ligands are restricted on the nanoparticle surfaces. The ligand ratio could then be calculated after proper etching of the metal cores to release ligands from nanoparticle surfaces. Common etching methods include thermal and chemical decomposition using etchant such as iodine, potassium cyanide and concentrated base/acid. It is also possible to calculate absolute ligand quantities on nanoparticle surfaces with the help of an external reference molecule. As an example, ¹H NMR has been used to quantify the ligand exchange between different types of thiolated ligands on gold nanoparticle surfaces⁹⁴. By comparing the integrated peak intensity to a standard curve and further verifying with inductively coupled plasma optical emission spectroscopy, a correlation between the exchange efficiency with ligand types and concentration was achieved and two exchange pathways, exchange and backfilling, could be identified.

For complex ligand shells such as mixed ligand protected nanoparticles, the chemical shifts and line broadening effects are further influenced by the neighbouring ligand species. Recently, ¹H NMR and 2D nuclear Overhauser effect spectroscopy (NOESY) measurements have been utilized to study various types of mixed ligand shell structures, as shown in Figure 1.10⁵⁷. The up-field shift of aromatic ligands was used as an indication of the neighbouring environment of the ligands. Approximately, the surrounding of a molecule in the ligand shell can be classified into two categories, the 'bulk' and interface. For randomly mixtures, the chemical shifts should have linear dependence on composition due to the sample possibility of finding both categories. For the Janus morphologies, the trend is no longer linear since the possibility of interfacial molecules decrease inversely with the increase of composition, while for patchy particles the situation become more complex and the trend depends on the evolution of the shape of phase separation domains. Additionally, the cross-peaks in NOESY measurements allows for the determination of average proximity between the two molecules. Arising from dipole-dipole coupling interactions, NOE cross-peak could only be observed when the nuclear spins are close enough (<0.5 nm). Therefore, the absence of cross-peaks could distinguish Janus particles from other types of morphologies.

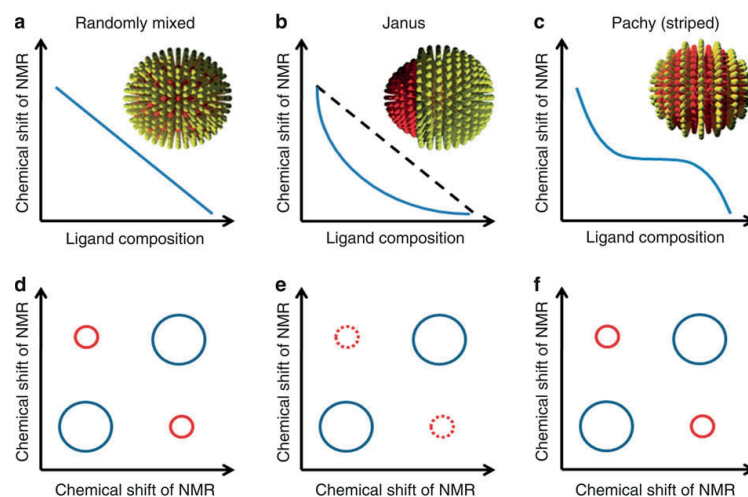


Figure 1.10 (a–c) Chemical shift of NMR as a function of ligand composition for randomly mixed, Janus and patchy nanoparticles, respectively. (d–f) NOESY of randomly mixed, Janus and patchy nanoparticles, respectively. Image reproduced from reference⁵⁷.

As a successful example of study nanoparticle systems combining 1D and 2D NMR techniques, the study above still has certain limitations such as the choice of ligands (to observe the cross-peaks) and tenability of the ligand shell composition. However, it demonstrates the possibility of studying complex ligand shell structures with the library of NMR techniques. The limitations could be overcome by measuring nuclei whose chemical shift is more sensitive and broader ranges, such as ^{13}C NMR. More detailed structural and dynamic information of mixed ligand protected gold nanoparticles could be obtained by applying other advanced NMR techniques and also combining with various simulation methods. There are already some encouraging examples on model nanoparticle systems such as gold nanoclusters¹¹⁶. Also, solid state NMR (ssNMR) has been applied to the study of ligand shell structures of nanoparticles. For example, in the work of Lennox and co-workers^{117,118}. There is currently no study on the monolayer morphology using ssNMR, since the ligand shells might be interdigitated in solid state and thus the chemical environment of ligands is not only affected by the morphology but also the inter-nanoparticle interactions. But the technique is undoubtedly interesting to be explored for the study of how nanoparticles interact in solid states.

1.5.2.2 Vibrational spectroscopy

Vibrational spectroscopic techniques are also powerful candidates for the characterization of core-shell nanoparticles. Being relatively simple and requiring small amount of sample,

techniques such as FTIR could provide detailed molecular information such as functional groups, molecular bonding and ligand chain conformation. The spectroscopic characterization of n-alkanes and polymers has long been well established, which most of the time form the basis of the successful application of IR on ligand shell protected nanoparticles^{11,117}. For example, Murray et al have examined thoroughly alkanethiol protected metal nanoparticles protected with different ligand chain lengths with the peaks at C-H stretching region well assigned¹¹⁸. It was found that the surface defect density of the protecting ligands is similar to the one on flat surfaces, while the ligand chains are mainly in the trans conformation once the chain length exceeds 5 carbons. Such very first study helped establishing a structural model of alkanethiol monolayers absorbed on nanoparticle surfaces and elucidated the relationship and differences between 2D SAM and 3D SAM¹¹⁹.

One of the main advantages of FTIR is its sensitivity to molecular conformation. The change of the frequency of each vibration modes provides information about the differences in the local chemical environment. It was found that the frequency of CH₂ stretching in alkane chains are influenced by intramolecular conformation disorder, such as gauche conformations, and by the amount of libro-torisional modes¹²⁰. As the ligand chain conformation deviates more from trans conformation, the CH₂ stretching frequency would increase. In a mixture system, the change in CH₂ frequency could be even more complicated as the intermolecular coupling and interaction between chains might also play an important role. One can assume that molecules that doesn't feel the perturbation in a mixture system would give rise to a CH₂ stretching frequency close to the one in homoligand nanoparticles, while those molecules standing at the phase boundaries feel different intermolecular interactions leading to a shift in frequency. Our group has utilized such phenomena in FTIR to characterize phase separation in binary ligand shell on gold nanoparticle surface¹²¹. By monitoring CH₂ stretching frequencies upon increasing the concentration of a second ligand, it has been shown that phase separated ligand shell exhibit nonlinear trend in chemical shifts, in sharp contrast to the linear trend in homogenous mixing ligand shells.

The limitations of FTIR for more detailed analysis of ligand shell structures lie in the lack of understanding of origin of the shift of vibrational frequencies. However, being a much faster and versatile tool, FTIR could serve as a high throughput tool to determine whether the ligand shells are randomly mixed or phase separated.

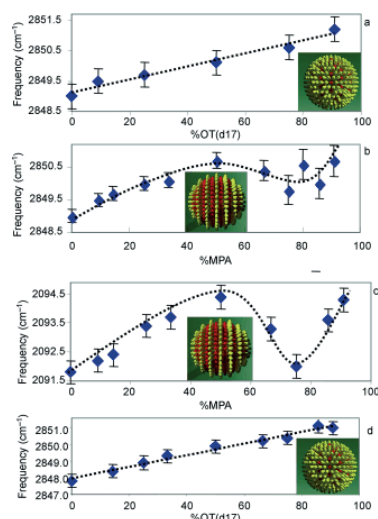


Figure 1.11 FTIR data of mixed ligand nanoparticles with random mixing and stripe-like morphologies. Image reproduced from reference¹²¹.

1.5.2.3 Mass Spectroscopy

Mass spectroscopy (MS) techniques have also been advancing rapidly in characterizing core-shell nanoparticles. MS techniques methods essentially provide information on the composition of the samples. The spectra present the intensity of different ions as a function of their mass-to-charge ratio. The composition of the samples can be then inferred by correlating the measured fragmentation pattern to the theoretical pattern of a particular compound. Following the instrumentation improvement around the 2000s, softer ionization methods, electrospray ionization (ESI) and matrix-assisted laser desorption/ionization (MALDI), grew in popularity¹²². These two methods decrease the amount of fragmentation of analyte during ionization thus allow for the analysis of fragile macromolecules.

The primary utilization of mass spectra focuses on measuring core size, ligand identity, and the molecular formula of metal nanoparticles¹²³. By assuming that the metal core has a fcc packing and certain density, an approximate core diameter could be calculated from the mass spectra. However, the ionization of core-shell nanoparticles often leads to fragmentation, which is the reason why it has been hard to obtain MS spectra of intact ligand protected nanoparticles and calculate the exact formula of the nanoparticles. Indeed, it was only possible until 2008 that the first MALDI spectra of Au₂₅ nanoparticles with intact ligand shells were achieved by Dass et al¹²⁴. Similarly, the first MALDI and ESI spectra of silver clusters, Ag₄₄, were reported in 2012 by our group¹²⁵. The utility of a unique matrix, trans-2-

[3-(4-tert-butylphenyl)-2-methyl-2-propenylidene] malononitrile (DCTB) was one of the keys. Unlike other universal matrixes that transfer a proton to the sample, DCTB assists ionization by electron transfer. Very recent work has extended the effective range of MALDI-MS characterization of gold clusters to 76.3 kDa, 115kDa and 207kDa^{126–128}. For the 207kDa specie, the number of core atoms is calculated to be around 940 corresponding to a diameter close to 3nm¹²⁹.

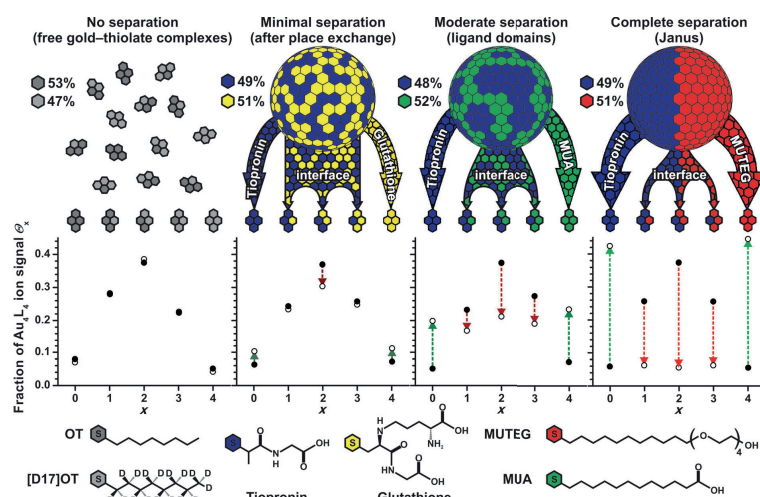


Figure 1.12. MALDI data of mixed ligand nanoparticles. Phase separation of ligands are inferred by the distribution of fragmentation patterns. Image reproduced from reference¹³⁰.

As mentioned above, one of the hindrance of MALDI analysis on nanoparticles is the tendency of fragmentation. However, recently it has been shown that such phenomena could be utilized to provide information on the ligand shell morphology of nanoparticles. A very interesting work was reported by Harkness et al, in which MALDI was used to examine the phase separation behaviour of various mixed ligand protected nanoparticles¹³⁰. The authors make use of the fact that Au_4L_4 was the most abundant ion species within fragments of gold nanoparticles. Such Au_4L_4 ions should be either desorbed directly from the nanoparticle surfaces or formed from the rearrangements of the surface staple motifs. Therefore, the distribution of $Au_4L_xL'_{(4-x)}$ of the binary ligand shells could reflect the arrangements of the two ligands on nanoparticle surfaces. For example, for ligand shells with random morphology, the distribution of each fragments would follow binomial distribution. While the higher the degree of phase separation, the larger deviation from binomial distribution would present. A systematic study of various ligand pairs was performed on nanoparticles with both hydrophobic and hydrophilic ligand shells, Figure 1.12. It was also shown that from this method, two nanoparticles with the same ligand ratio but from different synthetic procedures

exhibit different degree of phase separation. Recently, the same method has been used to characterize mixed ligand protected silver nanoparticles^{63,131}. Combining with computer simulations, it was shown that such technique could provide quantitative information on the size of phase separation domains.

1.5.2.4 Electron Spin Resonance

The advantage of using EPR for NP characterization is that it offers a sensitive detection of free radicals such as thiolated nitroxides that can be incorporated as part of the mixed ligand shell. Molecular conformation state and lateral mobility of the thiolated free-radical, for instance, on the surface of gold NPs could be studied^{98,99,132}.

Gentilini *et al* used a free radical molecule (dialkyl nitroxide) as a reporter for the patchiness of the mixed ligand shell. Particles with the ligand shell made of perfluoroalkyl (F8-TEG) and alkyl amphiphilic (C8-TEG) thiols were analyzed¹³³. Dialkyl nitroxide partitions almost exclusively close to the fluorinated ligands within the ligand shell, and has EPR signals that are sensitive to local polarity. It was found that the EPR signal of the NPs was practically identically to that generated by fluorinated homoligand NPs, thus indicating the presence of patches in the ligand shell. Only particles with a ligand shell that strongly adsorbs the probe, and with a marked difference in the wettability of the patches can be studied by this approach. The spatial resolution of this approach remains undetermined.

1.5.2.5 Adsorption-based Fluorescence Spectroscopy or SERS

The arrangement of thiol molecules within the ligand shell can also be indirectly inferred from its absorption capacity to absorb an analyte. Bonomi *et al.* studied the adsorption of a charged analyte ATP (adenosine triphosphate) with gold NPs coated with a mixture of cation terminated thiols (such as those with TACN•Zn^{II} triazacyclononane or trimethylamine headgroups) and inert TEG triethyleneglycol-terminated thiols¹³⁴. By varying the amount of the former in the ligand shell, it was shown by a fluorescence titration that the saturation amount of ATP on the ligand shell had a nonlinear, bell-curved trend with a maximum at an intermediate ligand ratio (in between 0.5-0.7). Because the multiply-charged ATP can interact with several of the cation terminated thiols simultaneously, it can be used to assess the morphology of the ligand shell. A titration experiment in which monoligand-coated NPs was mixed was done as a control and resulted in a linear horizontal trend. This result confirms that

the ligand shell of the mixed ligand coated NP is not completely de-mixed as the Janus morphology. Instead, with the help of simulation it was demonstrated that at the intermediate ligand ratios the charged ligands formed patchy domains that are both large enough to promote maximum binding and spaced just far apart enough by the inter TEG thiols to minimize electrostatic repulsion. Likewise, Stewart *et al.* used silver NPs coated with pentanethiol and negatively charged mercaptopropanesulfonic acid and observed a markedly saturated absorption of a positive SERS-active analyte ZnTMPyP at only at the ligand shell composition 1: 1¹³⁵. In consideration of ligand clustering geometry, it was suggested that clustered domains of both ligands were formed. This arrangement allows an incoming ZnTMPyP to find at least one negatively charged ligand on any part of the NP, hence promoting most efficient binding.

Chapter 2 Analogy in proteins and nanoparticles: insights from structural biology

This chapter lists some structural similarities between proteins and patchy nanoparticles. A brief introduction on how small angle scattering and mass spectrometry techniques are applied to study protein structures are described. The main motivation of this thesis to translate structural biology tools to patchy nanoparticles is discussed.

While the design of patchy nanoparticles is an emerging field, Nature has always been exploiting the unique characteristics of complex surfaces. Biomolecular entities such as proteins and lipid membranes all present surfaces that are heterogeneous at nanoscale both chemically and geometrically. For example, the hydrophobic part of a globular protein can constitute more than 60% of its solvent accessible surface area. The cell membranes have been postulated to contain nanoscale lipid rafts together with various types of proteins and carbohydrate chains, ending up with a highly heterogeneous and dynamic surface. Great efforts have been devoted to elucidate the structures of biomacromolecules, which resulted in the development of a library of advanced techniques. In this chapter, I attempt to give a brief summary on the effects of hydrophobic patchy structures on protein properties. A particular focus is on how solution scattering and mass spectrometry techniques are applied to analyse the structure of proteins. An analogy between proteins and nanoparticles is made in terms of surface properties and structural characterization, which lays the conceptual foundation of this thesis.

2.1 Protein as a patchy nanoparticle

One of the main driving forces for protein folding is the hydrophobic interactions¹³⁶. As a result, globular protein often has a compact ‘core’ composed of interacting secondary structures and the surface of the protein is generally more hydrophilic. However, there are still a significant amount of apolar residues exposed at the protein surfaces forming patchy type domains. Exposed to aqueous environment, these hydrophobic patches often play important roles in determining the intermolecular interactions of proteins, such as hydration¹³⁷, ligand binding as well as protein-protein interactions¹³⁸. Such surface patches are often found to be compositionally and geometrically complicated, whose structure is related to the specific functions of the proteins. For example, the balance between surface hydrophobicity and hydrophilicity of enzymes determines its catalytic efficiency¹³⁹. In the case of membrane proteins, the hydrophobic patches often have defined sizes which is commensurate with the thickness of lipid bilayers¹⁴⁰. Here, I attempt to list several effects of the surface hydrophobic patches on the interfacial properties of proteins. Although an exhaustive summary is beyond the scope of this thesis, the main purpose to inspire the research in patchy nanoparticles by showing how the fine tuning of surface structures could have profound effects on the behaviour of nanoparticles.

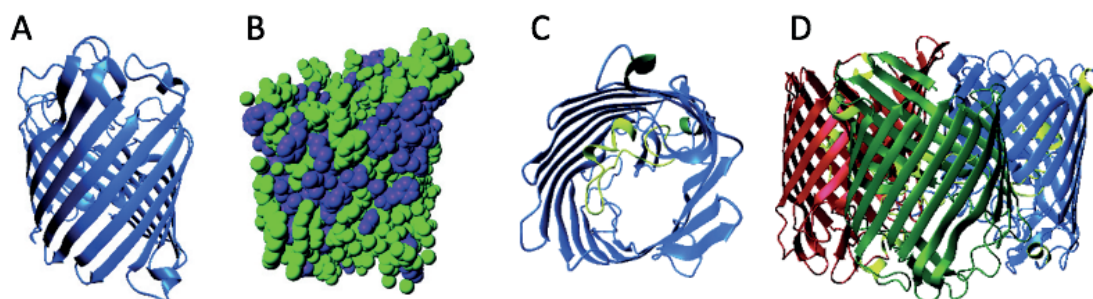


Figure 2.1 Structural presentations of the OmpF porin protein. (A) Porin monomer featuring barrel-like structure. (B) Space-fill representation of the hydrophobic and hydrophilic residues of porin. (C) Top down projection illustrating the pore structure of the protein. (D) Structure of the trimer self-assembly structure of the porins. Images reproduced from reference¹⁴¹.

As the first example, the textbook description of the structure and functions of a porin protein is discussed¹⁴¹. As shown in Figure 2.1, OmpF porin is a representative channel forming membrane protein with interesting structure-property relationships. The overall arrangement of the porin (Figure 2.1A) is a barrel type structure composed of β -strands that are bonded

through intermolecular H-bonds. The outer surface is featured with hydrophobic patches/stripes with certain sizes (Figure 2.1B) while the inner pore is lined with polar residues that allows the control on the selective transportation of molecules or ions across membranes (Figure 2.1C). The porins are normally found in trimer form, in which the main driving forces of the assembly is through the hydrophobic interactions among the proteins.

To a first approximation, if one regards the porin as a hollow nanoparticle with patchy surfaces, several conclusions could be drawn on how the hydrophobic/hydrophilic patches determines the function of the proteins:

- Interaction between the hydrophobic patches and cell membranes

The hydrophobic bands on the surface of porin has a size that is commensurate with the thickness of cell membranes. Specifically, the hydrophobic patches are rich in aromatic side chains and has a band width of around 3 nm. Similar size range for the hydrophobic regions could also be found on other types of membrane proteins¹⁴¹. Therefore, in this case, the size of the hydrophobic patches determines how the proteins interact with other molecules. Similar behaviour has also been found for amphiphilic gold nanoparticles, where the hydrophobic components in the ligand shell lead to the tendency of self-assembly with lipid bilayers⁸². It has been found that the size range of the nanoparticle diameter is also crucial for the self-assembly of mixed ligand nanoparticles with lipid bilayers^{142–144}.

- Hydrophilic cavity and the binding with ions

The cavity of the porin protein has a size of around 1 nm in diameter, although it is not uniform across the protein. Polar residues could be found surrounding the cavity and form H-bond with water molecules. The identity and the organization of such hydrophilic side chains determines largely the properties of the pore, such as the selectivity towards the anions¹⁴¹. Through X-ray crystallography, it has been elucidated that how a loop of amino acids inside the pore determines the charge discrimination ability of the porin. Similar construction of mixed ligand nanoparticles has also been demonstrated from our lab, which shows how the content and organization of hydrophobic and hydrophilic molecules could determine the selectivity of ion-binding by the nanoparticles⁵⁰.

- Intermolecular self-assembly driven by hydrophobic interactions

The main driving forces of the trimer structure of porins is the hydrophobic interactions between the side patches. Due to the structure of the protein, delicate balance between the interaction of lipids and protein themselves are achieved. The same principle is found for many protein systems, such as coiled coil motif¹⁴⁵ and the trans-membrane alpha helices¹⁴⁶. The existence of hydrophobic patches is a necessary condition but not sufficient. It has been shown that for coiled coil protein structures, both the organization of the hydrophobic patches and the surrounding polar groups show great influence on the assembly tendency and the equilibrium structures, such as dimers, trimers, or hexamers¹⁴⁷. Likewise, the design of the geometry of patchy nanoparticles starts to attract much attention in the nanotechnology field. The directions and relative positions of the patches have been stressed in addition to the amount of hydrophobic moieties in determining the nanoparticle self-assembly behaviour⁴⁰.

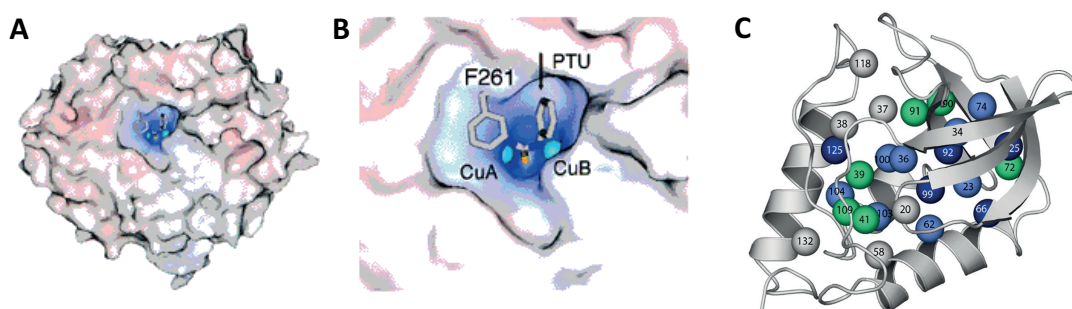


Figure 2.2 Structure overview of enzymes. (A) Hydrophobic binding pocket of a catechol oxidase. The positive charge potential is presented in blue while negative potential is in red. (B) Molecular details of the active site of the enzyme. The metal ions are surrounded by hydrophobic moieties, especially the aromatic side chains. (C) pK_a values of 25 lysines at different positions of an enzyme, SNase. Color coding denotes the shifts of pK_a values compared to free lysines. The grey beads represent no detectable shifts while the green ones have the highest shifts. Images reproduced from references^{148,149}.

While porin is just one of the examples in which the hydrophobic/hydrophilic patches on protein surfaces determines almost all the functions of the protein, the principle of interactions could be inspiring when examining other biomolecules or designing patchy nanoparticles. For example, another common type of proteins, i.e. enzymes, could also bring novel insights on the structure-property relationships of patchy surfaces. As shown in Figure 2.2, enzymes generally exhibit well defined structure-property relationships and are good examples to be

studied in the framework of chemistry. The high specificity/selectivity of the enzyme catalysis is highly related to the surface and geometrical properties of the proteins. Moreover, what is often ignored is the effect of patchy surface characteristics on the overall structure of the enzyme itself. Here, using two representatives but simple examples, I summarize two structural features of enzymes that could be inspiring for patchy nanoparticles.

- Effect of hydrophobic patches on the specificity of enzymes

The primary lock and key theory of enzymes is indeed a supramolecular chemistry view of the interaction between two molecules¹⁵⁰. The first step for efficient catalysis is in fact the selective binding of the substrates. As shown in Figure 2.2, the active sites of most of the enzymes are generally very polar, e.g. in the case of catechol oxidase, the catalyzing functional groups are charged copper ions. However, it is also interesting to find that the charged/polar cavity of the enzyme is surrounded by hydrophobic residues, especially those with aromatic side chains. The design of hydrophobic functional groups contributes to the van de Waals interaction with the catechol molecules and their relative geometry is essential for the selectivity¹⁴⁸. Researches have also taken advantage of such structural features to design targeted drug molecules. For nanoparticles, it has also been shown that the catalysis efficiency of a sulfonate terminated ligand protected gold nanoparticles could be significantly enhanced when the ligand is combined with certain amount of hydrophobic ligands⁴⁶. The composition and the morphology of the mixed monolayer have been found to be the key in the catalytic performance of the nanoparticles.

- pKa of polar residues in the hydrophobic interior of proteins

Due to the large differences of dielectric constant between water and the protein interior, charged species are energetically un-favored. The proteins would be destabilized in the presence of charged groups in the hydrophobic inner core. However, many of the active sites of enzymes are composed of charged ion groups. Such incorporation of charges in close proximity to hydrophobic plays an important role for the catalytic ability of the protein. Recently, Bertrand and co-workers have quantified the pKa values of all the 25 lysines at different sites of the SNase protein¹⁴⁹. It is found that in general, the pKa values of the lysines are higher in the interior of the protein than free amino acid. The degree of the pKa shift depends on the surrounding residues and the conformation of the proteins. Such interplay between charged species and the hydrophobic patches has started to attract much attention¹⁵¹.

Similar behavior of the effect of hydrophobicity on the ion-pairing has also been reported on model self-assembled monolayers¹⁵².

In conclusion, the variety of the protein surfaces could be regarded a rich resource for the exploration of structure-property relationship at nanoscale. Currently the surface complexity of patchy nanoparticles is still far from comparable as proteins. The opportunities lie in the design and synthesis of functional patchy surfaces with defined structures as well as using patchy nanoparticles as model systems in order to understand better the surface properties of proteins.

While proteins and patchy nanoparticles share many structural similarities, it is natural to explore the possibility of translating the techniques in structural biology into the characterization of patchy nanoparticles. In the past century, huge progress in structural biology have equipped the field with many advanced methods. This includes microscopy based techniques such as high resolution optical microscopy¹⁵³, electron microscopy (including cryo-tomography)¹⁵⁴ and single molecule techniques such as AFM¹⁵⁵. There is also a library of spectroscopic based methods, such as mass spectroscopy¹⁵⁶, solution small angle X-ray/neutron scattering¹⁵⁷ and NMR spectroscopy¹¹³.

However, for the characterization of patchy nanoparticles, the main technique has been scanning tunneling microscopy with some rare examples of limited utilization of other types of techniques¹⁷. The lack of suitable techniques is partly due to the nature of the nanoparticle itself. The overall small size and the existence of large fraction of heavy metals prohibits the use of most of the microscopic techniques. For example, although cryo-TEM has been used recently to resolve the structure of the gold core with atomic resolution, the organic ligand shell could not be analyzed due to its low contrast and disordering. On the other hand, there is a growing interest in the application of various spectroscopic techniques in the characterization of patchy nanoparticles. NMR has been one of the best example, by combining the ¹H NMR and NOESY, it is possible to qualitatively determine the phase separation of organic molecules on nanoparticle surfaces⁵⁷. Other techniques such F-NMR⁶⁰, HSQC, TOCSY and ROESY have recently also been applied to the study of ligand shell of nanoparticles¹¹⁶.

In the following two sections, I will give an overview on the application of two types of spectroscopic techniques in the study of protein structures, i.e. solution small angle scattering,

mass spectrometry based techniques. As already described in chapter 1, although there are a few reports utilizing these techniques in nanoparticles, all the current studies are only primitive. Great potentials are waiting to be explored.

2.2 Solution X-ray and neutron scattering of biomacromolecules.

The main references for this section are from three books: *Structure Analysis by Small-Angle X-Ray and Neutron Scattering (Springer Science)*¹⁵⁸; *Elementary Scattering Theory (Oxford University Press)*¹⁵⁹; *Small Angle X-Ray and Neutron Scattering from Solutions of Biological Macromolecules (Oxford University Press)*¹⁶⁰. Interested readers are recommended to refer to these books for more details.

The history of small angle scattering (SAXS and SANS) techniques has been land marked with several major developments of the theoretical/analytical methods and the improvements of instrumentation. The seminal work of Guinier at 1930s put forward some of the main concepts such as the extraction of size and shapes from small angle scattering¹⁵⁸. In the 1940s, the quantitative analysis on the inhomogeneous systems was established by Debye and Bueche, which lays the foundation for the calculation of scattering intensities that many methods are using nowadays¹⁵⁸. Later studies have summarized how different macroscopic properties and invariants are related to the scattering profiles quantitatively. Studies on Indirect Fourier Transform have then allowed the calculation of real space distance distribution functions from scattering data¹⁶¹. Currently, a growing interest on solution small angle scattering rises due to the application of *ab initio* methods in retrieving low resolution structures for biomacromolecules¹⁶². Nowadays, SAXS and SANS are widely coupled with other types of characterization techniques such as AUC, NMR and crystallography for accurate assessment of structural and dynamical details of macromolecules and their complexes in solution¹⁶⁰. Advancements on the data analysis are still continuing with developments in the ensemble based methods for the analysis of more dynamic and complicated systems¹⁶³. In this section, a brief introduction on the basics of small angle scattering is given with particular focuses on the *ab initio* shape determination methods. Examples of how small angle scattering is applied to the study of protein structures and functions are shown.

2.2.1 Experimental setup for small angle scattering

The experimental setup and conducting for a small angle scattering experiment is relatively simple. A schematic illustration of a typical solution scattering experiment is shown in Figure 2.3A, a collimated beam is guided pass the sample and the time averaged scattered intensity of the X-ray (or neutron) beam is recorded on a 2D detector. The distances between the sample and detector determines the resolution on the scattering profiles, i.e. with larger distances X-rays that scattered by lower angles could be resolved. Therefore, by combining measurements at several different detector distances, it is possible to access a wide range of scattering angles, which inversely corresponds to the length scale resolution in real space.

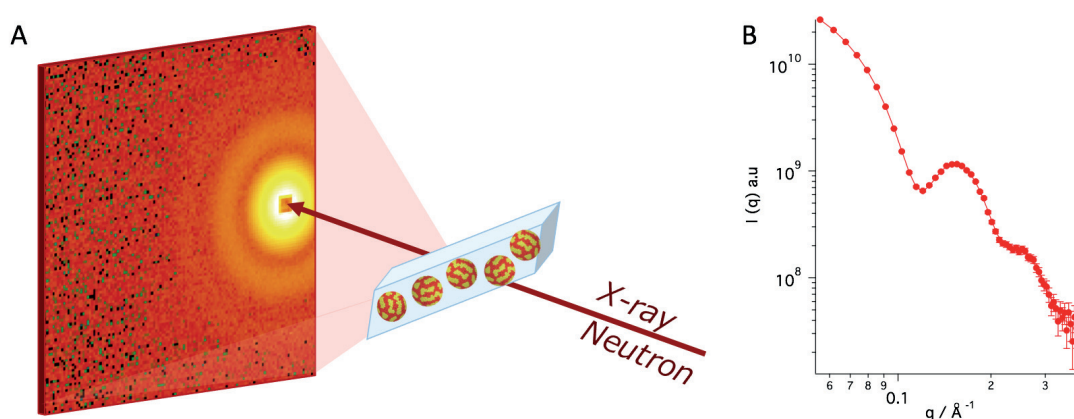


Figure 2.3 Schematic illustration of a solution small angle scattering experiment (A) and the one dimensional scattering curves after the radial averaging and the subtraction of solvent background.

The recorded 2D scattering patterns are then radially averaged resulting in the one dimensional scattering curves, especially for systems without specific macroscopic orientation, which is often true for solution scattering measurements. The differences between the scattering curves of the sample and that of the solvents are subtracted yielding the scattering contributions from the samples, as shown in Figure 2.3B as an example. The scattering intensities could be normalized by substances with known intensity such as water or standard protein solutions so that the intensity at absolute scales could be achieved. The setup of a small angle scattering experiment is simple and flexible and therefore allows the measurements at various sample conditions, such as at different temperatures, sample conditions (concentrations) and/or combined with different equipment such as stopped flow

devices, rheology cells, and other in situ spectroscopic instruments such IR and DSC. For lab based X-ray instruments, the measurement time are in the order of minutes or hours, while at synchrotrons, sub-ms time resolution could be achieved. For neutron measurements, the beam intensity is generally lower than X-rays and the measurements could take hours depending on the geometry and sample conditions.

2.2.2 Basic concepts and overall parameters

Below a simple overview of solution scattering theory is described. For the purpose of this thesis, we are only focusing on the scattering of monodisperse dilute solutions. Discussions on the polydisperse samples or interacting samples are referred to the textbooks above. A scattering event of incident particle (X-ray or neutron) by samples could be described by the energy and momentum transfer during the process. In the context of this thesis, we are mainly interested in the elastic scattering, i.e. only for the cases where momentum transfer happens but no energy exchanges. The principle of scattering process by X-ray, electron and neutron is very similar. Therefore, below a general description of the small angle scattering is given. The uniqueness of neutrons compared to X-ray or electron is that scattering cross section of atoms for neutron is not a monotonic function of the atomic number. Neutrons interacts with atoms through spin interaction and nuclear forces and as a consequence, the scattering cross section is sensitive to isotopes and is almost random among elements. A unique and also practically useful property is that the scattering cross section of hydrogen is very different with its isotope deuterium. While hydrogen has negative scattering length, deuterium has almost the same scattering ability as gold atom. Therefore, one could use selective deuteration to label organic molecules in order to highlight them in the presence of heavy elements, which none of the X-ray and electron based techniques are capable of.

From the geometry shown in Figure 2.4A and the vector diagram, one can get the following relationship from the momentum transfer Q (also noted as q or s in literatures).

$$Q = k_i - k_f \quad \text{and} \quad Q = \frac{4\pi\sin\theta}{\lambda} \quad \text{for} \quad |k_i| = |k_f| \quad (2.1)$$

The wave functions of the incident and the scattered beam are written as:

$$\psi_i = \psi_o e^{ikz} \quad \text{and} \quad \psi_f = \psi_o f(\lambda, \theta) \frac{e^{ikr}}{r} \quad (2.2)$$

where $f(\lambda, \theta)$ represents the possibility of a X-ray or neutron particle with wavelength λ to be scattered at certain direction. In the cases of neutrons, the $f(\lambda, \theta)$ is the scattering length (b) of the atom and is independent on the wavelength and scattering angle. The value of b is dependent on the interaction between neutron with the nucleus and thus has isotopic effects and do not vary linearly with atomic number. This lays the foundation of the contrast variation techniques in neutron scattering. For X-rays, the value b depends on the wavelength and increases monotonically with the increase of atomic number. This is because the interaction of X-rays with atoms are through electromagnetic interactions. Furthermore, the sum of scattering length from an atom over all the scattering angles gives the scattering cross section, which has the physical meaning of the scattering rate divided by the incident flux:

$$\sigma(\lambda) = 2\pi \int_{2\theta=0}^{\pi} |f(\lambda, \theta)|^2 \sin 2\theta d2\theta = 4\pi |b|^2 \quad (2.3)$$

When considering the scattering from an assembly of atoms, as illustrated in Figure 2.4B, the scattered wave takes the form of:

$$\psi_f = \psi_o e^{i\mathbf{k}_f \cdot \mathbf{r}} \sum_{j=1}^N f_j(\lambda, \theta) \frac{e^{i\mathbf{Q} \cdot \mathbf{R}_j}}{|\mathbf{r} - \mathbf{R}_j|} \quad (2.4)$$

Here $f(\lambda, \theta) = \beta(\mathbf{r}) dV$ and $\beta(\mathbf{r})$ is the scattering length density function of the material, which contains the structural information of the whole scattering object. The modulus square of the scattered wave is then linked to the rate of scattering by:

$$\left(\frac{d\sigma}{d\Omega} \right)_{\text{el}} \propto \left| \iiint_V \beta(\mathbf{r}) e^{i\mathbf{Q} \cdot \mathbf{r}} d^3\mathbf{r} \right|^2 \quad (2.5)$$

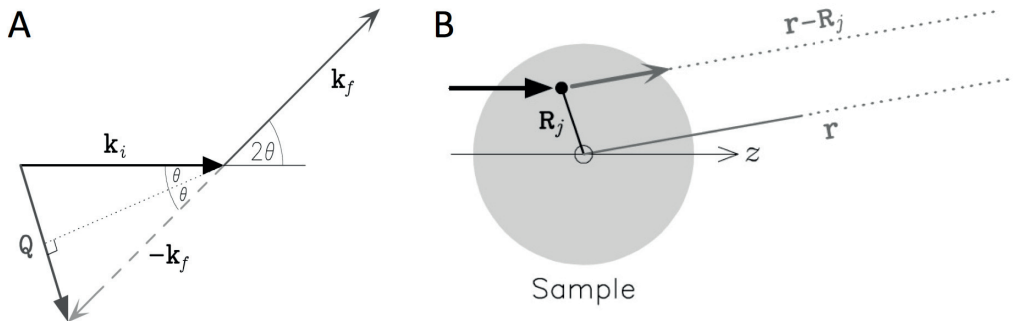


Figure 2.4 Schematics of X-ray or neutron being scattered. (A) scattering from a single fixed atom and scattering vector; (B) scattering from an assembly of atoms. The equations and

images are modified according to *Elementary Scattering Theory*, D.S. Sivia, 2011, Oxford University Press¹⁵⁹.

From the above expression, analytical form factors of different shapes could be calculated. For example, for the simplest case of spherical object, since the nanoparticle shape as well as the orientation both have the spherical symmetry, the expression could be simplified as:

$$\left(\frac{d\sigma}{d\Omega}\right)_{\text{el}} \propto N \left[\frac{4\pi |\beta_1 - \beta_o|}{Q} \right]^2 \left| \int_0^R r \sin(Qr) dr \right|^2 \quad (2.6)$$

The integration gives the following relation, where j_1 is called the spherical Bessel function:

$$\int_0^R r \sin(Qr) dr = \frac{\sin(QR) - QR \cos(QR)}{Q^2} = R^2 j_1(QR) \quad (2.7)$$

Therefore, the scattering equation of spheres becomes:

$$\left(\frac{d\sigma}{d\Omega}\right)_{\text{el}} \propto N \left[V_p |\beta_1 - \beta_o| \frac{3j_1(QR)}{QR} \right]^2 \quad (2.8)$$

Here the V_p is the volume of the particle. The analytical scattering equations of many different regular shapes have been derived and one of the great summarize is listed in the documentation of SasView software.

For the scattering profile at very high scattering angles, the scattering equation could be approximated by the following expression:

$$\left(\frac{d\sigma}{d\Omega}\right)_{\text{el}} \longrightarrow \left(\frac{N}{V}\right) \frac{2\pi S_p}{Q^4} |\beta_1 - \beta_o|^2 \quad (2.9)$$

This is the famous Porod's law, where the V is the illumination volume of the sample and the S_p is the surface area of the scattering object. For spherical shapes, the scattering intensity decays at high scattering angle with the power law of q^{-4} . For disc and rod shaped object, the power law is q^{-2} and q^{-1} respectively.

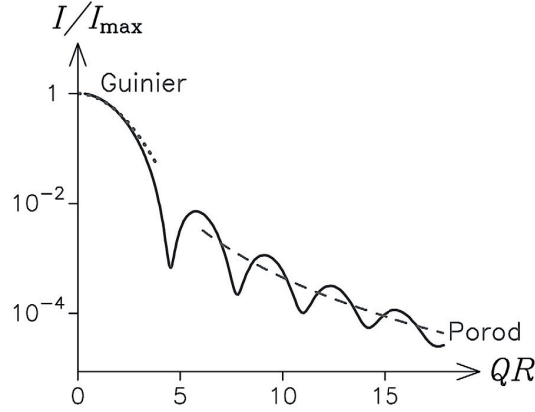


Figure 2.5 Guinier and Porod region of a scattering profile. Pictures adopted from *Elementary Scattering Theory*, D.S. Sivia, 2011, Oxford University Press¹⁵⁹.

As one can see from Figure 2.5, different q ranges in the scattering profile could be analyzed to give information on different aspect of the scattering object. At the low angle region, if one performs the Taylor expansion to the scattering intensity, the higher order contribution could then be neglected when the q is small.

$$e^{i\mathbf{Q}\cdot\mathbf{r}} = 1 + i\mathbf{Q}\cdot\mathbf{r} + \frac{1}{2!}(i\mathbf{Q}\cdot\mathbf{r})^2 + \dots \quad (2.10)$$

For nanoparticles with central symmetry, the scattering profile becomes:

$$\left(\frac{d\sigma}{d\Omega}\right)_{\text{el}} \approx \left(\frac{N}{V}\right) V_p^2 |\beta_1 - \beta_o|^2 \left\langle \left| 1 - \frac{1}{2V_p} \iiint_{V_p} (\mathbf{Q}\cdot\mathbf{r})^2 d^3\mathbf{r} \right|^2 \right\rangle_{\Theta} \quad (2.11)$$

And the following relationship could be further derived in the famous form of Guinier approximation:

$$\log_e \left[\left(\frac{d\sigma}{d\Omega}\right)_{\text{el}} \right] \approx \log_e \left[\frac{\Phi m}{\rho N_A} |\beta_1 - \beta_o|^2 \right] - \left(\frac{R_g^2}{3} \right) Q^2 \quad (2.12)$$

Here R_g is the radius of gyration:

$$R_g^2 = \frac{1}{V_p} \iiint_{V_p} r^2 d^3\mathbf{r} \quad (2.13)$$

Therefore, from the Guinier analysis, it is possible to calculate unambiguously the molecular weight and the R_g of the particles, although one should note the restrictions on the application of the Guinier approach, i.e. typically $qR_g < 1$.

Due to the fact that the measured intensity of small angle scattering is the squared modulus of the wave function, it is impossible to directly retrieve the exact scattering length density

functions from the data. However, the autocorrelation function of the scattering length density function could indeed be correlated with the intensity by:

$$\left(\frac{d\sigma}{d\Omega}\right)_{\text{el}} \propto 4\pi \int_0^{d_{\text{max}}} r^2 g(r) \frac{\sin(Qr)}{Qr} dr \quad (2.14)$$

The pair correlation function could be further converted to the probability of finding two atoms separated by r distance, which is the pair distance distribution function:

$$P(r) \propto 4\pi r^2 g(r) \quad (2.15)$$

Mathematically, the $P(r)$ can be calculated from Fourier transforms by:

$$P(r) \propto \frac{2}{\pi} \int_0^{\infty} Q r \left(\frac{d\sigma}{d\Omega}\right)_{\text{el}} \sin(Qr) dQ \quad (2.16)$$

However, practically the direct calculation of $P(r)$ is impossible, due to the noise background, instrument resolution and the incomplete q range measured. The application of indirect methods in the 1980s from works of Glatter, Svergun and Moore as well as some recent developments have enabled routine calculation of $P(r)$. An example of SAXS pattern and the corresponding $P(r)$ function is shown in Figure 2.6. One of the important messages one can get from $P(r)$ is the D_{max} value, which stands for the maximum distances in the scattering object. In the case of nanoparticles, it equals to the overall diameter of the nanoparticle. The shape and sometimes the multiple peaks in $P(r)$ could provide information on the shape and distribution of scattering length distribution of the particles.

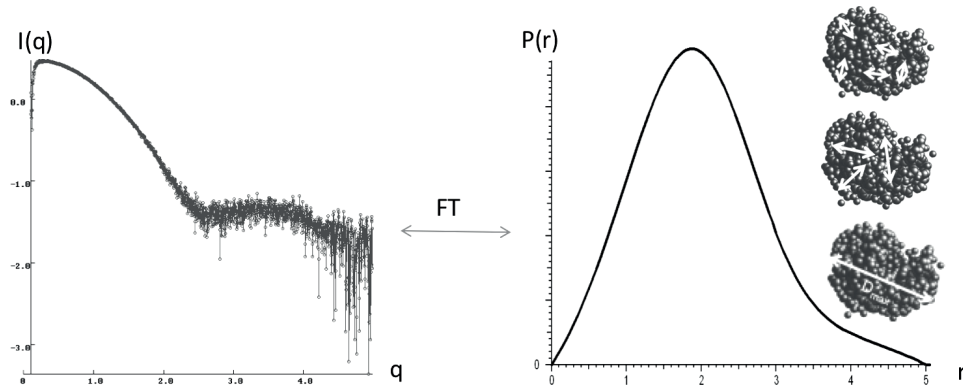


Figure 2.6 Calculation and structural information obtained from $P(r)$. Data plots are obtained and modified from small angle scattering biological data bank (<https://www.sasbdb.org>).

2.2.3 *Ab initio* and other advanced data analysis methods

Analytical methods are of great importance in interpreting small angle scattering data. It offers a rapid way of quantifying the shapes and length scales and structural characteristics from scattering data. It is of special importance when quantitative comparison between different systems are required. On the other hand, the limitations of such analysis are also obvious. know *a priori* knowledge on the category of the structure/shape of the scattering object must be given for a model to be built. In the cases when no other techniques could be used to provide supporting information, assumptions need to be made, which often leads to rough models. When it comes to structures with complex shapes and scattering length density distribution, it is not trivial to propose a suitable analytical form factor.

Therefore, great efforts have been devoted in the field on reconstruction 3D models from small angle scattering data without preset assumptions. In the earlier studies, the trial and error based methods was applied in order to compare the scattering profile of proposed structures with experimental ones¹⁶⁴. *Ab initio* based methods that utilize Monte Carlo type calculations were reported in the late 1990s¹⁶⁵. Thanks to the introduction of spherical harmonics, which significantly reduces the calculation time compared to methods using Debye equation, DAMMIN has become the most widely using algorithm for fitting the small angle scattering data¹⁶⁵. The implication of this algorithm includes:

- Generation of a spherical search volume composed of closely packed beads. The diameter of the search volume is determined by the D_{\max} value calculated from pair distribution function. Each bead is assigned (typically begin with random assignment) to be either the sample components (e.g. proteins or RNAs) or the solvent and the theoretical scattering curves are then calculated as:

$$I(q) = \left\langle \left(\sum_k^K \Delta\rho_K A(q)_K \right)^2 \right\rangle_{\Omega} \quad (2.17)$$

where A is the scattering amplitude of the bead with a contrast of $\Delta\rho_K$.

- Simulated annealing iterations are then applied to the bead model. For each iteration, the assignment of one of the beads is changed and the corresponding scattering curves are calculated. The goal of the iterations is to minimize the overall discrepancy (χ^2 , as defined below) between the experimental data and the calculated data from the model. The utilization of simulated annealing allows the acceptations of changes that leads to higher discrepancy with a probability function, which allows finding geometries that

are closer to global minimum compared to simple Monte Carlo search. Other fitting constraints such as looseness, interconnectivity and volume fraction could also be taken into consideration and act as penalties when minimizing the χ^2 ¹⁶⁶.

$$\chi^2 = \sum_k \frac{1}{N_k - 1} \sum_{j=1}^{N_k} \left[\frac{I_{\text{exp}}^{(k)}(q_j) - c_k I_{\text{calc}}^{(k)}(q_j)}{\sigma^{(k)}(q_j)} \right]^2 \quad (2.18)$$

Where the index k runs over the scattering curves, N_k are the numbers of experimental points, c_k are scaling factors and $I_{\text{calc}}(q_j)$ and $\sigma(q_j)$ are the intensities calculated from the subsets of the beads belonging to the appropriate phases and the experimental errors at the momentum transfer q_j , respectively.

- As the fitting procedure is a stochastic process and that the ab initio reconstruction would lead to non-unique solution, typically the fitting procedure is run for multiple times and the resulting models could be compared and averaged in order to identify the structural features and minimize the ambiguity. Recently, it has also been used to study the resolution of the generated 3D models.

The ab initio method have received great success analyzing the solution structure of a large amount of biomacromolecules and their complexes and further confirmed by high resolution techniques such as crystallography and electron microscopy¹⁶⁷. A typical fitting result of DAMMIN method is shown in Figure 2.7. The same method could also be applied to neutron scattering data analysis. In the case of SANS, the assignment of the beads could be one of the multiple components of the sample or the solvents. Data-set with multiple contrast conditions could be fitted simultaneously using the method, as provided by MONSA program. Furthermore, recent development of packages such as GASBOR have used the chain-like residues to represent amino acid residues with physical constraints to build 3D models with even higher resolution¹⁶⁸. The fitting of the curves could be extended to high q values and much detailed information could be thus revealed from the modelling.

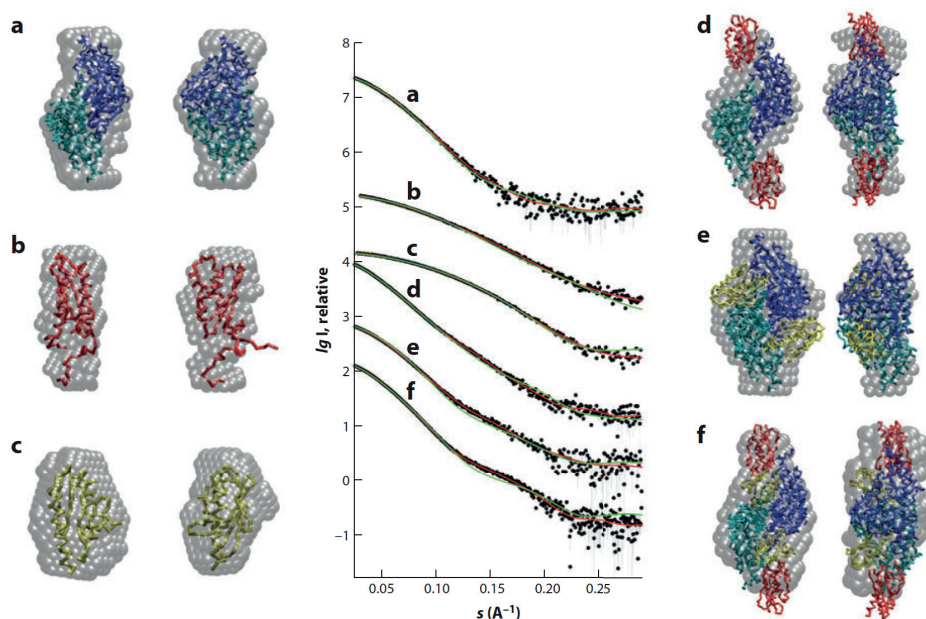


Figure 2.7 SAXS data analysis using ab initio model reconstruction (a-c) and rigid body refinement (d-f). Black dots are experimental data, red full lines are the fitting from DAMMIN calculations and the green curves are calculated from high resolution protein structures and rigid body refinements. Figure copyright from reference, reproduced with permission¹⁷⁰.

When high resolution structures are available from high resolution techniques such as crystallography, it is also possible to compute the theoretical scattering profiles from the atomic structures, as implemented in packages such as CRY SOL, FOX, AquaSAXS and many others¹⁶³. These programs allow one to fit the hydration layer density, excluded volume and or the heterogeneity of the hydration water density. The experimental scattering data are fitted by adjusting the parameters on hydration water as well as protein conformation, either coarse grained or explicitly. Such analysis could help identifying/validating the high resolution structures, e.g. calculated from NMR. Recently, it has also been applied for the structure refinement of protein conformation in solution¹⁶⁹. The continuous developments of algorithms have enabled more and more accurate description of the solution structures of proteins.

Small angle scattering has also found growing application in the analysis biomolecular complexes in solution. One of the advantages of scattering techniques is that it is not limited by the size or the solution states of the macromolecules. The organization of proteins and/or RNAs into large nanoscale complexes is hard to be characterized by other types of techniques,

especially in solution states. The rigid body analysis enables the computation of the scattering patterns from macromolecular complexes and fit to the experimental data by adjusting the relative position and conformation of each component in the complex¹⁷⁰. The fitting could be performed via a manual interactive way or fully automated. The scattering profile of each component and the complex could be simultaneously provided and the scattering from single proteins could be calculated from programs such as CRY SOL. The rigid body analysis has been successfully applied to the study of many important protein complexes and been endorsed with functions such as resolving missing pieces of fragments in the protein complexes that could not be resolved by the high resolution method¹⁷¹.

2.2.4 Recent advances in the application of SAS

In solution, the structure of many proteins are flexible or even intrinsically disordered. Small angle scattering has becoming one of the most important tools for the study of the structures of such proteins. The development of ensemble based analysis techniques in the past decades have been focusing on interpreting the scattering pattern through a library of possible models. The scattering curves could be regarded as linear combinations of different components. In this way, the distribution of species with varying sizes (R_g and D_{max}) could be quantitatively extracted. The method is very often combined with other techniques such as SEC, FTIR, NMR and computer simulations in order to guide the selection of library or act as constraints for the final fitting results¹⁷².

There are many other exciting advances of the small scattering technique as a result of the development of algorithm and instrumentation. For example, the application of anomalous SAXS enables the exploring of multi-component system; in situ SAS measurements at synchrotrons or XFEL facilities allows the study into the fast kinetics of proteins in solution. SAXS has also becoming a tool for high-throughput screen analysis, which will have great potential in both fundamental researches as well as industrial applications.

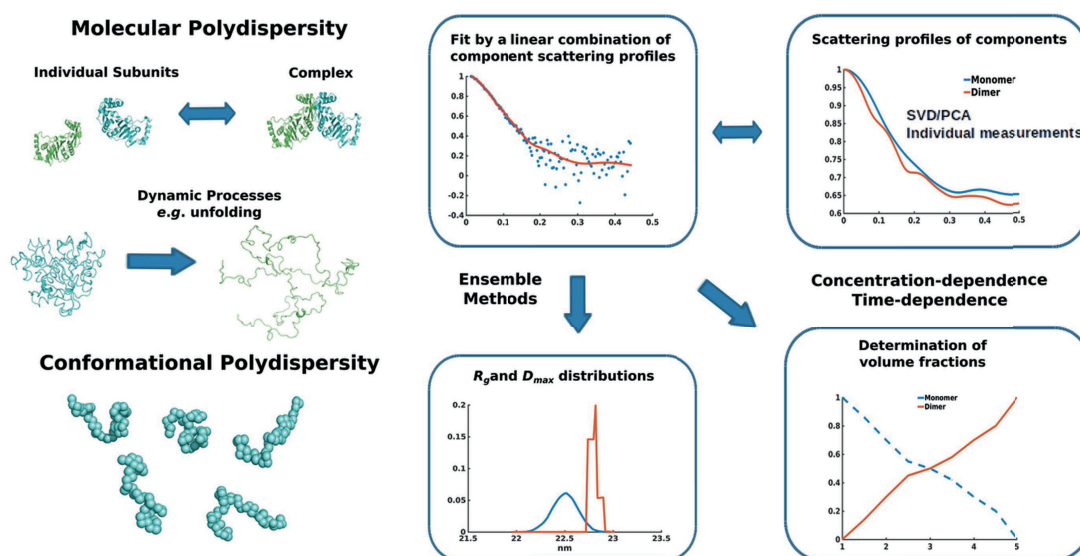


Figure 2.6 Schematic of the application of small angle scattering for the study of mixture of protein samples. The mixture could be composed of different molecular species or conformation distribution of the proteins in solution. Figure adopted from reference¹⁷².

2.3 Mass spectrometry study of the structure and dynamics of proteins

The application of mass spectrometry on proteins is another fast developing field. Although the general principle for the mass spectrometry has been established for a long time, its utilization on proteins or other types of biomacromolecules started to emerge only from the 1980s. The development of two ionization techniques, i.e. Electrospray Ionization (ESI) and Matrix Assisted Laser Desorption Ionization (MALDI) has been the main impetus for the field, which were awarded Nobel Prize in chemistry in 2002. While both techniques are similar in that they are ‘soft ionization’ methods, the working principles and applications are very different. ESI utilizes the electrospray process, in which small charged liquid droplets are generated by high voltage, followed by the evaporation and fission, which generate the final ions of the analytes. The ESI process often generates multiple charged ions, which can be advantageous since the accessible mass range could be extended and the solution charge status of the macromolecule could also be inferred. Furthermore, the ESI setup enables coupled measurement/techniques such as chromatography and stopped-flow devices. On the other hand, MALDI is a technique that ionizes the macromolecules by transferring the laser energy through specific matrix molecules. Compared to ESI, MALDI produced mainly single charged species and thus the analysis of intact molecular weight is much simpler. The wide

molecular weight range and the condition of measurement in bulk made MALDI very useful for large molecules as well as advanced imaging applications.

Despite the great advancement in the ionization techniques and the high resolution instrument available today, it may seem to be unclear whether/how mass spectrometry based technique could give information on protein structures other than molecular weight. In fact, one of the reasons for the field's fast development is due to the emergence of many innovative and creative concepts/methodologies that translate the structural features into the differences in mass. Taking advantage of the high accuracy on mass peaks, most of the methods utilizes the 'mass shift' as a sensitive readout. The application of three common techniques, i.e. crosslinking, hydrogen exchange and chemical labelling, are described.

2.3.1 Chemical cross linking

An emerging and powerful technique in studying the conformation and the intermolecular interactions of proteins is the chemical cross-linking method^{173,174}. This technique adopts a bi-functional small probe molecule to link two residues on proteins that are close in 3D space. Through a bottom-up digestion approach, detailed cross-linking profile is then examined by mass spectrometry. Thanks to the high resolution and quantification ability of the current instrumentation, one could translate the cross-linking distance profile into the 3D structure of proteins and their complexes, with the aid of advanced computation software. A typical workflow on human serum albumin is shown in Figure 2.8¹⁷⁵. The distribution of the experimental crosslinks stands for the possibility of finding certain sequences in close proximity. In total 43 cross-linking events were discovered, including the linking of different inter-alpha helices. The mapping generated by computer modelling software achieved good agreements with single crystal structures.

The choice of cross-linking reagents is one of the first considerations in this type of measurements. Amino acid residues such as lysine and cysteine are the main targets of the reaction sites. The so called cross-linking limit is determined by the chain length of the bifunctional molecules, which could be regarded as the special resolution of the crosslinking method in discriminating proximal residues¹⁷⁵. Recently, 'zero-length' and genetic encoded amino acid derivative cross-linkers have been developed, which could give even higher accuracy for such measurements¹⁷⁶.

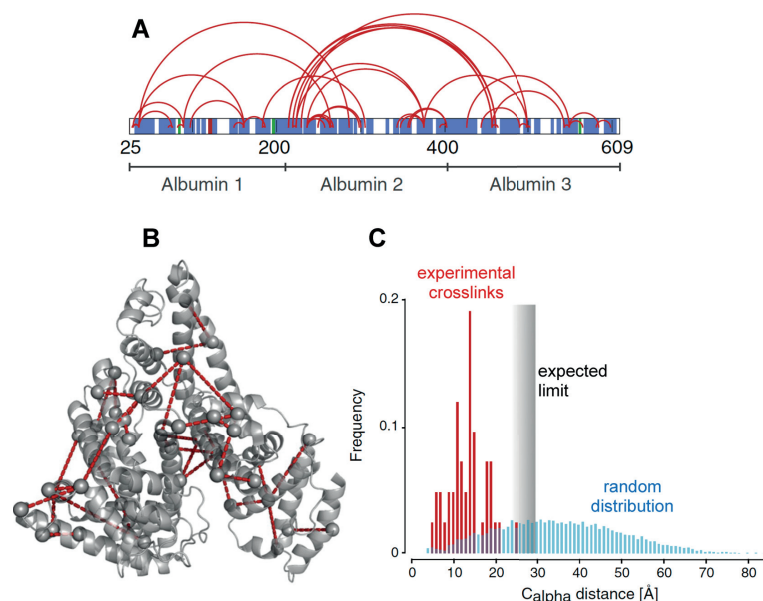


Figure 2.8 Cross-linking mass spectrometry based analysis of human serum albumin. (A) A map of the cross-linking profile on the whole protein sequence. (B) Visualization of the cross-linking positions on the 3D structure of the protein. (C) Frequency distribution of the cross-linking distances compared to a random distribution of the lysine pairs. Image reproduced from reference¹⁷⁵.

There are still several difficulties in the cross-linking technique. First and most importantly is the urge for more advanced data analysis methods, since there are a formidable numbers of possible cross-linking events that need to be sampled for a complete analysis. A large library and an effective sampling algorithm need to be developed, while promising applications of isotope labelled cross-linkers could largely help the process. Second, one needs to deal with imperfect cross-linking events with this method, such as the dead-end products and intermolecular links. Furthermore, the application of cross-linking mass spectrometry *in vivo* may be a future direction, while the development of suitable bifunctional groups that are able to penetrate the membranes is the key.

2.3.2 Hydrogen exchange and chemical labelling mass spectrometry

Hydrogen exchange mass spectrometry is another exciting and powerful method for the study of the structure and dynamics of proteins¹⁵⁶. The principle of the hydrogen exchange method is based on the fact that active hydrogens bound to nitrogen, oxygen or sulphur atoms in proteins undergo constant exchange with the solvent molecules. The exchange rate of the hydrogen is highly dependent on the local solvent properties, such as pH, temperature, and

hydrophobic interactions. For example, the exchange reaction of amide can be catalyzed through either acid or base routes. The rate of exchange reaches the minimum at the pH of 2.5-3.0, which can be often used to quench the reaction. Further, the amide hydrogens on the surface of a protein could be fully exchanged at a time scale of seconds while the exchange of amide hydrogens at the hydrophobic interior of the protein could take even days to be exchanged. Therefore, by quantifying the exchange kinetics, it is possible to study the conformation and dynamics of the proteins in solution. A typical measurement procedure of hydrogen-deuterium exchange (HDX) experiment is described in Figure 2.9¹⁷⁷. The HDX process is quenched at different reaction stage by adjusting the pH of the solution. Then a bottom-up approach is usually used to study the kinetics of different sequences by the enzymatic digestion the proteins. Quantitative analysis on the HDX profile could then yield detailed mapping of protein conformations, such as the solvent accessible surface area. HDX has enabled the study of protein functions that no other types of techniques could achieve. For example, it is possible to extract the mechanism of protein-ligand or protein-protein interactions in a quantitative way and even with millisecond time resolution. Such developments enable a better understanding of the protein structures and could also be applied for applications such as drug discovery.

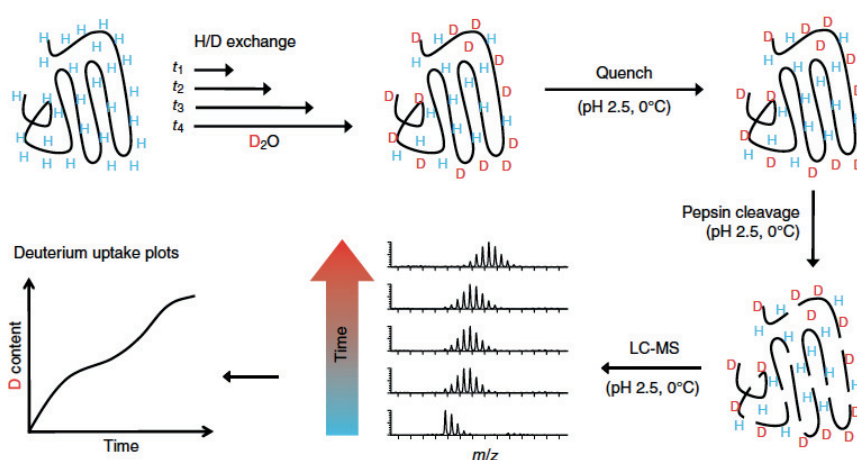


Figure 2.9 Schematic of a typical procedure of hydrogen deuterium exchange mass spectrometry. The protein is exposed to D_2O for a certain period of time for the active hydrogens to be exchanged. The reaction is quenched at low pH followed by the cleavage by the enzymes. The detailed exchange kinetics of different sequences are extracted which gives information on the conformation of proteins in solution. Image reproduced from reference¹⁷⁷.

The fundamental idea of HDX exploits the mass shift of isotope labelling in order to probe the solvent interactions and reactivity of amide bonds. Similar principle could also be used by

chemical labelling of the peptides¹⁷⁵. For example, fast photo-chemical oxidation of the proteins has become a useful tool recently to study the conformation change of proteins since the oxidation labelling occurs at faster rate than the dynamics of protein conformation. Other reactive chemical species such as radicals and tags have also been explored for such purposes. In summary, a rich choices of techniques have opened doors of many different possibilities using mass spectrometry for the structural characterization of proteins. A combination of mass spectrometry techniques with other classical methods such as small angle scattering, cryo-TEM would have great potential for future applications.

2.4 Scope of this thesis

This chapter has introduced the main motivations of my thesis work, which stem from the analogy between proteins and patchy nanoparticles. From a physical chemical point of view, these two types of materials share large amount of similar interfacial properties. As pointed out in the above section, the surface patchy structures determine the interaction of both proteins and nanoparticles with other molecules, including solvents, small biomolecules and biomacromolecules. However, such properties could not be explained by classical colloidal theories. One of the reasons is that the dimensions of the patches as well as the overall size of nanoparticle/proteins are in a range that is commensurate with surrounding matrix molecules, such as solvents and ions. As a result, many assumptions in colloidal theory do not hold, and thus the surface properties are often not additive and could not be easily predicted⁷. Meanwhile, the structure of both objects pose great challenges in the experimental characterization of their structures.

Luckily, one can take the advantage of each of the systems to understand the other. While patchy nanoparticles are an emerging field with only STM being the main characterization method before this thesis, structural biology has been developed for decades with great advances in a variety of techniques. In this thesis, I have adopted and applied two main techniques from biology to the study of nanoparticles, i.e. SANS and mass spectrometry. The analysis has helped the study of the structure of mixed ligand nanoparticles, atomically precise nanoclusters and explained the mechanism of ligand exchange reactions on gold nanoparticles. As a consequence, I demonstrate that now one can control the morphology of mixed ligands through ligand exchange or thermal treatments. The combination with advanced computational methods is a key that benefits both experimental techniques. Especially for MALDI-TOF MS, the original idea of utilizing reverse Monte Carlo

simulations is inspired by the data analysis methods in bio-SANS. Prior to this work, there was few studies that have introduced such analytic methods in the interpretation of mass spectra, which might further be translated to the characterization of other types of materials such as copolymers.

On the other hand, protein sciences could also be benefited from the research in patchy nanoparticles. While the coexistence of hydrophobic and hydrophilic residues is a ubiquitous phenomenon for proteins, little is known about the effects of such surfaces, although obviously such complexity would establish specific interaction with water as well as with other interfaces. The direct study of such interfaces is truly challenging as proteins are constantly sampling a large conformational space and hence the interface is constantly changing through a series of patchy conformations. The patchy nanoparticles could then be regarded as a model surfaces that are less complex and more static. In this thesis, I have shown how the patchy nanoparticles could help elucidate fundamental questions in surfaces sciences such as why the water structures and interfacial properties are non-additive at nanoscale. Ongoing research projects have focused on how the surface patchiness governs the intermolecular interactions between the nanoparticles. Both results are not only important for the future applications of nanoparticles in different fields, but also are key to the understanding of biological processes such as protein folding, enzyme functions and aggregation of proteins.

Promising as it is, translating the understanding from patchy nanoparticles back to proteins still has a long way to go. However, the discoveries along the way have enabled many exciting new opportunities for nanoparticles, such as ion-sensing, catalysis, drug delivery as well as nanomedicines for viruses. I hope this thesis could help laying the foundations for more of such discoveries in the future.

Chapter 3 Quantitative 3D analysis of the morphology of mixed ligand nanoparticles by small angle scattering

This chapter establishes the application of small angle neutron scattering on mixed ligand protected nanoparticles. *Ab initio* models are built for various type of nanoparticles and validated with molecular dynamic simulations. The strength and limitation of this technique is discussed.

Disclosure: *This chapter is substantially derived from a draft of the manuscript that is now accepted in Nature Communications as “Quantitative 3D analysis of the morphology of mixed ligand nanoparticles by small angle scattering.”*

At present there are a number of great approaches for the characterization of the core of nanoparticles. However, when it comes to structures of the ligand shell, few reliable techniques have been developed. A complete characterization is only possible if a single crystal can be made and solved, which is limited for a small fraction of the very small particles that we call nanoclusters. When single crystal analysis is impossible (i.e. the vast majority of the known nanoparticles), the approaches capable of characterizing the ligand-shell are qualitative in nature, which can only distinguish between patchy, Janus, and random morphology. The only partial exception is the case of scanning tunneling microscopy for the morphology of stripe-like domain. This chapter shows that the combination of Small Angle Neutron Scattering with *ab initio* calculations (along the lines of what is done in structural biology) leads to robust and quantitative solution of 3D models of both the ligand shell and the core of the nanoparticles. The approach can distinguish various morphologies of ligand shell and even the ones with very similar structures. The method could be used on systems that have not been characterized with other state-of-the-art techniques. Furthermore, it demonstrates how tools from structural biology can be applied to the studies of nanomaterials.

3.1 Introduction

Self-assembled monolayer (SAM) protected gold nanoparticles (AuNPs) have been widely employed in numerous research fields like catalysis, electronics and biology⁵. One of the keys to their success is the ligand shell (LS) that provides the nanoparticles with a surface that is readily tunable. The LS is a SAM whose composition can be tuned almost at will in order to achieve certain desired properties. The picture is not as simple though. It has been shown that as composition changes so does the morphology of the LS⁶⁷. In many cases, domains, such as stripe-like, patchy, Janus, and randomly mixed morphologies, appear in binary mixtures of ligands. More complex morphologies are predicted when multiple components are present in the ligand shell. The LS morphology plays an important role in a number of the nanoparticles' interfacial properties, such as interfacial energy²¹. Furthermore, patchiness in nanoparticles has been shown to play a key role in controlling assembly properties of nanoparticles.

Despite the importance of the monolayer organization, characterization of ligand morphologies remains a challenge. Scanning tunneling microscopy (STM) has been one of the main techniques to observe ligand organizations on gold nanoparticle surfaces^{105–107}. However, STM has limitations. First, it can only characterize particles in vacuum, air, or in non-solvent liquids. Second, the characterization is based on the imaging of the top part of the nanoparticles (approximately one fourth of the surface), hence it is hard to characterize complex morphologies. Third, only a few particles are imaged and often these are the particles that present clearer morphologies. Fourth, as common to all microscopy techniques, when images do not show any features it is difficult to tell if this is because of the particles or of the sample preparation. As possible alternatives, infrared spectroscopy¹²¹ and NMR⁵⁷ are able to probe the chemical environments of ligands in different morphologies, but they require a series of measurements on particles at varying ligand ratios. Moreover, these techniques lead to a qualitative and discrete answer (Janus vs patchy vs random) with no information on the characteristic length scales. Other methods, such as electron paramagnetic resonance and fluorescence, only probe the distribution of specific labeling molecules as an indication of the heterogeneity of mixed monolayers and cannot offer direct information of the morphologies¹⁷. Recently, mass spectroscopy has also been utilized to infer LS morphologies by examining the distribution of gold-thiolate fragments¹³⁰. This method works in the dry state. The analysis of the fragments' statistical distribution is compared to a given morphology and the analysis of the residues used to infer a deviation from such morphology; however, extracting characteristic length scales is a tall order.

Given the challenges in determining the LS morphology, different theoretical approaches have been employed to understand the thermodynamics phenomena that determine the organization of the LS. In her pioneering works, Glotzer and co-workers revealed the origin of stripe-like patterns formed by two immiscible ligands on AuNPs through atomistic and mesoscale simulations⁵¹. It was found that a balance between the enthalpy of phase separation (that would lead to macrophase separation) and a conformational entropy (that pushes towards the increase in interface length) leads to the formation of stripe-like domains. The conformational entropy component could arise either from a length mismatch or from a difference in bulkiness of the ligands. Overall this approach predicts three types of LS morphology: Janus when the entropy components are irrelevant, randomly mixed when enthalpy is small, and stripe-like (or locally ordered patchy) when the two components are balanced⁵⁹. Many more models have been proposed up to now elaborate on Glotzer's findings and it has been key to develop molecular models always more realistic. To date, few computational studies^{69,178} deal with the formation of patterns in monolayers composed by mixtures of more than two ligands with very attractive predictions that could not be experimentally confirmed at that time due to the lack of any experimental technique able to handle more than a binary mixture.

Small angle X-ray and neutron scattering (SAXS and SANS) have been widely employed in structural biology to provide unique insights in the structure of biomolecules and their complexes in solution¹⁷⁹. SANS is a natural candidate for the structure determination of organic ligand shells surrounding heavy metal elements. A tremendous difference in the scattering cross section between hydrogen and deuterium opens a unique opportunity of studying organic ligand shells in presence of heavy elements such as gold. However, till now, there are only few studies utilizing SANS to determine the ligand shell of gold nanoparticles^{108,180–182}. Most of them characterize homoligand shells in terms of global parameters such as its averaged density, thickness and rigidity. Only in a few publications SANS was employed for the characterization of the morphology of mixed ligand AuNPs, in all cases to provide a simple qualitative identification of the LS organization (Janus and stripe-like). In the previous work¹⁰⁸, SANS was used to assess patchiness on gold nanoparticles but no quantitative models were derived.

The work is presented as follows. In the first part I focus on demonstrating how a Monte Carlo calculation method can be safely used to interpret SANS data and generate low-

resolution models. As a well-known system nanoparticles featuring stripe-like morphologies were selected for this task. I then move to test the robustness of the fitting method and prove that both ligand and solvent contrast variations can be interchanged to build low-resolution models with similar results. Having established that, I analyze particles with random and Janus type morphologies and perform a systematic analysis of nanoparticles with various ligand ratios and core sizes. A novel ‘bandage-like’ morphology was determined by SANS, which is ambiguous for STM and is hard to be distinguished from Janus features. Finally, I show as an example that this method can also be extended to measure ternary SAMs on gold nanoparticle surfaces.

3.2 Test of the SANS/MONSA method

In order to perform SANS on nanoparticles a few conditions need to be met. First, the particles must be colloidally stable (or soluble) in a given solvent, e.g. reaching ~10 mg/ml (0.1% v/v) for 4 nm gold nanoparticles without aggregation. Second, the particles must be monodisperse (see discussion below). Third, the ligands used for the particles must be available in a deuterated form. Of all patchy particles, striped nanoparticles are the most studied; so, they are well-suited as reference. With the aim of testing the validity of a SANS-based approach we selected gold nanoparticles coated with phenylethanethiol (PET) and dodecanethiol (DDT) (Figure 3.1A). Based on the theoretical considerations highlighted in the Introduction, these two ligands of different length and with a strong tendency to phase separation are expected to generate well-pronounced stripe-like domains and meet all of the three conditions mentioned above. The particles were synthesized according to Stucky’s protocol leading to monodisperse nanoparticles¹⁸³. Multiple syntheses were performed, using either both ligands hydrogenated, or with one of the two ligands fully deuterated (hereafter we will place a “d” in front of acronyms indicating molecular names to represent the perdeuterated form of the molecule). We produced PET-DDT, dPET-DDT, and PET-dDDT particles. As expected, all three syntheses lead to nanoparticles of the same size and same polydispersity index. Using TEM we determined that the average core diameter was 4.4 ± 0.4 nm (see methods section) for all the PET-DDT, dPET-DDT, and PET-dDDT nanoparticles. We assume that the composition of the particles was independent of the deuteration. The quality of the fits achieved throughout this work supports the validity of this assumption. For the all hydrogenated particles we dissolved them to determine the ligand shell composition by ¹H NMR (all particles described in this work showed no sharp NMR peaks before dissolution, i.e. reasonably almost no free ligands, see method section). The ratio achieved was PET:

DDT=0.57: 1. For SANS measurements, deuterated toluene was used as solvent for both dPET-DDT and PET-dDDT AuNPs.

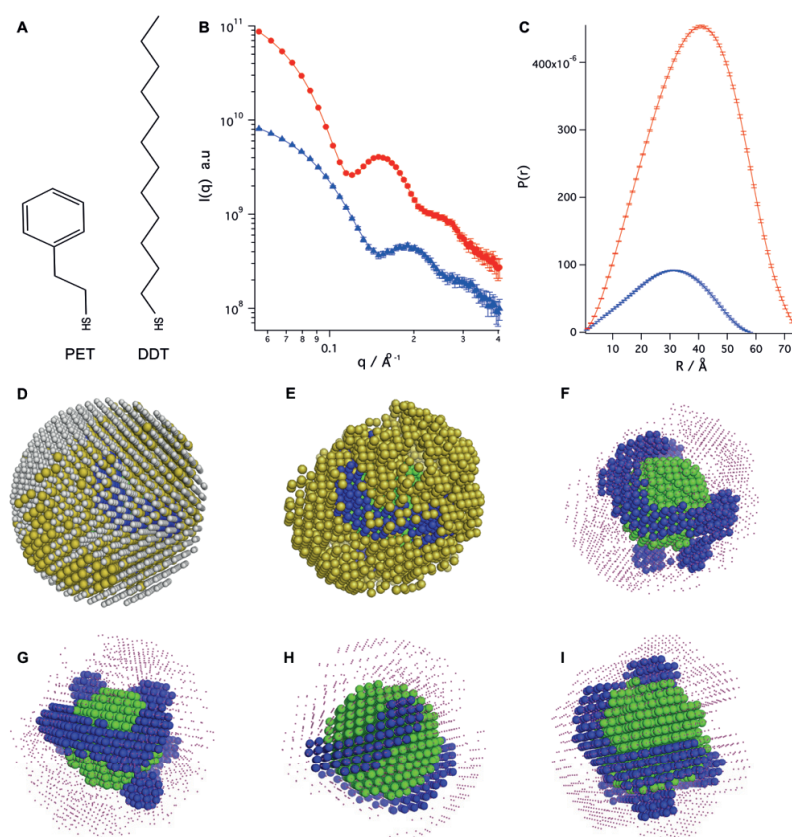


Figure 3.1 SANS data and ab initio models of dPET-DDT and PET-dDDT nanoparticles. (A) Structure of PET and DDT molecules. (B) SANS data (dots) and fits (full lines) of dPET-DDT (red) and PET-dDDT (blue) nanoparticles. The fits are from MONSA fitting and correspond to the theoretical scattering curves of each model. The final χ value of the model fitting is 0.79, indicating the good quality of the fits. (C) Pair distance distribution function $P(r)$ of dPET-DDT (red) and PET-dDDT (blue) calculated from SANS data. (D) 3D low-resolution model built by fitting the two SANS data. All four phases, i.e. solvent (white), DDT (yellow), PET (blue), gold (green), are shown. (E) Three phase model hiding solvent phase. (F) Three phase model highlighting shorter ligands (PET) in different projections. DDT phase is marked with small pink dots. (G-I) ab initio models of PET-DDT nanoparticles built by varying input fitting parameters: (G) 17% difference in volume fraction; (H) Fixing core sizes while adding no constraints on volume fraction; (I) Higher looseness demanded during fitting.

Small angle neutron scattering data were acquired for dPET-DDT and PET-dDDT (Figure 3.1B-C). The q range of all the SANS measurements are from 0.04 \AA^{-1} to 0.4 \AA^{-1} . The q_{\min} (0.04 \AA^{-1}) refers to the largest size information we can probe with our instrumentation set-up, which corresponds to around 16 nm in real space. As shown, the scattering patterns are significantly different under different ligand contrast conditions since information from different part of ligand shells is probed. The shift of the first minima of SANS data, which can be used to estimate the size of spherical objects, from 0.12 \AA^{-1} (52.3 \AA in real space) in dPET-DDT to 0.15 \AA^{-1} (41.9 \AA in real space) in PET-dDDT data, confirms that the overall size of the latter nanoparticles appears much smaller of that of the former due to the matched contrasts between longer ligand and solvent (see Table 1 in see methods section). The radius of gyration (R_g) is an invariant in SANS/SAXS measurements and measures the radii of gyration of the nanoparticle. It is calculated through the fitting of Guinier region of the scattering curves using the PRIMUS package¹⁸⁴. Indeed, the R_g also changed from 32.8 \AA for dPET-DDT to 23.7 \AA for PET-dDDT. In addition, pair distance distribution functions, $P(r)$, were calculated using GNOM package¹⁶¹. D_{\max} in the $P(r)$ data represents the largest distance in the system, which in our case is the overall diameter of the core-shell nanoparticles. The D_{\max} of PET-dDDT AuNP was $58 \pm 2 \text{ \AA}$, while D_{\max} of dPET-DDT AuNP was $75 \pm 2 \text{ \AA}$. The difference between D_{\max} and core size from TEM corresponds to the ligand shell and equals to a doubled length of the ligands. Therefore, the organic ligand thickness was found to be 7 \AA and 15 \AA for PET-dDDT and dPET-DDT AuNPs, respectively. This difference indicates that DDT ligand is around 8 \AA longer than PET in deuterated toluene. Considering the chain length difference between DDT and PET ligands being smaller than 6 carbon-carbon bond lengths, this result indicates that DDT ligands exist in an extended conformation in toluene and are well solvated, which in turn explains why toluene is a good solvent for PET-DDT systems.

A multiple phase ab initio bead model through simulated annealing was then built using the program MONSA from ATSAS package¹⁶⁵. A search volume was generated within a sphere of radius 38 \AA (which corresponds to the half the experimentally determined diameter D_{\max} for this system) containing densely packed beads of 2 \AA radius. Between 30 \AA and 38 \AA radius of the search volume only DDT and solvent phases were allowed according to the information from $P(r)$, while beads within the central 16 \AA radius are fixed to gold in order to reduce the calculation time and acting as physical constraints. All other beads are free to be assigned to all four possible phases. The aim of the Monte-Carlo search is to fit simultaneously both curves and minimize χ^{166} , the overall discrepancy between the

experimental data and fits. The calculated scattering patterns were properly smeared using Pedersen et al's resolution function. We have tested that using smaller or bigger bead sizes does not change the retrieved feature of the 3D model. The number of beads scales as a cubic function of the radius and so does the calculation time. Therefore, we use 2 Å as a compromise for the accuracy and the calculation time. A detailed description of the algorithm and expression of χ can be found in method section. Being a Monte Carlo method, the fitting procedure for each run is a stochastic process, therefore it is mandatory to run each data analysis several times, starting from different random configurations. Models from repeated calculations were found very similar to each other confirming the reliability of the results (see method section). Before starting the calculation procedure, the ligand shell composition was accurately derived from NMR data and converted into a volume ratio by assuming close packing for the ligands. A penalty on the quality of fitting was imposed to the construction when the bead ratio of the model deviates from the experimental ratio. This does not guarantee that the final ratio in the resulting model is the same as desired. Figure 3.1D-F shows the obtained models of PET-DDT nanoparticles. To better visualize multiple-phase models, we will present the most of the models as Figure 3.1F where longer ligands appear as small pink dots and the shorter ligand phase is highlighted with normal beads. The PET phase forms elongated domains with a thickness of 3 to 4 beads, i.e. around 1.2 nm to 1.6 nm. This feature is consistent across the whole nanoparticle surfaces, as shown in method section with different orientations. Constraints on different input parameters (volume fraction, core size, and looseness) were also taken into account (see method section) and they lead to resulting similar phase separated features (Figure 3.1G-I), indicating the robustness of the methodological approach.

3.3 Robustness of the method

One of the main limitations of the above calculations is the need of two ligands in per-deuterated form. This is obviously a limiting condition. It can in principle be avoided, if multiple contrasts are generated by varying the degree of deuteration of the solvent, or using different deuterated solvents. We tested whether this was possible in the PET-DDT reference system. Keeping PET deuterated, the same dPET-DDT AuNP sample was measured using deuterated chloroform as solvent, which changes the contrasts of the components (Table 1 in method section). Combining with the data from deuterated toluene, *ab initio* models could also be calculated (Figure 3.2C) with the overall phase separation features very similar to the

models built from ligand contrasts. Furthermore, when fitting all three data of different contrasts, models with consistent elongated domains were also obtained (Figure 3.2D).

The SANS curve in deuterated chloroform is distinctly different from that in deuterated toluene (Figure 3.2A). One of the most obvious features is the shift of the first minima from 0.12\AA^{-1} to a much lower angle (i.e. larger size), 0.072\AA^{-1} . Considering that DDT ligand chain is well extended in toluene, this shift cannot be due to the change in the ligand chain conformation, but rather reflect the different contrast conditions. As listed in Table 1, deuterated chloroform and deuterated toluene have noticeably different SLDs. While gold and ligand shell possess negative contrasts in deuterated toluene, both phases have positive contrasts in deuterated chloroform, and this should be the main reason for the differences in the SANS patterns. To further study the effect of the solvent, a mixture of deuterated (53%) and non-deuterated (47%) toluene solution was used to measure the same dPET-DDT sample yielding the same contrasts as deuterated chloroform; the resulted scattering pattern also shows the first minimum at 0.074\AA^{-1} , similar to the measurement in deuterated chloroform. This evidence confirms that the observed change is indeed due to the contrast and not to the difference in the nanoparticle structure.

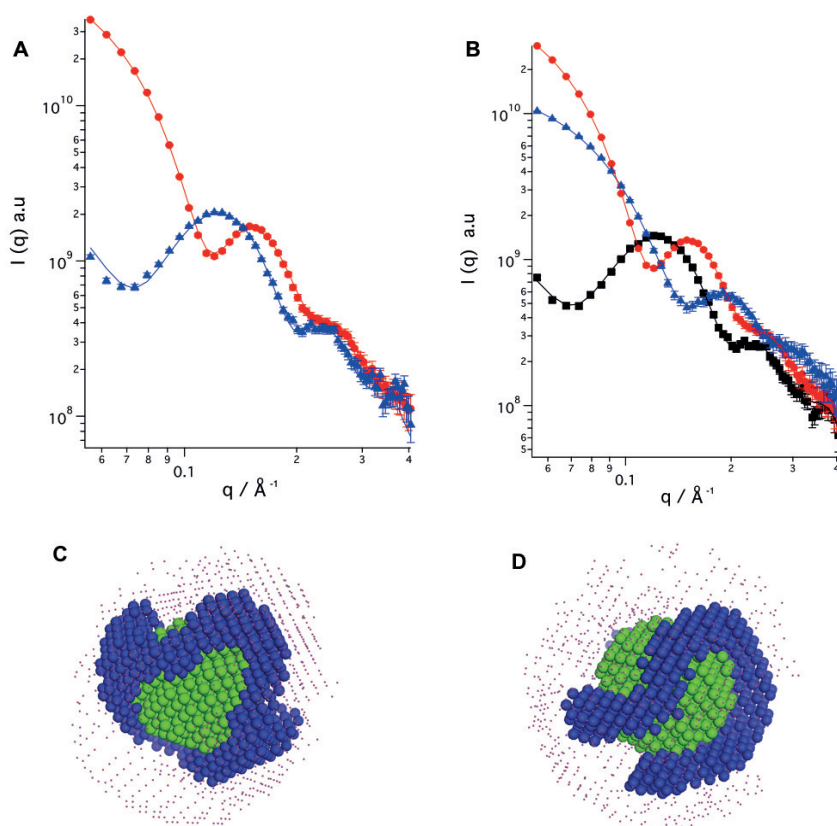


Figure 3.2 SANS data and *ab initio* models of dPET-DDT nanoparticles measured in different solvents. SANS data and fits (A) and model (C) from data in deuterated toluene (red) and deuterated chloroform (blue). SANS data and fits when combining three different contrasts (B) and the resulted model (D). The fits are from MONSA fitting and correspond to the theoretical scattering curves of each model. The final χ value of the model fitting is 0.81. In each three phase model gold is represented in green, PET in blue, and DDT as small pink dots.

3.4 Random morphology

Having assessed that SANS combined to MONSA reconstructions is able to reliably reveal stripe-like domains, the next necessary step is to determine if other morphologies are also correctly identified. In this regard, the first tested was a random distribution of two close-to-identical ligands. Thus, a mixture of DDT and dDDT chains was used as protecting ligands, i.e. DDT-dDDT and dDDT-DDT nanoparticles with a stoichiometric ligand ratio of 1:2. The SANS curves are presented in Figure 3A (note that here, different from the PET-DDT particles, the ligand ratio was the stoichiometric ratio of the feed). Considering that deuterated molecules should have almost the same chemical properties and affinity to gold as protonated ones, the final ratio should be nearly the same as the feed ratio. Previous studies performed with FTIR on octanethiol (OT) monolayers confirmed this assumption for OT-dOT nanoparticles¹²¹. The $P(r)$ functions show the same D_{max} , 80 Å, for both NPs (Figure 3.3B). From the TEM analysis (method section), the average core diameter of the AuNPs is 5.2 ± 0.5 nm, thus the thickness of DDT shell derived from D_{max} is 1.4 nm, in accordance to other studies¹⁸⁰. These two ligands are not expected to exhibit any significant phase separation (as found previously with FTIR and mass-spectroscopy studies), and indeed, *ab initio* model in Figure 3.3C shows a configuration close to random organization.

3.5 Janus morphology

We further tested SANS for Janus nanoparticles, which represent another key morphology often observed for polymer coated particles. We synthesized nanoparticles featuring a mixture of 11-mercaptoundecanoic acid (MUA) and DDT. The ligand ratio was found to be MUA: DDT=1.8: 1 and the average core diameter to be 4.0 ± 0.4 nm. SANS data in Figure 3D were collected using deuterated tetrahydrofuran (THF) as solvent. Coarse-grained simulations (Figure 3.3G-H) suggest a Janus-like arrangement of the ligands after equilibration in solvent medium. As shown in Figure 3F, the resulting morphology from SANS data fitting for this

particle also depicts phase-separated structures. Comparing the SANS pattern of MUA-DDT particles and that of DDT homoligand particles in Figure 3A, one could immediately note that MUA-DDT particles yield less sharp oscillations. This is related to the fact that Janus particles have an overall lower symmetry deviating from a concentric distribution of the components. This is most emphasized for dMUA-DDT, where the MUA phase is matched to the solvent, and the overall shape of the nanoparticles is no longer close to spherical. The $P(r)$ curves of the two SANS data sets yield the same D_{\max} value. This is due to the fact that MUA and DDT have almost the same chain lengths. In the Janus plane, the total diameter is still equals to core diameter plus twice the thickness of the ligand shell. As for the symmetry of $P(r)$, since the ligand ratio for the Janus nanoparticle is close to 1.5:1, the shape could be regarded as a hemisphere. The $P(r)$ of a hemisphere is still quite symmetric. The only difference would be slight shift of the peak center towards smaller distances. In mixed ligand nanoparticle cases, such shift is compensated by the differences in contrasts. (The ligand shell has much higher negative contrasts compared to gold, therefore the $P(r)$ should be shifted towards larger distances for spheres.)

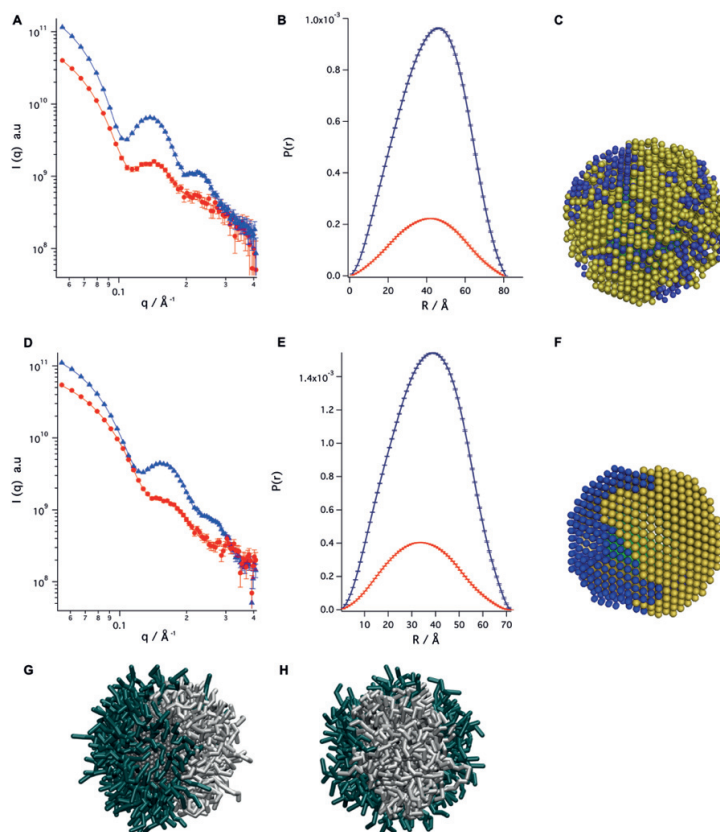


Figure 3.3 SANS data, ab initio models, and mesoscale morphology of homoligand and Janus type nanoparticles. SANS data and fits (A) and pair distance distribution function $P(r)$ function (B) of dDDT-DDT (blue) and DDT-dDDT (red) nanoparticles. The fits are from

MONSA fitting and correspond to the theoretical scattering curves of each model. The final χ value of the model fitting is 0.82. Low-resolution three phase model (C). SANS data and fits (D) and P(r) function (E) of MUA-dDDT (blue) and dMUA-DDT (red) nanoparticles. The final χ value of the model fitting is 0.92. Low-resolution three phase model (F) of MUA (yellow)-DDT (blue) nanoparticles. (G-H) Mesoscale morphology (front and side view) from DPD simulation of MUA (forest green)-DDT (grey) nanoparticles. Solvent not shown for clarity.

3.6 Stripe-like morphology

To further verify that differences in the characteristic dimensions within the same morphology could be reliably detected and visualized with SANS, we performed a series of systematic studies on selected PET-DDT nanoparticles while varying the size of the core or the ligand shell composition. These studies also helped us compare our results with available experimental evidences and published theoretical predictions.

The first systematic analysis was performed on three AuNPs with similar ligand ratio but different in core size. The synthesis of various sized nanoparticles was achieved through the fine tuning of solvent conditions, as described in the Method section. Specifically, we studied 3.2 ± 0.3 nm (PET: DDT= 0.65: 1), 4.4 ± 0.4 nm (PET: DDT= 0.57: 1) (which is the one presented above), and 5.5 ± 0.5 nm (PET: DDT= 0.47: 1) nanoparticles. The search volumes of the model construction were determined from their corresponding Dmax values, while the expected volume ratios of the components were calculated from the NMR data. The SANS data and fits are shown in Figure 3.4A-C, where the red curves stand for dPET-DDT samples, while blue curves represent PET-dDDT nanoparticles. All curves were obtained from measurements in d-toluene, the only exception being the blue curve in Figure 4C (dPET-DDT 5.5nm) that was measured in d-chloroform. For this latter particle, we used solvent contrast instead of ligand contrast as the desired PET-dDDT AuNP lacked the needed monodispersity. The ab initio models (Figure 3.4D-F) display systematic differences between the resulting morphologies. The thickness of the domains scales inversely with nanoparticle core size, as expected from theory that predicts an evolution towards Janus particles for smaller core sizes. The 5.5 nm AuNP showed stripe-like structures, around 0.8 to 1.2 nm in thickness consistent with the STM literature of particle of this size. The three ab initio models obtained from SANS fitting were then directly compared to the simulation results. A stripe-like arrangement of PET ligands was evident for all the diameters considered. This feature is pervasive over the whole NP shell. In nicely agreement with the picture retrieved from SANS fitting, typical

average dimension of these domains was found to increase decreasing the core diameter, from a value of 1.1-1.2 nm to a value of 1.6 -1.7 nm.

To further verify the agreement between the experimental and predicted morphologies, the program SUPCOMB was used to superimpose the SANS reconstructions onto the simulation results in 3D space. The program represents each input structure as an ensemble of points, then minimizes a normalized spatial discrepancy to find the best alignment of two models. The alignment shown was calculated overlapping the PET beads. As shown in Figure 3.4J-L, after re-orientation, the two models present striking similarity. The size and shape of the nanodomains of both models agree also very well.

Next we compared three 4.4 nm PET-DDT nanoparticles with ligand ratios of PET: DDT= 0.2: 1, 0.6:1, 1.2: 1. All the three nanoparticles were synthesized using the same solvent conditions, while the feed ratio of the ligand mixtures was varied in order to tune the final ligand ratio on the nanoparticles. The detailed synthetic procedure is described in the experimental method section. NMR, TEM, SAXS and TGA techniques were used to examine the ligand ratio, core size and ligand shell density of the nanoparticles. We can see from the reconstructed low-resolution models (Figure 3.4P-R) that the domains of PET phase evolve from small patches (Figure 3.4P) for PET: DDT=0.2: 1 ligand ratios, to thick stripes (Figure 3.4Q) for PET: DDT=0.6: 1 ligand ratios, and finally to percolated domains (Figure 3.4R) for PET: DDT=1.2: 1 ligand ratios.

The trend observed by SANS was tested against the morphology predicted by DPD simulations. As indicated in Figure 3.4S-U, when the percentage of PET ligand is small, PET ligands tend to organize in small elongated domains on the Au surface. Increasing the fraction of PET in the monolayer results in stripes which evolve into interconnected domains when the ligand fraction is almost equal. At the same time, the characteristic length scale of the domains slightly increases from 1.4-1.5 nm to 1.7-1.8 nm. Back side images of these nanoparticles can be found in method section. The good agreement between the two models was also confirmed by the superimposition performed by SUPCOMB. Figure 3.4V-X shows a remarkably good matching in term of domains size and shape between the two morphologies.

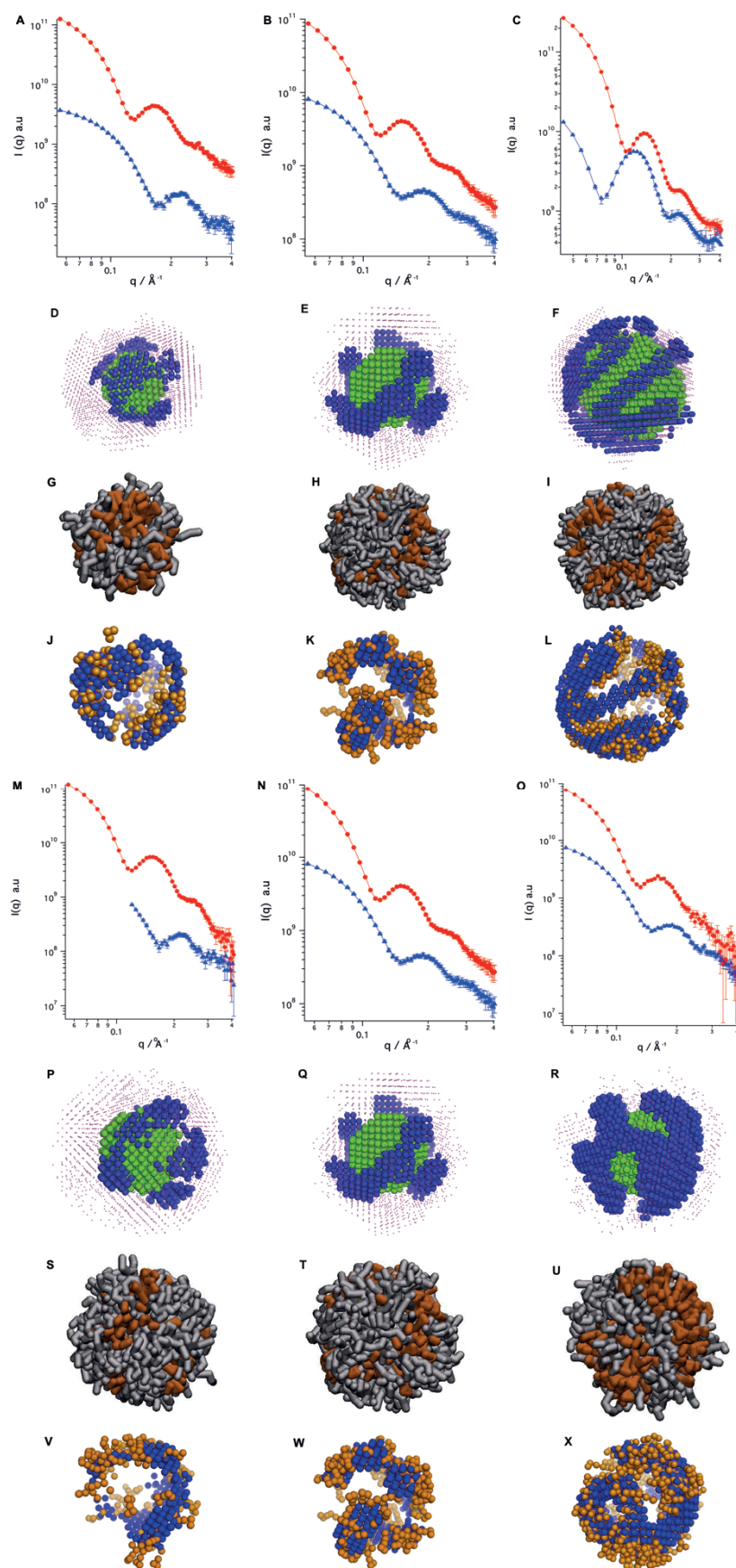


Figure 3.4 SANS data, ab initio models, mesoscale simulation results and model comparisons of PET-DDT nanoparticles with different core sizes and ligand ratio. In SANS data, red dots and curves represent the data and fits of dPET-DDT particles, while blue ones represent that of PET-dDDT particles. The fits are from MONSA fitting and correspond to the theoretical scattering curves of each model. In simulation models, grey sticks represent DDT ligands, while orange sticks represent PET ligands. Solvent is not shown for clarity and radius is not drawn to scale. Figure A-L compare same ligand ratio but different core sized AuNPs: (A) SANS data and fits (with a final χ value of the model fitting of 1.52), (D) model and (G) mesoscale morphology of 3.2 nm particle. (B) SANS data and fits (with a final χ value of the model fitting of 0.79), (E) model and (H) mesoscale morphology of 4.4 nm particle. (C) SANS data and fits (with a final χ value of the model fitting of 1.01), (F) model and (I) mesoscale morphology of 5.5 nm particle. Figure M-X compare AuNPs with same 4.4 nm core size but with different ligand ratios: (M) SANS data and fits (with a final χ value of the model fitting of 0.94), (P) model and (S) mesoscale morphology of PET: DDT=0.2: 1 particle. (N) SANS data and fits (with a final χ value of the model fitting of 0.71), (Q) model and (T) mesoscale morphology of PET: DDT=0.6: 1 particle. (O) SANS data and fits (with a final χ value of the model fitting of 0.71), (R) model and (U) mesoscale morphology of PET: DDT=1.2: 1 particle. Figure J-L and V-X and the 3D are the overlapping comparison of the PET phase of SANS and simulation model, generated using SUPCOMB program.

When feasible, besides mesoscale simulations, we also applied a different experimental technique, STM, to further validate the models built from SANS. The first system we attempted to analyze was the 4.4 nm PET-DDT 0.6: 1 AuNP. The presence of thick stripes makes difficult in principle to unambiguously image the NP surface by STM. Nevertheless, STM images collected during the analysis evidences the presence of domains with a typical size of around 1.6 nm which is in line with the value reported by SANS fitting and simulations. Then, we considered 5.5 nm PET-DDT AuNPs as our SANS model predicted features closer to the previous STM results. Indeed, in STM images elongated nanodomain structures appeared reproducibly, Figure 3.5A and 5B. The comparison between STM image and the SANS model shows consistent features with a typical domain size around 1.2 nm.

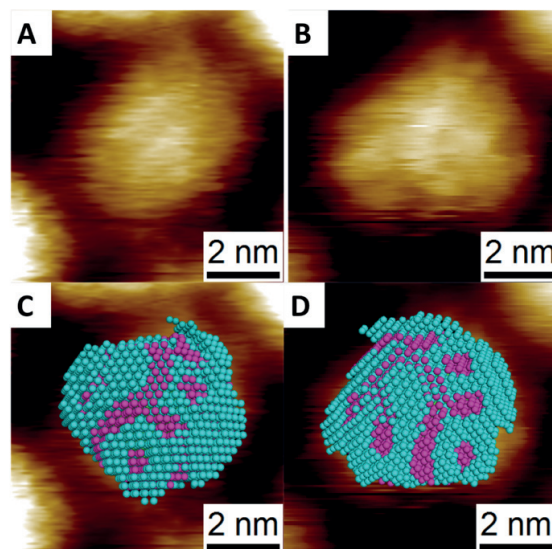


Figure 3.5 STM results and comparison. STM images (A and B) of 5.5 nm PET-DDT nanoparticles and comparison with SANS model (C and D) of 5.5 nm PET-DDT nanoparticles.

3.7 Bandage-like morphology

Further, we focused on mixed ligand nanoparticles where STM had proven to produce images hard to interpret, i.e. AuNPs protected with a mixture of 11-mercaptopundecanoic acid (MUA) and butanethiol (BT) (BT: MUA=0.3: 1). Preliminary STM images (method section) revealed a thick line on most of the AuNPs. Such feature could be interpreted to be due to the interface between domains in a Janus-type structure, but in such case the interface thickness would have been significant and different from what observed in previous publications. Alternatively, the thick line could have been a domain itself, which would have been a novel morphology not reported before. dMUA-BT and MUA-dBT AuNPs were measured in deuterated THF, Figure 3.6A, and the reconstructed low resolution models are presented in two different orientations in Figure 3.6B and 3.6C. The model illustrates a structure that agrees very well with the STM image, and unambiguously shows that the AuNPs have a bandage-like domain in the ligand shell. Such structure could be regarded as a special case of stripe-like morphology with only one stripe. While STM was not able to distinguish such morphology from Janus-type and nanoparticles with single stripe domain, SANS appears as a better tool in this regard.

The presence of a bandage-like feature of BT ligands was also confirmed by molecular calculations, Figure 3.6D-E. The domain is predicted to be 1.3-1.4 nm in width. Comparison between SANS reconstruction and simulation model was done using SUPCOMB package achieving remarkable agreement. From visual inspection of the molecular trajectories the belt seems not involving the entire nanoparticle surface and small patches or single isolated molecules can occasionally appear close to the belt during the simulation time (Figure 3.6E). Time evolution of the belt formation suggests the appearance of small patches of BT ligands; these spots then coalesce into a single cluster which stabilizes the bandage in the monolayer. This is the first time such ligand organization is observed on mixed ligand nanoparticles.

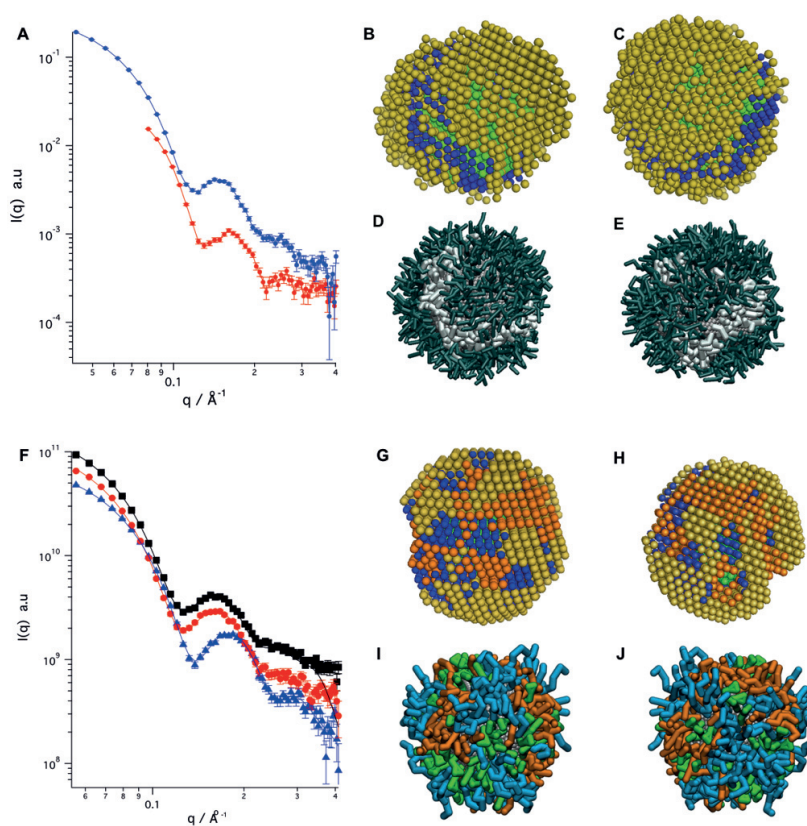


Figure 3.6 SANS data, ab initio models and mesoscale simulation results of MUA-BT and PET-OT-DDT nanoparticles. (A) SANS data in which red dots and curves represent the data and fits of dMUA-BT particles while blue ones are for MUA-dBT particles. The fits are from MONSA fitting and correspond to the theoretical scattering curves of each model, with a final χ value of the model fitting of 0.956. (B-C) ab initio models built from fitting SANS data. Yellow beads stand for MUA ligands while blue beads stand for BT ligands. (D-E) Mesoscale morphology resulting from DPD simulation of the MUA-BT nanoparticles. Forest green sticks represent MUA ligands while white sticks represent BT ligands. Solvent is not shown

for clarity. (F) SANS data in which red dots and curves represent the data and fits of PET-dOT-DDT nanoparticles, blue ones are for PET-OT-dDDT nanoparticles and black ones are for dPET-OT-DDT nanoparticles. The χ value of the model fitting is 0.956. (G-F) Low resolution model of dPET-OT-DDT ternary nanoparticles. Yellow, orange and blue beads stand for DDT, OT, PET ligands respectively. (I-J) Mesoscale morphology resulting from DPD simulations of the PET-OT-DDT nanoparticles. Green sticks represent PET ligands, orange sticks represent OT ligands and light blue is used for DDT chains. Solvent is not shown for clarity.

3.8 Ternary self-assembled monolayer

Finally, I applied SANS to study yet more complex surface structures, namely nanoparticles protected with a mixture of three different ligands. A library of morphologies for ternary SAM protected nanoparticles have been theoretically predicted previous⁶⁹, which greatly enriched the structural diversity of mixed monolayer protected particles. However, none of the current characterization techniques could be used to determine these structures. Here we present, for the first time, the structure of one type of ternary mixed ligand gold nanoparticles. PET-OT-DDT coated nanoparticles were synthesized using the same procedure of PET-DDT nanoparticles with ligand shells selectively deuterated. The size of the gold core was found to be 4.4 ± 0.4 nm while the ligand ratio was PET: OT: DDT= 0.8: 1: 1. The SANS data were collected in deuterated toluene for all PET-dOT-DDT, PET-OT-dDDT, dPET-OT-DDT nanoparticles, Figure 3.6F, and a 4-phase ab initio model was calculated using MONSA to simultaneously fit the three scattering curves. The obtained low-resolution model shows interconnected patchy structures (Figure 3.6G and 3.6H), with PET forming some small patches while OT and DDT phases being stripe-like.

Then, we went on comparing the organization of the ligands with the molecular calculations. Figure 3.6I-J reveals that PET, OT, and DDT ligands are phase separated within the monolayer. Computer simulations show that the shortest surfactant (green) typically forms isolated islands; elongated domains of OT (orange) are also easily discernible surrounded by DDT chains (light blue). Overall, the two techniques return a concordant picture of the complex morphology arising in ternary self-assembled monolayers.

3.9 Analysis of SANS data and MONSA modelling

The analysis of SANS data in our study consists of two main steps. First, typical distances such as the overall diameter, D_{max} and R_g , are determined from the data providing size and thickness of the ligand shell in a given solvent. The Monte Carlo fitting method therefore naturally uses these properties as constraints. Moreover, the oscillation feature of the SANS curves can give hints on the overall symmetry of the system.

The second step employed the construction of low-resolution models using programs from ATSAS package¹⁶⁷. The ab initio shape analysis method - MONSA has been used widely in structural biology to reconstruct low-resolution structures of biological macromolecules¹⁶⁵. The core-shell nanoparticles presented here have a monodispersity less of 10% (assessed both with TEM and SAXS, method section), thus the ab initio methods are expected to be applicable to the nanoparticle solutions yielding reasonably averaged structures¹⁸⁵. We tested thoroughly the robustness of the approach to prove that it can indeed reliably reconstruct nanoparticle structures. Calculations of each dataset were performed several times starting from different random configurations to make sure that the outcome models converge to similar structures. The modelling requires some input parameters, such as volume fraction, looseness, and core size. We investigated the influence of all of them and it should be stated that, when no input parameter is provided to the fitting software, results achieved can be unphysical, i.e. gold core with a large fraction of solvent exposed area. As shown in Figure 3.1, it is sufficient to fix only one of the two input parameters to get a robust model. Indeed, the data presented in this paper were mostly achieved assigning the volume fraction and let the core size be fit by the program, assuming monodispersed nanoparticles. In all cases the resulting core size was found in agreement with TEM data. When the core size was fixed, the model found volume fraction in agreement with the NMR data. Furthermore, we showed that the model was robust against varying up to 20% the input parameter of choice. When the input parameter deviates more, the model leads to unphysical results.

In order to validate the correctness of the resulting LS models we performed a few studies. First, we produced particles with a random distribution of ligands by design (coated with a mixture of dodecanethiol and deuterated dodecanethiol) and shown that the resulting ab initio model correctly predicts a random distribution. Then we analyzed particles with stripe-like domains and imaged them with STM. Analysis of the microscopy images shows that these domains are ~1.2 nm in thickness. Such result agrees quantitatively with the result of the ab

initio model. We then performed a series of systematic studies where either the size of the particles or the ligand shell composition was varied. All of these particles were also simulated at coarse-grain level. Results from the ab initio and mesoscale models for these particles are presented in Figure 3.4. The similarities are striking.

3.10 Interpretation of SANS data

As illustrated from low-resolution models of PET-DDT nanoparticles with different sizes, Figure 3.4A-L, SANS can distinguish between nanoparticles with stripe domains of 1.2 nm and 1.6 nm average thickness. The q range covered in this study is up to 0.4 \AA^{-1} , corresponding to 1.57 nm in real space. Therefore, it is interesting to understand more deeply how SANS can distinguish such small differences. To this purpose, we performed some calculations by generating models with predefined morphologies (stripes with 8 Å, 12 Å and 16 Å thickness) and calculating their theoretical SANS curves. The resulting profiles are markedly different (method section). This behaviour can be rationalized by considering that the diameter of the core-shell nanoparticle is less than 8 nm, and stripes with 1 nm thickness are commensurate to the overall nanoparticle size. Therefore, small differences of the domain sizes will result in considerable changes in the shape and symmetry of the overall nanoparticles, something that can be readily captured by SANS. We then tested morphologies presenting slightly disordered domains instead of regular stripes, i.e. 30% of the beads were moved from their original sites randomly. The calculated SANS curves from these models also showed distinguishable differences among themselves as well as when compared to particles with perfect stripes of the same thickness, method section. We should also state that we tested our ab initio model by feeding the SANS curves produced from these calculations and comparing the low-resolution model that resulted with the original model. Results are shown in methodsection and should be used as reference to understand the power of this approach.

3.11 Polydispersity and ensemble based analysis

The method developed here is undoubtedly powerful. It allows for the determination of the LS morphology of particles with a precision that no other technique can reach. It is also a relatively rapid method. The main assumption and limitation is the high monodispersity required to the sample. As for the metal cores, nanoparticle samples usually have a

distribution of core sizes and the resulted scattering pattern is an average over all the form factors. All of the nanoparticle samples used in this work have high monodispersity, i.e. less than 10% assessed with good agreement both by TEM and SAXS. Nevertheless, scattering pattern of AuNPs with only 20% polydispersity no longer exhibits any sharp oscillations, as shown in Figure 3.7.

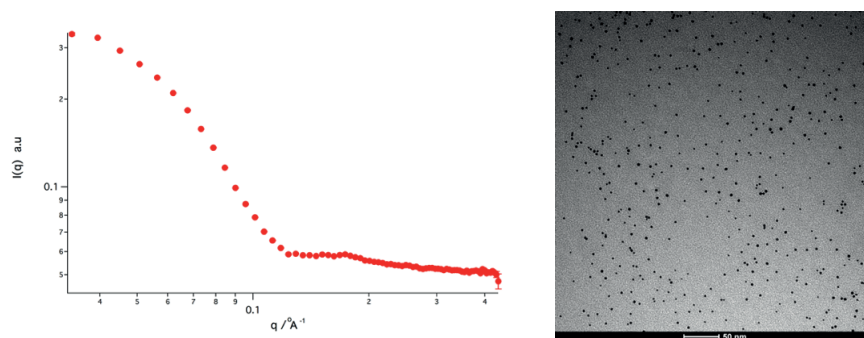


Figure 3.7. SANS and TEM of polydispersed gold nanoparticles protected with dodecanethiol. The nanoparticle size is 3.0 ± 0.6 nm based on statistics of more than 500 particles.

Unlike core size distribution, currently there are no suitable techniques available to assess the distribution of ligand ratios on nanoparticle surfaces. However, for smaller nanoparticles, i.e. atomically precise nanocluster, this issue has been addressed through mass spectrometry and HPLC¹⁸⁶, and to a smaller extent single crystal X-ray diffraction¹⁸⁷. It was found that narrow ligand shell compositional variations are present on these particles. More precisely, mixed ligand particles do not coexist with homoligands. Property-based studies on mixed-ligand particles of larger sizes strongly confirm this finding.

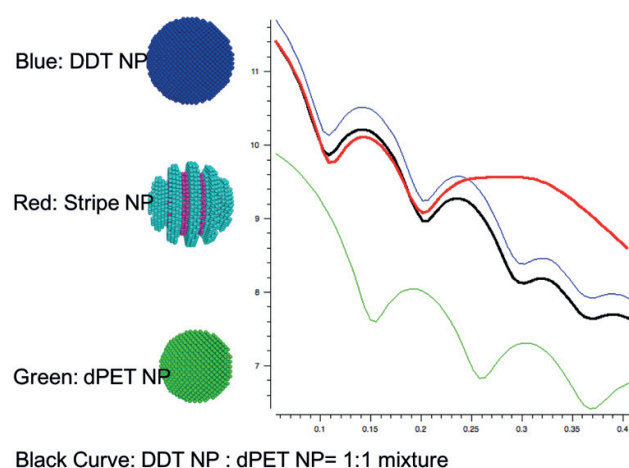


Figure 3.8 Theoretical calculation of the scattering intensity of DDT (blue curve) and dPET (green curve) homoligand protected nanoparticles. The theoretical scattering intensity of a

mixture of the two homoligand nanoparticles (black curved) are compared to the scattering pattern of stripe nanoparticles (red).

A more complex issue is that of polydispersity in ligand shell morphology. In order to test how the MONSA models could average multiple morphologies present in hypothetical samples, ensemble based analysis is performed. First of all, as shown in Figure 3.8, the scattering pattern of a mixture of two types of homoligand protected nanoparticles cannot fit the scattering of nanoparticles with stripe-like features. Especially at high scattering angles (above 0.2 \AA^{-1}), the SANS pattern is dominated by the phase separation features. Figure 3.9 shows that the sum of two Janus particles with an average 1:1 composition does not provide the scattering of a 1:1 Janus particle.

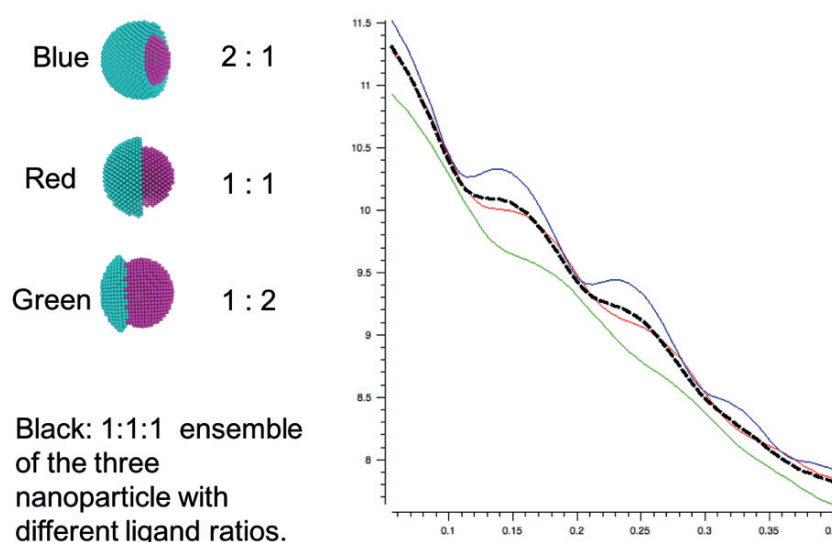
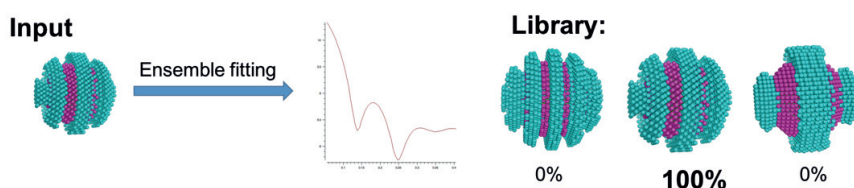


Figure 3.9 Theoretical scattering patterns of Janus nanoparticles with different ligand ratios (Blue=2:1, Red=1:1, Green=1:2). The scattering pattern of the mixture of the three nanoparticles is also calculated (black curve).

Ensemble based analysis is powerful technique in interpreting the small angle scattering data, especially in studying conformations of proteins in solution. Here we apply the same technique to fit SANS data with a library of mixed ligand nanoparticles with various morphologies by using OLIGOMER package. In Figure 3.10 are illustrated the results obtained when fitting the theoretical pattern of a perfect stripe-like nanoparticle using a library of possible morphologies. When the library includes the nanoparticle itself, the ensemble fitting finds 100% contribution from the same particle. When the library contains

different morphologies other than the nanoparticle itself, the ensemble fitting finds contributions mainly from morphologies that are most similar to the theoretical one. No component Janus or random morphology contributes to the fitting. The quality of the fitting is not as good as ab initio MONSA fitting at high scattering angles, which confirms again that the scattering pattern of a specific morphology does not simply equal to the combination of other types of morphologies.

A



B

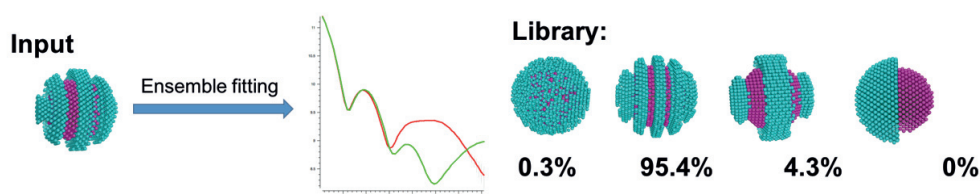


Figure 3.10 Ensemble based fitting of stripe-like nanoparticles. A) Fitting of the stripe nanoparticle with a library that contains the nanoparticle itself. The fitting result finds 100% contribution from the nanoparticle itself. B) Fitting of the stripe nanoparticle with a library where the nanoparticle is absent. The library contains a random morphology, stripe morphologies with different stripe thickness and a Janus morphology. All the nanoparticles in the library share the same ligand ratio and core size of the input stripe nanoparticle. The fitting result finds 95.4% contribution from the stripe nanoparticle with similar thickness. The rest of the contribution comes from random nanoparticles and stripe nanoparticles with thicker features. No contribution from the Janus morphology is found.

Then the ensemble method is applied to analyse experimental data. Stripe-like and Janus like nanoparticle were used as two examples. In Figure 3.11, a large variety of mixed ligand nanoparticle with different morphologies were used as a library to fit the experimental SANS data of the stripe-like nanoparticle. The library includes homoligand, random mixed, Janus-type and stripe-like nanoparticles with different stripe thickness. The result of this ensemble fitting shows that most of the contributions (89.5%) is coming from similar stripe nanoparticles with different thicknesses. Indeed, 32.1% and 26.6% contributions come from

two stripe-like nanoparticles that share similar stripe thickness with that retrieved from MONSA fitting. The program does not recognize any contribution from Janus and random type of morphologies. This ensemble analysis yield overall good quality fitting but significant difference could still be found especially at high scattering angles. Similar results were obtained for Janus nanoparticles with the ensemble analysis, Figure S22B. 65.0% contribution comes from a perfect Janus nanoparticle of similar ligand ratio while 32.7% contribution comes from a stripe-like nanoparticle with thick stripe domains. In this latter case it cannot be excluded that the sample itself did contain striped nanoparticles.

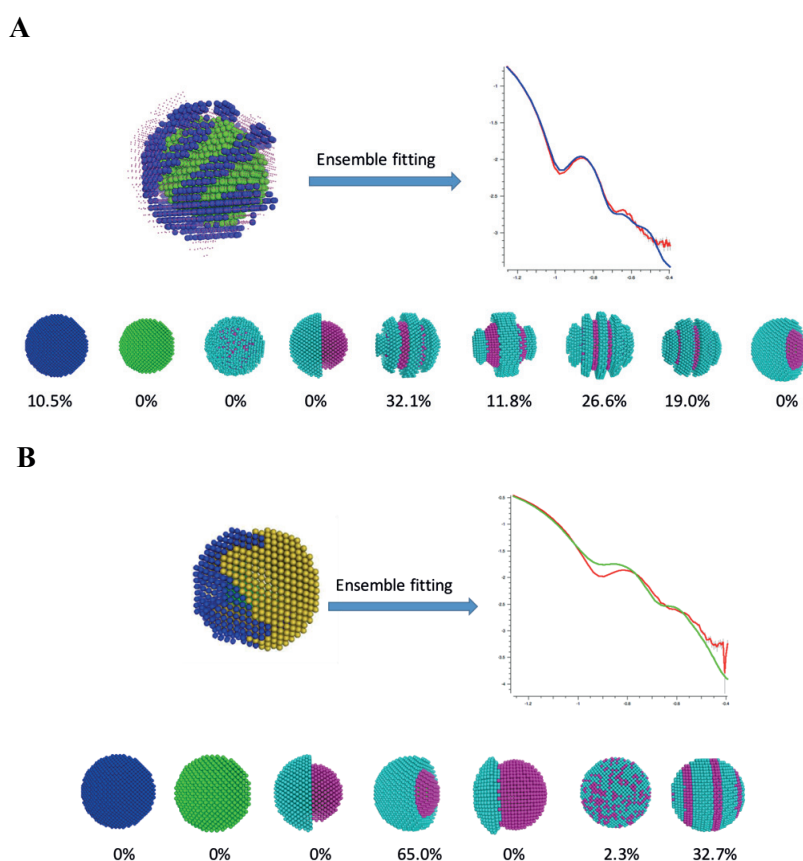


Figure 3.11 Ensemble fitting of experimental SANS data for a stripe-like nanoparticle (A) and Janus type nanoparticle (B), using a large library containing nanoparticles with various ligand shell morphologies. The experimental data are represented by the red curve while the fitting result is the blue curve. The contribution from each morphology in the library is listed.

Therefore, the results of all the ensemble analyses prove the validity of the MONSA fitting method. The fact that only the nanoparticles with similar features as MONSA model contributes to the fitting allows concluding that the reconstructions are representative. Although small polydispersity of ligand shell distribution is not avoidable, the features in the SANS pattern are determined mainly by the structure of phase separation domains on nanoparticles.

3.12 Limitations and scope of the technique

Beside the demand for high monodispersity, there are two more requirements in this method. First, sample concentration is of great importance for SANS experiments. Neutron sources are generally orders of magnitude less intense than normal X-rays. Therefore, exposure times are typically in the order of hours, depending on the detector position and sample concentration. To cover enough q -range, often more than one detector position is required. Moreover, once a component is matched out, the scattering intensities will further decrease. Considering all these effects, the concentration of samples should be relatively high, but it should remain low enough to minimize inter-particle interactions. Taken together these two constraints mean that one needs nanoparticles with a high colloidal stability. In our experience this means particles that can be in solution at a 10 mg/ml concentration with no appreciable aggregation.

The last requirement is that at least one deuterated ligand is needed so to have enough contrast between the two ligands, due to the fact that the SLD of protonated ligands are usually very close to each other. The approach shown here is based on multiple contrasts. This was achieved in our experiments for the most part by having both ligands deuterated. As shown in Figure 3.2, this requirement is not strictly necessary, as multiple contrasts can be achieved either by different mixtures of hydrogenated and deuterated solvents or by using different deuterated solvents. The former approach is more versatile but has the problem of inducing large amount of incoherent scattering. The latter approach requires that the particles not only be highly soluble in two different solvents but also be solvated in similar ways in both solvents. As a consequence, the two-deuterated ligand approach remains the major tool. Obviously, this is a limitation as often these deuterated ligands are not commercially available and need multiple-step chemical syntheses. However, many neutron facilities around the world have growing interests in establishing chemical deuteration capability to facilitate the availability of deuterated molecules that are essentially required for many SANS experiments.

Nevertheless, as long as the three requirements (monodispersity, solubility and deuteration) are met, SANS is a powerful tool to study the ligand-shell morphology of nanoparticles. For example, in this paper we relied on SANS to discover a new morphology that had not been discussed in literature before and that no alternative experimental method developed so far could distinguish it from other forms of patchy particles. This is the ‘belt-like’ structure shown in Figure 3.6A-E for MUA-BT NPs. This structure was also confirmed by molecular simulations. Furthermore, at present all techniques to characterize nanoparticles do not have the ability to reveal the morphology of three (or more) ligand nanoparticles. There are simulations with intriguing morphologies for these particles, but current experimental techniques can only determine whether these particles are patchy or not (and not in a simple way). We show here that in SANS the determination of the morphology for one of these particles is indeed possible (Figure 3.6).

3.13 Conclusion on SANS study of mixed ligand nanoparticles

In conclusion, it is demonstrated above that *ab initio* low resolution analysis using SANS is a powerful and versatile technique for the characterization of mixed ligand nanoparticles. Morphologies varying from random, Janus to complicated patchy/stripe-like structures can all be distinguished and visualized, and the size information can also be retrieved from this method. Importantly, SANS directly reveals the structural features of bulk structures thus avoiding potential sample preparation artefacts of microscopic methods.

With the unique opportunity to use contrast variation through isotope labelling, this approach could be further extended to yet more general characterization of complex structures. This study focus on AuNP, but the technique is not limited to materials and structure of either the core or the shell. For example, a silica nanoparticle, or metal alloy core or a non-spherical object can be quantitatively measured using this method as well (important requirement is a good monodispersity, i.e. that all particles have similar structures). Beside small organic molecules, the structure of macromolecules such as polymers, proteins or DNAs on surfaces could also be characterized. The approach is universal and could be employed to study the structure and interactions within rather complex systems. Given these advantages, I believe that the proposed method might become a general and necessary tool for the nanoparticle field.

3.14 Materials and Methods

Deuterated DDT and OT were purchased from CDN Isotopes, Inc. Synthetic procedures for deuterated PET and MUA can be found in Supplementary Information. All other chemicals were purchased from Sigma-Aldrich and used as received. STM measurements were done using Veeco Multimode Scanning Probe Microscopy. TEM images were taken using Philips CM12 operating at 100 kV. NMR spectra were recorded using Bruker 400MHz spectrometer using CDCl₃ as solvents. SAXS measurements were done using Rigaku BioSAXS 2000 machine. TGA measurements were done using TGA 4000 instrument from Perkin Elmer.

➤ Synthesis and characterization of mixed ligand gold nanoparticles

The nanoparticle synthesis followed the protocol reported by Stucky and co-workers with solvents and feed ratios of ligand mixtures varied¹⁸³. For 5.5 nm nanoparticles, toluene was used as solvent; for 3.2 nm nanoparticles, chloroform was used as solvent; for 4.4 nm nanoparticles, a 1: 1 mixture of toluene and chloroform was used. The ligand ratio on nanoparticle surfaces is controlled by the feed ratio during the reaction. In general, 123 mg triphenylphosphinegold (I) chloride and 0.25 mmol ligand mixtures were dissolved in the 40 ml corresponding solvents and heated to 70 °C. Then, 217 mg borane t-butylamine complex was added into the solution under rapid stirring. 40ml methanol was added to quench the reaction after 1h. Nanoparticles were precipitated overnight and then purified by repeated centrifugation and washing with acetone. The final black precipitates were dried in vacuum overnight.

The ligand density on nanoparticle surfaces were measured by TGA, Figure S23. The size and polydispersity of the nanoparticles were characterized by TEM (Figure 3.12) and SAXS (Figure 3.14). TEM analysis is based on statistics of more than 500 nanoparticles.

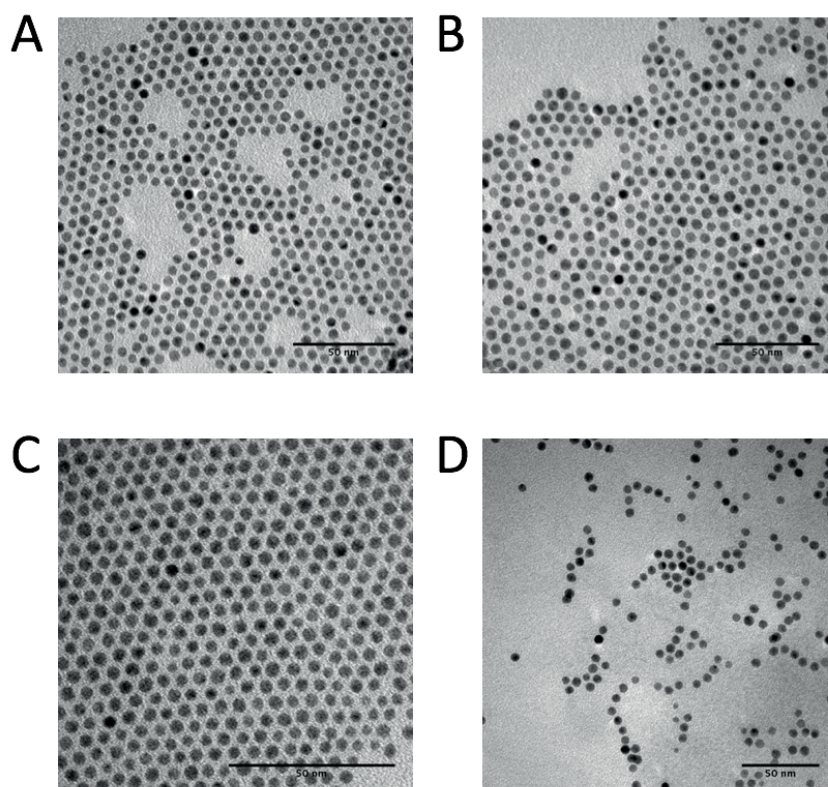
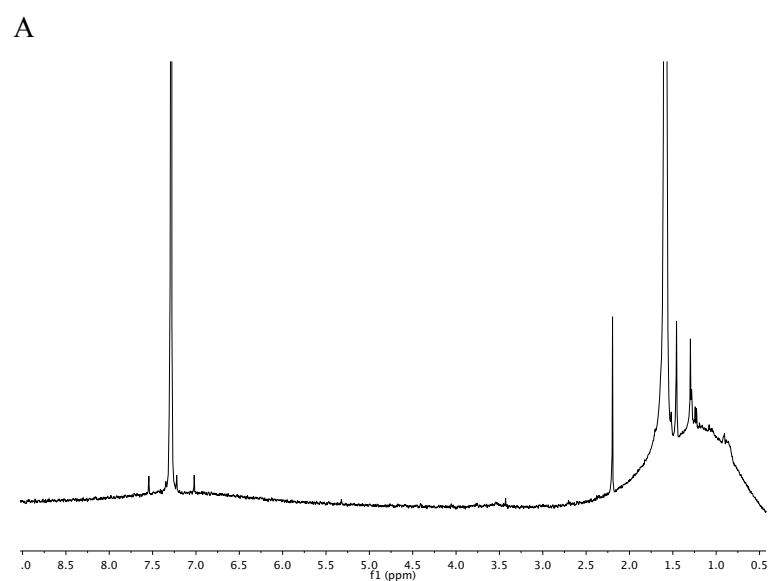
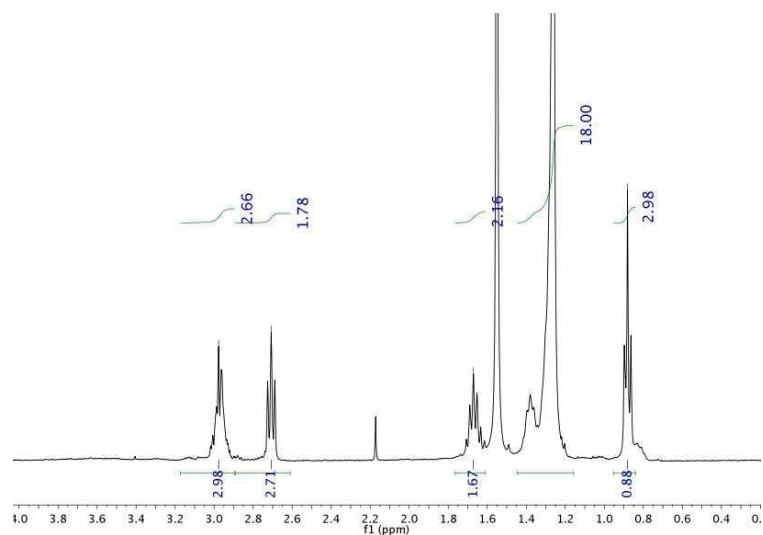


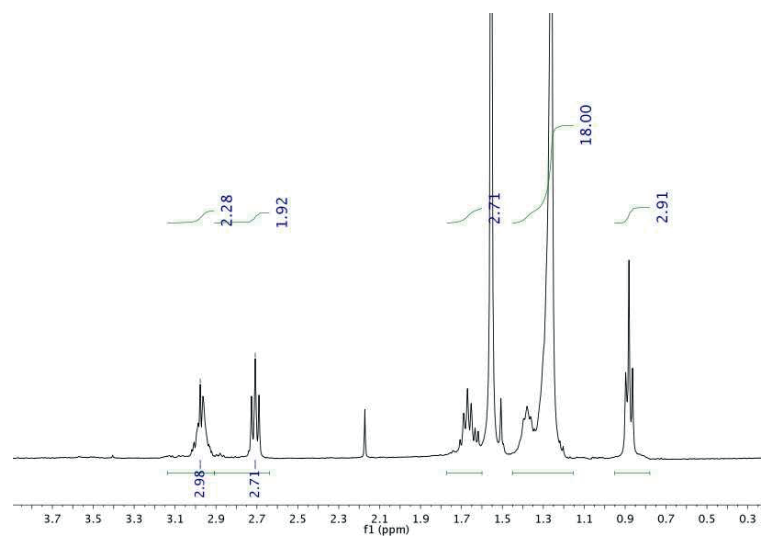
Figure 3.12. Typical TEM images of nanoparticles used in this work. (A) 4.4 ± 0.4 nm PET-DDT gold nanoparticles. (B) 5.2 ± 0.5 nm dDDT-DDT gold nanoparticles. (C) 3.2 ± 0.3 nm PET-DDT gold nanoparticles. (D) 5.5 ± 0.5 nm PET-DDT gold nanoparticles. All the averaged sizes are calculated based on statistics of more than 500 counts.



B



C



D

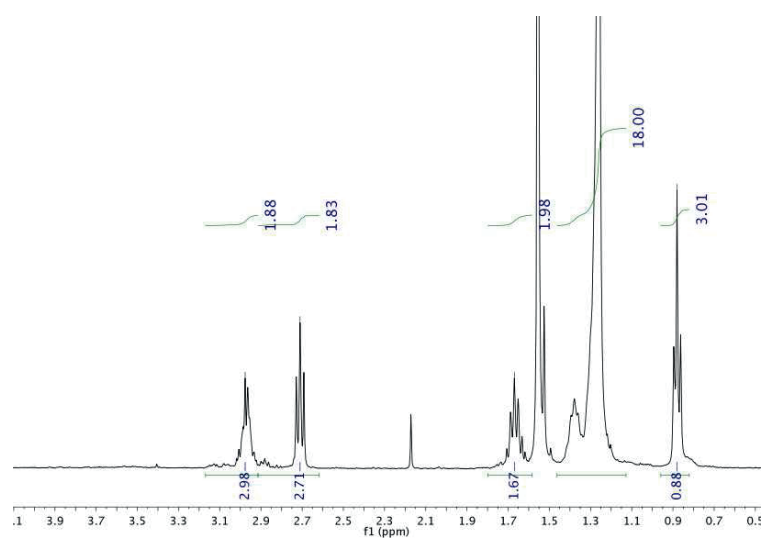
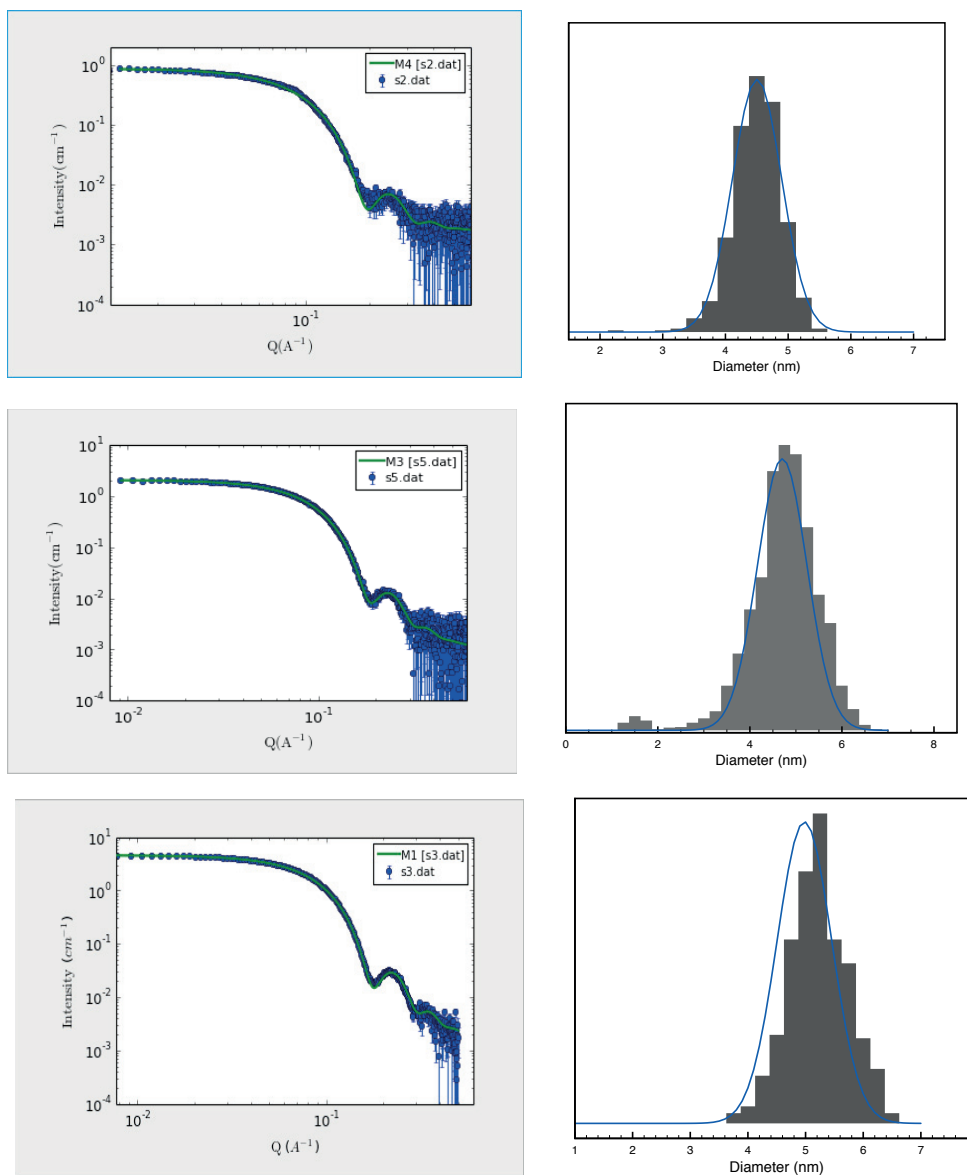


Figure 3.13. NMR data of PET-DDT nanoparticles. (A) Before core etching with iodine: the absence of peaks in the 2.5-3.2 ppm range indicates no unbounded ligands in the solution. NMR of (B) 3.2nm, (C) 4.4nm, (D) 5.5nm PET-DDT nanoparticles after etching with iodine, the methyl group from DDT and the methylene group of PET were used to determine the ligand ratios.



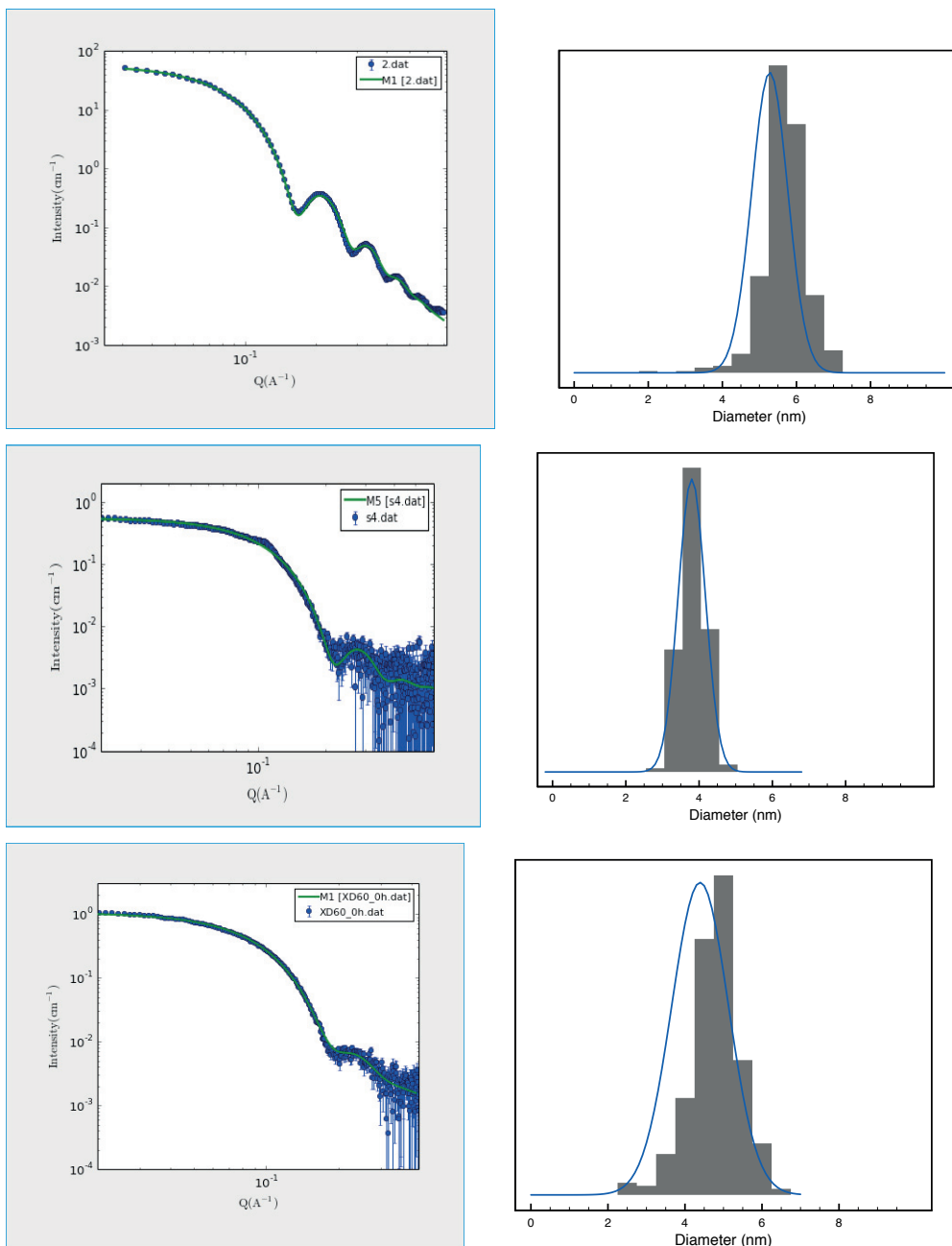


Figure 3.14. SAXS data and corresponding size distribution of 4.4 nm-diameter PET-DDT (0.57:1) nanoparticles; 4.5 nm-diameter PET-DDT (0.2:1) nanoparticles; 5.2 nm-diameter DDT homoligand nanoparticles; 5.5 nm-diameter PET-DDT (0.6:1) nanoparticles; 3.6 nm-diameter PET-DDT (0.6:1) nanoparticle and 4.2 nm-diameter DDT homoligand nanoparticles with 20% polydispersity. Size distribution curves are calculated from SAXS data (full line) using a Gaussian distribution model and histograms calculated from TEM data. All the SAXS data analyses are performed using SASview software. All the TEM analyses are conducted with imageJ software.

Table 3.1 Scattering length values used in the SANS modeling.

Molecules	gold	CDCl3	DDT	PET	toluene
SLD(\AA^{-2})	4.67E-06	3.16E-06	-3.68E-07	1.01E-06	9.41E-07
Molecules			dDDT	dPET	d-toluene
SLD(\AA^{-2})			5.70E-06	4.52E-06	5.66E-06

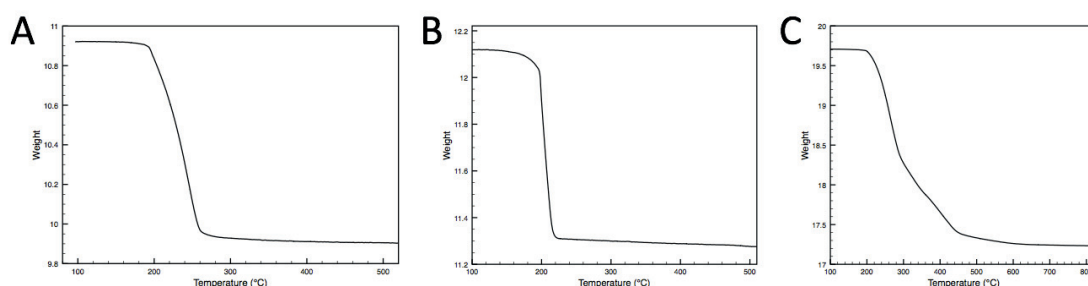


Figure 3.15 A) TGA data of 5.5 nm PET-DDT nanoparticles; the ligand density is found to be 93.9% of the highest covering density on nanoparticle surface (i.e. each thiol occupies an area of 21.4 \AA^2). B) TGA data of 4.4 nm PET-DDT nanoparticles; the ligand density is found to be 90.0% of the highest covering density on nanoparticle surface (i.e. each thiol occupies an area of 21.4 \AA^2). C) TGA data of 4 nm MUA-DDT nanoparticles; the ligand density is found to be 90.1% of the highest covering density on nanoparticle surface (i.e. each thiol occupies an area of 21.4 \AA^2). The ligand ratio (1.3:1 MUA:DDT) could be calculated since the two ligands decompose at different temperature.

➤ SANS measurements and data analysis

SANS measurements of PET-DDT, DDT homoligand and ternary ligand protected nanoparticles are mainly conducted on the SANS-I instrument at Paul Scherrer Institute, while the SANS data of the 5.5 nm PET-DDT nanoparticle, the MUA-BT and MUA-DDT nanoparticles were recorded on KWS-2 at Jülich Center for Neutron Science. Measurements were performed at 20 °C, using 1.5 m sample-to-detector distance, at 5 \AA wavelength with a collimation setup of 6 m and a q range from 0.05 \AA^{-1} to 0.4 \AA^{-1} . The sample concentration was approximately 10 mg/ml corresponding to a volume fraction of gold nanoparticles solution of around 0.1%. The two-dimensional scattering data were processed and reduced using BerSANS software including radial averaging, background subtraction, empty cell and transmission correction, and normalization to an absolute scale.

Scattering intensity from a dilute monodisperse solution is an average of scattering from all possible orientations of the particle, determined by $I(q)=\Sigma_{\Omega}(A^2(q))$, where $q=(4\pi\sin\theta)/\lambda$, is the scattering vector, while 2θ is scattering angle and λ is the wavelength of neutron or X-ray beam. In a SANS measurement, selective deuteration could be employed to highlight specific components. The scattering intensity thus becomes $I(q)=\Sigma_i^n(\Delta\rho_i V_i)^2 P_i(q)$, where $\Delta\rho_i=\rho_i-\rho_s$, is the contrast of component i against solvent and $P_i(q)$ is the form factor of each component. The partial amplitudes from the volume occupied by the k -th phase in a DAM are rapidly evaluated from the bead positions using spherical harmonics. Starting from a random configuration, simulated annealing (SA) is employed to search for a model composed by interconnected compact phases, which simultaneously fits multiple scattering curves from the constructs to minimize overall discrepancy:

$$\chi^2 = \sum_k \frac{1}{N_k - 1} \sum_{j=1}^{N_k} \left[\frac{I_{\text{exp}}^{(k)}(q_j) - c_k I_{\text{calc}}^{(k)}(q_j)}{\sigma^{(k)}(q_j)} \right]^2 \quad (3.1)$$

Here the index k runs over the scattering curves, N_k are the numbers of experimental points, c_k are scaling factors and $I_{\text{calc}}(q_j)$ and $\sigma(q_j)$ are the intensities calculated from the subsets of the beads belonging to the appropriate phases and the experimental errors at the momentum transfer q_j , respectively.

➤ Test of the Robustness of the Approach

To test the robustness of the proposed Monte-Carlo fitting method, different input parameters were used to fit the same data described above. Figure 3.1G shows the resulted model when the input volume fraction of PET-DDT was changed by 10% from NMR results, i.e. 22.9% for gold, 50.3% for DDT and 26.6% for PET. The low-resolution model, Figure 3.1G, built with these parameters still shows very similar features and the stripe-like elongated domain features remain substantially the same. When the volume fraction is further changed to more than 30%, the resulted model still shows elongated stripe-like domains, but the ligand shell structure becomes unphysical, with large bare-gold domains exposed to solvents. When no constraints are added to the volume fraction, i.e. volume fraction penalty is set to 0, but the gold core size is fixed, similar phase separation features are still observed (Figure 3.1H). Other input parameters such as looseness of beads are also changed and all the models are run several times starting from random configuration, yielding always similar results (Figure 3.16).

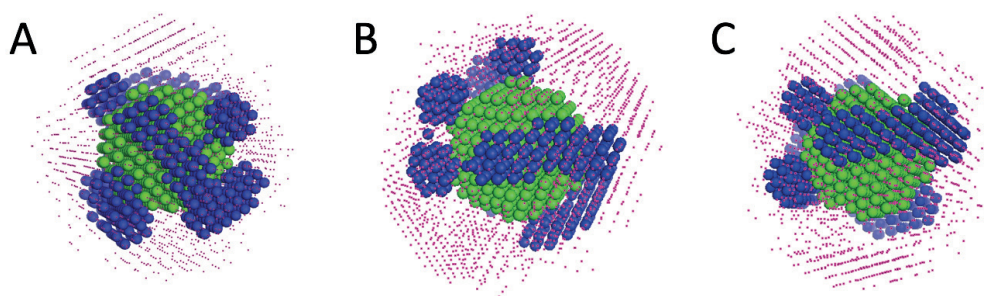


Figure 3.16. Low-resolution models built from different starting random configurations.

FTIR measurements of PET-DDT and PET-dDDT nanoparticles

In order to prove that the deuteration does not affect the ligand ratio on the nanoparticles, we used FTIR to measure the PET-DDT and PET-dDDT samples. As shown below, the FTIR spectra of a mixture of DDT and dDDT homoligand nanoparticles were recorded at varying molar ratios of the nanoparticles, Figure S3A. The ratio of the intensity of the CH₂ and CD₂ stretching peaks was then calculated and plotted against the molar ratio of the nanoparticles in order to build a calibration curve, Figure S3B. Then the FTIR spectra of PET-DDT and PET-dDDT nanoparticles were recorded, Figure S3C. The CD₂ peak intensity of the PET-dDDT nanoparticles was then converted to the corresponding CH₂ intensity using the calibration curve discussed above. The ratio of between the intensity of the aromatic CH stretching and the aliphatic CH₂ stretching was then calculated for both the PET-DDT and PET-dDDT nanoparticles. For the former it was found to be 0.14 and for the latter it was found to be 0.13. We believe that these two values are within error one to each other indicating that the two particles have the same composition. We notice that these ratios do not indicated the stoichiometry on the ligand shell as they have not been corrected for the relative intensity of the two types of the peaks.

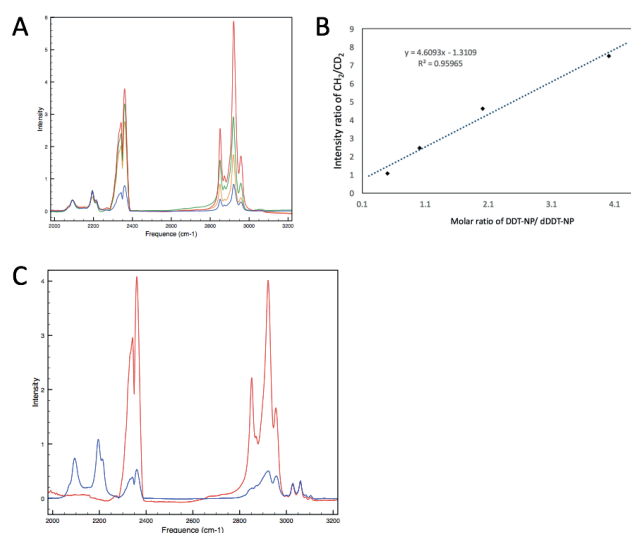


Figure 3.17 FTIR analysis on the ligand ratio. A) FTIR spectra of DDT-NP and dDDT-NP mixtures at varying ratios from 0.3 to 0.8. B) Calibration curve of the CH₂/CD₂ peaks. C) FTIR spectra of the PET-DDT nanoparticle (red) and PET-dDDT nanoparticle (blue).

Chapter 4 Solution structures and molecular weight determination of atomically precise nanoclusters determined by small angle neutron scattering

This chapter presents the analysis of atomically precise nanocluster using small angle neutron scattering technique. Solution structures of the clusters are compared to their single crystal structures. Furthermore, the molecular weight of both the metal core and ligand shell could be determined without the need of mass spectrometry.

Disclosure: *The work in this chapter is in preparation for a manuscript to be submitted*

Atomically precise clusters are at the center of intense research efforts. They can be fully characterized by single crystal x-ray diffraction, often with the support of mass spectroscopy. However, not all the known nanoclusters have been successfully determined by these two methods, which is due to the limitations such as the requirement of high quality single crystals and the effective ionization of the sample as well as the interpretation of mass spectra. One is often left with questions about the charged state of the clusters, whose assignment, through mass spectroscopy, is possible but not trivial. Moreover, no studies could be applied to the study of the solution behaviour of the nanoclusters and to verify whether the crystal structures could be translated. In this chapter, I show that small angle neutron scattering can correctly evaluate the diameter of atomically precise nanoclusters. This can be used to determine the presence of counter-ions around such nanocluster, thus helping with the determination of the charged state of the clusters in solution. Furthermore, not always mass spectroscopy can be achieved on these clusters, either because they are too big or because they are not stable enough. For gold cluster, I show that it is possible to determine the molecular weight of the core and the molecular shell using a SAXS and SANS respectively. The power-law relationship between the scattering invariants and molecular weight of gold nanoclusters has been established. Finally, in this work, I show that the structures of a few clusters solved by single crystal x-ray spectroscopy are consistent with the structures that SANS identifies in solution.

4.1 Introduction

Atomically precise metal nanoclusters are an emerging type of material¹⁸⁸. Different as other colloidal nanoparticles, these nanoclusters are absolutely monodisperse, i.e. they can be represented by defined chemical formula and their structures could be resolved by crystallography. The studies on this type of material have unveiled many key knowledges in nanotechnology, such as the total structures of nanoparticles and the emergence of surface plasmonic resonance. The well-controlled sizes allow the fine tuning of the properties of the nanoparticles for various applications, such as catalysis, electronics, optics and drug delivery¹⁸⁹.

All the great potentials of the nanoclusters are based on the characterization of their structures. Single crystal X-ray diffraction has been the dominant technique for this task. However, until now, only a few crystal structures of nanoclusters have been solved^{25,190–192}. Accurate structures of many, including those that have been discovered long time ago like Au₁₄₄, are still unknown. This is due to the fact that obtaining good quality single crystals is very often a formidable challenge. Even the determination of atomic composition is not trivial, which relies mainly on mass spectrometry techniques. The ionization of the sample and the interpretation of the spectra, especially for large nanoclusters, tend to be difficult. Furthermore, when it comes to nanoclusters that carries charges, the charge states are often hard to be determined directly. Due to their small sizes, stability and the hybrid metal-organic structures, the utilization of many other techniques such as electron microscopy and NMR are limited. Furthermore, the characterization on the solution structure of the nanoclusters has not been well-studied yet. For example, the dimensions of the organic ligand shell as well as the counter-ion distribution surrounding charged nanoclusters in solution is not clear, although such information is directly related to the applications of these materials.

In this chapter, I show that small angle neutron scattering (SANS) is versatile tool for the characterization of the solution structure of nanoclusters. First I compared the results of five different silver nanoclusters^{25,191,193}, i.e. Ag₃₇₄, Ag₁₃₆, Ag₄₄, Ag₃₂ and Ag₁₆, with their known crystal structures and found good consistency. For nanoclusters that are intrinsically charged, such as Ag₄₄ and Ag₃₂, the SANS data suggest that the counter-ions are closely bound to the nanoclusters in solution, i.e. within ~ 1 nm distance to the nanocluster surfaces. Considering that the overall sizes of nanoclusters are generally less than 5 nm, the influence of the counter-ions on the properties thus should always be taken into consideration to predict their

behaviour in solution states. I then analyzed three gold nanoclusters with different core atom numbers¹⁹⁴, i.e. Au₁₄₄, Au₁₀₄ and Au₃₈. Although the crystal structures of two of gold nanoclusters are still not reported yet, results from our SANS data agree well with theoretical predictions.

More importantly, efforts on determining the accurate size information from scattering patterns are presented here. It is shown here that if combined with small angle X-ray scattering (SAXS) and contrast matching SANS, the accurate mass of both the core and ligand shell of the nanoclusters could be calculated. Adopting the recently introduced correlation volume analysis, we have derived power-law relationship for the nanoclusters. The main advantage of solution neutron and X-ray measurements is that formation of crystals is not required and the sample preparation is relatively simple. The ability of the SANS to assess both accurate size and mass information would give chemists valuable information rapidly and could also be combined with computer simulations for samples whose crystal structures are not known yet.

4.2 SANS analysis of silver nanoclusters with known crystal structures

Figure 4.1 shows the comparison between the crystal structures of five silver nanoclusters with their SANS data and corresponding distance distribution function, $P(r)$, calculated using GNOM software. The synthesis of all the nanoclusters follows previous reports and together with experimental setup for the SANS measurements are described in supporting information. We first focus on the determination of overall sizes of nanoclusters from D_{\max} value, calculated for the $P(r)$. D_{\max} stands for the largest pair distance in the scattering object, which takes into account of both the metal core and ligand shell for nanoclusters. The deviation of D_{\max} evaluation from small angle scattering has been found to be less than 2 % for protein samples, which means Å accuracy for nanoparticles below 5 nm. As demonstrated in Figure 4.1, the D_{\max} values match perfectly with crystal structures for Ag₃₇₄, Ag₁₃₆ and Ag₁₆ samples. However, for Ag₄₄ and Ag₃₂, the D_{\max} are significantly larger than only the core-shell size of the nanoclusters. Good agreement could only be achieved when one takes into consideration the counter-ions, tetraphenylphosphonium, in both cases. The Ag₄₄ nanocluster carries high negative charge, i.e. 4 -, per molecule. While the overall diameter of the nanocluster is around 2.8 nm, the D_{\max} gives 4.4 nm, which means that the counter-ions accounts for 1.6 nm in thickness. For the case of Ag₃₂, the overall diameter and D_{\max} are 2.5 nm and 3.2 nm,

respectively. The smaller space occupied by the counter-ions are due to both smaller amount of negative charges (2-) of the Ag₃₂, as well as the lower dielectric constant of the solvent (chloroform for Ag₃₂ and dimethylformamide for Ag₄₄).

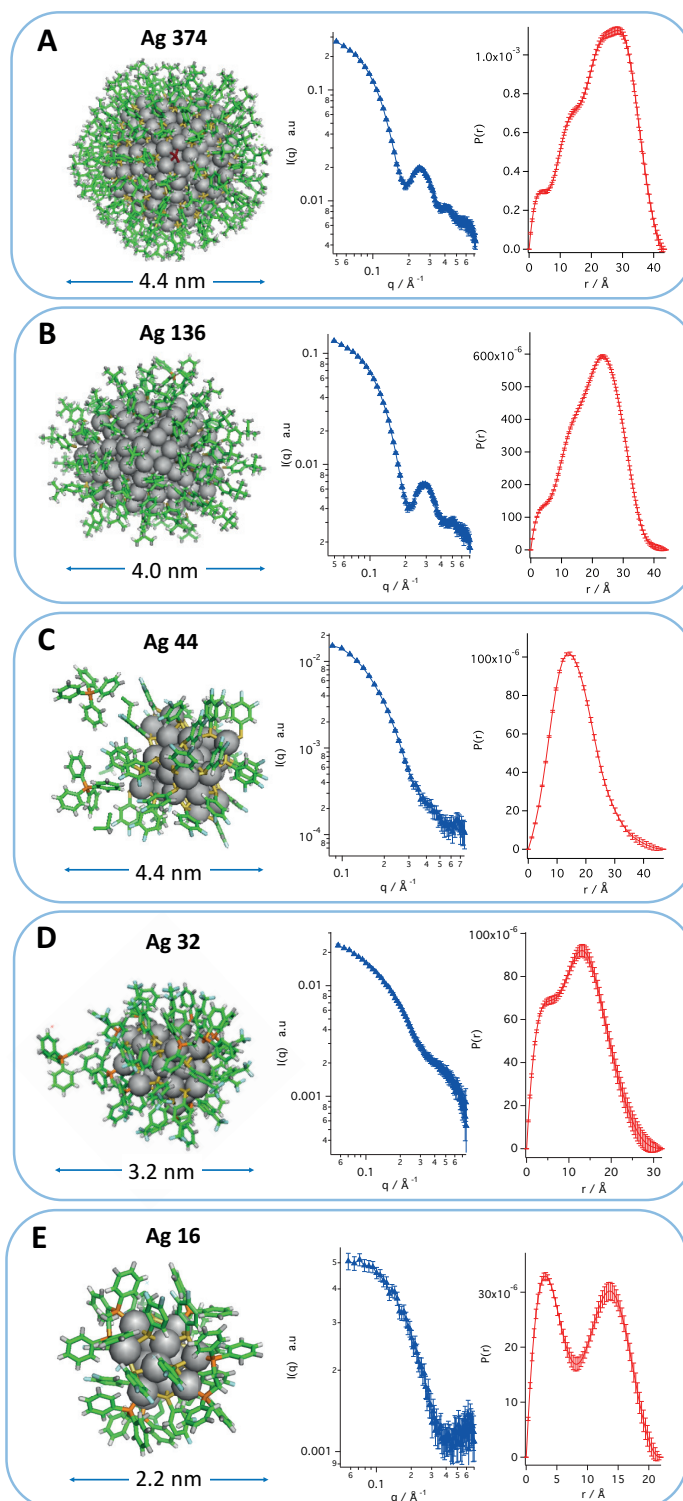


Figure 4.1. Comparison between the single crystal structures with SANS data and corresponding $P(r)$ for Ag_{374} (A), Ag_{136} (B), Ag_{44} (C), Ag_{32} (D) and Ag_{16} (E). In all the single crystal plots, grey spheres stand for silver atoms while green sticks are organic molecules. The SANS data for Ag_{374} , Ag_{136} and Ag_{16} are collected using deuterated chloroform as solvent while for the Ag_{44} and Ag_{16} the solvents are deuterated dimethylformamide and deuterated dichloromethane, respectively. Single crystal structure plots of the silver nanoclusters are reproduced from references^{25,191,193}.

The SANS patterns are then analyzed in more details. One could notice that the Ag_{374} and Ag_{136} data gives oscillation features that are similar to spherical nanoparticles. This is due to the fact that their sizes and shape symmetries are very close to conventional colloidal nanoparticles. For the other three nanoclusters, the existence of counter-ion results in larger deviation from spherical shapes and the extreme small size would not show oscillation features in the q -range we measured. The data are then fitted with core-shell ellipsoid models using SasView software as listed in Table 4.1. While Ag_{374} , Ag_{136} and Ag_{16} data all yield good fitting with ellipsoid estimation, the Ag_{44} and Ag_{32} could not be fitted with satisfied quality. Such result further confirms that the effect of counter-ions on the shape of the nanoclusters in solution. In all the cases, SANS gives good estimation on the core diameter as well as the ligand shell thickness.

Table 4.1 Fitting parameters for different nanoclusters using core-shell ellipsoid model. R_{core} and R_{shell} stand for the radius of metal core and the thickness of the ligand shell, while r_a is the aspect ratio.

	D_{max} (nm)	R_{core} (nm)	r_a	R_{shell} (nm)
Ag_{374}	4.4 ± 0.2	1.5 ± 0.2	0.66 ± 0.02	0.7 ± 0.1
Ag_{136}	4.0 ± 0.1	1.2 ± 0.3	0.69 ± 0.03	0.8 ± 0.1
Ag_{16}	2.2 ± 0.1	1.1 ± 1.0	0.48 ± 0.30	0.6 ± 0.1
Au_{144}	3.5 ± 0.1	1.1 ± 0.1	0.80 ± 0.10	0.6 ± 0.1
Au_{104}	3.1 ± 0.2	1.0 ± 0.2	0.55 ± 0.04	0.6 ± 0.3
Au_{38}	2.8 ± 0.2	0.6 ± 0.5	0.51 ± 0.11	0.7 ± 0.1

4.3 SANS analysis on the solution structure of gold nanoclusters

We then moved on to apply the same analysis to three types of gold nanoclusters, i.e. Au₁₄₄, Au₁₀₄ and Au₃₈. Detailed synthesis could also be found in supporting information. As shown in Figure 4.2, the D_{\max} are found to be 3.5 nm, 3.1 nm and 2.8 nm for the three samples, respectively. Fitting parameters by core-shell ellipsoid models are also listed in Table 1. Note that only Au₃₈ cluster has been determined by single crystal X-ray diffraction. We therefore only compared its result with the crystal structure. Previous theoretical predictions have been performed on Au₁₄₄ and the result agrees well with the prediction. However, much less is known about the structure of Au₁₀₄. Our result suggests that it is composed of a core of 2.0 nm in long axis with a 0.6 aspect ratio and a ligand shell of 0.6 nm.

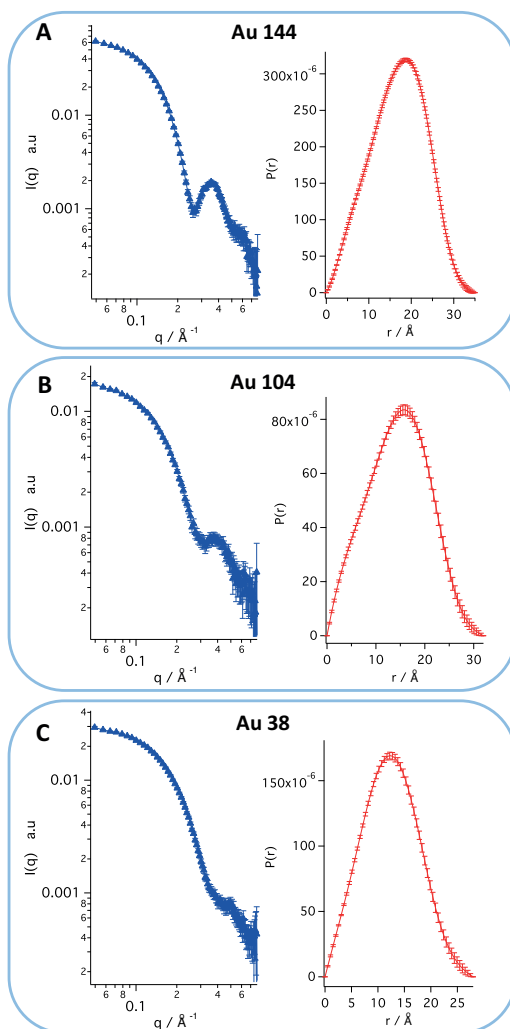


Figure 4.2. SANS data and $P(r)$ plots of Au₁₄₄ (A), Au₁₀₄ (B) and Au₃₈ (C) nanoclusters. All the SANS data are collected using deuterated toluene as solvent.

4.4 Power-law relationship for the molecular weight of nanoclusters

Further, we would like to address the issue of estimating exact molecular weight for nanoclusters. Recently, J. Tainer and co-workers have defined a new invariant in SAXS¹⁹⁵, i.e. volume of correlation (V_c) to determine the mass of protein sample with an averaged error < 4%. The invariant is independent of concentration of the sample and could thus avoid systematic errors of concentration measurements in conventional Guinier method. It has been found that ratio of the squared V_c to radii of gyration (R_g) defines the value Q_R , which follows a power-law with the mass of a protein.

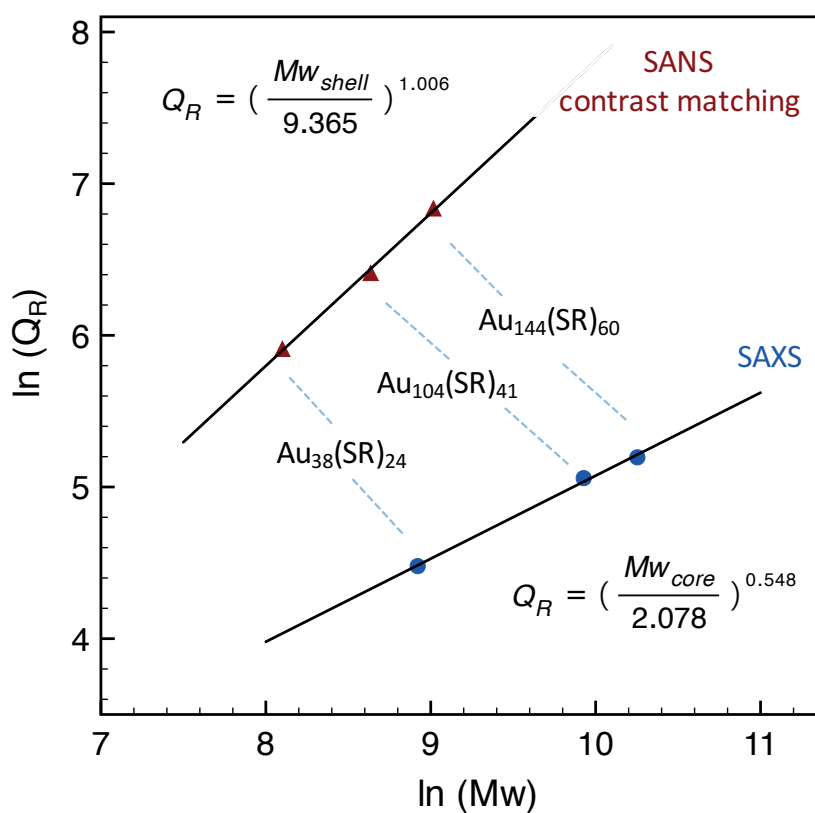


Figure 4.3 Power-law relationship between the Q_R and the mass of the nanoclusters' core and ligand shell. The calculation of were performed using ScÅtter software. The differences of the exponent come from different contrast conditions. The exponent for the gold core is calculated from SAXS data while for the ligand shell, it was calculated from contrast matching SANS data.

Here, we apply this analysis method to the nanoclusters. SANS data of the three gold nanoclusters were acquired using a mixture of deuterated and non-deuterated toluene as

solvent in order to match the contrast of the gold core. SAXS patterns on the same nanoparticles were also performed, in which only gold core contributes to the scattering intensity due to the high electron density of gold compared to organic molecules. We then successfully derived the power-law relationship between the Q_R and molecular weight (M_w) for both the nanocluster's core and ligand shell, as shown in Figure 4.3. Similar to the cases of proteins, the data points of the three gold nanoclusters follow nicely the linear trend, which confirms the accuracy of the analysis.

In conclusion, we have demonstrated the capability of SANS in the structural determination of atomically precise nanoclusters. Accurate core and ligand shell sizes could be readily determined by this method. We found that different than solid states, other effects such as counter-ions are not negligible for nanoclusters in solution. Furthermore, for nanoclusters whose single crystal structures are not known or even whose molecular weight are challenging to determine, contrast matching SANS offers a new way of estimating such information together with SAXS. The huge success of solution scattering in biological samples in recent years are largely due to the fact that proteins are monodisperse samples, which enabled precise analysis of the scattering data. Compared to other types of colloidal nanoparticles, atomically precise nanoclusters are much more similar to proteins. Therefore, we envision that solution scattering would obtain growing importance in the analysis of nanocluster's structures as well as their interactions in solution.

4.5 Materials and Methods

The gold nanoclusters in this study were kindly provided by our collaborator, Prof. Rongchao Jin's lab. The silver nanoclusters used in the study were synthesized by Dr. Huayan Yang. The silver nanoclusters were crystallized and the SANS measurements were performed after dissolving the crystalline powders to ensure the purity of the samples.

SANS measurements all the nanoclusters were performed on D22 AT Institut Laue-Langevin except that the Ag_{44} sample were measured on KWS-2 at Jülich Center for Neutron Science. Measurements were performed at 20 °C, using 1.4 m sample-to-detector distance, at 2.8 Å wavelength with a collimation setup of 5.6 m and a q range from 0.04 Å⁻¹ to 0.8 Å⁻¹. The sample concentration was approximately 10 mg/ml corresponding to a volume fraction of gold nanoparticles solution of below 0.1%. The two-dimensional scattering data were

processed and reduced using Grasp software including radial averaging, background subtraction, empty cell and transmission correction, and normalization to an absolute scale.

SAXS measurements were done using Rigaku BioSAXS 2000 machine. Borosilicate glass capillaries with inner thickness of 1mm was used for the samples solutions. Roughly 0.1 mg/ml concentration of the nanocluster solution was used for the measurements.

The $P(r)$ analysis were performed using GNOM software in ATSAS packages. The fitting of the SANS data was done using SasView software with the core-shell ellipsoid model. The volume of correlation of the SAXS and SANS data was analysed using Scatter software.

Chapter 5 Reverse Monte Carlo analysis of MALDI-TOF spectra

This chapter establishes a method to retrieve information on the organization of mixed ligands on nanoparticles using reverse Monte Carlo method. A detailed description of the algorithm as well as test analysis on ideal models and experiments are presented.

Disclosure: *The work in this chapter is in preparation for a manuscript to be submitted*

As described in Chapter 1, the utilization of MALDI-TOF on mixed ligand nanoparticles have several advantages. First, the method is rapid, allowing for the screening of large amount of samples. Given a well-prepared sample, a typical MALDI measurement on one sample takes only a few minutes. Second, the technique is versatile and applicable for both gold and silver nanoparticles independent of their solubility. Last but more importantly, mass spectrometry in general has high resolution and accuracy in determining the exact weight and the abundance of the molecules/fragments. Therefore, in principle the method could offer quantitative analysis on the morphology of mixed ligand SAM.

Current data analysis method of MALDI use a single number, i.e. sum-square-residue (SSR), to evaluate the deviation of the fragment distribution against certain distribution. SSR acts as an indicator of the degree of phase separation when the fragment pattern is compared to binomial distribution, corresponding to random ligand shell morphology. Some threshold values are then assumed to classify the morphology of ligand shells (such as random, patchy and Janus) based on the range of SSR. Such data treatment summarizes the whole MALDI spectra into one value, which is obviously an over-simplification of the information provided in the data. Furthermore, the choice of thresholds for the SSR evaluation of the phase separation is arbitrary. Especially for patchy nanoparticles, the variations of morphologies are large, like stripe-like, checkerboard-like and isolated domains with different shapes. The ability and extent of this method to distinguish all these different morphologies has not been

demonstrated yet. Examination into the detailed distribution of all the fragments could be a promising strategy for quantitative analysis of MALDI data.

In this chapter, a novel method to reconstruct 3D organizations of the binary ligand on nanoparticles from MALDI spectra using Reverse Monte Carlo (RMC) calculation is presented. The construct of the algorithm is demonstrated together with its validity through fitting data from idealized model systems, such as Janus, patchy and random morphologies. The method is also tested against experimental data on silver nanoparticles. Furthermore, the retrieved model of a silver nanoparticle was compared to the SANS results, achieving good agreement. It is a first time that two different types of techniques are being used on the same sample quantitatively. The simple but accurate characteristic of MALDI combined with RMC calculations would make this method one of the most powerful tool for the community.

5.1 Reverse Monte Carlo and description of the algorithm

Reverse Monte Carlo is a data analysis method that enables the fitting of experimental data by generating a 3D model of the studied sample through an iterative approach^{196,197}. It was first introduced to analyze the structure of liquid and disordered materials from scattering data¹⁹⁸. In a typical implementation of this approach, a model containing N beads/atoms of the studied system is generated from which the theoretical pattern of a certain type of measurement is calculated. The calculated pattern is then compared to the experimental data by calculating their discrepancy, i.e. averaged sum squared residue, χ^2 . Then the assignment of a randomly chosen bead/atom is changed to generate a new model and have its χ^2 compared. Based on whether the χ^2 is minimized, then the new model is accepted or rejected and the program continues the iteration until the χ^2 is below a certain value or a certain amount of iteration is reached. The procedure could be accompanied by other constraints on the system, for example, physical constraints such as the size of the object or external information from other types of measurements. Very often the iteration procedure adopts the simulated annealing approach in which the un-improved changes/moves could also be accepted by a probability that scales with a temperature factor¹⁹⁹. In this way the search for the optimum model has a higher chance to find the global minimum solution.

Since its introduction, the RMC has been applied in many fields of scientific data analysis. For example, scattering data (small/wide angle X-ray/Neutron scattering, reflectometry) on disordered and polycrystalline samples that are often very hard to analyze could be interpreted through this approach^{196,197}. Other examples include NMR and X-ray Absorption Spectroscopy for which RMC could give novel insights in the structure of various materials²⁰⁰.

The advantage of RMC is obvious that it offers a versatile approach to interpret data whose features are complex in nature. The insight on the structure of a material is in direct space while very often the experimental data is indirect, such as in Fourier space or statistical. The method could be combined with other types of experimental input to achieve a quantitative analysis of the data. Still RMC suffers from some limitations such as the expenses in calculation power and lack of uniqueness of the retrieved model. The latter is actually related to the intrinsic property of the sample as often they are polydisperse, dynamic and complex. To some extent, the results retrieved by RMC could be regarded as a sampling of the averaged structure of these samples.

Here, I present for the first time the application of RMC on the analysis of MALDI-TOF data of mixed ligand nanoparticles. A bead model of ligand shell is calculated by fitting the experimental MS data of the metal-thiolate complexes. The RMC procedure in this study could be summarized as:

- Generation of the search space. A sphere surface composed of N number of uniformly distributed beads is generated. The size of the sphere and the number N are external information from other measurements such as TEM and TGA. These supplemental data are important as they act as both constraints and defines the type of nanoparticles that MS data alone could not tell. Other information could also be taken into consideration and act as penalty during the fitting process such as NMR on the ligand ratio. Each of the N bead could be assigned to either 0 or 1, representing the two different ligands. A random assignment of the values is usually used as the starting point of the iteration.
- Calculation of the theoretical mass spectra. The peak intensity distribution of different thiolate fragment is calculated from the model generated. Taking silver nanoparticle as an example, the formula of the fragments can be expressed as $Ag_nA_xB_{n-x}$, where x is the number of A ligand in the fragment composed of n ligands of A and B in total. For silver nanoparticles, practically n could range from 2 to 10 during a proper measurement. Then a simulated fragmentation process is performed. Local fragment distributions are calculated from the local areas consisting of one center molecule and the nearest several molecules. In total N local areas are summed by treating each position as the central position. By assuming that the mixed monolayer is fragmented in a random way during the ionization and desorption process, the probabilities of each $Ag_nA_xB_{n-x}$ fragment locally can be calculated using the binominal distribution:

$$\omega_x = \frac{\sum_{k=1}^N \binom{n}{x} \cdot \varphi_A^x \cdot \varphi_B^{n-x}}{N} \quad (4.1)$$

in which φ_A and φ_B are the local ligand ratio, represented by:

$$\varphi_A(k) = \frac{N_A(k)}{N_A(k) + N_B(k)} \quad , \quad \varphi_B(k) = \frac{N_B(k)}{N_A(k) + N_B(k)} \quad (4.2)$$

Then the discrepancy between the experimental mass distribution and that of the model generated are calculated and represented by the number of averaged sum squared residue, χ^2 .

- Iteration process. The value of a randomly selected bead in the model is then flipped and the new fragment distribution pattern is calculated. If the χ^2 of the new model is lower than the previous one, then the assignment change is accepted. Otherwise the modification is rejected. The updated model is used again as the starting model for the next iteration step. Iteration could be stopped after a certain number of steps or when χ^2 value is below certain number, e.g. 10^{-3} .

5.2 Validity and efficiency of the algorithm

As a proof of concept, the algorithm is first tested with idealized nanoparticle with defined morphologies. To start with, a Janus-type morphology was generated on the surface of a nanoparticle with 4 nm core diameter, as shown in Figure 5.1. The theoretical fragmentation patterns of the Janus model are then calculated and used as the input experimental data for the RMC program. Interesting, through more than 10^4 iterations, the resulted model shows exactly the same feature as the original Janus model, as presented in Figure 5.1. The final χ^2 of the fitting is 9.9×10^{-5} , indicating the quality of the fitting. The mass intensity distributions of different types of fragments are all very close to that of the input values. The RMC fittings was run several times while similar results could always be obtained.

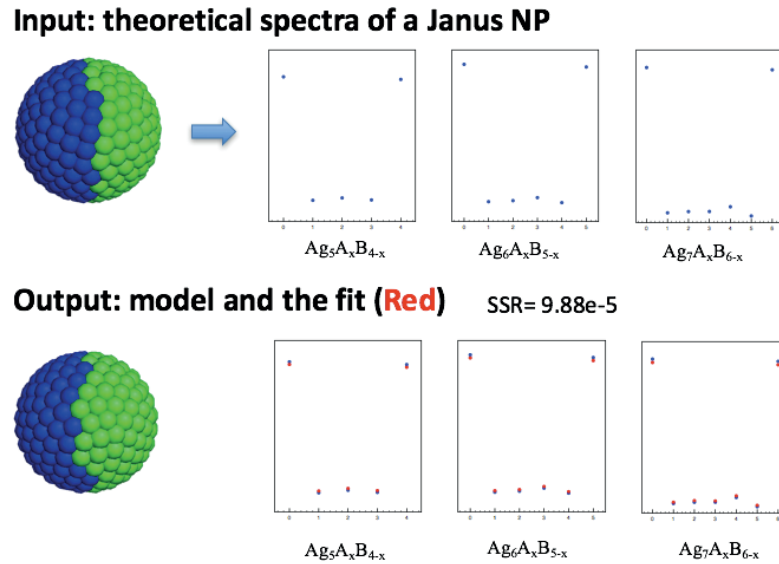


Figure 5.1 The RMC fitting of an idealized Janus type nanoparticle. The input models and the calculated mass intensity distributions (blue points) are shown on the top, while the output model and fits (red points) are presented on the bottom.

Furthermore the efficiency of the RMC process is tested. The program is run multiple times with different number of iteration steps. The output models and χ^2 values are recorded. As shown in Figure 5.2, the satisfying Janus features was obtained after around 4×10^4 iterations, which takes around 10-minute computer time. From this efficiency plot, the evolution of the morphologies during fitting could be seen. The χ^2 decreases rapidly, with 1000th iterations giving more than 2 magnitudes drop of the value, which takes less than 2 minutes of calculation time. The variations of the χ^2 of each iteration steps are generally around 10% and the as obtained models show similar models. The results here also demonstrate the sensitivity of χ^2 values on the differences between two types of different morphologies. As the final model looks exactly the same as input Janus morphology, one could safely assume that the morphology of two types of nanoparticles are the same when the χ^2 are in the order of 10^{-4} . When χ^2 value is around 10^{-3} , the morphology looks closer to large patchy type. Although it is similar to that of Janus, one could conclude that when χ^2 values are above 10^{-3} , detectable differences between the two morphologies could be seen. Significant deviations would present when χ^2 values are above 10^{-2} . Such assignment of χ^2 values is close to the threshold from previous literatures, but it is the first time to be systematically demonstrated.

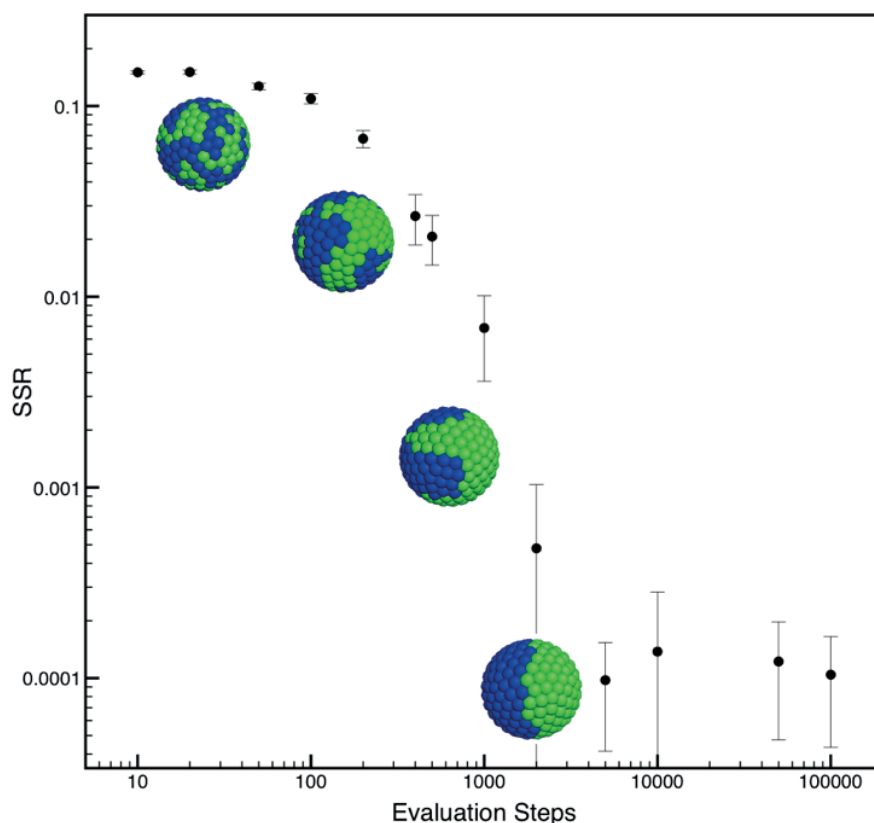
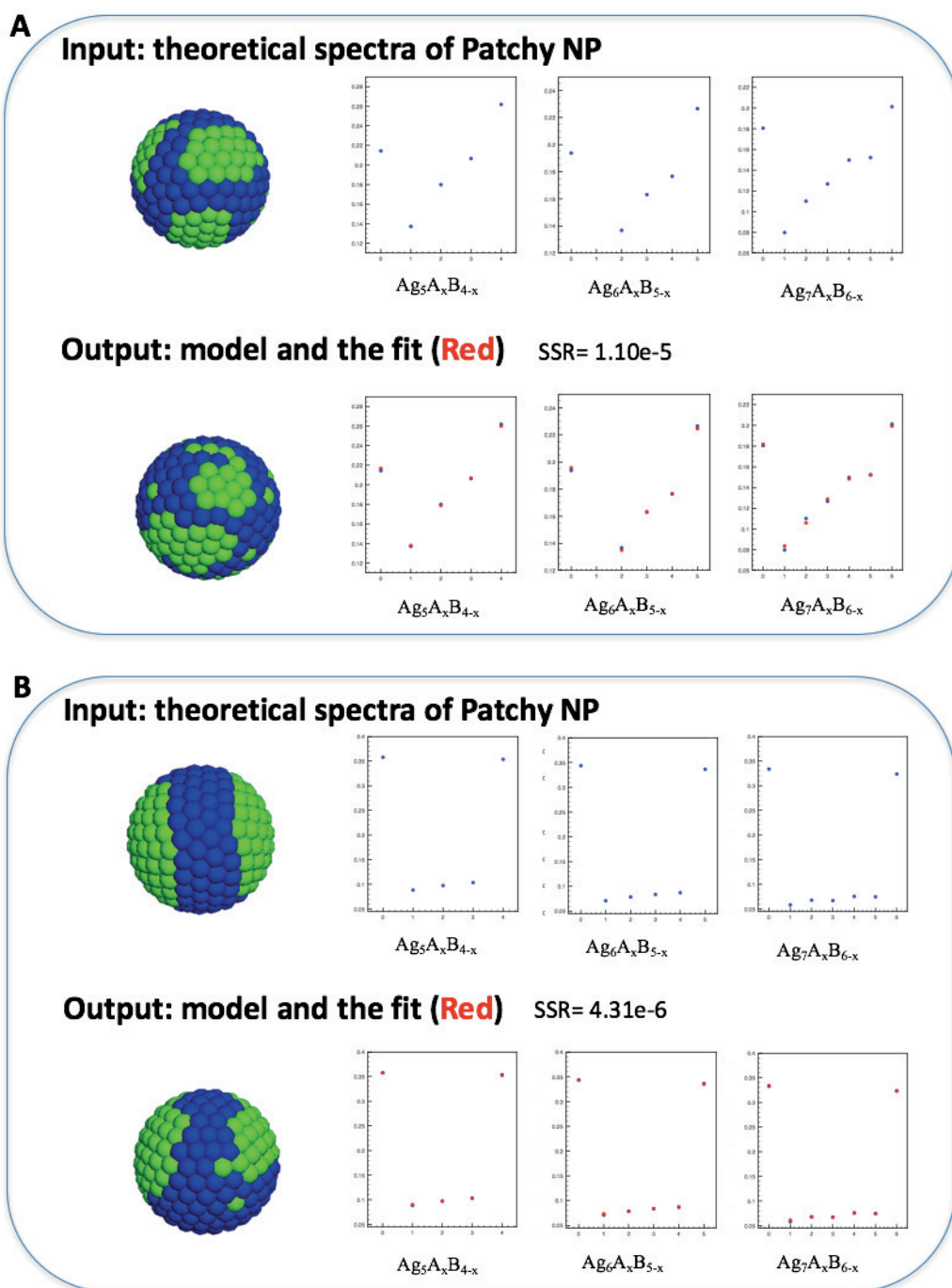


Figure 5.2 Efficiency and convergence of the RMC process. For every 1000 iteration steps, the calculation time required is around 2 minutes.

While Monte Carlo very often lead to trapped solutions at local minimum, the results for Janus morphology look rather robust. It might be due to the fact that the features and the corresponding mass spectra of Janus type nanoparticles are quite unique. Therefore, we continue to test this algorithm on several other types of morphologies, i.e. patchy nanoparticles with complex morphologies. The results are summarized below.



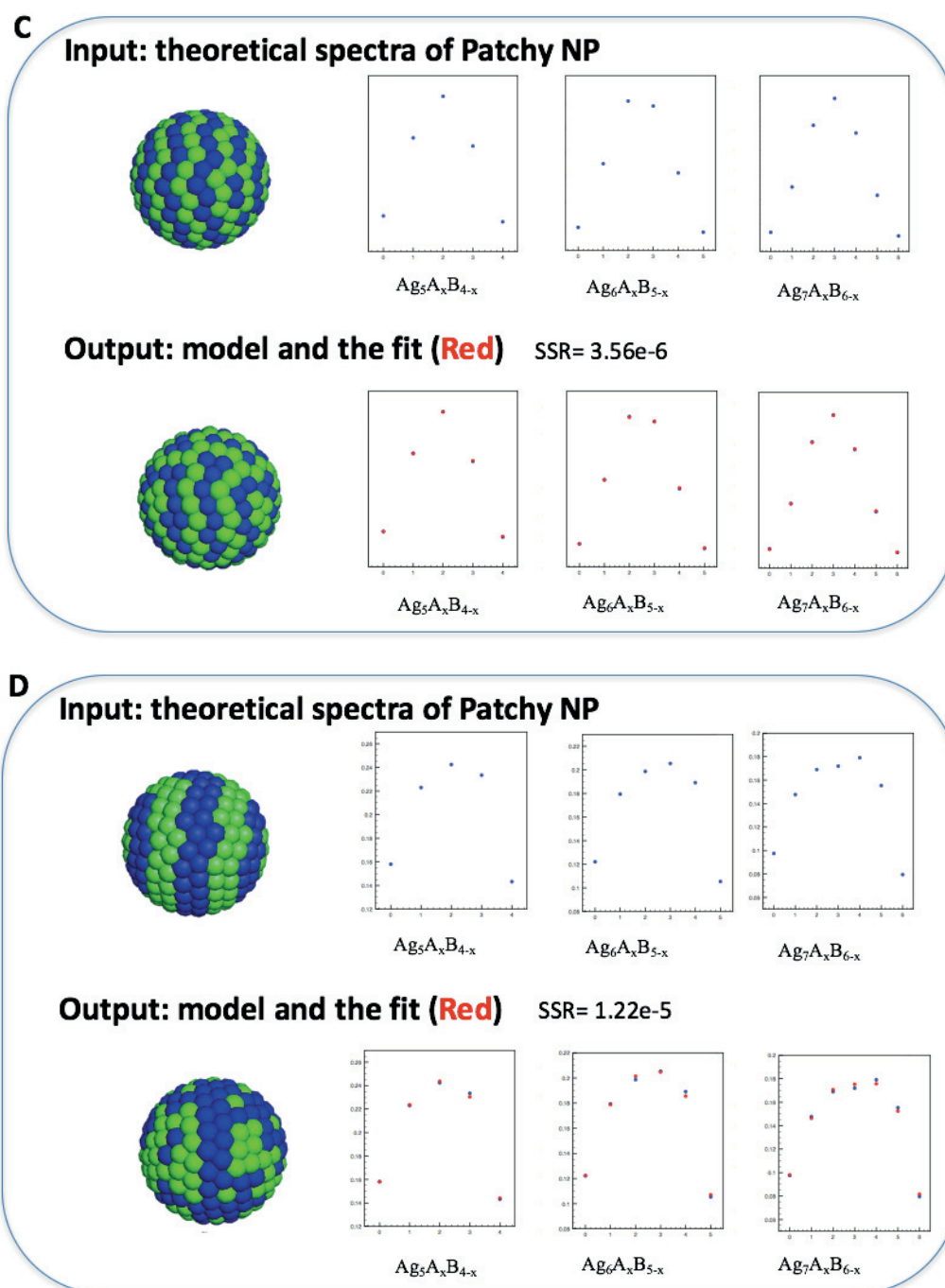


Figure 5.3 Test of RMC method on nanoparticles with different types of morphologies. A) Nanoparticle with separated patchy domains. B) Nanoparticle with two large patchy domains. C) Nanoparticle with thin stripe-like features. D) Nanoparticle with thicker stripe-like features.

As shown in Figure 5.3, in general RMC could successfully retrieve the structural features of the ligand shell morphologies on nanoparticles. For patchy nanoparticles with either several separated patchy domains or the one with two large domains, the reconstructed models show

similar type of ligand organization. While the relative positions of the patches and the regularity of patches are not exactly the same, they could be due to the ambiguity in the nature of the mass spectra, since different types of nanoparticles may end up with similar mass spectra. While organization the stripe-like morphologies could be modelled as well, the fitted model lacks the regularity compared to the idealized stripes. Such ‘defects’ in the morphology on one hand could be due to either the local minimum during the fitting. On the other hand, since the χ^2 for the final fit is below 2×10^{-5} , these results again point out the resolving power of the MALDI-TOF technique in discriminating mixed ligand shell morphologies.

To summarize, combined with RMC modelling method, MALDI-TOF spectra can be used to retrieve the 3D organization of mixed ligands on the surface of nanoparticles by fitting the fragment distribution patterns. It is the first time the sensitivity of this technique to different morphologies are quantified and visualized. The method could become a powerful tool since it transforms the statistical information in mass spectra into directly visual models. Due to its rapid and versatile nature, it could be applied to many nanoparticles with complex ligand shell morphologies.

5.3 Analysis of experimental MALDI data for silver nanoparticles

After establishing the RMC method using idealized systems, it is then applied to the interpretation of experimental data. Silver nanoparticles are chosen as examples, since the MALDI spectra of them gives the distribution patterns of various type of fragments. As a fitting method, the more input fragmentation information, the more accurate is the fitting results. Four nanoparticles coated with different pairs of ligands are synthesized using ligand exchange reaction starting from the same dodecanethiol (DDT) protected nanoparticle. The ligand pairs are butanethiol (BT) - DDT, hexanethiol (HT) - DDT, octanethiol (OT) - DDT and phenylethanethiol (PET) - DDT. The detailed synthesis and ligand exchange reaction procedures could be found in the Method section. As an example of the MALDI-TOF spectra of silver nanoparticles, the MALDI spectra of PET-DDT silver nanoparticle on various types of the fragments are shown in Figure 5.4 below. The mass intensity distributions for 6 types of different fragments could all be well resolved. The technique is also able to capture other types of fragments which is only limited by the analysis method/ protocol that we used for the instrument available. The mechanism of why and how silver nanoparticles could be fragmented much more efficiently than gold nanoparticles is also a very interesting topic which might be related to the different surface structures of the two types of metal cores.

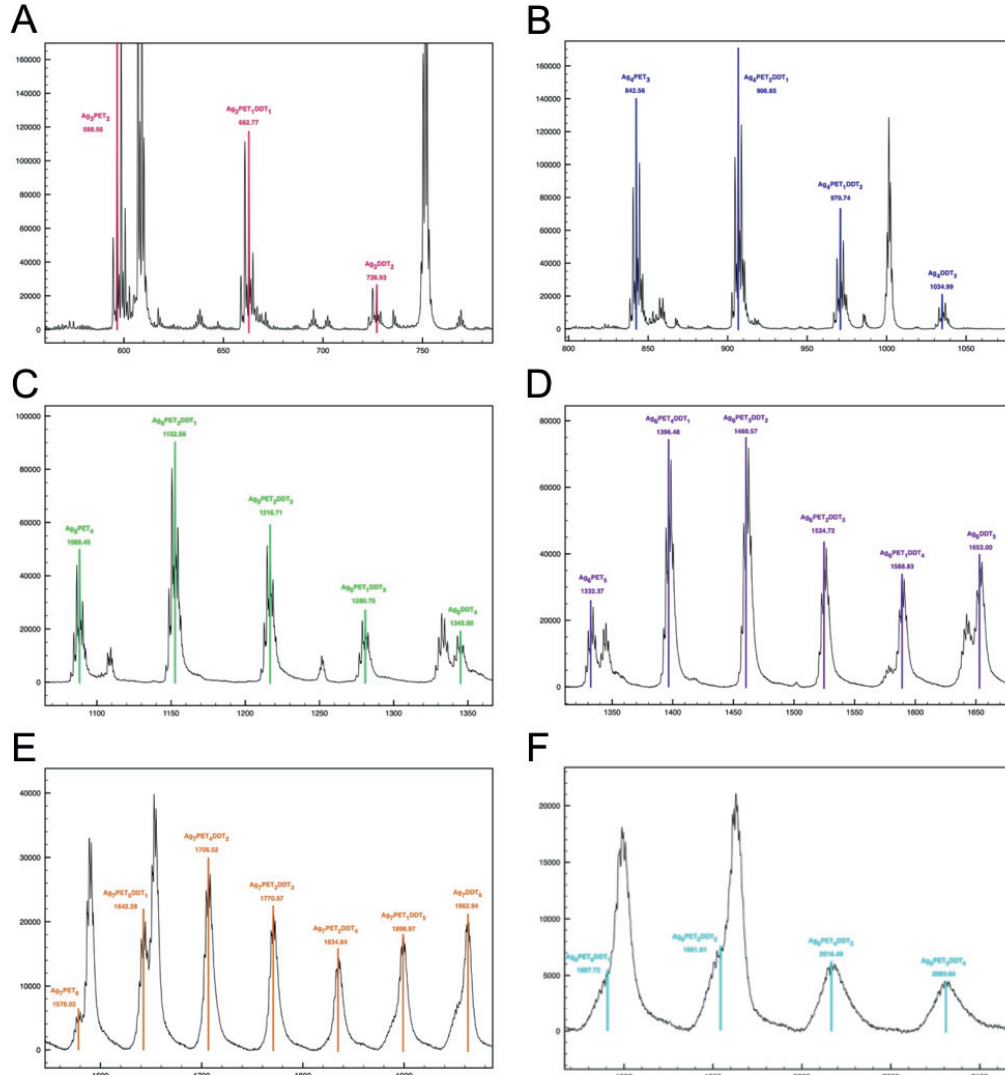


Figure 5.4 MALDI mass spectrum of the $Ag_{n+1}L_n$ ion fragments from Ag NPs functionalized with a mixture of DDT and PET ligands. Fragment families of Ag_3L_2 , Ag_4L_3 , Ag_5L_4 , Ag_6L_5 , Ag_7L_6 , Ag_8L_7 fragments are detected and shown from A to F respectively.

We first analyze the spectra using the evaluation of χ^2 as performed in the previous literatures. Figure 5.5 shows the $Ag_5A_xB_{4-x}$ fragment distributions of all the four nanoparticles. While performing the analysis, the ligand ratio could be simultaneously determined by the equation below:

$$\theta = \sum_{i=0}^4 i * P_i \quad \text{with} \quad P_i = \frac{n_i}{\sum_{i=0}^4 n_i} \quad (4.3)$$

n_i is the intensity of fragments containing i ligand A; P_i is the fraction of the fragment containing i ligands A; θ is the coverage of the ligand A.

It is found that the ligand ratio for the four nanoparticles are: BT% = 13%, HT% = 29%, OT% = 30%, PET% = 63%. The corresponding binomial distribution is then calculated and marked in the intensity plots. For BT-DDT protected Ag NPs, we can observe a relatively small deviation from the binomial model with the χ^2 being 0.07, indicating that the phase separation is relatively small on the surface of Ag NPs. For HT-DDT and OT-DDT protected Ag NPs, the deviations become larger and the χ^2 are also larger, which is 0.26 and 0.21 respectively. This indicates a stronger phase separation in these two AgNPs. The PET-DDT functionalized Ag NPs show the smallest $\chi^2 = 0.04$, while the Ag₅A₄B₀ and the Ag₅A₀B₄ fragments have higher fraction compared to binomial distribution, which corresponds to small patchy formation.

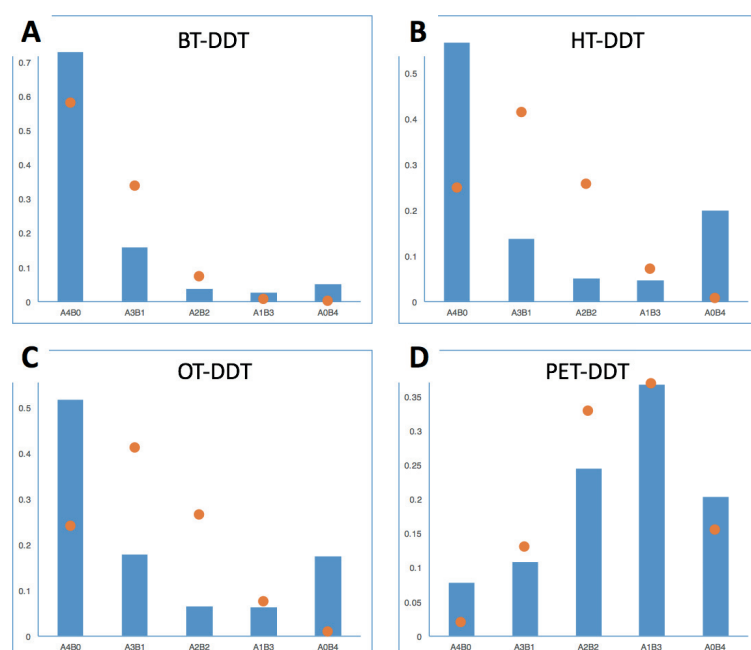


Figure 5.5 Distribution of fragment mass intensities and corresponding binomial distribution (random organization) for four different silver nanoparticles, i.e. A) BT-DDT; B) HT-DDT; C) OT-DDT; D) PET-DDT.

While χ^2 is a rapid indicator in interpreting the phase separation degree of the ligand shell, one can notice that the conclusions drawn based on this number is vague. Meanwhile, the detailed deviation of each fragment from random morphology is neglected. Adopting the RMC method described above, the models for the morphology of binary ligand shell are built, as shown in Figure 5.6. From the RMC results, it is clear that all the four nanoparticles have patchy type morphology, but the sizes of the patches are significantly different. The OT-DDT nanoparticles present several separated patches while the HT-DDT nanoparticle shows two

major bigger patches and the BT-DDT nanoparticle has the smallest patch sizes and some randomly distributed BT ligands. In the case of PET-DDT nanoparticle, both separated small patchy domains as well as some short stripe-like features are presented.

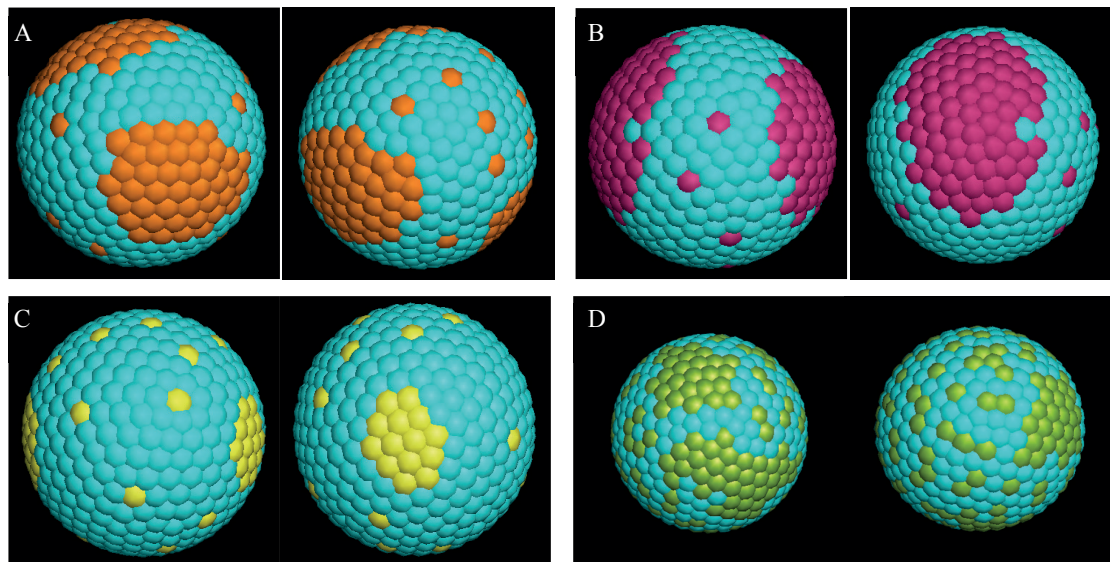


Figure 5.6 3D visualized Ag NPs models by RMC calculation. A) OT-DDT protected Ag NPs; B) HT-DDT protected Ag NPs; C) BT-DDT protected Ag NPs show a patchy surface pattern. D) PET-DDT protected Ag NPs shows a stripe-like surface pattern. The blue spheres stand for DDT ligands, the orange ones are OT ligands, the pink ones are HT ligands, the yellow spheres are BT ligands and the green ones are PET ligands.

In summary, this section shows that RMC method could indeed be applied to interpret the experimental MALDI-TOF data on silver nanoparticles. While χ^2 can be used to infer roughly the phase separation category of the nanoparticle, it fails to distinguish the differences between similar patterns such as the OT-DDT and HT-DDT data. RMC correlates the detailed information of each fragments with structural features. The size of the domains as well as their relative positions could be directly visualized. The versatility of the method could be therefore widely appreciated if one tends to build the structural-property relationship of mixed ligand nanoparticles.

5.4 Comparison with SANS results

Similar to SANS combined with MONSA method, the RMC allows for the extraction of real space information from otherwise indirect experimental mass spectroscopic data. Although

both methods are powerful and have multiple advantages, there are certain limitations with both. For example, polydispersity of the sample would largely affect the interpretation of models, as all the spectroscopic techniques measure the averaged structural information. Furthermore, both techniques have by definition low resolution in retrieving the length scale information. While other types of supporting data are always useful acting as constraints during the fitting, the modelling would give much more convincing results when two types of different techniques could be combined and cross validate themselves. Both SANS and MALDI have potential in the quantitative analysis of the structure of ligand shells, while they are probing the ligand shell through completely different mechanisms. It is therefore tempting to combine this two method on the analysis of the same sample and compare the results directly and quantitatively.

SANS study on the same PET-DDT silver nanoparticle is performed successfully, since the sample shows good size monodispersity as required by SANS method described in the previous chapter. In order to distinguish the contrasts between the two ligands, the nanoparticle was synthesized using deuterated PET under the same synthetic conditions using Stucky's method followed by solvent fractionation, as described in details in Method section. TEM analysis, Figure 5.7A, was performed on this nanoparticle show that it has a narrow size distribution of 6.4 ± 0.5 nm. SANS data were then collected using deuterated toluene and a mixture with 22% toluene as solvents, as shown in Figure 5.7B. MONSA program was then used to fit the two SANS curves of different contrast conditions. 3D beads model was obtained with good quality fitting to the experimental data as shown in Figure 5.7B and C. The reconstructed model shows that as predicted by RMC analysis of the PET-DDT silver nanoparticle, the nanoparticle has a patchy type morphology while there are also some locations of disordered stripe-like domains.

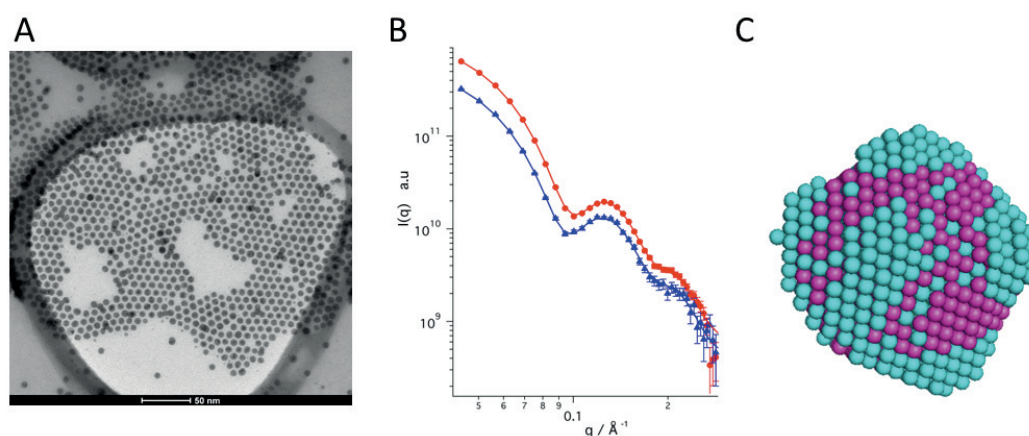


Figure 5.7 TEM and SANS characterization of the dPET-DDT mixed ligand protected silver nanoparticle. A) TEM indicates a core diameter distribution of 6.4 ± 0.5 nm. B) SANS data (dots) and fits (full line) of the dPET-DDT silver nanoparticle. Red curve represents the data measured in deuterated toluene while the blue curve is measured using 22% toluene and 88% deuterated toluene mixture. C) 3D bead model of the nanoparticle obtained by MONSA fitting of the SANS curves. The red beads stand for PET while blue beads are DDT phase.

In conclusion, for the first time the models obtained from RMC fitting method on MALDI-TOF data could be combined and compared with SANS modelling enabling a cross validation of both techniques. Considering that the two characterization techniques are very different in mechanism, the good agreement of the 3D models achieved by the two methods leads to the morphology analysis of the nanoparticle much more convincing. In fact, until now, there are only a few study that have used multiple techniques in the characterization of the same mixed ligand nanoparticle. Examples include the joint utility of STM with NMR⁵⁷ and SANS¹⁰⁸. However, in both cases, a quantitative analysis is missing. Both SANS and MALDI techniques have the potential to be quantitatively compared to other techniques such as STM, IR and NMR. As discussed in the Chapter 1, due to the complex nature of the mixed ligand shell morphologies, the integrative characterization approach would be of great advantage for the field and for a comprehensive understanding of the structure of mixed SAM structures.

5.5 Materials and methods

5.5.1 Synthesis of mixed-ligand silver nanoparticles (Ag NPs)

A modified Stucky method²⁰¹ was adopted for the synthesis of silver nanoparticles. First dissolve 110 mg silver trifluoroacetate (CF_3COOAg) in the mixture of 20 mL chloroform and 20 mL toluene. Add 120 μL 1-Dodecanthiol (DDT) and stir for 10 mins at 70 °C followed by 434 mg tert-butylamine-borane (TBAB) reducing agent and stir vigorously for an hour. Upon the completion of reaction, quench the mixture with 40 mL methanol (CH_3OH) and let it cool down naturally. Add methanol, wash and centrifuge the Ag NPs three times. Leave the sample inside a vacuum box overnight until the sample dry out. The solution changes from yellow to milky at the beginning of the experiment, upon addition of reducing agent, the color changes into dark purple.

Then homoligand protected silver nanoparticles was ligand exchanged with various ligands. 20 mg DDT protected Ag NPs we weighed. The volume of the ligands we need for ligand exchange of Ag NPs was calculated according to the molar ratio of ligand DDT: the other ligand = 1: 10. Homo-ligand Ag NPs were dissolved in around 2 mL of chloroform. The Ag NPs were then combined with various amounts of the thiol ligands and stir for 24 h and then thoroughly washed.

5.5.2 Preparation of samples for MALDI-MS analysis

After synthesis of metal nanoparticles, we prepared the samples for MALDI-MS analysis. In our case, trans-2-[3-(4-tert-Butylphenyl)-2-methyl-2-propenylidene malononitrile (DCTB) is used as the matrix substance. Using chloroform (CHCl_3) as the solvent, a solution of the matrix is made and mixed with the sample solution in volume ratio 1:1. This final mixture solution is spotted onto a metal plate, which will then be sent into the analyzing machine. As the solvent vaporizes, the nanoparticles are embedded into the recrystallized matrix crystal, which can then be used for further analysis. The detailed procedure is described below:

- 1) Dissolve 10.0 mg DCTB in 0.4 mL chloroform to make 25.0 mg/mL matrix solution.
- 2) Weigh 1.0 mg nanoparticles sample and dissolve it in 0.1 mL chloroform to make 10 mg/mL sample solution.
- 3) Mix solution 1 and solution 2 together at volume ratio 1:1.
- 4) Take 1 μL of the mixture solution with a pasteur pipet and spot it on the MALDI-MS stainless steel plate. Wait until the solute evaporate thoroughly. For the mixed-ligand Ag NPs samples, a modified sandwich crystallization method was utilized.

The processed spectra are plotted using Plot software and peaks are identified manually. Then the mass-to-charge ratio of the peaks are compared to the theoretical calculation results of different combination of thiol ligands, thus identifying the intensity of those peaks. For each ligand–ligand combination (i.e., each possible value of x and y for fragment $\text{Ag}_x\text{A}_y\text{B}_{x-y-1}$, where x ranges from 4 to 8, y ranges from 0 to x), the ion intensity are summed and divided by the total intensity of all $\text{Ag}_x\text{A}_y\text{B}_{x-y-1}$ ions to obtain the real probability $P_{w,i}$. The binomial distribution was calculated and compared to the experimental data to get the SSR of the system.

Chapter 6 Control the morphology of mixed ligand nanoparticles

This chapter examines the mechanisms of two synthetic processes of mixed ligand nanoparticles, i.e. ligand exchange reaction and thermal annealing. Thanks to the development of the characterization methods described above, morphological evolution of nanoparticles during the two reaction conditions could be monitored. The work presented here could act as a guide for rational design of mixed ligand nanoparticles with desired morphologies.

Disclosure: The first section 6.1 of this chapter is a lightly rewritten version of the article, "Evolution of the Ligand Shell Morphology during Ligand Exchange Reactions on Gold Nanoparticles." Zhi Luo*, Jing Hou*, Laure Menin, Quy Khac Ong, and Francesco Stellacci. *Angewandte Chemie* 129, no. 43 (2017): 13706-13710.

Mixed ligand nanoparticles have presented many unique structure-property relationships. Therefore, one of the main goals of the current research is to design the morphology of ligand shells that are highly controllable. Theoretical works have illustrated that the separation is not only determined by the enthalpy driving force, but also influenced by interfacial entropy. It has also been shown that the thiol-gold bonds (or with other types of metals) have certain degree of mobility and reversibility that allow for their partial desorption and re-organization. Thermodynamic considerations therefore predict the feasibility of controlling the morphology of the ligand shell. However, experimental studies have not been reported mainly due to two reasons. First is the role of kinetic factors in addition to thermodynamics. The mobility of ligands on metal surfaces may not be fast enough to allow for equilibrium organization at all times. The lack of suitable characterization methods is obviously another obstacle.

Thanks to the development of the SANS and MALDI techniques, experimental studies on the control mixed ligand shell morphologies could be performed for the first time. In this chapter, I present two ways of tuning the mixed ligand organizations, i.e. through ligand exchange reaction and thermal annealing. The first study aims at the investigation of a process where

kinetics is expected to play a very important role. The wide applications of ligand exchange reactions on different types of nanoparticles also call for a better understanding of such processes. The second part addresses whether it is possible to alter the ligand shell morphology with suitable thermal processes. If done in a controllable way, both processes could allow a careful design of the NP properties.

6.1 Evolution of the ligand shell morphology during ligand exchange reactions

Ligand exchange reactions are one of the main synthetic approaches to achieve gold nanoparticles coated with a mixture of ligand molecules. A number of studies have investigated the mechanism for this reaction. Current knowledge is limited to the evolution of the composition of the ligand shell. Nothing is known on the evolution of the morphology, although it is accepted that nanoparticles coated with mixture of ligands can have ligand shells with complex morphologies, e.g. random or patchy. Here, adopting the MALDI-TOF technique the evolution of the ligand shell composition and morphology during ligand-exchange reactions is monitored. When replacing 1-dodecanethiol with biphenyl-4-thiol, the expected evolution in composition is observed. At the same time, the ligand shell starts as a random mixture and gradually evolves towards a patchy morphology. In fact, when the composition has reached a plateau (and reaction is generally assumed to be finished), the ligand shell morphology keeps evolving for days, probably slowly approaching its equilibrium configuration. This work could serve as a guide for the design of ligand exchange reactions that lead to the desired ligand shell morphology.

6.1.1 Ligand exchange reaction on nanoparticles

A nanoparticle's ligand shell (LS) determines most of the interfacial properties through both its composition and morphology^{21,26,27}. For this reason, great efforts have been made to develop synthetic approaches that lead to LS of disparate compositions. A definite advantage of noble metal nanoparticles is that once synthesized it is possible to vary their LS composition using a simple replacement reaction called ligand-exchange reaction (LER)⁸⁹. The characteristics and the mechanism for the LER have been extensively investigated, as described in Chapter 1.

It is known that gold nanoparticles with LS composed of a mixture of different ligand molecules can present various LS morphologies, ranging from random, Janus, patchy, to stripe-like domains⁵¹. The morphology of the LS has been shown to play a key role in determining a number of the nanoparticles' properties, from interfacial energy²¹, assembly²⁰², to biological properties⁷⁴. Yet, to date, nothing is known on the LS morphology evolution during a LER. It is obvious that when starting from nanoparticles coated with a single ligand (homoligand), the initial LS morphology is a homogenous distribution of such ligand. During

the replacement reaction with a second ligand, there are many possibilities. For example, the LS could develop a patch of the incoming ligand that subsequently spreads into a homogenous distribution. The opposite could also happen; an initial homogenous/random distribution of the incoming ligand could slowly/rapidly evolve into a patchy or Janus morphology. Different LS evolution pathways, could lead to particles with nominally the same composition but with different interfacial properties, generating, for example, batch-to-batch or laboratory-to-laboratory differences. At present, there is no study on the topic.

This lack of investigation is partly due to the fact that the accepted approaches to experimentally evaluate the LS morphology (e.g. STM, AFM, NMR, FT-IR) are complex and not suited for the analysis of different time points in a reaction. Recently, mass spectrometry (MALDI-TOF-MS) has been developed as a rapid and relatively simple tool to investigate the morphology of the LS for gold and silver nanoparticles. The basic principle is based on a seminal idea presented in Harkness et al's work¹³⁰. It takes the advantage of the fact that MALDI process generates fragments from nanoparticles that are composed of a number of gold atoms linked together with a number of thiolated ligands. The key assumption in this approach is that these fragments represent a statistical sampling of the nanoparticle surface. Therefore, the mass distribution pattern of different fragments carries structural information of the nanoparticle surface, and specifically of its LS morphology. In the mixed ligand case, it is reported²⁰³ that the most abundant fragment, i.e. gold-thiolate complex, is Au_4L_4 . Other types fragments may also present in the spectra but very often have weak intensities to allow for quantitative analysis. In the case of mixed ligands, the Au_4L_4 fragment would have five different ligand combinations ($\text{Au}_4\text{L}_x\text{L}'_{4-x}$). The probability distribution of these combinations critically depends on the LS morphology. For example, for a Janus particle the two most common fragments should be the ones containing only one type of ligand, while for a random structure the probability of finding all five combinations should follow a binomial distribution. Consequently, by comparing the mass distribution pattern of such fragments to the theoretically expected ones of a given morphology, it is possible to infer the morphology of the LS. The value of sum-of-squares residual (SSR) has been proposed to quantify the differences of two MALDI spectra. The SSR is calculated by squaring and summing the residual between the normalized experimental intensity of each fragment and that of a given morphology. For example, by quantifying the deviation from binomial distribution (corresponding to random morphology), one can calculate the degree of phase separation of the mixed ligand on nanoparticle surfaces. In general, it has been found that if the SSR against binomial distribution is less than 1.0×10^{-2} , the nanoparticles are expected to present random

morphology. While SSR above 1.0×10^{-1} indicates significant big domains or Janus type morphology, SSR in between 1.0×10^{-2} and 1.0×10^{-1} means that the LS has patchy or stripe-like morphology.

It should be noted that with mass spectrometry, the true LS composition can be readily defined and hence morphology and composition determined at the same time¹²³. One additional advantage of using MALDI-TOF to study the LS of nanoparticles is that there are minimal requirements on the sample size/distribution or on the particles solubility. The key idea in this paper is to isolate reaction products from a LER and after a thorough (but rapid) cleaning procedure, to analyze it by MALDI-TOF so to obtain both LS composition and structure as a function of reaction time.

6.1.2 Monitoring the morphologies

1-dodecanethiol (DDT) protected nanoparticles 4.1 ± 0.6 nm in diameter is synthesized with a one-phase method and purified as described in the method section. All characterizations performed on these nanoparticles are presented in the supporting information. Then the LER was performed by dissolving 40 mg of such DDT coated NP in 20 ml of chloroform. Then 40 mg of biphenyl-4-thiol (BPT) ($t=0$ of the reaction) was introduced in the solution under vigorous stirring to start the LER. Such combination of ligand mixtures was chosen as nanoparticles coated with mixture of these two ligands were established to present a variety of LS morphologies (from patchy to Janus-type depending on the particles size and LS composition) when synthesized with another approach (direct one-phase method). It was also shown that the introduction of BPT ligand by LER leads to interesting dielectric properties at the nanoparticle interfaces.

MALDI spectra (shown in Figure 1) of the $\text{Au}_4\text{L}_x\text{L}'_{4-x}$ species were collected on samples derived from 2 ml aliquots of solution extracted from the LER at different time points. All the five fragment peaks were obtained from reflection mode with high resolution (with mass errors around 12 ppm, shown in in Figure S1). The lack of resolution of samples after 48 hours is partly due to the lower solubility of nanoparticles after ligand exchange. The NPs in the aliquots were precipitated by addition of excess methanol and subsequent washing with multiple centrifugation steps in methanol and acetone (see Experimental Section for details). From each spectrum, the ligand ratio was calculated by summing up the frequencies of all five fragments weighed by the number of ligands in each fragment (equations in Experimental

Section). The resulting plot, Figure 2, for LS composition as a function of LER time agrees quantitatively (for the same ligands) and qualitatively (for other type of ligands) with data reported in literature. The SSRs between the experimental data and binomial distribution at such ligand ratio was then calculated as a measurement of degree of deviation from random morphology. The SSRs of all the MALDI spectra are listed in Table S1.

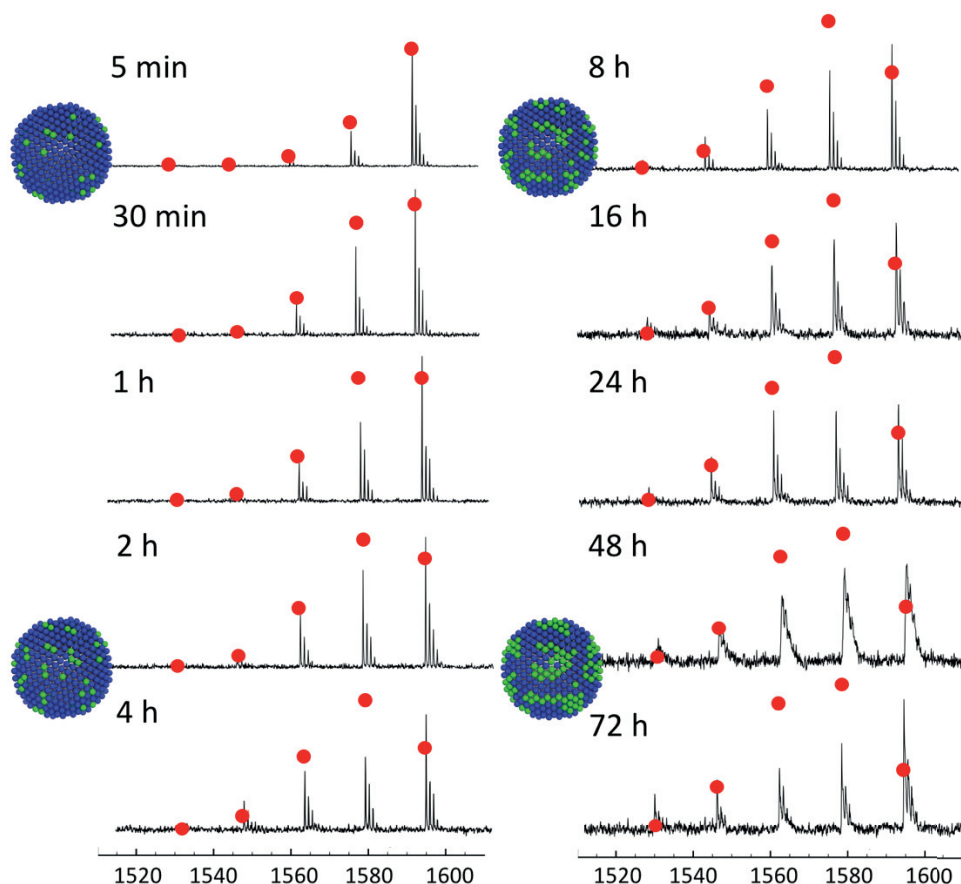


Figure 6.1 MALDI-TOF spectra of ligand exchange process. Red dots indicate binomial distribution (corresponding to random morphology) at each ligand ratio. From left to the right, the five peaks are assigned to be Au_4BPT_4 , $\text{Au}_4\text{DDT}_1\text{BPT}_3$, $\text{Au}_4\text{DDT}_2\text{BPT}_2$, $\text{Au}_4\text{DDT}_3\text{BPT}_1$, Au_4DDT_4 respectively. Cartoons are representations of the type of morphology at each stage. Image reproduced from reference⁶⁸.

The fraction of BPT on nanoparticle surfaces is already found to be around 9% after 5 minutes' reaction time, indicating a relatively fast initial step. As clearly showed in Figure 6.1, the intensities of the fragments follow the binomial distribution. The SSR at this starting stage is 5.2×10^{-3} suggesting that the initial steps of the reaction favor a random distribution of the incoming ligands. The reaction kinetic follows a second order diffusion limited Langmuir

model as describe by Lennox and co-workers. Similarly, the coverage of BPT reaches a plateau of 35% at the time of 24 hours, although the BPT in solution is at a concentration of 10 equivalents relative to DDT on NPs, in agreement with what was discovered previously. A detailed study of the LER shows that minimal phase separation starts to appear (SSR increases to above 1.0×10^{-2}) as the rate of exchange in composition of the LS starts slowing down (30 minutes) and the BPT coverage reaches 18%. This trend continued to around 8 hours' reaction time, corresponding to 32% coverage of BPT ligand, while the SSR gradually increases, indicating the formation of bigger phase separation domains (SSR above 3.0×10^{-2}). In the following 64 hours, the composition varies minimally ($\sim 4\%$) but the LS slowly progresses towards a patchy morphology. The SSR increased to 8.3×10^{-2} , indicating that the ligand shell domains kept growing with reaction time. It should also be noted that the ligand density remained the same during the whole LER process, as measured by TGA (method section).

To better understand the mechanism of the evolution of LS morphologies, the process of LER when incoming ligand stoichiometry is increased from 10 to 50 equimolar was investigated. All the measured MALDI spectra are shown in the method section. The plots of BPT coverage versus time are presented in Figure 6.2. As expected, the increase of BPT concentration (from 10 to 50 fold) leads to a larger fraction of BPT on the particles (from 35% to 55%) after LER. The kinetic curves were fit with the same second order diffusion limited Langmuir model (fitting parameters listed in Table 6.2). At the beginning of the exchange reaction, the higher BPT concentration results in a faster reaction rate with BPT coverage being already $\sim 18\%$ after 5 minutes. Yet, the general trend for the evolution of the morphology was found to be similar for both stoichiometry conditions. At the beginning, BPT ligand adds to the nanoparticle surface in a random morphology, patches are developed over time. In contrast to the 10-fold reaction, the SSR remained less than 1.0×10^{-2} for up to 8 hours, indicating that the mixed ligand morphology remained very close to random until the BPT coverage reached the equilibrium. Small phase separation domains gradually developed afterwards, with the SSR increasing to 2.0×10^{-2} after 3 days. The comparison between the two exchange conditions reveals that the mechanism of LER is most probably determined by both kinetics and thermodynamics. The fast initial step is a kinetically controlled process while thermodynamic equilibrium is reached slowly over time. The SSR for the two LER conditions plateaus at different values, indicating a larger degree of patchiness for the 10-fold LER reaction conditions. There are many possible explanations for this observation. One could claim that in the 50-fold case the kinetic barrier for reaching equilibrium is very large.

Or one could attribute the difference to the final ligand shell stoichiometry. In the 50-fold case the final stoichiometry is close to 1:1 and this, based on previous literature, should lead to thin stripe-like domains, which would give a lower SSR when compared to the thicker patches that are expected in the 2:1 final stoichiometry observed for the 10-fold reaction.

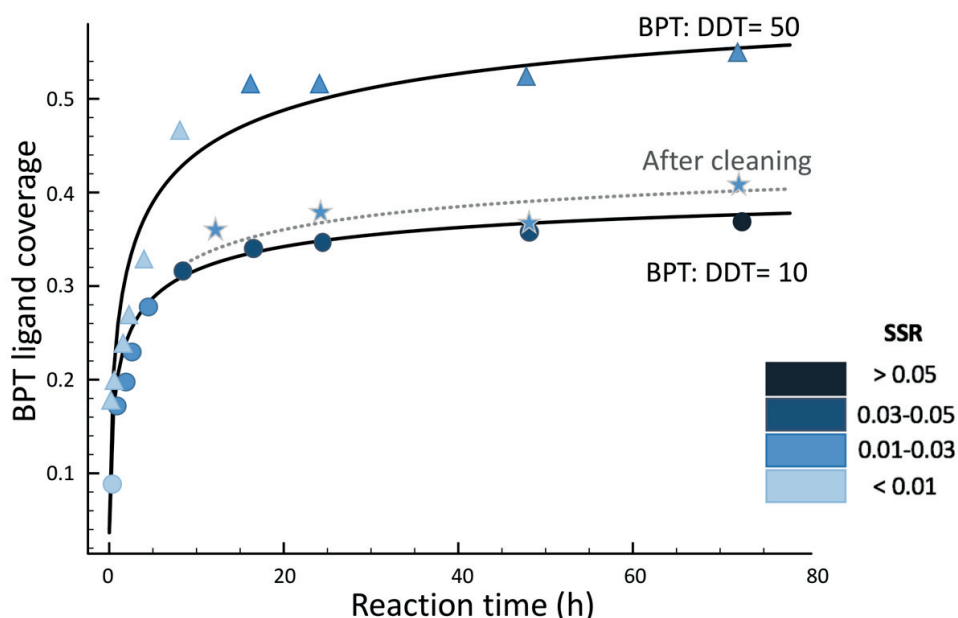


Figure 6.2 Evolution of BPT ligand coverage and mixed ligand morphology with time. Round dots represent the reaction with 10 folds BPT ligands while triangle dots represent 50 folds' reaction. The star dots and grey line represent the samples after quenching and cleaning at 8 hours. The color of each dot indicates the degree of phase separation with color scale of SSR listed on the right side. Image reproduced from reference⁶⁸.

To further explore the mechanism for the LS morphology evolution, the evolution of the SSR for nanoparticles in solution in the presence and absence of extra ligands is examined. In other words, it is interesting to know whether, once the stoichiometry equilibrium is reached, the LER continues or the variation of SSR is solely due to exchanges on the nanoparticles' surface. The 10-fold reaction is compared to a LER reaction performed in the same condition but quenched at 8 h where the washed particles were placed again in pure solvent. Quenching at 8 h is chosen because at that time the BPT ligand coverage starts reaching the equilibrium plateau. After vacuum drying, the nanoparticles were re-dissolved in chloroform with the same concentration (2 mg/ml) and evolution of morphology was examined using MALDI-TOF-MS. All the MALDI spectra are shown in method section. As shown in Figure 6.2, there is no obvious change in SSR over time in this case. Even after 3 days, the SSR remains 2.5 x

10^{-2} (starting from 2.0×10^{-2}). In this case the most probably equilibrium morphology has an SSR of 8.0×10^{-2} , far from the final SSR in pure solvent. This results act as an indication that, in the absence of extra ligands and LER, the evolution of the ligand shell morphology is a very slow phenomenon at room temperature. This conclusion is supported by the fact that if the nanoparticle solution is heated at 70 °C for 4 hours, the fragment distribution becomes very close that of LER after 72 hours (with SSR around 6.0×10^{-2}). The reorganization of ligands on the nanoparticle surfaces is thus most probably mediated by the free ligands in solution through desorption-reabsorption mechanism, but the final morphology appears to be insensitive to the specific mechanism and to all other reactions that should be taking place in solution.

To further test the validity of this study, a LER for DDT nanoparticles with its deuterated analogue (dDDT) is performed, knowing that at thermodynamic equilibrium the mixed ligand particles should show a homogenous LS morphology. The tendency of phase separation of these two ligands is minimal and it has been proven previously by similar FTIR and MALDI analysis that the ligand shell morphology is a random mixture of DDT and dDDT¹²¹. All the measured MALDI data are shown in method section. The LER needs to be performed in slightly different conditions, as the amount of incoming ligand (dDDT) used was only 1.5 equivalent. The reason why this stoichiometry is chosen for dDDT is that unlike the LER with BPT, it is found the final dDDT-DDT ligand ratio on the nanoparticle was very close to the feed ratio. The kinetic of the exchange reaction is also much faster than BPT ligands. Such result agrees well with the fact that the chemical nature of dDDT and DDT is very similar. From Figure 6.3B, one can see that the dDDT coverage already reaches around 16% after 5 minutes. Interestingly, the ligand shell morphology is patchy at this stage with the SSR being around 7.0×10^{-2} . While the reaction proceeds, the SSR gradually decreases. SSR decreased to be less than 1.0×10^{-2} at around 24 hours when the ligand ratio also reaches equilibrium. The final SSR measured was 0.2×10^{-2} , indicating that the final morphology of the LS is random as expected. These results also seem to suggest that the initial morphology is critically dependent of the kinetics of the reaction, apparently faster reactions favor domain formation. Similar LER features are further observed during the exchange of DDT nanoparticle by 1-undecanethiol (UDT). The chemical structure of UDT is very close to that of DDT with only one carbon less in the alkane chain. Therefore, also in this case we expected an equilibrium random morphology. As shown in method section, it is found that the ligand distribution of UDT-DDT nanoparticle starts as a patchy morphology (with SSR higher than 5×10^{-2}). As the reaction proceeds, the morphology gradually evolves to almost random

after 24 hours. As in the dDDT case, the reaction rate is very fast. With the feed ratio of UDT being 4 times DDT on surface, the coverage of UDT reached more than 40% in 5 minutes, with a final coverage of 62%.

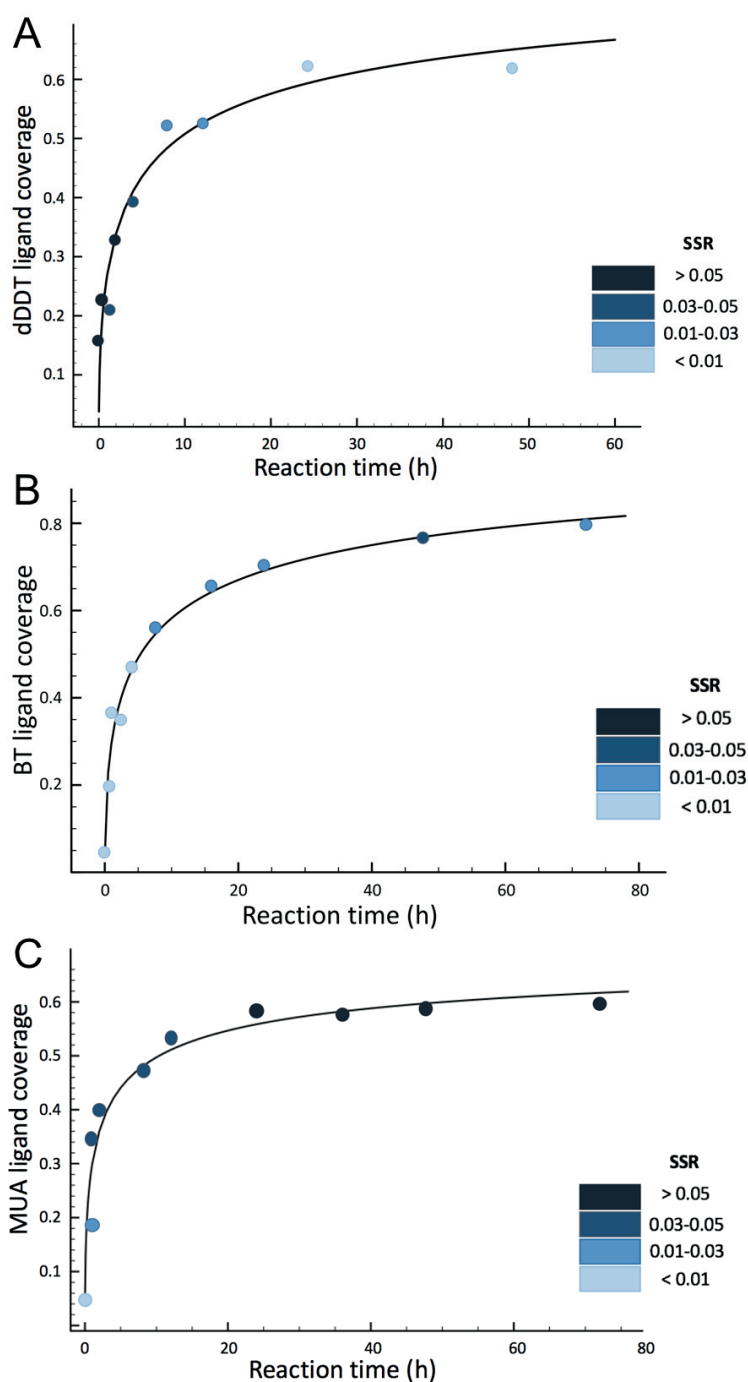


Figure 6.3 A) Evolution of dDDT ligand coverage and mixed ligand morphology with time. The incoming dDDT ligand is 1.5 folds of DDT ligands on nanoparticle surface. B) Evolution of BT ligand coverage and morphology with time. The incoming BT ligand is 50 folds of

DDT ligands on nanoparticle surface. C) Evolution of MUA ligand coverage and morphology with time. The incoming MUA ligand is 10 folds of DDT ligands on nanoparticle surface. The color of each dot indicates the degree of phase separation (color scale of SSR listed on the right side). Image reproduced from reference⁶⁸.

To broaden our study, the exchange reaction of DDT nanoparticles with two other types of thiolated ligand is investigated, i.e. 4-butanethiol (BT) and 11-mercaptoundecanoic acid (MUA). All the MALDI spectra are presented in method section. Figure 6.3 shows that the exchange by both BT and MUA ligands shares the same trend as DPT ligand. The monolayer morphology starts as a random configuration with the SSR below 1.0×10^{-2} . At the third day, the SSR reached a value SSR of 3.0×10^{-2} (coverage 80%) indicating a final morphology of small patches. Meanwhile, the SSR of MUA-DDT nanoparticle reached 3.0×10^{-2} after 1 hour and gradually evolved to 7.2×10^{-2} after 72 hours. The differences in the final degree of phase separation is due to the different chemical nature of the two ligands. Both results confirm that the final morphology of ligand shell is largely determined by thermodynamic equilibrium. It is possible that the LER pathway described here is a general mechanism for thiolated ligand exchange on gold nanoparticles. Yet, it must be pointed out the significant differences between this sets of results and the results for the DDT-dDDT and DDT-UDT case. In the first cases the initial state is random and there is a slow evolution towards patchy. In the latter cases, the opposite is true. These results will be the core of future studies.

In conclusion, the detailed mechanisms of ligand exchange reactions between thiolated ligands on gold nanoparticles are examined. It is discovered that the incoming ligand adds to nanoparticle surfaces in a random way at the beginning while patchy domains gradually grow as the reaction proceeds. By comparing the kinetics of different exchange ligands we suggest an initial phase under kinetic control followed by a slow convergence towards thermodynamic equilibrium. The results here indicate that with a careful choice of both the amount of exchange ligand and the reaction time, the ligand shell composition as well as its morphology can be tuned. This work could act as a guide in the design of reproducible mixed ligand nanoparticles achieved by LERs.

6.2 Effect of thermal annealing on the ligand shell morphologies

The phase separation of mixed ligands has been postulated to be a thermodynamic driven process, which shares close resemblance with the morphology of copolymers and

microstructure of multiple component alloy. Therefore, it is natural to come up with the questions whether it is possible to tune the ligand shell morphologies using thermal treatment. Currently, there are no report on this topic, especially from experimental studies. However, as presented in the previous section, it is clear that the morphology of the mixed ligands strongly depends on the synthetic routes^{31,130}. Room temperature ligand exchange reactions lead to morphologies that are kinetically trapped, depending on the stoichiometry of the reaction as well as the reaction time. While the morphology evolution at room temperature has been shown to be very slow in the absence of free thiol molecules, it seems that heating at mild conditions could accelerate such process. This process can be regarded as annealing if the morphology change converges towards a different phase separation state after heating and cooling cycles. Otherwise, such heating process might only lead to situations where entropy dominates the disordering of ligands.

In this section, SANS is adopted to study the effect of temperature in great details. The reason why SANS is used for this study is that currently SANS is the only technique that could follow the change in ligand shell morphology during the annealing reaction with enough resolution on the morphology differences. The core size differences, if any, could also be detected by SANS, since a mild condition that only changes the ligand shell organization but not the metal cores are of great importance. The SANS data are supported with other techniques such as TEM, NMR, TGA to confirm that all other parameters of nanoparticles remained constant except ligand shell morphology. The evolution of the ligand shell morphology was followed in real time in order to extract the kinetics of the reaction. The annealing process is tested to see if a different mechanism by tuning the cooling rate of the solution is possible. PET-DDT ligand pairs have been used as the main example since the SANS analysis on this type of nanoparticles has been shown to be robust. Furthermore, other types of ligand pairs are also examined in order to prove the universality of the annealing process. The results demonstrated here offers the first and one of the most important guideline for the later control on the morphology of the nanoparticles, which lays the foundation for the study on the interfacial water structure in the next chapter.

6.2.1 Synthesis and annealing of the nanoparticles

Gold nanoparticles coated with a mixture of phenylethanethiol (PET) and dodecanethiol (DDT) were investigated. The PET ligands are deuterated in order to generate different contrasts with DDT ligands. The nanoparticles were synthesized using ligand exchange

reaction at room temperature similar to the conditions described in the previous section and then annealed at 60 °C for 1 day. The detailed the procedures are also described in the Materials and Methods section. The reason why 60 °C was chosen as the reaction temperature is based on the fact that the core of nanoparticles will be significantly affected if heating above 80°C. If the size of the core is not well controlled, it is impossible to isolate the effect of thermal treatment from the effects of sizes. This is because good monodispersity is the prerequisite for SANS measurements and that the core sizes also have great effects on the equilibrium of the ligand shell morphology.

Multiple techniques are then used to prove that the composition and core size of the nanoparticles are not influenced. As shown in Figure 6.4, TGA, NMR and TEM studies of nanoparticles before and after heating procedures could all overlap within errors in the measurements. The core size of the nanoparticles has been found to be 5.0 ± 0.5 nm from the TEM image analysis. The ligand ratio of PET: DDT was found to be 0.7: 1 for both nanoparticles. The differences in TGA measurements were found to be within 2% and indicated a high covering density of the ligands ($\sim 92\%$ of the highest packing density.)

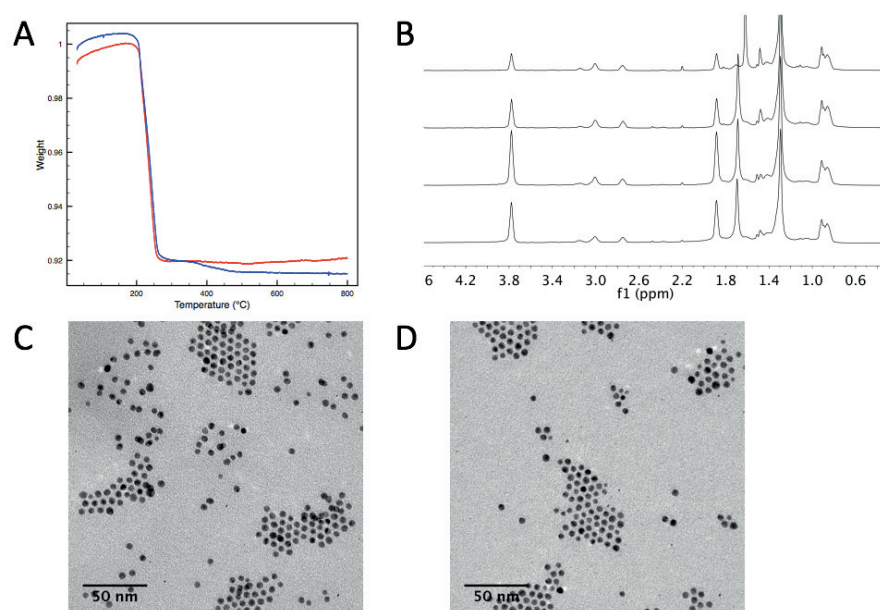


Figure 6.4 A) TGA and B) NMR results of PET-DDT NPs before and after annealing, showing no detectable change of ligand density and ratio. C) TEM images of nanoparticles before (left) and after (right) annealing, showing that the core sizes of the nanoparticles are not affected by the heating treatment.

6.2.2 Morphology evolution during heating and annealing

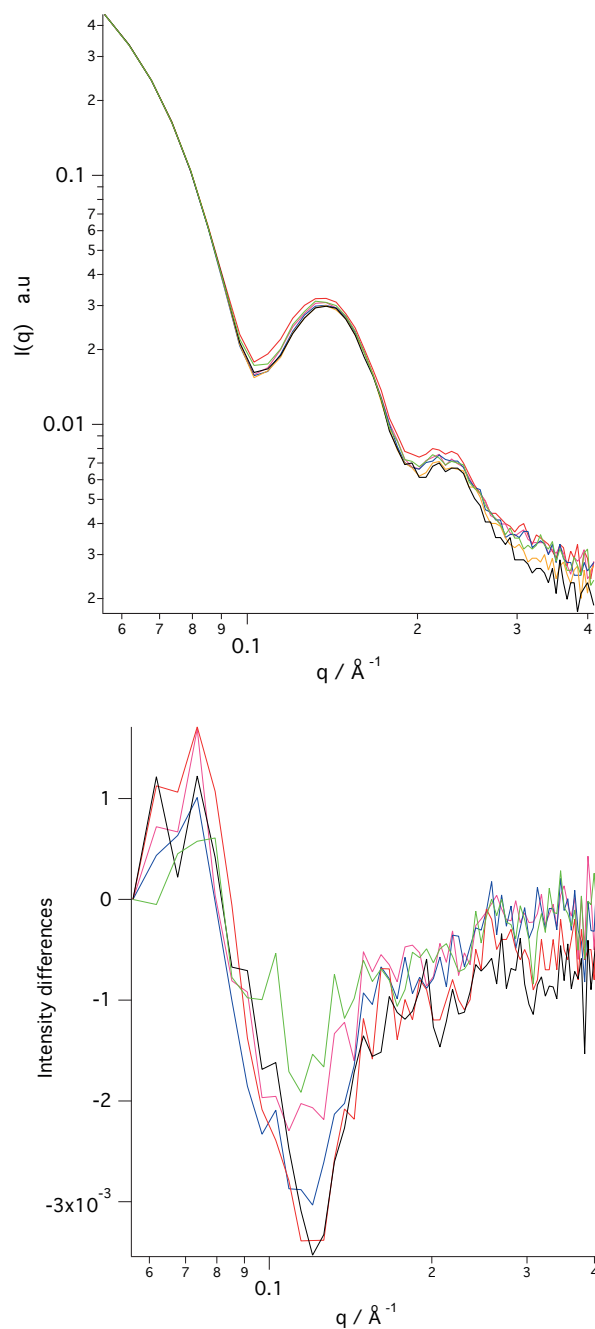


Figure 6.5 up: SANS curves of PET-DDT NPs before annealing (red) and annealed for 0.5h (green), 1h (pink), 4h (blue), 12h (orange) and 24h (black); bottom: Differences between annealed curves and non-annealed curves.

The annealing process was then followed with SANS measurements by rapid cooling the nanoparticle solution at different reaction times, i.e. 0.5h, 1h, 4h, 12h and 24h. As shown in Figure 6.5, the SANS curves show good overlapping at low q ranges (Guinier region),

indicating that the radii of gyration of the nanoparticles remained same. In nanoparticle systems with multiple contrasts, the radius of gyration is affected by both the core size as well as the ligand ratio of scattering object. Therefore, combined with the information from other supporting techniques discussed above, the overlap of scattering curves at low q confirms that the overall size and composition of the nanoparticles remained constant. While at higher q ranges, i.e. $> 0.08 \text{ \AA}^{-1}$, the SANS curves show obvious differences among nanoparticles. In general, the oscillation features in the scattering profiles becomes sharper for nanoparticles after annealing. Such evolution is a sign of the higher symmetry of the shape of the nanoparticles, indicating that a more centrosymmetric distribution of scattering length densities in the nanoparticles are presented after the thermal treatment. It could be seen that the effect of annealing starts to appear as early as 30 minutes, which confirms that thiol molecules have higher mobility on nanoparticles at 60°C . Considering that many of the direct synthesis of nanoparticles, especially with the Stucky's protocol²⁰¹, are conducted at similar temperatures for more than 1 hour, such results suggests that direct synthesis of mixed ligand nanoparticles could have higher possibility of achieving equilibrium morphologies.

The SANS profiles of nanoparticles were subtracted by the SANS curve before the thermal treatment in order to give a clearer clue of change at different scattering angles. As shown in Figure 6.5B, one could see that most of the differences occur between 0.09 \AA^{-1} to 0.15 \AA^{-1} , corresponding to the first oscillation features. The small differences at even higher angles could be mainly due to the effects of incoherent scattering.

To better visualize the effect of annealing, *ab initio* models as shown in Figure 6.6, were calculated from the SANS curves with different ligand contrasts using MONSA packages as described in Chapter 3. From the 3D models, one could see that the nanoparticle before annealing shows mainly patchy like morphology linked with elongated domains. After the thermal treatment, the morphology of the nanoparticles becomes similar to the PET-DDT nanoparticles from direct synthesis as shown in Chapter 3. Although there are still domains with thick sizes, the general trends of the phase separation features are towards thinner stripe-like structures. Statistical analysis on the distribution of the stripe-like domains gives $1.8 \pm 0.5 \text{ nm}$ and $1.6 \pm 0.6 \text{ nm}$ for nanoparticles before and after the thermal treatment.

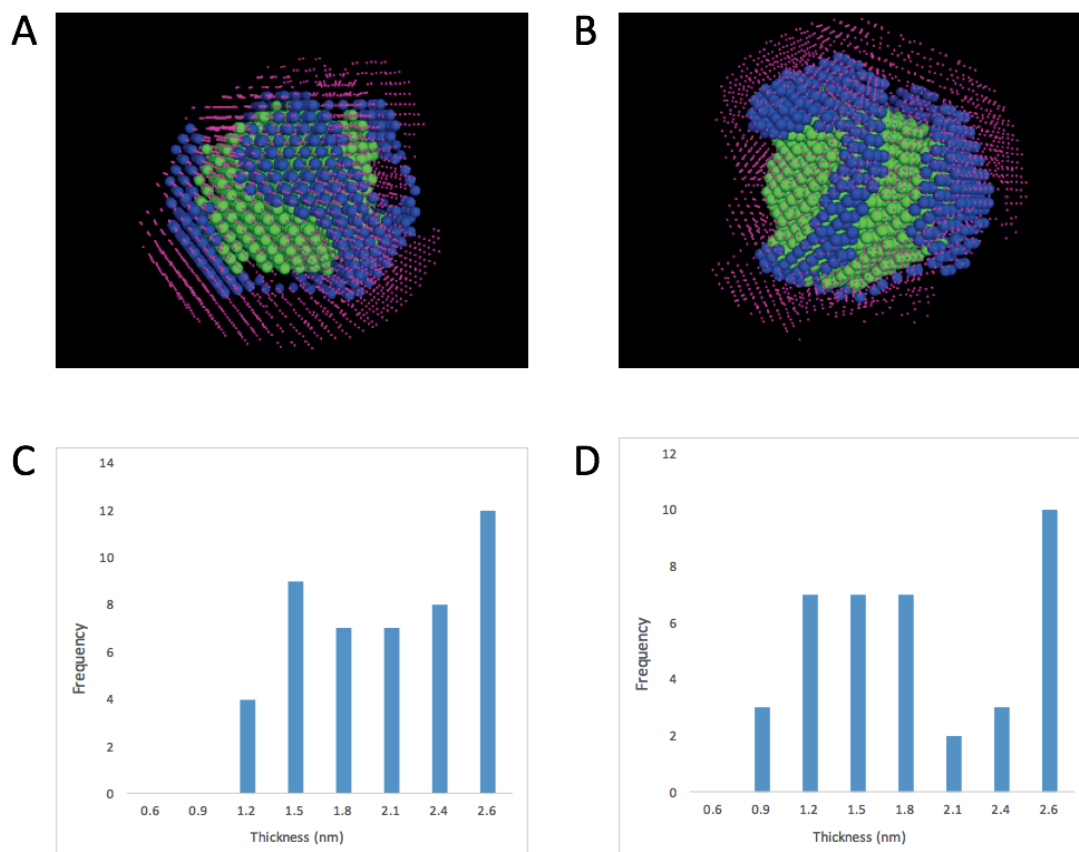


Figure 6.6 A) *Ab initio* model of PET-DDT nanoparticle before annealing showing mainly patchy domains; B) *Ab initio* model of nanoparticle after annealing showing thinner stripes. The statistical analysis on the thickness of the patchy domains are shown in C) and D) for nanoparticles before and after annealing. A shift towards thinner stripe-like domains are present after annealing.

From the SANS measurements, it can be seen that the mixed ligand morphology would evolve towards more symmetric shape upon heating. Although such differences are small, it could be readily captured by SANS. One question remains as for whether the structure seen after thermal treatment is driven by thermodynamics and whether the structure before heating is at equilibrium state or not. SANS analysis following the annealing reaction at different cooling rate is then performed. As shown in Figure 6.7, the red curve and the blue curve are the same as in Figure 6.5, representing the scattering profile of nanoparticles before and after 4 hours annealing. While the other three curves are measured for slow cooling rate at 0 °C, 30 °C and 40 °C respectively. From the SANS profiles, one can see that while the scattering curves overlap at both long and high angle regions, the oscillation features of the peaks show obvious differences. While the nanoparticles after cooling at 30 °C and 40 °C are almost the

same with the shape symmetry being in between close to the 4-hour heating morphology, the nanoparticle after cooling at 0 °C is closer to the nanoparticle before thermal treatment. The ligand shell morphology does not completely evolve back to the original structure, indicating that the morphology of the nanoparticle synthesized by ligand exchange reactions is not at equilibrium and trapped kinetically. Nanoparticles show the same profile after repeating the thermal treatment. Therefore, the results shown here demonstrate the possibility of performing annealing treatment on nanoparticles in order to tune their morphologies.

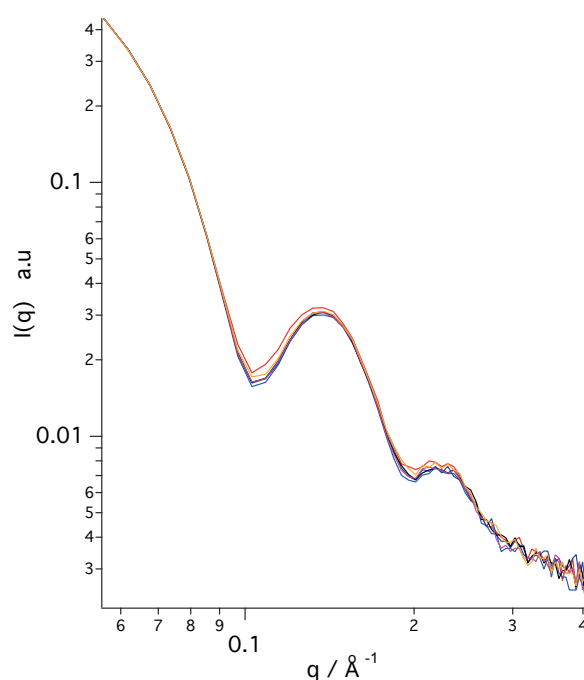


Figure 6.7 SANS profiles of nanoparticles before heating and annealed at different cooling rates. The red curve stands for nanoparticle before heating, while the orange, pink, black and blue curves are nanoparticles cooled at 0 °C, 30 °C, 40 °C and rapidly quenched.

6.2.3 Thermal treatment of other ligand pair protected nanoparticles

The final question we would like to address is whether such annealing effects are unique only for the PET-DDT mixed ligand pairs or if it is a universal phenomenon. The heating experiments on two other types of mixed ligand pairs are conducted, i.e. dMPA-OT and MUS-dOT nanoparticles. As shown in Figure 6.8, while the MUS-dOT nanoparticle does not show obvious differences upon heating, the dMPA-OT nanoparticle shows significant effects. Such results show that the effect of annealing depends on different types of nanoparticles, and probably related to the different synthetic procedures.

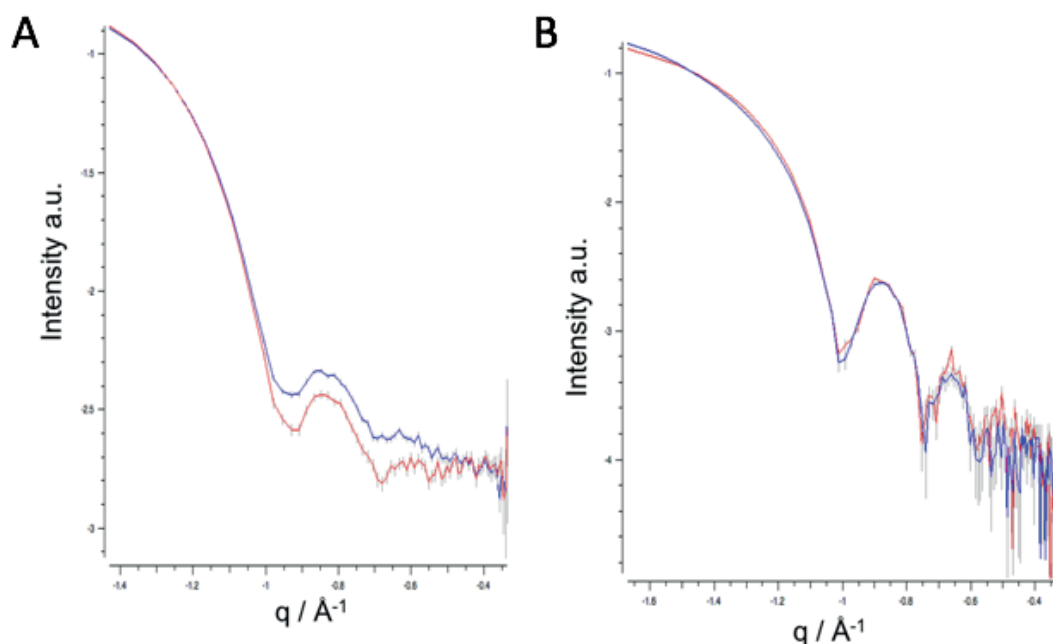


Figure 6.8 The effect of annealing on two different types of mixed ligand nanoparticles, i.e. dMPA-OT (A) and MUS-dOT (B). The blue curves in both plots stand for nanoparticles before annealing while the red curves are after annealing.

In conclusion, it is shown here that thermal annealing could become an effective way of controlling the morphology of mixed ligand nanoparticles. When a nanoparticle is synthesized at conditions that inhibit reaching the thermodynamic equilibrium, or when the equilibrium reached are far from the equilibrium at another temperature, it is possible to generate nanoparticles with the same composition and core sizes but only differs in the organization of ligand shell structures. While the degree of differences depends on different nanoparticles, the general trend is that the morphology of nanoparticles becomes more symmetric upon heating, which agrees well with previous thermodynamic considerations. Together with the section 6.1, I have shown here the mechanisms of two possible pathways for tuning the structures of mixed ligand nanoparticles. The fine tuning of morphologies offers a practical way for the future experimental studies that requires control over the ligand shell organizations.

6.3 Materials and Methods

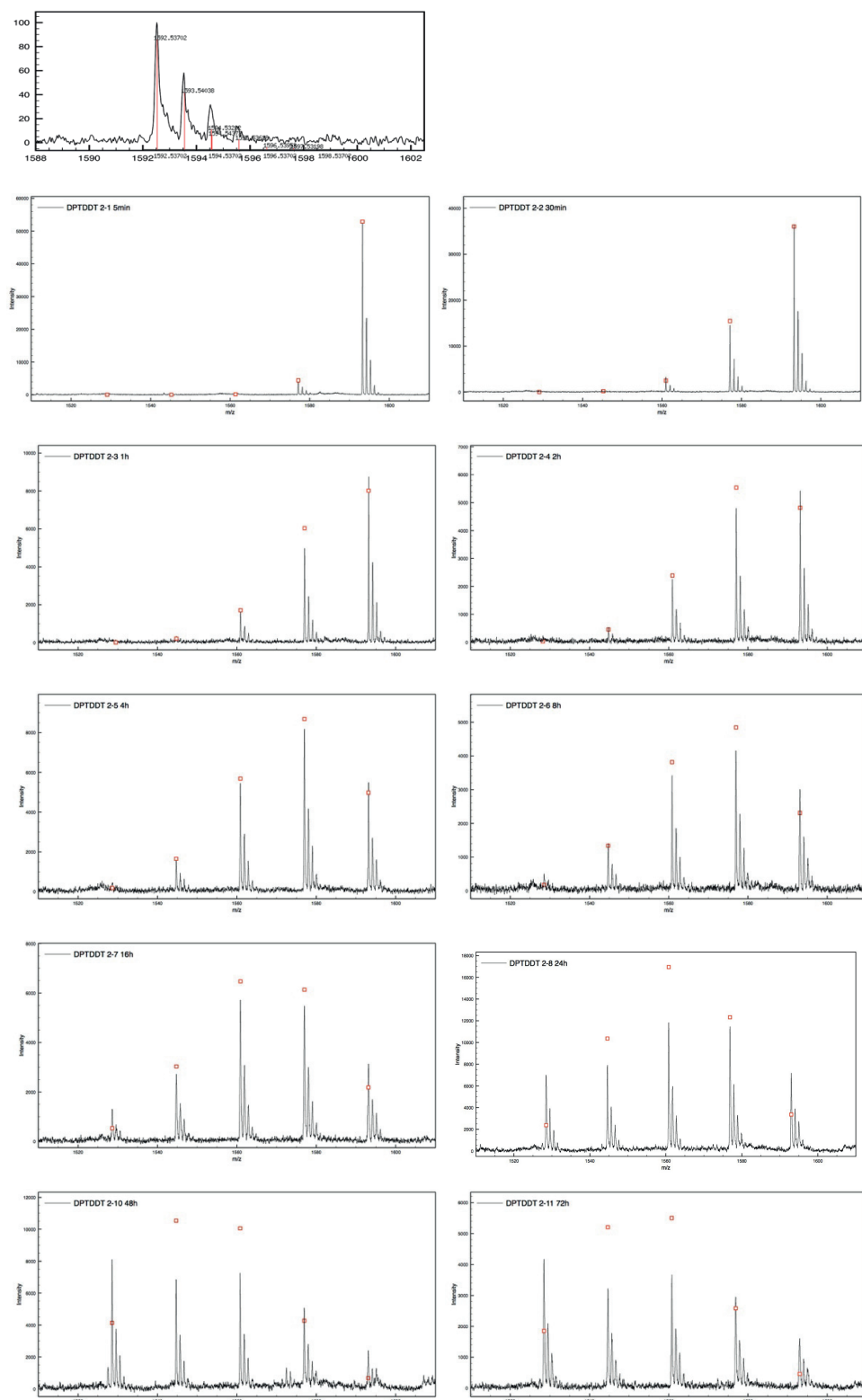


Figure 6.9 up: Experimental mass spectra compared to theoretical monoisotopic mass. The mass errors are 12 ppm. below: MALDI-TOF spectra of 50 folds' BPT ligand exchange to DDT gold nanoparticles. Red dots indicate binomial distribution at each ligand ratios. From left to the right, the five peaks are assigned to be Au₄BPT₄, Au₄DDT₁BPT₃, Au₄DDT₂BPT₂, Au₄DDT₃BPT₁, Au₄DDT₄ respectively.

Table 6.1 BPT coverage and SSR evolution with the increase of time.

Reaction time (h)	10 eq BPT		50 eq BPT	
	BPT coverage	SSR	BPT coverage	SSR
0.083	8.8%	0.0052	17.7%	0.0002
0.5	17.7%	0.0114	18.2%	0.0012
1	20.0%	0.0161	23.2%	0.0097
2	23.1%	0.0173	26.6%	0.0086
4	27.9%	0.0262	32.5%	0.0095
8	31.9%	0.0331	46.5%	0.0098
16	34.2%	0.0311	51.5%	0.0120
24	34.9%	0.0491	51.4%	0.0107
48	36.3%	0.0364	52.3%	0.0170
72	37.0%	0.0830	54.6%	0.0194

Fitting of the LER data to the second order diffusion limited Langmuir model⁹⁷:

$$\Theta(t) = \frac{Ak\sqrt{t}}{1 + k\sqrt{t}} \quad (6.1)$$

Table 6.2 Fitting parameters of Langmuir model.

Parameters	10 eq BPT	50 eq BPT	50 eq BT
A	0.423	0.675	1.053
K	0.947	0.581	0.391

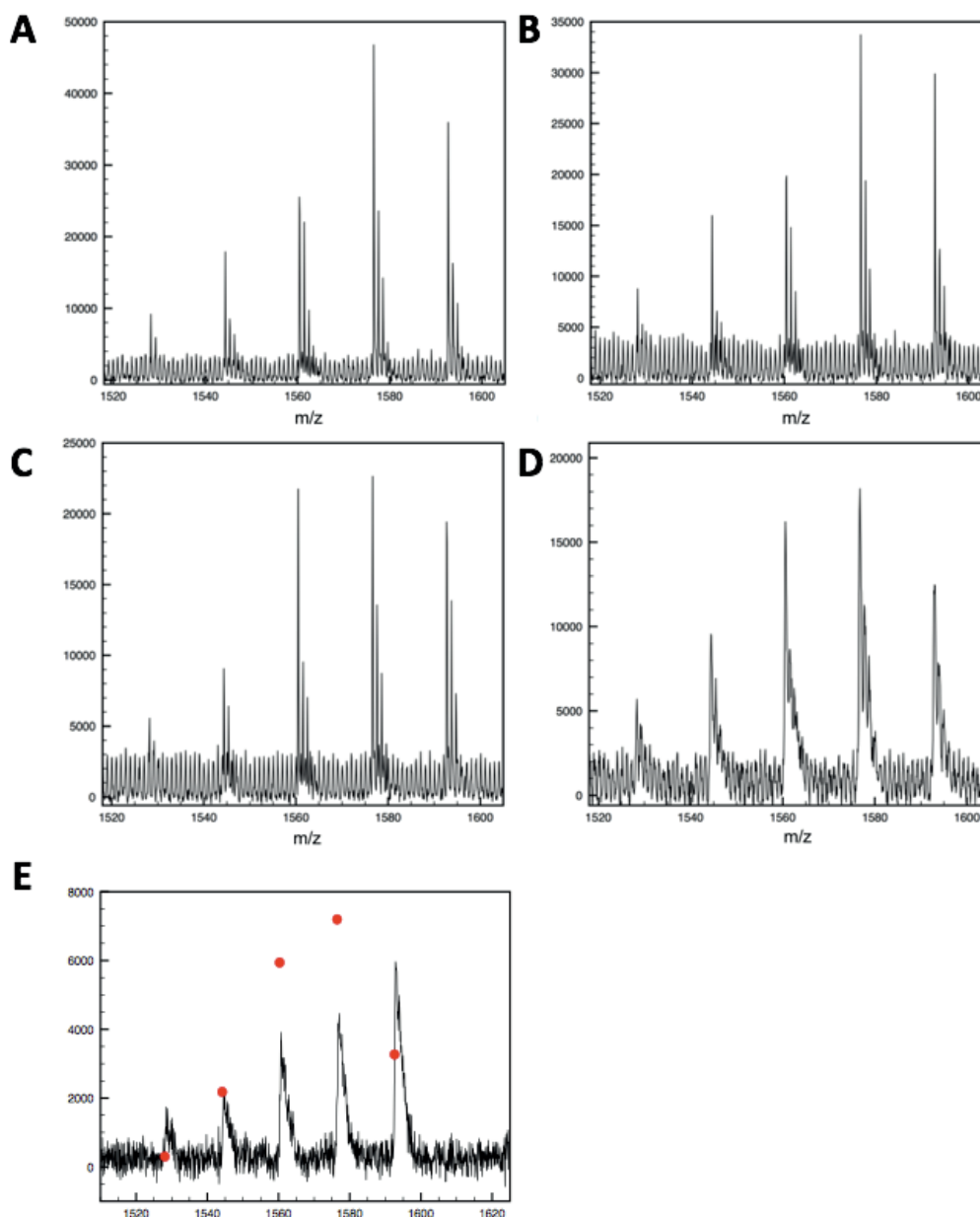


Figure 6.10. MALDI data of BPT-DDT nanoparticles after washing at 8 hours. From left to the right, the five peaks are assigned to be Au_4BPT_4 , $\text{Au}_4\text{DDT}_1\text{BPT}_3$, $\text{Au}_4\text{DDT}_2\text{BPT}_2$, $\text{Au}_4\text{DDT}_3\text{BPT}_1$, Au_4DDT_4 respectively. a) BPT-DDT nanoparticles after 12 hours LER time. b) BPT-DDT nanoparticles after 24 hours LER time. c) BPT-DDT nanoparticles after 48 hours LER time. d) BPT-DDT nanoparticles after 72 hours LER time. e) Clean BPT-DDT nanoparticles after annealed at 70 °C for 4 hours.

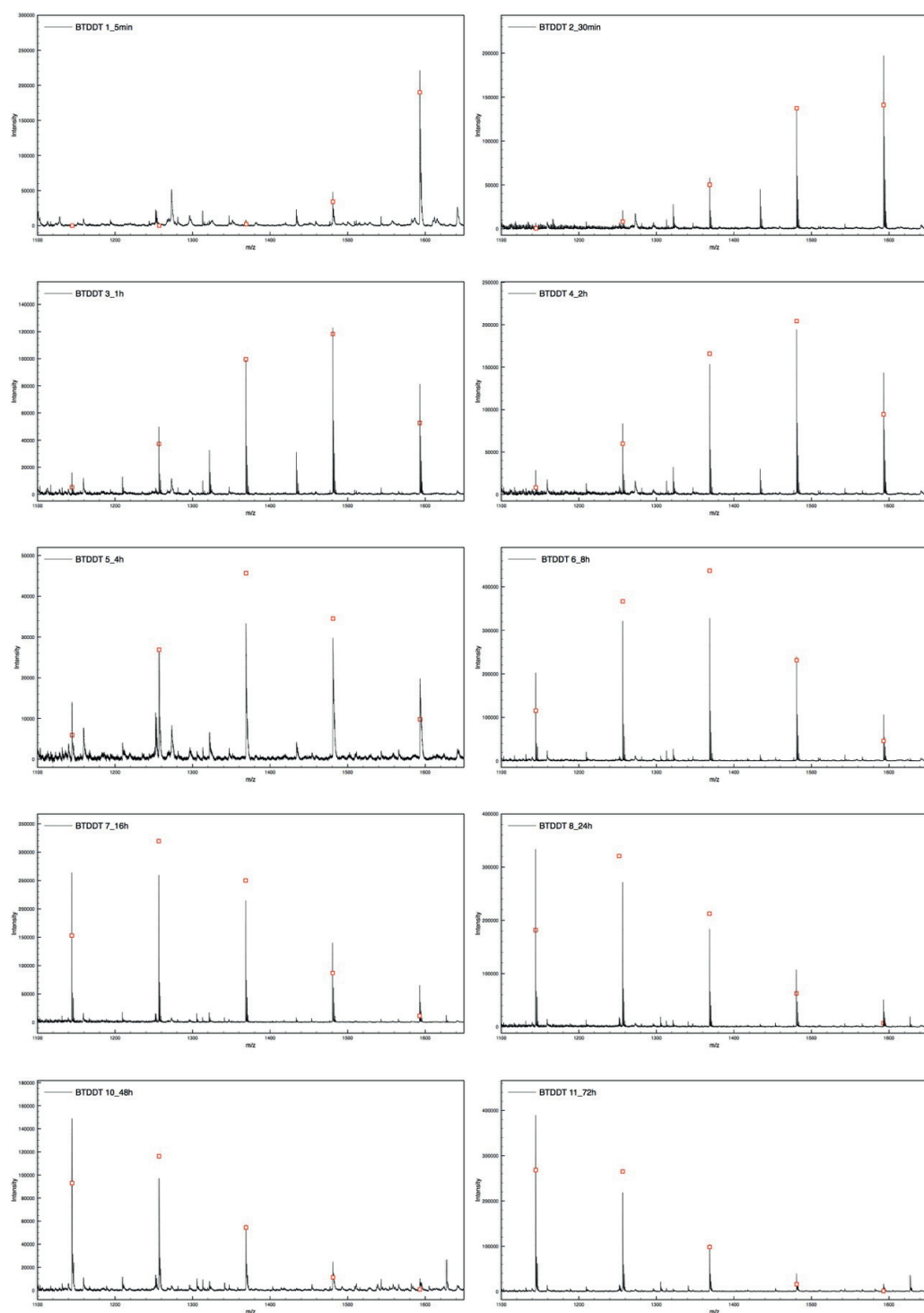


Figure 6.11. MALDI-TOF spectra of 50 folds' BT ligand exchange to DDT gold nanoparticles. Red dots indicate binomial distribution at each ligand ratios. From left to the right, the five peaks are assigned to be Au_4BT_4 , $\text{Au}_4\text{DDT}_1\text{BT}_3$, $\text{Au}_4\text{DDT}_2\text{BT}_2$, $\text{Au}_4\text{DDT}_3\text{BT}_1$, Au_4DDT_4 respectively.

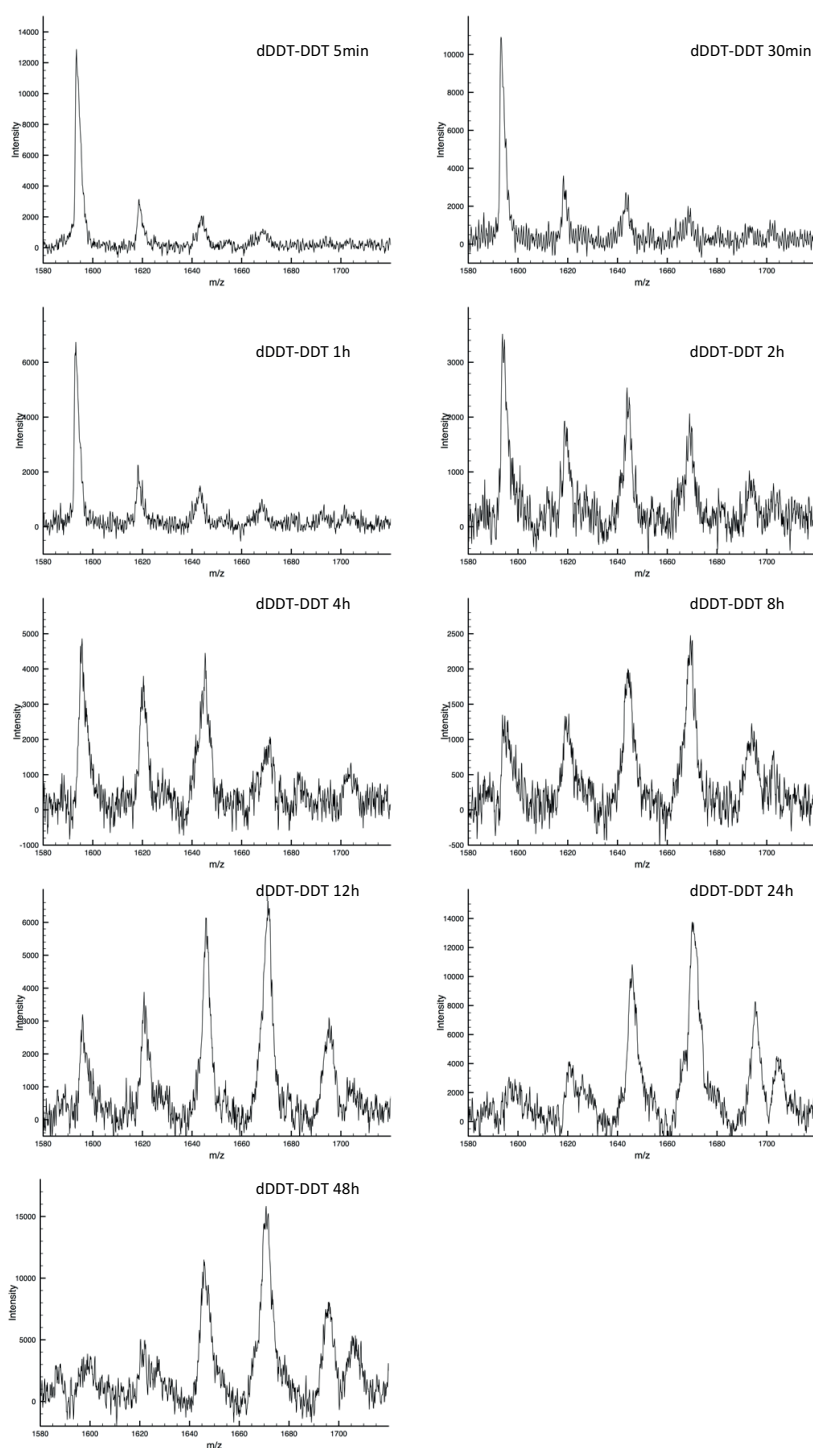


Figure 6.12. MALDI-TOF spectra of 1.5 folds' dDDT ligand exchange to DDT gold nanoparticles. From left to the right, the five peaks are assigned to be Au_4dDDT_4 , $\text{Au}_4\text{DDT}_1\text{dDDT}_3$, $\text{Au}_4\text{DDT}_2\text{dDDT}_2$, $\text{Au}_4\text{DDT}_3\text{dDDT}_1$, Au_4DDT_4 respectively. The measurements were performed in linear mode of the instrument which leads to the lower resolution here.

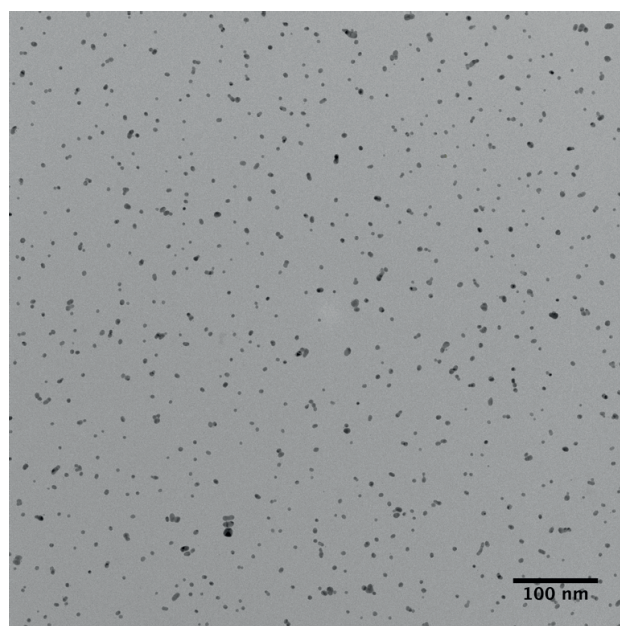


Figure 6.13. TEM data of DDT nanoparticles used for ligand exchange reaction in this work.

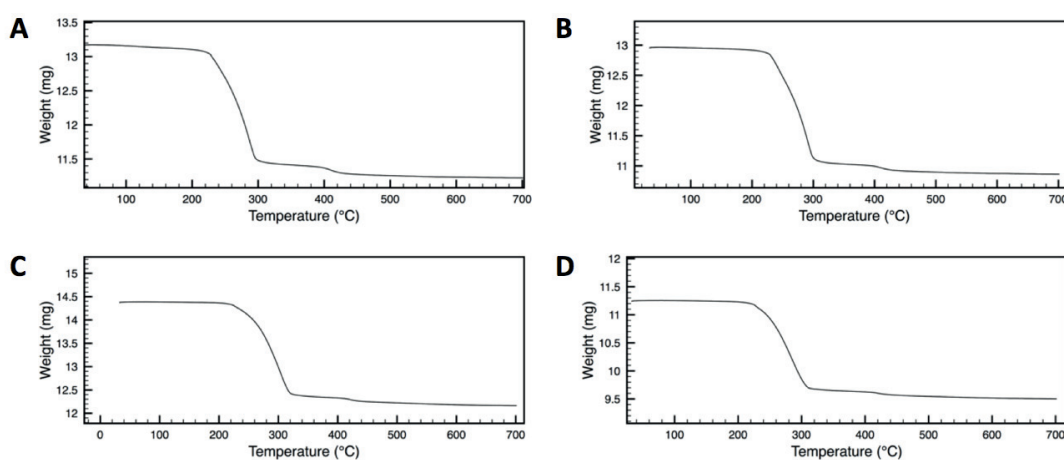


Figure 6.14. TGA data on BPT-DDT nanoparticles at different reaction stages. a) DDT nanoparticle before ligand exchange. b) BPT-DDT nanoparticle after 8 hours LER. c) BPT-DDT nanoparticle after 24 hours LER. d) BPT-DDT nanoparticle after 72 hours LER. The ligand density remained same during the LER being around 90%.

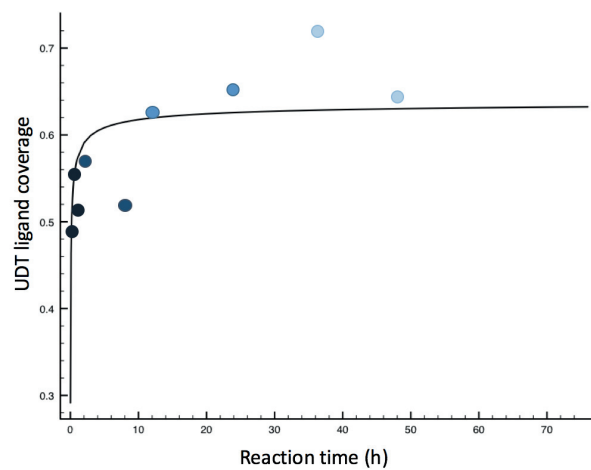


Figure 6.15. Evolution of UDT ligand coverage and mixed ligand morphology with time. The colour of each dot indicates the degree of phase separation with color scale of SSR listed on the right side.

Chapter 7 Structure of interfacial water at nanoscale heterogeneous surfaces

This chapter represents a major advance in the wetting phenomena at nanoscale. The contribution of morphology to the interfacial energy and water structure is separately demonstrated for the first time, without the convolution of chemical composition.

Disclosure: *The work in this chapter is in preparation for a manuscript to be submitted*

Every folded protein presents an interface with water that is composed of domains of varying hydrophobicity. The current understanding is that domains contribute to wetting additively. Yet, a number of recent simulations and experiments on patchy surfaces of varying hydrophobicity have clearly pointed towards a non-additive effect of chemical groups on work of adhesion, hydrophobic forces, and other interfacial properties. Most likely, the time averaged water structure at these interfaces is what determines such non-additivity. Here, the first experimental exploration on how the organization of hydrophobic and hydrophilic patches affects the structure of the interfacial water is presented. As model compounds, surfaces made of NPs identical in core size, ligand shell composition and density are used. Through a thermal treatment, two types of such NPs differing only in the ligand shell organization were produced. The pre-treated particles had patches of ~ 2.1 nm, while the post-treated had patches of ~ 1.3 nm. Sum Frequency Generation measurements of the interfacial water show distinctively different spectral features. An interpretation of the spectra based on previous literature and molecular dynamics simulations is given, indicating that the H-bonding structure at the interface is controlled by the patchiness of the original surface. These results point to the local (*i.e.* structural) nature of the concept of hydrophobicity and will have great consequences in our understanding of the wetting of proteins.

7.1 Introduction to the non-additivity of interfacial energy

A number of protein properties, such as folding, ligand binding and hydration, have been postulated to be dependent, at least in part, to the time averaged structure of interfacial water (TASIW)²⁰⁴. A hypothesis is that the interfacial patches of proteins constrains the TASIW to specific structures, that in turn plays a key role in the intermolecular interactions of proteins^{205,206}. Although a number of simulations seems to support these ideas, a direct evidence for such statements is missing. The spatial and temporal complexity of the protein/water interface has not allowed for a key experiment to be performed yet. On the other hand, classical thermodynamic treatments for multicomponent interfaces would exclude such effects, as work of adhesion (W_{SL} , the main component in interfacial energy) is supposed to be additive and consequently the TASIW should be solely dependent on the solid surface composition. A mounting number of evidences have been produced to support a non-additive nature of interfacial energy^{7,21,152,207}. First there has been extensive computational studies suggesting strong effects of patchiness on the density of interfacial water. Recent papers have evidenced proximal effects when hydrophobic and hydrophilic patches coexist on surfaces. Abbott showed structural and chemical effects on hydrophobic forces²⁰⁷, while Aida showed local effects on ion pairing¹⁵². Some of us²¹, demonstrated that the geometrical arrangement of hydrophobic and hydrophilic patches can determine as much as $\sim 25\%$ of the total W_{SL} . It is highly likely that the TASIW is the common cause for the non-additivity of all of the properties described above. Probably it plays a role also in determining some of observed non-additivity in colloidal properties.

In all the experimental cases discussed above, model surfaces have been used, since proteins remain too hard to study. A common approach is the use of self-assembled monolayers (SAMs) composed of hydrophobic and hydrophilic patches, which resemble the surfaces of proteins. Probing the TASIW on such surfaces is still a significant challenge, as one cannot compare surfaces of different compositions. At present, it is impossible to decouple effects due to composition from effects due to local structure. Hence, there is no experimental evidence on the role of patchiness on TASIW. Here, the model compounds, i.e. gold nanoparticles (NPs) coated with SAMs composed of a binary mixture of hydrophobic/hydrophilic ligands that separate into patches are used thanks to the studies of the previous chapters. The synthesis produces nanoparticles with patches of ~ 2.1 nm characteristic length scale. After thermal treatment, these patches reduced to ~ 1.3 nm in length scale, with all the other chemical and structural parameters of the NPs remaining the

same. The size of the patches leads to a difference of ~ 15 mN/m in W_{SL} , strongly proving the non-additivity of such property. Importantly we show here, through Sum Frequency Generation (SFG) measurements, that the water structure is drastically affected by the patchiness with very different peaks in the H-bonding region.

The concept of hydrophobicity is associated with that of W_{SL} , as one of the most common ways of quantifying hydrophobicity is to measure contact angle, as demonstrated in Figure 7.1. It is accepted that W_{SL} is strongly related to the nature of interfacial water. Hydrophobicity is also related to water structure, as hydrophobic interactions are associated with entropic phenomena that stem from extended H-bonding network. Hence hydrophobicity, W_{SL} , and water structure are all closely related to each other. As a consequence, by demonstrating that TASIW (as well as the W_{SL}) depends on the local structure of patchy surfaces we also show that hydrophobicity is a local concept.

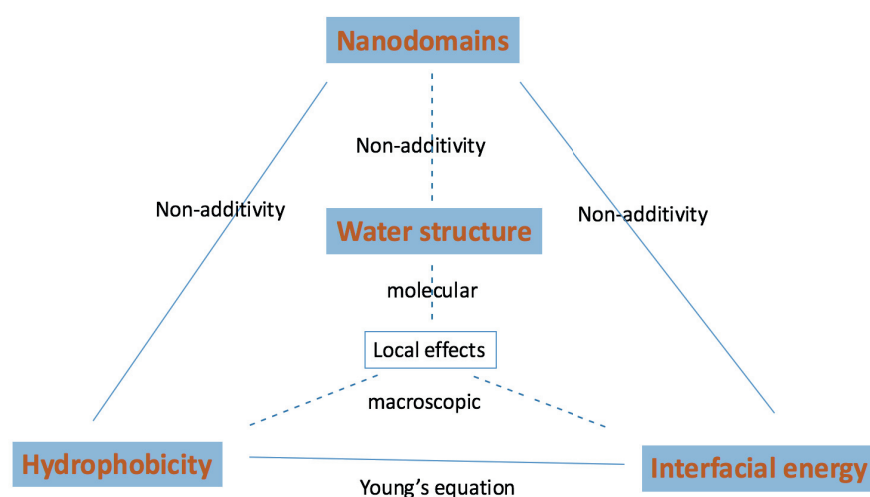


Figure 7.1 Demonstration of the non-additivity of hydrophobicity, interfacial energy and water structure to the nanoscale domain structures.

7.2 Model patchy nanoparticles

Gold NPs coated with a binary mixture of 3-mercaptopropionic acid (MPA) and 1-octanethiol (OT) are used as the model. These NPs were chosen as they form patchy ligand shells, due to the fact that MPA is hydrophilic and OT hydrophobic, and that the longer OT gains conformational entropy at the edges of the patches. Also, they are expected to have non-additive W_{SL} as they have non-monotonic solubility in various solvents. Similar patchy NPs

have shown ligand shell morphologies that are practically frozen at room temperature, but could be changed by gentle heating⁶⁸. The MPA ligand is exchanged to monodisperse OT gold NPs at room temperature. The resulting NPs were then heated at 70 °C for 4 h, in order to bring the ligand shell morphology to a different thermodynamic state. All the detailed synthesis and characterization procedures are described in method section.

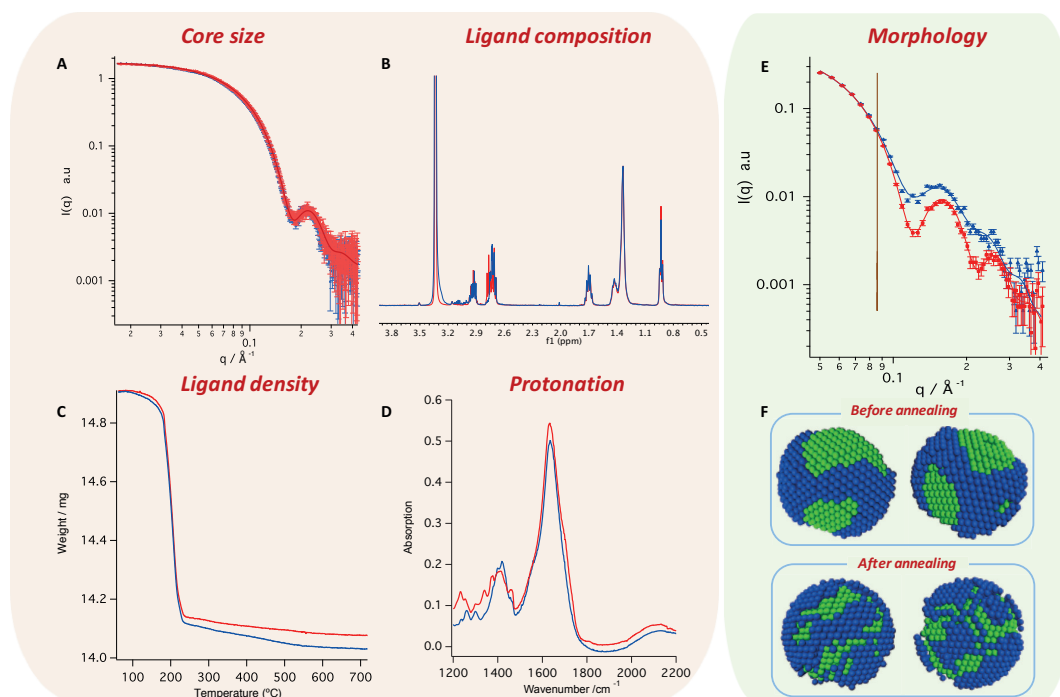


Figure 7.2 Characterization of gold NPs. (A) SAXS data on both NPs give a core size of 4.9 ± 0.6 nm. (B) The measured ligand ratio from NMR is MPA: OT = 0.95: 1 for both NPs. (C) TGA results show that the ligand density is unaffected by the thermal treatment. (D) FTIR measurements show that MPA ligands are mainly deprotonated on both NPs. A morphological characterization of the ligand shell has been performed using SANS (E). The overlap in the low q region (below 0.083 \AA^{-1} corresponding to the overall size of the NP in real space, as indicated by the vertical line) confirms that the two NPs have the same radius of gyration. The scattering curves at higher q range for the thermally treated NP show that the shape is more symmetric compared to the untreated NPs. By fitting SANS spectra, we obtained the models presented in (F) that show a clear difference on the size of the domains. Detailed fitting procedures are described in SM. In the SANS model, the blue beads stand for OT ligands while the green ones are MPA ligands. In all plots the blue and red lines refer to NPs before and after thermal treatment respectively.

After thermal-treatment, care was taken to ensure that no changes had happened to the NPs and that only the ligand shell morphology had changed. First, we performed small angle X-ray scattering (SAXS) on the NPs to make sure that core size and polydispersity of the gold core had not changed. In Figure 7.2A, the SAXS curves for the two NPs are shown, the remarkable degree of overlap between the curves proves that the gold core was not affected by the thermal treatment. We then compared the NMR of the ligand shells after etching of the gold core. As shown in Figure 7.2B, no changes in the average composition of ligand shells could be found. We then performed thermogravimetric analysis (TGA) to ensure that ligand desorption had not occurred. In Figure 7.2C, we show that the changes in the ligand density are within the errors of the measurement (the difference in the plateau is $< 2\%$). Finally, Fourier transform infrared spectroscopy (FTIR) measurements confirmed that the protonation state of the carboxylic acid had not changed.

As opposed to all other measurements performed to characterize the NPs before and after heating, small angle neutron scattering (SANS) leads to significantly different scattering curves (Figure 7.2E), showing substantial changes in the scattering form factors for the two NPs. Such changes in form factors, given all the other measurements described above, can be assigned solely to differences in shape (i.e. ligand shell morphology) for the NPs. We were able to determine the morphology of the patches using SANS combined with *ab initio* calculations as described in reference. Detailed fitting procedures could be found in SM. The resulting models are shown in Figure 7.2F. By quantifying the characteristic length-scales of the patches from SANS model, we find thicker patches of 2.1 ± 0.6 nm and thinner patches of 1.3 ± 0.3 nm for the NPs before and after thermal treatment. Both morphologies do not evolve at room temperature and that the morphological evolution is driven by the gain in conformation entropy of the OT ligands. Hence for the thin patchy morphology one would expect a higher gauche to trans ratio for the ligands compared to the one with thick patches. Indeed, the difference in the ligand shell ordering is also confirmed by SFG spectra at C-H region, as shown in method section. In summary, two NPs with the same core size and ligand shell composition, but only different in the morphology of ligand domains have been successfully synthesized.

7.3 Structure of interfacial water surrounding the patchy surfaces

SFG measurements are then adopted to investigate the TASIW. Deuterated water (D_2O) was used as the SFG set-up available to us does not reach the region for H_2O signal. Also, the use of D_2O allowed less concerns about residual water traces in the ligand shell of the NPs. The SFG results are shown in Figure 7.3B. The spectra have two broad band features: a peak at $\sim 2375\text{ cm}^{-1}$ and a peak at $\sim 2530\text{ cm}^{-1}$. The former one corresponds to OD with higher D-bond strength than the latter one, i.e. water molecules that are more strongly D-bonded. Water molecules at the interface with the two NPs experience different intermolecular D-bond environments. In the case of water at the interface with thick patches, the 2530 cm^{-1} band is mostly a shoulder of the 2375 cm^{-1} band. For the case of the thin patches, the 2530 cm^{-1} band has almost the same intensity as the 2375 cm^{-1} band. Multiple spectra were recorded on different films. Additional representative spectra are shown in method section. The general conclusion is that in the case of thin patches the ratio of the 2530 cm^{-1} band to the 2375 cm^{-1} band is larger than that for the thick patches. A simplistic interpretation of these data is that water molecules are less structured near the thin patches than near the thick patches.

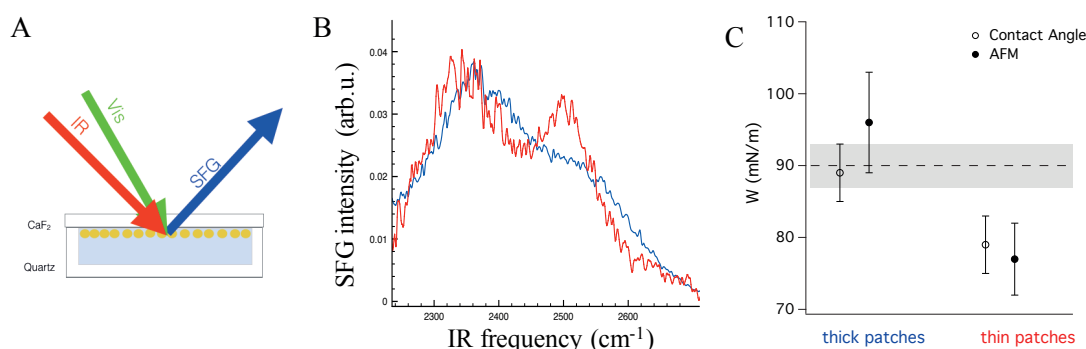


Figure 7.3 Characterization of the water structures around the NPs. (A) Schematic of the SFG setup. Detailed procedures and parameters are described in SM. (B) SFG spectra collected at the NPs-water interface. The D-bond network has significantly higher fraction of weak bonds for NPs with thin patches. (C) Measurements of the W_{SL} from both contact angle and AFM confirm that the NPs with thin patches are more hydrophobic.

The effect of such differences on W_{SL} is further examined. First, contact angles are measured for films of the two NPs and derived the W_{SL} , as listed in Table 7.1. In Figure 7.3C, the W_{SL} for the NPs having thick patches is close to the average of the W_{SL} of the two homoligand NPs, while a significant deviation is found for the NPs with thin patches. To further confirm these data, a recently developed technique based on small amplitude modulation atomic force

microscopy (AFM) is used to measure the W_{SL} . Also in this case a significant difference between the two samples (Figure 7.3C) is found. It should be stressed that this latter technique is based on different working principles than contact angle measurements, hence it strongly confirms the previous data. Furthermore, this technique measures W_{SL} on single NPs and hence is insensitive to film structure. Averaging the results from the two independent techniques we can conclude that the difference between the W_{SL} on the two NPs is 15 ± 7 mN/m, the NPs with thin patches being more hydrophobic.

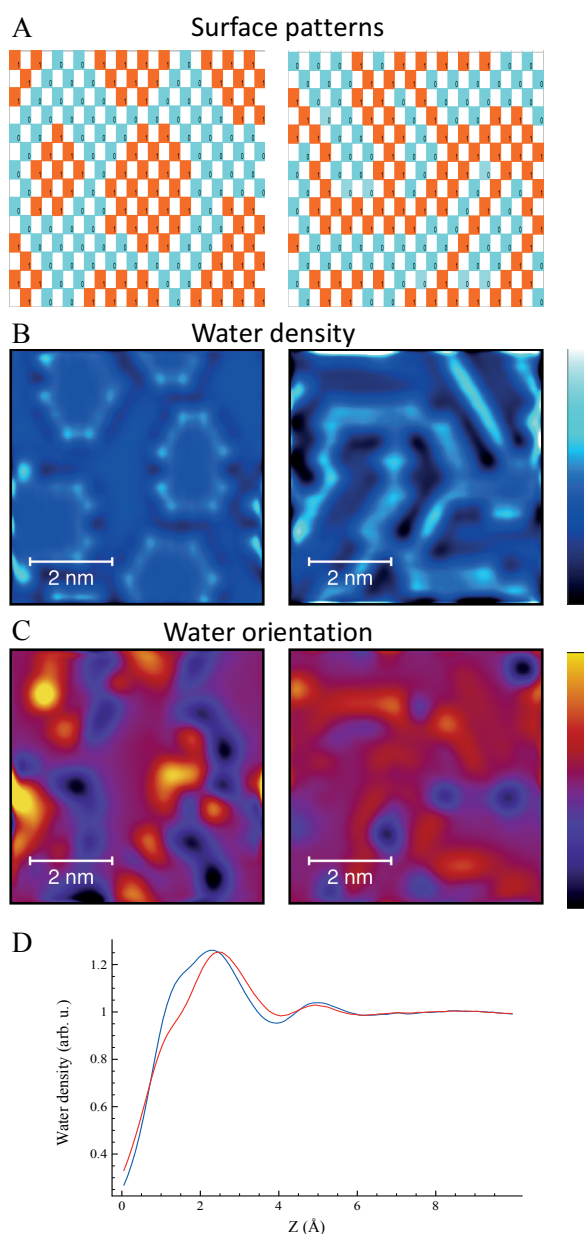


Figure 7.4 MD Simulations results. (A) The geometry of the simulated surfaces. Red and blue dots mark the positions of MPA and OT ligands respectively. (B) Water density in the first nanometer near the surface. Higher contrast is visible on the surface with thin patches, which

means that the fluctuation of water density is higher. (C) Orientation of water molecules near the surfaces. Water molecules have higher fraction orienting towards the surface for thick patchy morphology. (D) Profile of the water density perpendicular to the surface.

7.4 Molecular interpretation of the non-additivity

The conclusion from the measurements described above is that the patchiness on the NPs determines the TASIW and consequently the W_{SL} . To further understand this phenomenon, atomistic simulations are performed on flat surfaces, on which mixed ligands were placed in patchy morphologies closely resembling the ones that were found on the NPs, as shown in Figure 7.4A. As shown in Figure 7.4D, the profiles of the water density perpendicular to the surfaces are found to be different for the two NPs. The first coordination layer of water is closer to the surfaces with thick patches. An integration over the first 0.6 nm of water (where the water density is that of the bulk) leads to a 3% difference between the two NPs. This is in good agreement with the experiments as it finds a difference between the two surfaces. Since higher density is associated with hydrophilicity, the simulations find the surface with thick patches to be more hydrophilic, as experiments do.

Results from the simulations were then analyzed to better understand the TASIW that form at these interfaces. Figure 7.4C shows the time averaged angular distributions of the water dipoles at the interfaces. It is obvious that the two surfaces lead to drastically different angular distributions. The surface with thick patches favors a higher fraction of dipoles perpendicular to the interfaces, while the surface with thin patches leads to a distribution of dipoles mostly parallel to the interface. The latter distribution should lead to a better and more extended H-bonding network than the former, in good agreement with the SFG data.

In conclusion, it is shown here that the W_{SL} of a water/patchy surface is non-additive, and that the TASIW is dependent on the surface patchiness. This work proves that for multiple components surfaces, concepts such as hydrophobicity cannot be assumed to be absolute and they critically depend on the surroundings and the overall structures. Hence, when analyzing a folded protein one would need to carefully consider the folding structure before reaching conclusions on the water wetting of specific residues. This is in good agreement with the finding that the hydrophilicity of amino acid residues on proteins is remarkably different from the one of free molecules.

7.5 Materials and Methods

➤ Chemicals

Chloro(triphenylphosphine)gold(I) ($\geq 99.9\%$ trace metals basis, Aldrich), 1-Octanethiol ($\geq 98.5\%$, Aldrich), 3-Mercaptopropionic acid (HPLC, $\geq 99.0\%$, Aldrich), 3-Mercaptopropionic-2,2,3,3-d₄ Acid (98 atom % D, C/D/N Isotopes Inc.), borane t-butylamine complex (97%, Aldrich), Acetone (HPLC, $\geq 99.8\%$, Aldrich), Methanol (HPLC, $\geq 99.9\%$, Aldrich), Ethanol (HPLC, $\geq 99.8\%$, Aldrich), Chloroform (HPLC, $\geq 99.9\%$, Aldrich), Toluene (HPLC, 99.8%, Aldrich), Sulfuric acid (98.0%, Aldrich), (3-Mercaptopropyl)trimethoxysilane (95%, Aldrich), Hexane (99%, Aldrich), Iodine ($\geq 99.99\%$ trace metals basis, Aldrich), Tetrahydrofuran-d₈ (≥ 99.5 atom % D, Aldrich), Chloroform-d (99.8 atom % D, Aldrich), Methanol-d₄ (99.96 atom % D, Aldrich). All chemicals were used as received.

➤ Synthesis of 1-Octanethiol protected gold nanoparticles

The OT homo-ligand protected nanoparticles were synthesized following a modified protocol of Stucky and coworkers. 123 mg chloro(triphenylphosphine)gold(I) was dissolved in 40 ml 1:1 mixture of chloroform and toluene. 0.25 mmol OT ligand was added to the solution. The mixture was heated to 70 °C for 15 minutes. Then, 217 mg borane t-butylamine complex was added quickly into the solution under stirring. The color of the solution changed from brown to dark red. After 1 hour of reaction, 40 ml methanol was added to quench the reaction and the solution was cooled down to room temperature. Nanoparticles were precipitated as black powder and purified by repeated centrifugation using acetone and methanol. The final black precipitates (~40 mg) were dried under vacuum overnight.

➤ Synthesis of MPA-OT mixed ligand gold nanoparticles by ligand exchange reaction

40 mg OT homo-ligand protected nanoparticles were dissolved in 20 ml chloroform. 2.3 μ l MPA was added to the solution under vigorous stirring. After 6 hours of reaction at room temperature, 20 ml toluene was added to precipitate the nanoparticles. The precipitate was washed multiple times using chloroform and toluene, and then dried under vacuum overnight.

➤ Thermo-treatment of MPA-OT mixed ligand nanoparticles

20 mg MPA-OT nanoparticles was dissolved in 5 ml ethanol (containing 0.01% v/v sulfuric acid). The solution was heated at 70°C under stirring for 4 hours before cooled down to room temperature. Then the nanoparticles were precipitated by adding 30 ml hexane and washed using chloroform before dried under vacuum overnight.

➤ SANS

SANS measurements were conducted on the SANS-I instrument at Paul Scherrer Institute and further confirmed on KWS-2 instrument at Jülich Center for Neutron Science. For both measurements, a nanoparticle solution at a concentration of 10 mg/ml were used corresponding to a volume fraction of less than 0.1%. Measurements at SANS-1 were performed at 20 °C, using 1.5 m sample-to-detector distance, at 5 Å wavelength with a collimation setup of 6 m covering a q range from 0.03 Å⁻¹ to 0.5 Å⁻¹. Similarly, Measurements on KWS-2 were performed at 20 °C, using 1.7 m sample-to-detector distance, at 4.7 Å wavelength with a collimation setup of 8 m and a q range from 0.03 Å⁻¹ to 0.5 Å⁻¹. The data acquisition time was 2 hours for each sample. The two-dimensional scattering data were processed and reduced using BerSANS or QtiKWS software for the radial averaging, background subtraction, transmission correction, and normalization to the absolute scale.

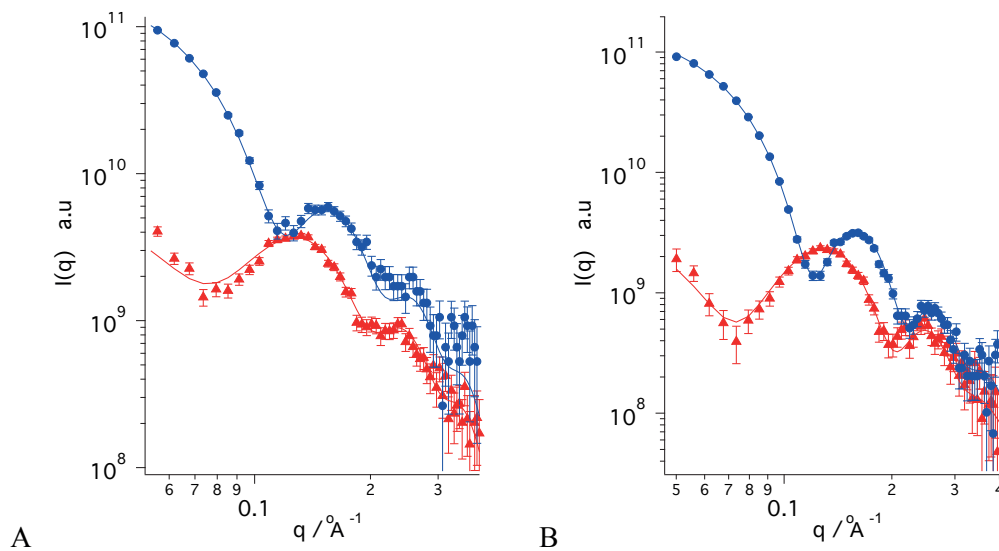


Figure 7.5 SANS data of nanoparticle before (A) and after (B) annealing. In both plots, the blue curve stands for measurements in deuterated tetrahydrofuran while the red curve are data measured in deuterated chloroform.

➤ Other measurements

SAXS measurements were performed using Rigaku BioSAXS 2000. The SAXS data were fitted using SasView software by a core-shell sphere model assuming Gaussian distribution. NMR spectra were recorded using Bruker 400MHz spectrometer. Deuterated methanol was used as the solvent. TGA measurements were done using TGA 4000 instrument from Perkin Elmer. Around 15 mg of nanoparticle samples were used. The glow of nitrogen gas is at 20.0 ml/min. The samples were heated from 50°C to 750°C, at 5.0 C/min. The 6700 Nicolet instrument from Thermo Fischer Scientific was used for measuring the IR spectra. Nanoparticle solution was drop-casted on the ATR crystal and dried completely. 512 spectra were taken at 2 cm⁻¹ resolution and averaged for each sample. Baseline correction was performed using the OMNIC software.

➤ Contact angle

Glass slides was first repeatedly cleaned using ethanol and acetone to remove surface contaminants. Then they are immersed with freshly prepared base solution for 1 hour and rinsed with deionized water thoroughly before dried under vacuum. Then 50 mM (3-Mercaptopropyl)trimethoxysilane acetone solution was used to immerse the slides for 4 hours in order to functionalize the surface. The glass surfaces were then rinsed multiple times with ethanol and deionized water. 0.5 ml of nanoparticle ethanol solution (0.1 mg/ml) was then evenly drop-casted onto the glass slides. The slides were then completely dried under vacuum before the contact angle measurements. Contact angle were measured using DataPhysics OCA 35 Instruments. More than 10 drops of 5 ul were deposited on different sites of the substrates.

Table 7.1 Contact angle measurements of the work of adhesion.

Sample	Contact Angle	Work of adhesion
Pre-heating Nanoparticle	76 ± 3 °	89 ± 4 mN/m
Post-heating Nanoparticle	85 ± 3 °	79 ± 4 mN/m
MPA Nanoparticle	38 ± 2 °	128 ± 1 mN/m
OT Nanoparticle	106 ± 5 °	52 ± 6 mN/m

➤ SFG

Vibrational SFS spectra were recorded using the setup for SFG experiments described in reference²⁰⁸. An 800 nm regeneratively amplified Ti:sapphire system (Spitfire Pro, Spectra physics) seeded with an 80MHz 800 nm oscillator (Integral 50, Femtolasers) was operated at a 1 kHz repetition rate to pump a commercial OPG/OPA/DPG system (HE-TOPAS-C, Light Conversion), which was used to generate infrared pulses. The visible beam was split off directly from the amplifier, and spectrally shaped with a home-built pulse shaper. The angle between the 10 mJ visible (VIS) beam (800 nm, FWHM 15 cm1) and the 6 mJ infrared beam (3–4.5 mm, FWHM 160 cm1) was 20 (as measured in air). The focused laser beams were overlapped in a sample cuvette with a path length of 0.2 mm. The reflected SF light was collimated using a plano-convex lens (f.15 mm, Thorlabs LA1540-B) and passed through two short-wave pass filters (3rd Millenium, 3RD770SP). The SF light was spectrally dispersed with a monochromator (Acton, SpectraPro 2300i) and detected with an intensified CCD camera (Princeton Instruments, PI-Max3) using a gate width of 10 ns. The acquisition time for a single spectrum was 150 s. A Glan-Taylor prism (Thorlabs, GT15-B), a half-wave plate (EKSMA, 460-4215) and a polarizing beam splitter cube (CVI, PBS-800-050) and two BaF2 wire grid polarizers (Thorlabs, WP25H-B) were used to control the polarization of the SFG, VIS and infrared beams, respectively. All measurements were performed in the SSP polarization combination. The optical path was closed in a box filled with nitrogen, in order to reduce scattering from air. The collection of the full spectra was achieved by overimposing multiple spectra collected shifting the wavelengths of the IR beam by 200 nm every time.

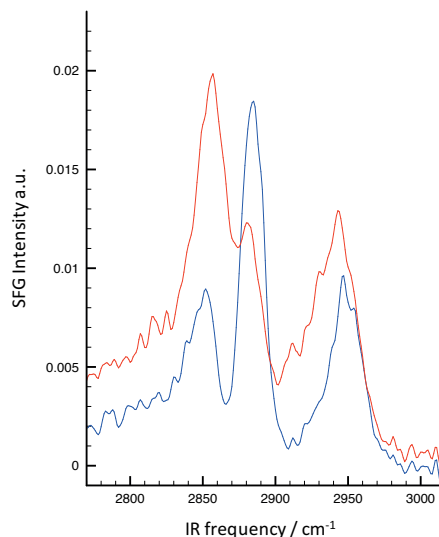


Figure 7.6 SFG spectra on the C-H regions of the nanoparticles before (blue) and after annealing (red).

➤ AFM

Atomic force microscopy images were collected in amplitude modulation mode on a commercial Cypher ES system (Asylum Research/Oxford Instruments, Santa Barbara, CA). The temperature was kept constant at 25 °C during all the measurements. The sensitivity of the cantilevers (Olympus RC800 PSA, lever number 1, Olympus, Tokyo, Japan) was evaluated from force curves and the spring constant was measured from their thermal spectra. The cantilevers were driven acoustically.

Chapter 8 Conclusions and perspectives

In this chapter, a summary and an outlook on the development of mixed ligand nanoparticle characterization techniques are discussed. Based on current status, the field would become mature and link the structures of mixed ligand nanoparticles with their applications in a closer way. Furthermore, how the field of patchy nanoparticles are protein surface science could learn from each other is discussed.

***Disclosure:** Part of the summary on microscopic techniques are included in the version of the article, "Characterization of Ligand Shell for Mixed-Ligand Coated Gold Nanoparticles." Ong Quy*, Zhi Luo*, and Francesco Stellacci. Accounts of chemical research 50, no. 8 (2017): 1911-1919.*

8.1 Summary on the current status of mixed ligand nanoparticle characterization

Currently, four major techniques have been developed for the characterization of mixed ligand nanoparticles, i.e. STM, NMR, SANS, MALDI. While they could all offer valuable insights on the self-assembled structures on nanoparticles, each technique focuses on different aspects. STM and NMR are the main two methods before this thesis. The first established technique, STM, was the main method for the direct imaging of the structural features of stripe-like nanoparticles. Thanks to the resolution of this technique, it is now routine to achieve images of ligand shells with molecular (or close to molecular) resolution. Adopting PSD in the analysis of STM images, it is possible to measure the thickness of stripe-like domains (semi-)quantitatively. There are still several limitations of STM. First the sample preparation for STM is already not trivial. A good quality film of nanoparticles is required which is often conducted by Langmuir-Blodgett method. One also has to make sure that the nanoparticles are free from organic ligands to avoid contamination of the tip. Moreover, while STM has been very successful in determining the structural features of stripe-like morphologies, it is still challenging to apply it on other complex morphologies such as Janus

and patchy. As only the top cone of the nanoparticles is imaged, it is impossible to get a complete picture of the nanoparticles. The other technique, NMR, offers accurate chemical information along with the structural features of patchy nanoparticles. ^1H NMR remains essential for many basic characterization of mixed ligand nanoparticles, such as the ligand shell composition and purity. In terms of determination of the ligand shell morphologies, current method is based on qualitative determination of whether the chemical shifts are additive with composition. Although it is a straightforward method, the data analysis method for NMR spectra still has plenty of room for improvement. Furthermore, currently NOESY is the only 2D NMR technique that has been applied for the structural determination, while there are a large variety of other types of multi-dimensional NMR techniques developed in structural biology. Exploration of other advanced NMR techniques as well as the development of advanced analytical methods are the obvious directions.

Two technique have been developed in this thesis, i.e. SANS and MALDI-TOF MS. The two methods have some similarities in the fact that both of them could generate 3D models for a direct visualization of the overall structure of nanoparticles through the utilization of Monte Carlo type calculations. Unlike microscopy, both method allow for the measurement over the bulk sample. With SANS, we prove that it is possible to extract characteristic length information from the 3D models. The unique ability of SANS in determining different types of morphologies with the high sensitivity (e.g. distinguishing two very similar structures of nanoparticles before and after annealing) has made it the most versatile technique for the characterization mixed ligand structures so far. However, the two main limitations of SANS are the requirement of high monodispersity of the nanoparticle sizes as well as the requirement of deuterated molecules. With the development of synthetic methods for nanoparticles and ligand molecules, it is promising that these two limitations could be mitigated.

On the other hand, MALDI-TOF-MS is very promising due to its simplicity and versatility on the type or properties (e.g. solubility and polydispersity) of the nanoparticle. Thanks to its advantages, the mechanisms of ligand exchange reaction of mixed ligand nanoparticles have been successfully unveiled. The degree of patchiness could be rapidly assessed with the calculation of SSR (sum square residual), for which a protocol has been built. The 3D models could also be built by fitting MALDI-TOF data using Monte Carlo calculations for silver nanoparticles. The method offers a quick way of estimating the organization of binary ligands and allows the comparison with SANS and computer simulations. The future of MALDI

based measurements could be in the high throughput screening of large amount of nanoparticle samples.

In general, microscopy techniques that have been developed (STM and AFM) or those under development (such as TEM) only characterize a few particles and have complex sample preparation and image interpretation requirements. Moreover, while the microscopy techniques are suitable for a detection of a morphology (e.g. stripe or Janus), they are weak in determining its absence. All microscopy techniques developed to date only produce 2D projections of the 3D object in study, which is another obvious limitation. On the contrary, spectroscopy techniques can be used to characterize the whole ensemble of particles in bulk which is their main advantage. However, presently they have two limitations. The first stems directly from their strength, that is, if an ensemble contains too large variations (in particle size, shape, ligand shell composition, and/or morphology) the resulting spectroscopy measurement will be difficult to interpret or lead to wrong conclusion; hence, uniform samples are required. Unfortunately, uniformity in ligand shell morphology is not simple to achieve if there is no measurement that can establish it. At present, it can only be inferred through property measurements. The second limitation of all the presented spectroscopy measurements is that the resulted data are often not direct as in microscopy, where one could visualize the structural features. Therefore, advanced data analysis techniques are of great importance.

8.2 Advanced data analysis methods

The major development of SANS and MALDI techniques presented in this thesis work benefits largely from the utilization of advanced data analysis techniques, such as simulated annealing and reverse Monte Carlo calculations. The same also goes for STM analysis, whose quantitative ability was greatly facilitated after the introduction of PSD analysis. It is not unusual that experimental data from certain techniques are not fully interpreted due to the lack of proper analytic methods. MALDI-TOF MS is one of the most obvious examples. In the earlier development of MALDI for the mixed ligand nanoparticle characterization, studies have been only using the SSR value as an indication of the phase separation. The full spectra were summarized into a single value, which naturally leads to oversimplification of the data analysis. Similar situation could now still be found for other techniques such as NMR and FTIR, where only a qualitative conclusion could be drawn based on the non-linear dependence of chemical shifts on composition. Many possibilities are available for a more

thorough analysis of the NMR and FTIR data. Especially for NMR, the demand for advanced data analysis and modelling methods would be in high demand when other NMR tools are explored. The same applies also to less studied techniques such as EPR and electrochemistry based techniques. Furthermore, when modelling experimental data such as SANS and MALDI-TOF MS, the fitting procedure could be also combined with molecular dynamic simulations in order to generate more precise structural information. For microscopic techniques, the requirements are slightly different since they have been established to offer high resolution information directly. One of the directions would be the tomography analysis, i.e. reconstruction of 3D structures from the 2D projected images, which would lead to a great advancement in the revealing detailed structures of the nanoparticles.

Another consideration is that very often the limitation of a technique is due to the lack of knowledge on the method itself. For example, the shift of peaks in NMR spectra is governed by complex factors such as surface heterogeneity, monolayer defects and ligand organization. Similarly, the formation mechanism of the Au₄L₄ fragment under MALDI process is unknown and hence one could not explain why some types of the nanoparticles don't yield good fragmentation in the mass spectra. A comprehensive and detailed data analysis might offer us insights into the mechanism of the techniques, which in turn could lead to a better understanding of the structure of the mixed ligand nanoparticles.

8.3 Integrative characterization

Although powerful, all the techniques mentioned above have certain limitations. For example, STM and other microscopic techniques lack statistics over the whole sample and the interpretation of images from complex morphologies is beyond current capabilities. Meanwhile, spectroscopic techniques such as MALDI-TOF and SANS could not deal with samples with very high polydispersity and extracting quantitative information is a tall order. Up till now, almost all the studies on patchy nanoparticles utilize only a single technique to assess the morphology of ligand shell. A comprehensive picture has not been drawn yet. If the advantages of the different techniques effectively could be joined effectively, not only could the quantitative patchy features be confirmed but different insights regarding the structures of the nanoparticles could be gained. Hence, in order to comprehensively characterize the morphology of patchy nanoparticles in the future, effective combinations of multiple techniques are of high importance. A full understanding of the sample could thus enable the control on fine structures of patchy nanoparticles and leading to the findings of novel

properties that we could not achieve before. Once a comprehensive characterization approach is established, several goals could then be achieved. For example, a phase diagram of the morphology of mixed ligand nanoparticles could be drawn. While theoretical studies have predicted the evolution of patchy morphologies with the change of ligand ratio and nanoparticle sizes, the experimental evidences still lack far behind. The joint application of multiple techniques could open such opportunity since different types of nanoparticles could all be assessed, which is practically impossible with only a single technique. The field would greatly progress since a full library of various patchy nano-structures will be available.

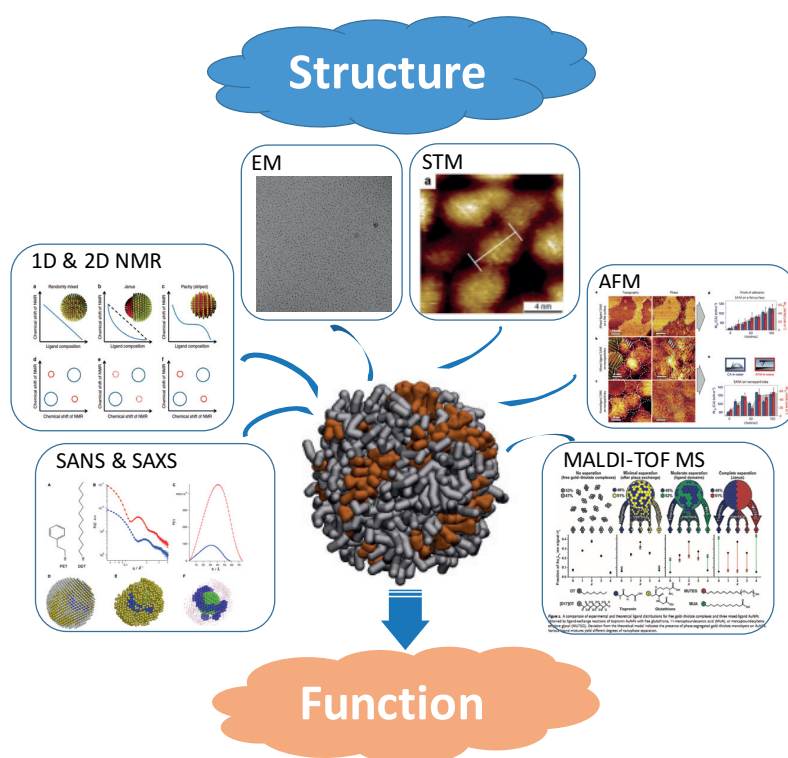


Figure 8.1 Integrative characterization of mixed ligand nanoparticles. A standardized characterization protocol might be established when different characterization techniques could be combined. Taking the advantages of each technique, mixed ligand nanoparticles with any types morphologies could be readily studied. In this way, a better link between the structure and function of mixed ligand nanoparticles could be established.

The availability of a complete characterization toolbox is a sign of maturity of the field, since it indicates that samples with any type of morphologies could be resolved. One of the outcome could be the establishment of a standardized characterization protocol from which researchers could choose the most suitable technique for each type of nanoparticles.

Intelligent processes that integrate all the existing approaches and automate the analysis procedures could also be expected to advance the field.

8.4 In situ characterization

All the current techniques do not cope well with the dynamics of the change of domain structure, i.e. in fact they have not yet been successfully used for following the change of the shell structure. The time scale of the ligand shell (re)organization has not been studied in depth. The information on the kinetics is relevant to the many topics such as the formation mechanism of the mixed ligand nanoparticles, how the ligand shell structure respond to environments and the stability of ligand shell protected nanoparticles in general. For example, although it is known for a long time that the thiols could diffuse on nanoparticles, the underlying mechanism is unclear, let alone the quantification on the kinetics such as diffusion barriers and mobility of different thiol molecules. Such mystery might be solved if one could combine MALDI-TOF or SANS with a technique that has high temporal accuracy. The 3D structures as well as quantification on the ligand compositions could be retrieved in real time. A thorough understanding of molecular diffusion on nanoparticle surfaces is invaluable for the design and fundamental theory developments of patchy nanoparticles. Similarly, future development would include the design of ‘smart’ nanoparticles or patchy nanoparticles that could adapt to different environments. In these cases, new challenges will be posted to the characterization at different time scales.

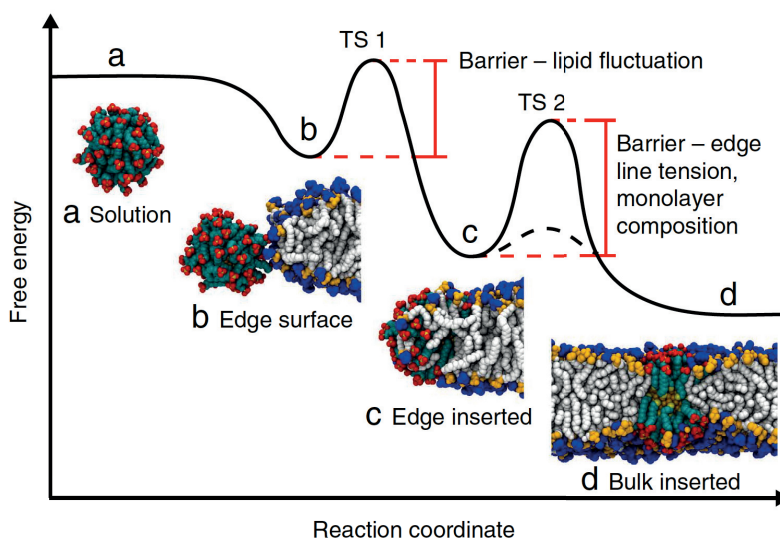


Figure 8.2 Structural changes of mixed ligand protected nanoparticles when interacting with lipid membranes. Images reproduced from reference⁸².

It is also of great importance to characterize NPs in situ/ in operando, for example, when NPs interact with other molecules biological entities or in a catalytic reaction. As shown in Figure 8.2, the conformation of the mixed ligand shell would undergo substantial changes when self-assembling with lipid bilayers. Such studies could link directly the structure of nanoparticles with their functions. In these cases, either new methods will have to be developed to selectively resolve NPs against the complex environment or an integrated approach utilizing multiple techniques are required.

8.5 Enriching the library of mixed self-assembled monolayer morphologies

In this thesis, two major methods, ligand exchange reaction and annealing, have been studied in depth on their detailed mechanism. The final purpose for such research is to find ways to control the morphologies in a more rational way. Further dedication of designing morphologies with unique structures would be of great benefits for the field. For example, if one could control the spatial distribution and domain sizes of a patchy type nanoparticle, then it could be used as a multi-valent nano-building block for construction of supramolecular hierarchical structures. The surface properties such as the interaction of nanoparticles with proteins could then also be fine controlled. For example, with defined ligand shell morphology, it could be possible to tune the protein corona formation around nanoparticles, which is one of the dreams of nanoparticle based drug delivery researches.

Prior to this work, computer simulations have predicted the formation of a variety of different morphologies for mixed ligand shells^{69,178}. Experimental studies lack far behind for the realization of such variety. For example, the phase diagram of the mixed self-assembled monolayers has not been reported yet. A full description of how ligand shell morphology evolves with temperature, ligand ratio, nanoparticle core size, ligand chain length mismatch as well as types of ligands would greatly advance our knowledge of this material.

Furthermore, self-assembled monolayers composed of ternary or even quaternary component have been studied by molecular dynamic simulations, Figure 8.3. The significance of such study is the possibility of achieving more complicated structures, which might be reach closer

resemblance of natural surfaces such as proteins. The library of functional nanoparticle will be expanded to another dimension if this could be realized experimentally. Preliminary results seem to be promising as it has been shown in the thesis one type of ternary ligand shell structure by SANS.

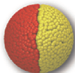

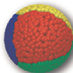

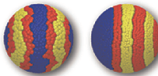
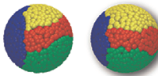

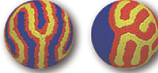
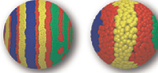

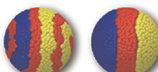
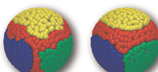
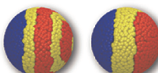

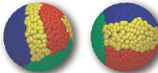
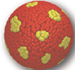
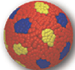

	Binary	Ternary	Quaternary		
Small NP radius					
Base Case					
Large NP radius					
1 short surfactant					
2 short surfactants					
3 short surfactants					
Excess of short surfactant					

Figure 8.3 Predictions of the morphologies of multi-component mixed ligand shells. Image reproduced from reference¹⁷⁸.

8.6 Translating back to proteins and other systems

As described in Chapter 2, the initial inspiration of the thesis works comes from the observations on the structure of proteins. Mixed ligand nanoparticles are used for two purposes. First, they act as mimetics that could achieve unique functions by resembling the patchy surface structures of proteins. Secondly, they are also model systems that could help us better understand the surface phenomena of proteins. For example, we have shown in this thesis that the interfacial energy and the structure of hydration water surrounding patchy nanoparticles show the non-additive relationship with proteins. The geometry/ organization of the patches plays a key role in determining the interaction of proteins with water. While such conclusion is very hard to be drawn directly from proteins due to the intrinsic complexity of protein surfaces, it has great consequences on the understanding of the protein biophysics. For example, currently the routine estimation for the hydrophobicity of protein surfaces is through

the utilization of ‘hydrophobic scales’, which are defined depending on the measurement approaches such as partition coefficients or liquid chromatography. Such hydrophobic scales are not unified and sometimes could lead to deviated predictions. After the illustration of the local effects and non-additivity of the patchy surfaces, a modified ‘hydrophobic scale’ that takes into account the proximal effects might be developed. Another example might be for the understanding or design enzymes. Since the active center of the enzymes are very often polar residues that are surrounded by hydrophobic residues, the roles of water during catalytic reactions are vital and not well understood. The general principle that extracted from nanoparticle models could be translated back to such enzyme systems for a better understanding or the development of artificial enzymes.

Moreover, the established techniques could also be applied to the characterization of other types of materials. For example, many dendrimers that share similar complex surface structures have been reported. And growing interests have been seen on making nanoparticles with organic cores, including the single chain polymeric nanoparticles or nano-gels. Such materials have been utilized as drug carriers or catalytic surfaces, resembling the functions of mixed ligand nanoparticles. Other types materials include quantum dots, carbon nanoparticles and metal organic framework based nanoparticles. The methods explored in this thesis could become promising tools for the characterization of these new materials.

Bibliography

1. Verma, A. & Stellacci, F. Effect of surface properties on nanoparticle-cell interactions. *Small* **6**, 12–21 (2010).
2. Eustis, S. & El-Sayed, M. a. Why gold nanoparticles are more precious than pretty gold: noble metal surface plasmon resonance and its enhancement of the radiative and nonradiative properties of nanocrystals of different shapes. *Chem. Soc. Rev.* **35**, 209–217 (2006).
3. Jans, H. & Huo, Q. Gold nanoparticle-enabled biological and chemical detection and analysis. *Chem. Soc. Rev.* **41**, 2849–66 (2012).
4. Daniel, M.-C. & Astruc, D. Gold nanoparticles: assembly, supramolecular chemistry, quantum-size-related properties, and applications toward biology, catalysis, and nanotechnology. *Chem. Rev.* **104**, 293–346 (2004).
5. Love, J. C., Estroff, L. a, Kriebel, J. K., Nuzzo, R. G. & Whitesides, G. M. *Self-assembled monolayers of thiolates on metals as a form of nanotechnology. Chemical reviews* **105**, (2005).
6. Pengo, P. *et al.* Gold nanoparticles with patterned surface monolayers for nanomedicine: current perspectives. *European Biophysics Journal* 1–23 (2017). doi:10.1007/s00249-017-1250-6
7. Silvera Batista, C. A., Larson, R. G. & Kotov, N. A. Nonadditivity of nanoparticle interactions. *Science (80-.).* **350**, (2015).
8. Gooding, J. J., Mearns, F., Yang, W. & Liu, J. Self-Assembled Monolayers into the 21st Century: Recent Advances and Applications. *Electroanalysis* **15**, 81–96 (2003).
9. Neouze, M.-A. & Schubert, U. Surface Modification and Functionalization of Metal and Metal Oxide Nanoparticles by Organic Ligands. *Monatshefte für Chemie - Chem. Mon.* **139**, 183–195 (2008).
10. Schreiber, F. Self-assembled monolayers: From ‘simple’ model systems to biofunctionalized interfaces. *J. Phys. Condens. Matter* **16**, R881–R900 (2004).
11. Badia, A., Lennox, R. B. & Reven, L. A dynamic view of self-assembled monolayers. *Acc. Chem. Res.* **33**, 475–481 (2000).
12. Ostuni, E., Chapman, R. G., Holmlin, R. E., Takayama, S. & Whitesides, G. M. A survey of structure-property relationships of surfaces that resist the adsorption of protein. *Langmuir* **17**, 5605–5620 (2001).
13. Ghosh Chaudhuri, R. & Paria, S. Core/shell nanoparticles: Classes, properties, synthesis mechanisms, characterization, and applications. *Chemical Reviews* **112**, 2373–2433 (2012).
14. Huang, X., Jain, P. K., El-Sayed, I. H. & El-Sayed, M. A. Gold nanoparticles: interesting optical properties and recent applications in cancer diagnostics and therapy. *Nanomedicine* **2**, 681–693 (2007).
15. Kotov, N. a. & Stellacci, F. Frontiers in nanoparticle research: Toward greater

- complexity of structure and function of nanomaterials. *Advanced Materials* **20**, 4221–4222 (2008).
16. Jackson, A. M., Hu, Y., Silva, P. J. & Stellacci, F. From homoligand- to mixed-ligand-monolayer-protected metal nanoparticles: A scanning tunneling microscopy investigation. *J. Am. Chem. Soc.* **128**, 11135–11149 (2006).
 17. Ong, Q., Luo, Z. & Stellacci, F. Characterization of Ligand Shell for Mixed-Ligand Coated Gold Nanoparticles. *Acc. Chem. Res.* **50**, 1911–1919 (2017).
 18. Moyano, D. F. *et al.* Fabrication of corona-free nanoparticles with tunable hydrophobicity. *ACS Nano* **8**, 6748–6755 (2014).
 19. Lattuada, M. & Hatton, T. A. Synthesis, properties and applications of Janus nanoparticles. *Nano Today* **6**, 286–308 (2011).
 20. Nel, A. E. *et al.* Understanding biophysicochemical interactions at the nano-bio interface. *Nat. Mater.* **8**, 543–557 (2009).
 21. Kuna, J. J. *et al.* The effect of nanometre-scale structure on interfacial energy. *Nat. Mater.* **8**, 837–842 (2009).
 22. Mahmoudi, M. *et al.* Protein-nanoparticle interactions: Opportunities and challenges. *Chemical Reviews* **111**, 5610–5637 (2011).
 23. Geyer, T., Born, P. & Kraus, T. Switching between crystallization and amorphous agglomeration of alkyl thiol-coated gold nanoparticles. *Phys. Rev. Lett.* **109**, 1–5 (2012).
 24. Liu, X., Li, H., Jin, Q. & Ji, J. Surface tailoring of nanoparticles via mixed-charge monolayers and their biomedical applications. *Small* **10**, 4230–42 (2014).
 25. Yang, H. *et al.* Plasmonic twinned silver nanoparticles with molecular precision. *Nat. Commun.* **7**, 12809 (2016).
 26. Centrone, A. *et al.* The role of nanostructure in the wetting behavior of mixed-monolayer-protected metal nanoparticles. *Proc. Natl. Acad. Sci.* **105**, 9886–9891 (2008).
 27. Uzun, O. *et al.* Water-soluble amphiphilic gold nanoparticles with structured ligand shells. *Chem. Commun.* 196–198 (2007). doi:10.1039/b713143g
 28. Dahdal, Y. N. *et al.* Coated Citrate Capped Gold Nanoparticles Used as a Model Surface. *Langmuir* **30**, 15072–15082 (2014).
 29. Laaksonen, T., Ahonen, P., Johans, C. & Kontturi, K. Stability and electrostatics of mercaptoundecanoic acid-capped gold nanoparticles with varying counterion size. *ChemPhysChem* **7**, 2143–2149 (2006).
 30. De, M. *et al.* Synthetic ‘chaperones’: nanoparticle-mediated refolding of thermally denatured proteins. *Chem. Commun.* **46**, 3504 (2008).
 31. Jackson, A. M., Myerson, J. W. & Stellacci, F. Spontaneous assembly of subnanometre-ordered domains in the ligand shell of monolayer-protected nanoparticles. *Nat. Mater.* **3**, 330–336 (2004).

32. De, M. *et al.* Sensing of proteins in human serum using conjugates of nanoparticles and green fluorescent protein. *Nat. Chem.* **1**, 461–5 (2009).
33. Lesniak, A. *et al.* Effects of the presence or absence of a protein corona on silica nanoparticle uptake and impact on cells. *ACS Nano* **6**, 5845–5857 (2012).
34. Liu, X. *et al.* Enhanced Retention and Cellular Uptake of Nanoparticles in Tumors by Controlling Their Aggregation Behavior. 6244–6257 (2013).
35. Verma, A. *et al.* Surface-structure-regulated cell-membrane penetration by monolayer-protected nanoparticles. *Nat. Mater.* **7**, 588–95 (2008).
36. Güçlü, K., Ozyürek, M., Güngör, N., Baki, S. & Apak, R. Selective optical sensing of biothiols with Ellman's reagent: 5,5'-Dithio-bis(2-nitrobenzoic acid)-modified gold nanoparticles. *Anal. Chim. Acta* **794**, 90–8 (2013).
37. Xie, J., Zheng, Y. & Ying, J. Y. Highly selective and ultrasensitive detection of Hg(2+) based on fluorescence quenching of Au nanoclusters by Hg(2+)-Au(+) interactions. *Chem. Commun. (Camb)*. **46**, 961–3 (2010).
38. Boal, A. *et al.* Self-assembly of nanoparticles into structured spherical and network aggregates. *Nature* **404**, 746–8 (2000).
39. Devries, G. a *et al.* Divalent metal nanoparticles. *Science* **315**, 358–61 (2007).
40. Hermans, T. M. *et al.* Self-assembly of soft nanoparticles with tunable patchiness. *Nat. Nanotechnol.* **4**, 721–726 (2009).
41. De, M., Ghosh, P. S. & Rotello, V. M. Applications of Nanoparticles in Biology. *Adv. Mater.* **20**, 4225–4241 (2008).
42. Gupta, R. B. & Kompella, U. B. *Nanoparticle Technology for Drug Delivery*. **159**, (CRC Press, 2006).
43. Shi, Y., Goodisman, J. & Dabrowiak, J. C. Cyclodextrin capped gold nanoparticles as a delivery vehicle for a prodrug of cisplatin. *Inorg. Chem.* **52**, 9418–26 (2013).
44. Dufour, F., Fresch, B., Durupthy, O., Chaneac, C. & Remacle, F. Ligand and Solvation Effects on the Structural and Electronic Properties of Small Gold Clusters. *J. Phys. Chem. C* **118**, 4362–4376 (2014).
45. Goldmann, C. *et al.* Charge Transfer at Hybrid Interfaces: Plasmonics of Aromatic Thiol-Capped Gold Nanoparticles. *ACS Nano* **9**, 7572–7582 (2015).
46. Ghosh, A., Basak, S., Wunsch, B. H., Kumar, R. & Stellacci, F. Effect of composition on the catalytic properties of mixed-ligand-coated gold nanoparticles. *Angew. Chemie - Int. Ed.* **50**, 7900–7905 (2011).
47. Templeton, A. C., Wuelfing, W. P. & Murray, R. W. Monolayer-protected cluster molecules. *Acc. Chem. Res.* **33**, 27–36 (2000).
48. Templeton, A. C., Hostetler, M. J., Kraft, C. T. & Murray, R. W. Reactivity of Monolayer-Protected Gold Cluster Molecules: Steric Effects. *J. Am. Chem. Soc.* **120**, 1906–1911 (1998).
49. Bergen, J. M., Von Recum, H. A., Goodman, T. T., Massey, A. P. & Pun, S. H. Gold

- nanoparticles as a versatile platform for optimizing physicochemical parameters for targeted drug delivery. *Macromol. Biosci.* **6**, 506–516 (2006).
50. Cho, E. S. *et al.* Ultrasensitive detection of toxic cations through changes in the tunnelling current across films of striped nanoparticles. *Nat. Mater.* **11**, 978–85 (2012).
 51. Singh, C. *et al.* Entropy-mediated patterning of surfactant-coated nanoparticles and surfaces. *Phys. Rev. Lett.* **99**, 226106 (2007).
 52. Schreiber, F. Structure and growth of self-assembling monolayers. **65**, (2000).
 53. Biebuyck, H. A. & Whitesides, G. M. Interchange between monolayers on gold formed from unsymmetrical disulfides and solutions of thiols: evidence for sulfur-sulfur bond cleavage by gold metal. *Langmuir* **9**, 1766–1770 (1993).
 54. Aizenberg, J., Black, A. J. & Whitesides, G. M. Control of crystal nucleation by patterned self-assembled monolayers. *Nature* **398**, 495–498 (1999).
 55. Stranick, S. J., Parikh, A. N., Tao, Y.-T., Allara, D. L. & Weiss, P. S. Phase Separation of Mixed-Composition Self-Assembled Monolayers into Nanometer Scale Molecular Domains. *J. Phys. Chem.* **98**, 7636–7646 (1994).
 56. Ong, Q. K., Zhao, S., Reguera, J., Biscarini, F. & Stellacci, F. Comparative STM studies of mixed ligand monolayers on gold nanoparticles in air and in 1-phenyloctane. *Chem. Commun.* **50**, (2014).
 57. Liu, X., Yu, M., Kim, H., Mameli, M. & Stellacci, F. Determination of monolayer-protected gold nanoparticle ligand-shell morphology using NMR. *Nat. Commun.* **3**, 1–9 (2012).
 58. Ghorai, P. K. & Glotzer, S. C. Atomistic simulation study of striped phase separation in mixed-ligand self-assembled monolayer coated nanoparticles. *J. Phys. Chem. C* **114**, 19182–19187 (2010).
 59. Kim, H. *et al.* Synthesis and characterization of Janus gold nanoparticles. *Adv. Mater.* **24**, 3857–3863 (2012).
 60. Şologan, M. *et al.* Patchy and Janus Nanoparticles by Self-Organization of Mixtures of Fluorinated and Hydrogenated Alkanethiolates on the Surface of a Gold Core. *ACS Nano* **10**, 9316–9325 (2016).
 61. Posocco, P. *et al.* Self-organization of mixtures of fluorocarbon and hydrocarbon amphiphilic thiolates on the surface of gold nanoparticles. *ACS Nano* **6**, 7243–7253 (2012).
 62. Egorov, S. a. Microphase separation of mixed polymer brushes physisorbed on cylindrical surfaces. *Soft Matter* **8**, 3971 (2012).
 63. Merz, S. N. *et al.* Theoretical and Experimental Investigation of Microphase Separation in Mixed Thiol Monolayers on Silver Nanoparticles. *ACS Nano* **10**, 9871–9878 (2016).
 64. Ge, X., Ke, P. C., Davis, T. P. & Ding, F. A Thermodynamics Model for the Emergence of a Stripe-like Binary SAM on a Nanoparticle Surface. *Small* **11**, 4894–4899 (2015).
 65. Fetisov, E. O. & Siepmann, J. I. Structure and Phase Behavior of Mixed Self-

- Assembled Alkanethiolate Monolayers on Gold Nanoparticles: A Monte Carlo Study. *J. Phys. Chem. B* **120**, 1972–1978 (2016).
66. Verma, A. *et al.* Surface-structure-regulated cell-membrane penetration by monolayer-protected nanoparticles. *Nat. Mater.* **7**, 588–95 (2008).
 67. Ghorai, P. K. & Glotzer, S. C. Atomistic simulation study of striped phase separation in mixed-ligand self-assembled monolayer coated nanoparticles. *J. Phys. Chem. C* **114**, 19182–19187 (2010).
 68. Luo, Z., Hou, J., Menin, L., Ong, Q. K. & Stellacci, F. Evolution of the Ligand Shell Morphology during Ligand Exchange Reactions on Gold Nanoparticles. *Angew. Chemie Int. Ed.* (2017). doi:10.1002/anie.201708190
 69. Pons-Siepermann, I. C. & Glotzer, S. C. Design of patchy particles using ternary self-assembled monolayers. *Soft Matter* **8**, 6226 (2012).
 70. Giovambattista, N., Debenedetti, P. G. & Rossky, P. J. Hydration behavior under confinement by nanoscale surfaces with patterned hydrophobicity and hydrophilicity. *J. Phys. Chem. C* **111**, 1323–1332 (2007).
 71. Bradford, S. M., Fisher, E. A. & Meli, M. V. Ligand shell composition-dependent effects on the apparent hydrophobicity and film behavior of gold nanoparticles at the air-water interface. *Langmuir* **32**, 9790–9796 (2016).
 72. Liu, X., Hu, Y. & Stellacci, F. Mixed-ligand nanoparticles as supramolecular receptors. *Small* **7**, 1961–1966 (2011).
 73. Van Lehn, R. C. & Alexander-Katz, A. Structure of Mixed-Monolayer-Protected Nanoparticles in Aqueous Salt Solution from Atomistic Molecular Dynamics Simulations. *J. Phys. Chem. C* **117**, 20104–20115 (2013).
 74. Hung, A. *et al.* Ordering surfaces on the nanoscale: Implications for protein adsorption. *J. Am. Chem. Soc.* **133**, 1438–1450 (2011).
 75. Stamatoiu, O., Mirzaei, J., Feng, X. & Hegmann, T. Nanoparticles in liquid crystals and liquid crystalline nanoparticles. *Top. Curr. Chem.* **318**, 331–394 (2012).
 76. Choudhary, A., Singh, G. & Biradar, A. M. Advances in gold nanoparticle-liquid crystal composites. *Nanoscale* **6**, 7743–56 (2014).
 77. Mangal, R. *et al.* Active Janus Particles at Interfaces of Liquid Crystals. *Langmuir* **33**, 10917–10926 (2017).
 78. Huang, R., Carney, R. P., Ikuma, K., Stellacci, F. & Lau, B. L. T. Effects of surface compositional and structural heterogeneity on nanoparticle-protein interactions: Different protein configurations. *ACS Nano* **8**, 5402–5412 (2014).
 79. Stellacci, F. *et al.* Effect of Particle Diameter and Surface Composition on the Spontaneous Fusion of Monolayer-Protected Gold Nanoparticles with Lipid Bilayers. **13**, 4060–4067 (2013).
 80. Campos, E. *et al.* Sensing single mixed-monolayer protected gold nanoparticles by the α -hemolysin nanopore. *Anal. Chem.* **85**, 10149–10158 (2013).
 81. Posocco, P. *et al.* Self-organization of mixtures of fluorocarbon and hydrocarbon

- amphiphilic thiolates on the surface of gold nanoparticles. *ACS Nano* **6**, 7243–53 (2012).
82. Van Lehn, R. C. *et al.* Lipid tail protrusions mediate the insertion of nanoparticles into model cell membranes. *Nat. Commun.* **5**, 4482 (2014).
 83. Liu, X. *et al.* Mixed-charge nanoparticles for long circulation, low reticuloendothelial system clearance, and high tumor accumulation. *Adv. Healthc. Mater.* **3**, 1439–47 (2014).
 84. Yang, H., Heng, X. & Hu, J. Salt- and pH-resistant gold nanoparticles decorated with mixed-charge zwitterionic ligands, and their pH-induced concentration behavior. *RSC Adv.* **2**, 12648 (2012).
 85. Lee, H. Y. *et al.* Self-assembly of nanoparticle amphiphiles with adaptive surface chemistry. *ACS Nano* **8**, 9979–9987 (2014).
 86. Iida, R. *et al.* Synthesis of janus-like gold nanoparticles with hydrophilic/hydrophobic faces by surface ligand exchange and their self-assemblies in water. *Langmuir* **31**, 4054–4062 (2015).
 87. Bain, C. D. *et al.* Formation of monolayer films by the spontaneous assembly of organic thiols from solution onto gold. *J. Am. Chem. Soc.* **111**, 321–335 (1989).
 88. Fleury, B. *et al.* Gold Nanoparticle Internal Structure and Symmetry Probed by Unified Small-Angle X-ray Scattering and X-ray Diffraction Coupled with Molecular Dynamics Analysis. *Nano Lett.* **15**, 6088–94 (2015).
 89. Kong, W. *et al.* A general strategy for ligand exchange on upconversion nanoparticles. *Inorg. Chem.* **56**, 872–877 (2017).
 90. Si, S. *et al.* Ligand Exchange on Au 25 Cluster with Chiral Thiols. 12966–12969 (2009).
 91. Abdulhalim, L. G., Kothalawala, N., Sinatra, L., Dass, A. & Bakr, O. M. Neat and complete: Thiolate-ligand exchange on a silver molecular nanoparticle. *J. Am. Chem. Soc.* **136**, 15865–15868 (2014).
 92. Pettibone, J. M. & Hudgens, J. W. Gold cluster formation with phosphine ligands: etching as a size-selective synthetic pathway for small clusters? *ACS Nano* **5**, 2989–3002 (2011).
 93. Korpany, K. V. *et al.* One-step ligand exchange and switching from hydrophobic to water-stable hydrophilic superparamagnetic iron oxide nanoparticles by mechanochemical milling. *Chem. Commun.* **52**, 3054–3057 (2016).
 94. Smith, A. M. *et al.* Quantitative Analysis of Thiolated Ligand Exchange on Gold Nanoparticles Monitored by ¹H NMR Spectroscopy. *Anal. Chem.* 150206131724008 (2015). doi:10.1021/ac504081k
 95. Pradhan, S., Brown, L. E., Konopelski, J. P. & Chen, S. Janus nanoparticles: Reaction dynamics and NOESY characterization. *J. Nanoparticle Res.* **11**, 1895–1903 (2009).
 96. Busby, M., Chiorboli, C. & Scandola, F. Relaxation dynamics and transient behavior of small arenethiol passivated gold nanoparticles. *J. Phys. Chem. B* **110**, 6020–6 (2006).

97. Kassam, A., Bremner, G., Clark, B., Ulibarri, G. & Lennox, R. B. Place exchange reactions of alkyl thiols on gold nanoparticles. *J. Am. Chem. Soc.* **128**, 3476–7 (2006).
98. Lucarini, M. *et al.* ESR spectroscopy as a tool to investigate the properties of self-assembled monolayers protecting gold nanoparticles. *Nanoscale* **2**, 668 (2010).
99. Ionita, P., Caragheorgheopol, A., Gilbert, B. C. & Chechik, V. EPR study of a place-exchange reaction on Au nanoparticles: two branches of a disulfide molecule do not adsorb adjacent to each other. *J. Am. Chem. Soc.* **124**, 9048–9 (2002).
100. Sperling, R. A. & Parak, W. J. Surface modification, functionalization and bioconjugation of colloidal inorganic nanoparticles. *Philos. Trans. R. Soc. A Math. Phys. Eng. Sci.* **368**, 1333–1383 (2010).
101. Synthesis, T., Nanoparticles, A. & Interface, L. Templated Synthesis of Amphiphilic Nanoparticles at the Liquid–Liquid Interface. 1044–1050 (2012).
102. Matsui, J. *et al.* Molecularly imprinted nanocomposites for highly sensitive SPR detection of a non-aqueous atrazine sample. *Analyst* **134**, 80–6 (2009).
103. Stirling, J. *et al.* Critical assessment of the evidence for striped nanoparticles. *PLoS One* **9**, e108482 (2014).
104. Yu, M. & Stellacci, F. Response to ‘Stripy Nanoparticles Revisited’. *Small* **8**, 3720–3726 (2012).
105. Ong, Q. K., Zhao, S., Reguera, J., Biscarini, F. & Stellacci, F. Comparative STM studies of mixed ligand monolayers on gold nanoparticles in air and in 1-phenyloctane. *Chem. Commun.* **50**, 10456–10459 (1045).
106. Biscarini, F. *et al.* Quantitative analysis of scanning tunneling microscopy images of mixed-ligand-functionalized nanoparticles. *Langmuir* **29**, 13723–13734 (2013).
107. Ong, Q. K. *et al.* High-resolution scanning tunneling microscopy characterization of mixed monolayer protected gold nanoparticles. *ACS Nano* **7**, 8529–8539 (2013).
108. Moglianetti, M. *et al.* Scanning tunneling microscopy and small angle neutron scattering study of mixed monolayer protected gold nanoparticles in organic solvents. *Chem. Sci.* **5**, 1232 (2014).
109. Lee, Z. *et al.* Direct Imaging of Soft–Hard Interfaces Enabled by Graphene. *Nano Lett.* **9**, 3365 (2009).
110. Yang, J. A. & Murphy, C. J. Evidence for Patchy Lipid Layers on Gold Nanoparticle Surfaces. (2012).
111. Meena, S. K. *et al.* Nanophase Segregation of Self-Assembled Monolayers on Gold Nanoparticles. *ACS Nano* **11**, 7371–7381 (2017).
112. Ishima, R. & Torchia, D. A. Protein dynamics from NMR. *Nature Structural Biology* **7**, 740–743 (2000).
113. Dyson, H. J. & Wright, P. E. Unfolded proteins and protein folding studied by NMR. *Chem. Rev.* **104**, 3607–3622 (2004).
114. Marbella, L. E. & Millstone, J. E. NMR Techniques for Noble Metal Nanoparticles.

Chem. Mater. 150311080127008 (2015). doi:10.1021/cm504809c

115. Ansar, S. M. *et al.* Determination of the binding affinity, packing, and conformation of thiolate and thione ligands on gold nanoparticles. *J. Phys. Chem. C* **115**, 653–660 (2011).
116. Salorinne, K. *et al.* Conformation and dynamics of the ligand shell of a water-soluble Au102 nanoparticle. *Nat. Commun.* **7**, 10401 (2016).
117. Schmitt, H., Badia, a, Dickinson, L., Reven, L. & Lennox, R. B. The Effect of Terminal Hydrogen Bonding on the Structure and Dynamics of Nanoparticle Self-Assembled Monolayers (SAMs): An NMR Dynamics Study. *Adv. Mater.* **10**, 475–80 (1998).
118. Badia, A., Cuccia, L., Demers, L., Morin, F. & Lennox, R. B. Structure and dynamics in alkanethiolate monolayers self-assembled on gold nanoparticles: A DSC, FT-IR, and deuterium NMR study. *J. Am. Chem. Soc.* **119**, 2682–2692 (1997).
119. Terrill, R. & Postlethwaite, T. Monolayers in three dimensions: NMR, SAXS, thermal, and electron hopping studies of alkanethiol stabilized gold clusters. *J. Am. Chem. Soc.* **117**, 12537–12548 (1995).
120. Zoppo, M. & Zerbi, G. in *Solidification Processes in Polymers* 48–50 (Steinkopff, 1992). doi:10.1007/BFb0115575
121. Centrone, A., Hu, Y., Jackson, A. M., Zerbi, G. & Stellacci, F. Phase separation on mixed-monolayer-protected metal nanoparticles: A study by infrared spectroscopy and scanning tunneling microscopy. *Small* **3**, 814–817 (2007).
122. El-Aneed, A., Cohen, A. & Banoub, J. Mass spectrometry, review of the basics: Electrospray, MALDI, and commonly used mass analyzers. *Applied Spectroscopy Reviews* **44**, 210–230 (2009).
123. Harkness, K. M., Cliffel, D. E. & McLean, J. A. Characterization of thiolate-protected gold nanoparticles by mass spectrometry. *Analyst* **135**, 868 (2010).
124. Dass, A., Stevenson, A., Dubay, G. R., Tracy, J. B. & Murray, R. W. Nanoparticle MALDI-TOF mass spectrometry without fragmentation: Au₂₅(SCH₂CH₂Ph)₁₈ and mixed monolayer Au₂₅(SCH₂CH₂Ph)_(18-x)(L)_x. *J. Am. Chem. Soc.* **130**, 5940–6 (2008).
125. Harkness, K. M. *et al.* Ag₄₄(SR)₃₀(4-): a silver-thiolate superatom complex. *Nanoscale* **4**, 4269–74 (2012).
126. Dass, A. Faradaurate nanomolecules: A superstable plasmonic 76.3 kDa cluster. *J. Am. Chem. Soc.* **133**, 19259–19261 (2011).
127. Kumara, C. & Dass, A. Au₃₂₉(SR)₈₄ nanomolecules: compositional assignment of the 76.3 kDa plasmonic faradaurates. *Anal. Chem.* **86**, 4227–32 (2014).
128. Kumara, C., Zuo, X., Ilavsky, J., Cullen, D. & Dass, A. Atomic Structure of Au 329 (SR) 84 Faradaurate Plasmonic Nanomolecules. *J. Phys. Chem. C* **329**, 150403102853007 (2015).
129. Kumara, C., Zuo, X., Cullen, D. A. & Dass, A. Faradaurate-940: Synthesis, Mass Spectrometry, Electron Microscopy, High-Energy X-ray Diffraction, and X-ray

- Scattering Study of Au $\sim 940 \pm 20$ (SR) $\sim 160 \pm 4$ Nanocrystals. *ACS Nano* **8**, 6431–6439 (2014).
130. Harkness, K. M., Balinski, A., McLean, J. a & Clifffel, D. E. Nanoscale phase segregation of mixed thiolates on gold nanoparticles. *Angew. Chem. Int. Ed. Engl.* **50**, 10554–9 (2011).
 131. Farrell, Z. *et al.* Development of Experiment and Theory to Detect and Predict Ligand Phase Separation on Silver Nanoparticles. *Angew. Chemie* **127**, 6579–6582 (2015).
 132. Ma, Y. & Chechik, V. Aging of gold nanoparticles: ligand exchange with disulfides. *Langmuir* **27**, 14432–7 (2011).
 133. Gentilini, C. *et al.* Formation of patches on 3D SAMs driven by thiols with immiscible chains observed by ESR spectroscopy. *Angew. Chemie - Int. Ed.* **48**, 3060–3064 (2009).
 134. Bonomi, R., Cazzolaro, A. & Prins, L. J. Assessment of the morphology of mixed SAMs on Au nanoparticles using a fluorescent probe. *Chem. Commun. (Camb)*. **47**, 445–7 (2011).
 135. Stewart, A., Zheng, S., McCourt, M. R. & Bell, S. E. J. Controlling assembly of mixed thiol monolayers on silver nanoparticles to tune their surface properties. *ACS Nano* **6**, 3718–3726 (2012).
 136. Camilloni, C. *et al.* Towards a structural biology of the hydrophobic effect in protein folding. *Sci. Rep.* **6**, 28285 (2016).
 137. Chandler, D. Interfaces and the driving force of hydrophobic assembly. *Nature* **437**, 640–647 (2005).
 138. Snyder, P. W. *et al.* Mechanism of the hydrophobic effect in the biomolecular recognition of arylsulfonamides by carbonic anhydrase. *Proc. Natl. Acad. Sci.* **108**, 17889–17894 (2011).
 139. Jones, S. & Thornton, J. M. Analysis of protein-protein interaction sites using surface patches. *J. Mol. Biol.* **272**, 121–132 (1997).
 140. Killian, J. A. & Von Heijne, G. How proteins adapt to a membrane-water interface. *Trends in Biochemical Sciences* **25**, 429–434 (2000).
 141. Whitford, D. *Proteins : structure and function*. (J. Wiley & Sons, 2005).
 142. Van Lehn, R. C. & Alexander-Katz, A. Membrane-embedded nanoparticles induce lipid rearrangements similar to those exhibited by biological membrane proteins. *J. Phys. Chem. B* **118**, 12586–12598 (2014).
 143. Van Lehn, R. C. & Alexander-Katz, A. Free energy change for insertion of charged , monolayer-protected nanoparticles into lipid bilayers. *Soft Matter* **10**, 648 (2014).
 144. Lin, J. & Alexander-Katz, A. Cell membranes open ‘doors’ for cationic nanoparticles/biomolecules: insights into uptake kinetics. *ACS Nano* **7**, 10799–808 (2013).
 145. Burkhard, P., Stetefeld, J. & Strelkov, S. V. Coiled coils: A highly versatile protein folding motif. *Trends in Cell Biology* **11**, 82–88 (2001).

146. Lemmon, M. A., Flanagan, J. M., Treutlein, H. R., Zhang, J. & Engelman, D. M. Sequence Specificity in the Dimerization of Transmembrane β -Helixes. *Biochemistry* **31**, 12719–12725 (1992).
147. Lupas, A. Coiled coils: New structures and new functions. *Trends in Biochemical Sciences* **21**, 375–382 (1996).
148. Klabunde, T., Eicken, C., Sacchettini, J. C. & Krebs, B. Crystal structure of a plant catechol oxidase containing a dicopper center. *Nature Structural Biology* **5**, 1084–1090 (1998).
149. Isom, D. G., Castaneda, C. A., Cannon, B. R. & Garcia-Moreno E., B. Large shifts in pKa values of lysine residues buried inside a protein. *Proc. Natl. Acad. Sci.* **108**, 5260–5265 (2011).
150. Koshland, D. E. The Key–Lock Theory and the Induced Fit Theory. *Angewandte Chemie International Edition in English* **33**, 2375–2378 (1995).
151. Isom, D. G., Cannon, B. R., Castañeda, C. A., Robinson, A. & García-Moreno E, B. High tolerance for ionizable residues in the hydrophobic interior of proteins. *Proc. Natl. Acad. Sci. U. S. A.* **105**, 17784–17788 (2008).
152. Chen, S. *et al.* Subnanoscale hydrophobic modulation of salt bridges in aqueous media. *Science* (80-.). **348**, 555–559 (2015).
153. Campagnola, P. J. *et al.* Three-dimensional high-resolution second-harmonic generation imaging of endogenous structural proteins in biological tissues. *Biophys. J.* **82**, 493–508 (2002).
154. Koster, A. J. & Klumperman, J. Electron microscopy in cell biology: integrating structure and function. *Nat. Rev. Mol. Cell Biol.* **Suppl**, SS6-10 (2003).
155. Hansma, H. G. *et al.* Probing biopolymers with the atomic force microscope: A review. *Journal of Biomaterials Science, Polymer Edition* **11**, 675–683 (2000).
156. Percy, A. J., Rey, M., Burns, K. M. & Schriemer, D. C. Probing protein interactions with hydrogen/deuterium exchange and mass spectrometry-A review. *Analytica Chimica Acta* **721**, 7–21 (2012).
157. Mertens, H. D. T. & Svergun, D. I. Structural characterization of proteins and complexes using small-angle X-ray solution scattering. *J. Struct. Biol.* **172**, 128–141 (2010).
158. Feigin, L. A. & Svergun, D. I. *Structure Analysis by Small-Angle X-Ray and Neutron Scattering. Current Opinion in Structural Biology* **12**, (Springer US, 1987).
159. Sivia, D. S. *Elementary scattering theory : for X-ray and neutron users.* (Oxford University Press, 2011).
160. Svergun, Dmitri; Koch, Michel H. J.; Timmins, Peter A.; May, R. P. *Small Angle X-Ray and Neutron Scattering from Solutions of Biological Macromolecules.* (Oxford University Press, 2013). doi:10.1093/acprof:oso/9780199639533.001.0001
161. Svergun, D. I. Determination of the regularization parameter in indirect-transform methods using perceptual criteria. *J. Appl. Crystallogr.* **25**, 495–503 (1992).

162. Petoukhov, M. V. *et al.* New developments in the ATSAS program package for small-angle scattering data analysis. *J. Appl. Crystallogr.* **45**, 342–350 (2012).
163. Rambo, R. P. & Tainer, J. A. Super-Resolution in Solution X-Ray Scattering and Its Applications to Structural Systems Biology SAXS: small-angle X-ray scattering. *Annu. Rev. Biophys* **42**, 415–41 (2013).
164. Konarev, P. V., Petoukhov, M. V. & Svergun, D. I. MASSHA - A graphics system for rigid-body modelling of macromolecular complexes against solution scattering data. *J. Appl. Crystallogr.* **34**, 527–532 (2001).
165. Svergun, D. I. Restoring low resolution structure of biological macromolecules from solution scattering using simulated annealing. *Biophys. J.* **76**, 2879–2886 (1999).
166. Franke, D., Jeffries, C. M. & Svergun, D. I. Correlation Map, a goodness-of-fit test for one-dimensional X-ray scattering spectra. *Nat. Methods* **12**, 419–422 (2015).
167. Franke, D. *et al.* ATSAS 2.8: A comprehensive data analysis suite for small-angle scattering from macromolecular solutions. *J. Appl. Crystallogr.* **50**, 1212–1225 (2017).
168. Svergun, D. I., Petoukhov, M. V & Koch, M. H. J. Determination of domain structure of proteins from x-ray solution scattering. *Biophys. J.* **80**, 2946–2953 (2001).
169. Mertens, H. D. T. & Svergun, D. I. Combining NMR and small angle X-ray scattering for the study of biomolecular structure and dynamics. *Arch. Biochem. Biophys.* **628**, 33–41 (2017).
170. Petoukhov, M. V & Svergun, D. I. Global Rigid Body Modeling of Macromolecular Complexes against Small-Angle Scattering Data. *Biophys. J.* **89**, 1237–1250 (2005).
171. Blanchet, C. E. & Svergun, D. I. Small-Angle X-Ray Scattering on Biological Macromolecules and Nanocomposites in Solution. *Annu. Rev. Phys. Chem.* **64**, 37–54 (2013).
172. Tuukkanen, A. T., Spilotros, A. & Svergun, D. I. Progress in small-angle scattering from biological solutions at high-brilliance synchrotrons. *IUCrJ* **4**, 518–528 (2017).
173. Peters, K. & Richards, F. M. Chemical cross-linking: reagents and problems in studies of membrane structure. *Annu. Rev. Biochem.* **46**, 523–551 (1977).
174. Sinz, A. Chemical cross-linking and mass spectrometry to map three-dimensional protein structures and protein-protein interactions. *Mass Spectrom. Rev.* **25**, 663–682 (2006).
175. Konermann, L., Vahidi, S. & Sowole, M. A. Mass spectrometry methods for studying structure and dynamics of biological macromolecules. *Anal. Chem.* **86**, 213–232 (2014).
176. El-Shafey, A. *et al.* ‘Zero-length’ cross-linking in solid state as an approach for analysis of protein-protein interactions. *Protein Sci.* **15**, 429–40 (2006).
177. Weiss. *Hydrogen Exchange Mass Spectrometry of Proteins: Fundamentals, Methods, and Applications.* (2016). at
<<https://books.google.com/books?hl=en&lr=&id=8nZjCwAAQBAJ&pgis=1>>
178. Pons-Siepermann, I. C. & Glotzer, S. C. Design of patchy particles using quaternary

- self-assembled monolayers. *ACS Nano* **6**, 3919–3924 (2012).
179. Petoukhov, M. V & Svergun, D. I. Applications of small-angle X-ray scattering to biomacromolecular solutions. *Int. J. Biochem. Cell Biol.* **45**, 429–37 (2013).
 180. Diroll, B. T. *et al.* Quantifying ‘softness’ of Organic Coatings on Gold Nanoparticles Using Correlated Small-Angle X-ray and Neutron Scattering. *Nano Lett.* **15**, 8008–8012 (2015).
 181. Von White, G., Mohammed, F. S. & Kitchens, C. L. Small-angle neutron scattering investigation of gold nanoparticle clustering and ligand structure under antisolvent conditions. *J. Phys. Chem. C* **115**, 18397–18405 (2011).
 182. Kim, S., Kim, T. H., Huh, J., Bang, J. & Choi, S. H. Nanoscale phase behavior of mixed polymer ligands on a gold nanoparticle surface. *ACS Macro Lett.* **4**, 417–421 (2015).
 183. Zheng, N., Fan, J. & Stucky, G. D. One-Step One-Phase Synthesis of Monodisperse Noble-Metallic Nanoparticles and Their Colloidal Crystals. 6550–6551 (2006).
 184. Konarev, P. V., Volkov, V. V., Sokolova, A. V., Koch, M. H. J. & Svergun, D. I. PRIMUS: A Windows PC-based system for small-angle scattering data analysis. *J. Appl. Crystallogr.* **36**, 1277–1282 (2003).
 185. Burian, M. *et al.* Considerations on the model-free shape retrieval of inorganic nanocrystals from small-angle scattering data. *J. Appl. Crystallogr.* **48**, 857–868 (2015).
 186. Jimenez, V. L., Leopold, M. C., Mazzitelli, C., Jorgenson, J. W. & Murray, R. W. HPLC of monolayer-protected gold nanoclusters. *Anal. Chem.* **75**, 199–206 (2003).
 187. Yang, H. *et al.* Crystal structure of a luminescent thiolated Ag nanocluster with an octahedral Ag₆(4⁺) core. *Chem. Commun. (Camb)*. **49**, 300–2 (2013).
 188. Jin, R. Quantum sized, thiolate-protected gold nanoclusters. *Nanoscale* **2**, 343–362 (2010).
 189. Jin, R., Zeng, C., Zhou, M. & Chen, Y. Atomically Precise Colloidal Metal Nanoclusters and Nanoparticles: Fundamentals and Opportunities. *Chemical Reviews* **116**, 10346–10413 (2016).
 190. Jadzinsky, P. D., Calero, G., Ackerson, C. J., Bushnell, D. A. & Kornberg, R. D. Structure of a thiol monolayer-protected gold nanoparticle at 1.1 Å resolution. *Science* **318**, 430–3 (2007).
 191. Yang, H. *et al.* All-thiol-stabilized Ag₄₄ and Au₁₂Ag₃₂ nanoparticles with single-crystal structures. *Nat. Commun.* **4**, 2422 (2013).
 192. Desiredy, A. *et al.* Ultrastable silver nanoparticles. *Nature* **501**, 399–402 (2013).
 193. Yang, H., Wang, Y. & Zheng, N. Stabilizing subnanometer Ag(0) nanoclusters by thiolate and diphosphine ligands and their crystal structures. *Nanoscale* **5**, 2674–7 (2013).
 194. Jin, R. Atomically precise metal nanoclusters: stable sizes and optical properties. *Nanoscale* **7**, 1549–1565 (2015).

195. Rambo, R. P. & Tainer, J. A. Accurate assessment of mass, models and resolution by small-angle scattering. *Nature* **496**, 477–81 (2013).
196. McGreevy, R. L. Reverse Monte Carlo modelling. *Journal of Physics Condensed Matter* **13**, R877–R913 (2001).
197. McGreevy, R. L. & Pusztai, L. Reverse Monte Carlo Simulation: A New Technique for the Determination of Disordered Structures. *Mol. Simul.* **1**, 359–367 (1988).
198. Keen, D. A. & McGreevy, R. L. Structural modelling of glasses using reverse Monte Carlo simulation. *Nature* **344**, 423–425 (1990).
199. Wills, a. . A new protocol for the determination of magnetic structures using simulated annealing and representational analysis (SARAh). *Phys. B Condens. Matter* **276–278**, 680–681 (2000).
200. Cuadros, J., Sainz-Díaz, C. I., Ramírez, R. & Hernández-Laguna, A. Analysis of Fe segregation in the octahedral sheet of bentonitic illite-smectite by means of FTIR, ²⁷Al MAS NMR and reverse Monte Carlo simulations. *Am. J. Sci.* **299**, 289–308 (1999).
201. Zheng, N., Fan, J. & Stucky, G. D. One-step one-phase synthesis of monodisperse noble-metallic nanoparticles and their colloidal crystals. *J. Am. Chem. Soc.* **128**, 6550–1 (2006).
202. Lee, H. Y. *et al.* Self-assembly of nanoparticle amphiphiles with adaptive surface chemistry. *ACS Nano* **8**, 9979–9987 (2014).
203. Harkness, K. M., Fenn, L. S., Cliffel, D. E. & McLean, J. A. Surface fragmentation of complexes from thiolate protected gold nanoparticles by ion mobility-mass spectrometry. *Anal. Chem.* **82**, 3061–3066 (2010).
204. Makarov, V., Pettitt, B. M. & Feig, M. Solvation and Hydration of Proteins and Nucleic Acids: A Theoretical View of Simulation and Experiment. *Acc. Chem. Res.* **35**, 376–384 (2002).
205. Fenimore, P. W., Frauenfelder, H., McMahon, B. H. & Parak, F. G. Slaving: Solvent fluctuations dominate protein dynamics and functions. *Proc. Natl. Acad. Sci.* **99**, 16047–16051 (2002).
206. Khodadadi, S. *et al.* Dynamics of biological macromolecules: not a simple slaving by hydration water. *Biophys. J.* **98**, 1321–1326 (2010).
207. Ma, C. D., Wang, C., Acevedo-Vélez, C., Gellman, S. H. & Abbott, N. L. Modulation of hydrophobic interactions by proximally immobilized ions. *Nature* **517**, 347–350 (2015).
208. Smolentsev, N., Smit, W. J., Bakker, H. J. & Roke, S. The interfacial structure of water droplets in a hydrophobic liquid. *Nat. Commun.* **8**, 15548 (2017).

Curriculum Vitae

Zhi Luo

École Polytechnique Fédérale de Lausanne
MXH 130 (Bâtiment MXH), Station 12
CH-1015 Lausanne, Switzerland

Phone: +41 787364379
Email: zhi.luo@epfl.ch

Education

École Polytechnique Fédérale de Lausanne, Switzerland

Ph.D. in Materials Science and Engineering Aug. 2013 – Present
Thesis: Advanced characterization methods for self-assembled organization on nanoparticles
Thesis advisor: Professor Francesco Stellacci

Tsinghua University, China

B.Eng. in Polymer Materials and Engineering Sept. 2009 – Jul. 2013
Thesis: Synthesis of biocompatible hydrogels based on Cyclodextrin/PEG polyrotaxane
Thesis advisor: Professor Yanbin Huang

Research Experience

Doctoral assistant, École Polytechnique Fédérale de Lausanne Aug. 2013 – Present
Lab of Professor Francesco Stellacci

- Characterized mixed ligand nanoparticles using small angle neutron scattering
- Investigated of interfacial water structure near nanoscale patterned surfaces
- Performed Monte Carlo calculations for MALDI-TOF spectra on nanoparticles
- Investigated the mechanisms of ligand exchange reactions on nanoparticles
- Developed new methods for the study of atomically precise nanoclusters
- Control the morphologies of mixed ligand nanoparticles with thermal treatment

Undergraduate research assistant, Tsinghua University Jun. 2011– Jun. 2013
Lab of Professor Yanbin Huang

- Investigated the threading mechanisms of cyclodextrin onto PEG
- Synthesized polyrotaxane using glutathione as the biocompatible end capper
- Synthesized polymers based on allyl-compounds for application in diet drug

Research intern, Chinese Academy of Sciences Jun. 2011- Aug. 2011
Lab of Professor Zhibo Li, co-supervised by Professor Harm-Anton Klok

- Synthesized Y-shape thermo-responsive polymer brush via controlled polymerization

Work Experience

Teacher, Phosphorus Education Company, China Jun. 2012 – Feb. 2013

- Math teacher for middle school students

Research intern, Sinopec Beijing Yanshan Company, China Aug. 2012

- Studied catalytic cracking process in oil refinery

Mentoring Experience

Teaching assistant, École Polytechnique Fédérale de Lausanne

Thermodynamics for material science
Surfaces and interfaces

2013 & 2014
2015

Master project supervisor

- Jing Hou (Fall 2015- Fall 2016)
Thesis title: Self-assembly behaviour of polymer grafted mixed ligand nanoparticles

Master semester project supervisor

- Jérôme Genton (Fall 2017)
Project title: Hydrogen-deuterium exchange mass spectrometry study of nanoparticles
- Baichuan Kou (Fall 2017)
Project title: Kinetics study of mixed ligand nanoparticle under thermal treatment
- Yue Wang (Spring 2017)
Project title: MALDI-TOF MS study of silver nanoparticles
- Lorenzo Vigo (Spring 2017)
Project title: Fractionation of mixed ligand protected atomically precise nanoclusters
- Yanfei Zhao (Fall 2016)
Project title: Theoretical calculations of MALDI-TOF spectra of nanoparticles
- Maxime Burgonse (Spring 2015)
Project title: Crystallization of silver nanoparticles
- Sebastian Wronski (Fall 2014)
Project title: Colloidal stability of ionic liquid grafted nanoparticles

Scholarships and Awards

- 'Highlight proposal' of the year, Heinz Maier-Leibnitz Zentrum 2015
- YuCaojian Scholarship for Excellent Students, Tsinghua University 2013
- Departmental Scholarship for Outstanding Students, Tsinghua University 2012
- Grand Prize for Chemical Product Design Competition 2011

Invited Talks

International Conference on Neutron Scattering (ICNS), Korean

Jul. 2017

Invited Oral Presentation: Small angle neutron scattering on Patchy Nanoparticles

Heinz Maier-Leibnitz Zentrum & Technical University of Munich, Germany

Feb. 2017

Invited Seminar: Structure and Interfacial Properties of Patchy Nanoparticles

Publications

[8] "Interpretation of MALDI-TOF spectra on mixed self-assembled monolayers using Monte Carlo calculations." **Zhi Luo**, Yanfei Zhao, Yue Wang, Aurel Radulescu, Francesco Stellacci. *In preparation*

[7] "Structure of interfacial water at nanoscale heterogeneous surfaces." **Zhi Luo***, Anna Murello*, David M. Wilkins, Filip Kovacic, Joachim Kohlbrecher, Aurel Radulescu, Quy K. Ong, Nikolaos Nianias, Halil I. Okur, Nikolay Smolentsev, Michele Ceriotti, Sylvie Roke, Francesco Stellacci. *In preparation*

[6] "Quantitative 3D determination of self-assembled structures on nanoparticles using small angle neutron scattering." **Zhi Luo**, Domenico Marson, Quy K. Ong, Anna Loiudice, Joachim Kohlbrecher, Aurel Radulescu, Anwen Krause-Heuer, Tamim Darwish, Sandor Balog, Raffaella Buonsanti, Dmitri I. Svergun, Paola Posocco & Francesco Stellacci. **Nature Communications**. *Just Accepted*

[5] "On the van der Waals interactions of n-alkanethiol covered Surfaces: From planar to curved surfaces." Fernando Cometto, **Zhi Luo**, Shun Zhao, Jimena Olmos-Asar, Marcelo Mariscal, Quy Ong, Klaus Kern, Francesco Stellacci, and Magalí Lingenfelder. **Angewandte Chemie** 129, no. 52 (2017): 16753-16757.

[4] "Evolution of the Ligand Shell Morphology during Ligand Exchange Reactions on Gold Nanoparticles." **Zhi Luo***, Jing Hou*, Laure Menin, Quy Khac Ong, and Francesco Stellacci. **Angewandte Chemie** 129, no. 43 (2017): 13706-13710.

[3] "Characterization of Ligand Shell for Mixed-Ligand Coated Gold Nanoparticles." Ong Quy*, **Zhi Luo***, and Francesco Stellacci. **Accounts of chemical research** 50, no. 8 (2017): 1911-1919.

[2] "Freestanding Ultrathin Nanoparticle Membranes Assembled at Transient Liquid–Liquid Interfaces." Le Ouay, Benjamin, Stefan Guldin, **Zhi Luo**, Sergio Allegri, and Francesco Stellacci. **Advanced Materials Interfaces** 3, no. 15 (2016): 1600191

[1] Song, Qiao, **Zhi Luo**, Xinming Tong, Yi Du, and Yanbin Huang. "Glutathione as the end capper for cyclodextrin/PEG polyrotaxanes." **Chinese Journal of Polymer Science** 32, no. 8 (2014): 1003-1009.

Synchrotron Beamtimes and Grants

European Synchrotron Radiation Facility (4 Shifts)	2016
Institut Laue–Langevin (2 Days)	2016
Jülich Centre for Neutron Science (11 Days)	2014-2017
Australian Nuclear Science and Technology Organisation (3 Days , Grant: \$ 26,880)	2014
Paul Scherrer Institute (18 Days)	2013-2017

Professional Skills

Experimental: SAXS/SANS, (Cryo-)TEM, MALDI-TOF MS, AFM, XPS, HPLC, NMR, DSC, FTIR, TGA, Ellipsometry, DLS, etc.

Programming: Python, Matlab, C, R, Igor Pro